Experiments on Laser-Based Particle Acceleration

Beams of Energetic Electrons and Protons

Svensson, Kristoffer

2016

Document Version:
Publisher's PDF, also known as Version of record

Experiments on Laser-Based Particle Acceleration

Beams of Energetic Electrons and Protons

Kristoffer Svensson

Doctoral Thesis
2016

LUND
UNIVERSITY

Experiments on Laser-Based Particle Acceleration –
Beams of Energetic Electrons and Protons

Printed in Sweden by Media-Tryck, Lund, 2016

Division of Atomic Physics
Department of Physics
Faculty of Engineering, LTH
Lund University
P.O. Box 118
SE–221 00 Lund
Sweden

http://www.atomic.physics.lu.se

Lund Reports on Atomic Physics, LRAP-527

ISBN: 978-91-7623-944-5 (print)
ISBN: 978-91-7623-945-2 (pdf)
ISSN: 0281-2762

To Elisabeth —You are the sunshine of my life.

Abstract

This thesis describes experiments involving laser-plasma-based acceleration of electrons and protons, using the techniques of laser wakefield acceleration (LWFA) and target normal sheath acceleration (TNSA). By using extremely high accelerating field strengths, up to the order of TV m^{-1}, it is possible to reach high kinetic particle energies over very short distances.

The multi-terawatt laser system at the Lund Laser Centre, with focused laser pulse intensities reaching over 10^{19} W cm^{-2}, was used in these experiments. The laser pulses were focused on different types of targets, depending on the acceleration technique. When using LWFA, the target was usually a gas, which is instantly ionized. As the laser pulse propagates through the plasma, a plasma wave is induced that can be used to accelerate electrons. As the electrons are accelerated, they also oscillate about the central axis, which produces betatron radiation that extends to x-ray energies. In the experimental investigations presented in this thesis, both supersonic gas jets and gas-filled capillary tubes were used as targets. When using TNSA, the targets were usually aluminum foils, while some experiments were carried out on structured targets and very small hollow spheres. When the laser pulse hits a solid target, electrons from the front surface of the target are driven through the target. As these electrons exit the rear surface, they form an electron sheath, which creates very strong electrical fields, in which positively charged particles, such as protons, can be accelerated.

In some of the LWFA experiments, electrons automatically enter the accelerating part of the plasma wave through a stochastic process called self-injection. This process was studied, and it was shown that temporal and spectral laser pulse self-compression and focal spot quality are important for electron injection to occur. A model predicting when self-injection occurs for certain parameters was also developed. In another study, it was found that the number density in supersonic gas flows depends on the choice of gas. To obtain better control over how the electrons are injected, density gradient injection was used, which resulted in electron beams with increased charge, decreased spatial divergence, and better shot-to-shot stability compared to electron beams relying on self-injection.

Experiments using gas-filled dielectric capillaries showed an order of magnitude increase in x-ray fluence compared to supersonic gas jets. The acceleration and x-ray

generation processes in capillary tubes were also studied in more detail, showing that the processes occurred over several millimeters.

In two of the TNSA studies, double laser pulses were used. It was found that the spatial separation and relative intensities of the two pulses were important, and affected the spatial profile of the resulting proton beams. A laser pulse separation on the order of the size of the laser spot was found to result in elliptical proton beam profiles. Furthermore, the elliptical profile could be tilted by changing the relative intensities of the two laser pulses, as a result of the transverse expansion of the electron sheath. This sheath expansion was also utilized with the hollow spherical targets, where an increase in proton number was observed in the energy range 5.5 MeV to 6.5 MeV.

Experiments on thin foil targets with very small surface structures showed that the spatial divergence of the proton beams was greatly affected by the structures on the rear surface.

Populärvetenskaplig sammanfattning

Inom vetenskap och forskning används ofta partiklar som färdas med hög hastighet. Partikelstrålar har användning inom, bland annat, biologi, kemi, medicin, materialvetenskap och grundläggande fysik. Large Hadron Collider (LHC) på CERN är en forskningsanläggning där positivt laddade protoner med mycket hög hastighet krockar med varandra för att hitta atomernas minsta byggstenar. Eftersom protonerna där färdas i nästan ljusets hastighet, innebär det att deras rörelseenergi är mycket hög då de krockar med varandra. Protonstrålar har även medicinska tillämpningar, till exempel för behandling av cancertumörer. Det finns dessutom anläggningar där elektroners energi ökas kraftigt, till exempel Max IV i Lund. Dessa elektronstrålar används rutinmässigt för att skapa mycket intensiv röntgenstrålning.

För att uppnå höga energier måste partiklarna accelereras över långa sträckor och därför är mycket stora acceleratorer nödvändiga. Detta betyder i sin tur mycket stora ekonomiska investeringar. En vanlig accelerator består av en serie ihåliga metallkonstruktioner, eller kaviteter, där elektriskt laddade partiklar accelereras med hjälp av elektriska fält. Den slutliga partikelenergin beror på den elektriska fältstyrkan samt accelerationslängden. Vid för höga fältstyrkor kommer dock acceleratorn att skadas, vilket begränsar de elektriska fält som kan användas för att accelerera partiklar. Detta i sin tur bestämmer den kortaste accelerationssträckan som krävs för att uppnå en viss energi hos partiklarna. Rent praktiskt innebär detta att många av dagens acceleratorer är mycket stora maskiner, ofta av storleksordningen hundratals meter.

Den här avhandlingen beskriver experiment där laddade partiklar istället accelereras till höga energier genom växelverkan mellan en mycket intensiv laserpuls och materia placerad i en vakuumkammare. Den höga ljusintensiteten nås genom att fokusera en laserpuls med hög effekt till en mycket liten fläckstorlek. Laserns fläckstorlek är ungefär 10 µm, vilket kan jämföras med tjockleken av ett mänskligt hårstrå, som vanligtvis är mellan 17 µm och 180 µm. Den höga effekten hos ljuset ges av att laserpulsen i tid är extremt kort, runt 35 fs. En fs är en miljondels miljarddels sekund (0,000 000 000 000 001 s) och under 35 fs hinner ljus endast färdas 10 µm,

vilket återigen är kortare än ett hårstrås tjocklek.

Då detta mycket starka laserljus växelverkar med materia skapas ett plasma, vilket innebär att de atomer som utgör strålmålet bryts isär och kvar finns fria elektroner och positiva joner. Plasma är ett så kallat aggregationstillstånd, på samma sätt som gas, vätska och fast form, och kan beskrivas som en gas av fria, laddade partiklar. Det går även att dela in plasmor i två olika typer; *ogenomskinliga* och *genomskinliga*, där skillnaden är att den förstnämnda reflekterar ljus, medan ljus kan färdas genom den andra. Den fysikaliska skillnaden mellan dessa plasmor är tätheten av fria elektroner, där ett genomskinligt plasma har lägre elektrontäthet än ett ogenomskinligt. I det arbete som beskrivs i denna avhandling skapas genomskinliga plasmor oftast genom att fokusera intensivt laserljus i en gas, ett ogenomskinligt plasma skapas däremot då laserpulsen växelverkar med ett strålmål i fast form, eftersom detta resulterar i en hög elektrontäthet. För att skapa ett plasma krävs endast den allra främsta delen av laserpulsen, varför den starkaste delen av den kommer att interagera med just ett plasma. Ljuset kommer att trycka undan elektriskt laddade partiklar från det mest ljusintensiva området, mot delar av plasmat där ljusintensiteten är lägre. Eftersom tidsrymden detta pågår är väldigt kort, så kommer endast de lättaste partiklarna att hinna förflyttas, det vill säga elektronerna.

För ett ogenomskinligt plasma kommer, som nämnts tidigare, laserpulsen att reflekteras. Däremot kommer de elektroner som tryckts undan av ljuset att färdas genom plasmat. Om strålmålet är en tunn folie kan då dessa negativt laddade elektroner tränga ut på andra sidan av strålmålet, vilket behåller sin struktur under denna tidsrymd. Elektronerna ger där upphov till ett mycket starkt elektriskt fält, med en typisk styrka av biljoner volt per meter, där positivt laddade partiklar från foliens baksida slits loss och accelereras. Denna accelerationsteknik kallas på engelska för *Target Normal Sheath Acceleration* (TNSA). I de experiment som utgör grunden till denna avhandling har protoner accelererats till energier runt 10 MeV (megaelektronvolt) över en sträcka som uppskattas till 10 µm. Protoner med denna rörelseenergi färdas då med ungefär 10 % av ljusets hastighet. I vissa av de utförda experimenten användes dubbla laserpulser, där deras relativa intensitet, rumsliga separation samt ankomsttid vid strålmålet kunde varieras. I några andra experiment användes istället strålmål med mer komplicerad geometri, till exempel små försilvrade, ihåliga sfärer samt folier med mycket små strukturer på ytan. I samtliga experiment har egenskaperna hos de resulterande protonstrålarna studerats.

Om ljuset istället interagerar med ett genomskinligt plasma tränger laserpulsen igenom och trycker undan elektroner ur sin väg vilka börjar att svänga fram och tillbaka runt sin ursprungliga position. Resultatet blir en periodisk förändring av elektrontätheten efter laserpulsen, där det inom vissa områden är en väldigt hög koncentration, medan det under vissa förutsättningar i andra inte finns några elektroner alls. Denna del kallas för en kölvåg bakom laserpulsen. Här kan laserpulsen liknas vid en båt som färdas framåt genom vattnet och ger upphov till en våg rakt bakom sig. Variationen av elektrontätheten kommer i sin tur att ge upphov till starka elektriska fält, vanligtvis av storleksordningen miljarder volt per

Tabell 1 Accelerationstekniker
Exempel på olika acceleratoranläggningar och motsvarande prestanda hos experiment från avhandlingsarbetet där TNSA och LWFA har använts

	Protoner		Elektroner	
Accelerator	Injektor vid LHC	TNSA	Injektor vid Max IV	LWFA
Partikelenergi [MeV]	50	10	3 000	300
Accelerationssträcka [m]	34	0,00001	300	0,003
Medelfältstyrka [MV/m]	1,5	1 000 000	10	100 000

meter. Denna fältstyrka är tusentals gånger starkare än de som kan användas i konventionella acceleratorer. Om en elektron inträder i en del av kölvågen där de elektriska fälten är accelererande kan dess energi ökas kraftigt över en mycket kort sträcka. Tekniken för att på detta sätt accelerera elektroner kallas på engelska för *Laser Wakefield Acceleration* (LWFA). I ett typiskt experiment under avhandlingsarbetet kunde elektronernas energier ökas från 0 MeV till mer än 300 MeV genom laser-materia växelverkan i en gasstråle med 3 mm i diameter. Hastigheten hos en elektron med så hög energi är mer än 99,999 % av ljusets hastighet i vakuum. Detta innebär att elektroner med så hög energi kommer att färdas i nästan samma hastighet som laserpulsen. Gasen släpps vanligtvis ut genom ett överljudsmunstycke och kommer då att bilda en stråle på samma sätt som när vatten med högt tryck släpps ut genom munstycket på en slang. Överljudsflöden används eftersom det är viktigt med en skarp övergång mellan vakuum och gas i LWFA-experiment.

En viktig aspekt rörande LWFA är hur elektroner placeras i kölvågen bakom laserpulsen. I den enklaste formen sker detta automatiskt via självinjektion vilket, som namnet antyder, sker av sig självt under rätt förutsättningar. Denna typ av partikelinjektion är dock en slumpmässig process, vilket innebär att det är stora variationer mellan olika elektronstrålars energiinnehåll. I avhandlingsarbetet har denna process studerats närmare för att bland annat klargöra hur laserfokusets kvalitet påverkar injektionen. I ytterligare experiment har även andra typer av injektionstekniker använts, som att använda kontrollerade ökningar och minskningar av tätheten i plasmat. Det har visat sig att välkontrollerade förändringar av elektrontätheten i ett plasma kan göra så att partikelinjektionen sker vid samma position för olika elektronstrålar, vilket gör att energivariationerna mellan dem minskas drastiskt. I ett annat viktigt experiment undersöktes om elektronstrålarnas egenskaper påverkas av vilken ursprungsgas som används i överljudsflöden. Utöver elektronstrålen kommer även intensiv röntgenstrålning att produceras under accelerationsprocessen och denna strålning har under avhandlingarbetets gång studerats för olika typer av genomskinliga plasmor.

En jämförelse mellan de plasmabaserade accelerationsteknikerna som beskrivits ovan och exempel på deras traditionella motsvarigheter återfinns i Tabell 1, där det tydlig framgår att TNSA och LWFA har mycket högre accelererande elektriska

fältstyrkor än deras respektive traditionella accelerationstekniker. Detta innebär att för att uppnå liknande energier som deras traditionella motsvarigheter krävs mycket kortare accelerationslängder, vilket är en mycket attraktiv egenskap hos plasmabaserade partikelacceleratorer. Ett problem med dessa tekniker är dock att accelerationslängden är begränsad och det kan vara problematiskt att förlänga den. För genomskinliga plasmor begränsas interaktionslängden av den längd som laserpulsen kan hållas fokuserad och ett sätt att förlänga denna är att använda en annan typ av strålmål. I denna avhandling har tunna, gasfyllda glasrör, eller kapillärer, använts. Inuti röret kan ljuspulsen ledas och på så sätt öka laserfokusets längd, vilket i slutändan kan leda till högre elektronenergier än för andra typer av strålmål. En viktig aspekt där konventionella acceleratorer än så länge överträffar LWFA och TNSA är repetitionshastigheten. I avhandlingsarbetet kunde upp till tio elektronpulser accelereras varje minut och för protoner kunde, i normalfallet, endast en puls accelereras varje minut. Detta kan jämföras med injektorn vid Max IV som har en repetitionshastighet på över 100 elektronpulser per sekund.

Forskningen som den här avhandlingen beskriver utgör en liten del av ett internationellt sett mycket aktivt forskningsfält, där ett av de övergripande målen är att skapa kompakta partikelacceleratorer. Det finns många möjliga tillämpningar, bland annat inom protonbaserad cancerbehandling. Det är dock mycket forskning som återstår innan strålar med de egenskaper som krävs för denna tillämpning kan produceras genom laserbaserad acceleration.

List of Publications

I **Supersonic Jets of Hydrogen and Helium for Laser Wakefield Acceleration**
K. Svensson, M. Hansson, F. Wojda, L. Senje, M. Burza, B. Aurand, G. Genoud, A. Persson, C.-G. Wahlström, & O. Lundh.
Phys. Rev. Accel. Beams **19**, 051301 (2016).

II **Self-Injection Threshold in Self-Guided Laser Wakefield Accelerators**
S. P. D. Mangles, G. Genoud, M. S. Bloom, M. Burza, Z. Najmudin, A. Persson, K. Svensson, A. G. R. Thomas, & C.-G. Wahlström.
Phys. Rev. ST Accel. Beams **15**, 011302 (2012).

III **Increasing Energy Coupling into Plasma Waves by Tailoring the Laser Radial Focal Spot Distribution in a Laser Wakefield Accelerator**
G. Genoud, M. S. Bloom, J. Vieira, M. Burza, Z. Najmudin, A. Persson, L. O. Silva, K. Svensson, C.-G. Wahlström, & S. P. D. Mangles.
Phys. Plasmas **20**, 064501 (2013).

IV **Laser Wakefield Acceleration using Wire Produced Double Density Ramps**
M. Burza, A. Gonoskov, K. Svensson, F. Wojda, A. Persson, M. Hansson, G. Genoud, M. Marklund, C.-G. Wahlström, & O. Lundh.
Phys. Rev. St Accel. Beams **16**, 011301 (2013).

V **Down-Ramp Injection and Independently Controlled Acceleration of Electrons in a Tailored Laser Wakefield Accelerator**
M. Hansson, B. Aurand, X. Davoine, H. Ekerfelt, K. Svensson, A. Persson, C.-G. Wahlström, & O. Lundh.
Phys. Rev. ST Accel. Beams **18**, 071303 (2015).

VI **Study of Electron Acceleration and X-Ray Radiation as a Function of Plasma Density in Capillary-Guided Laser Wakefield Accelerators**
J. Ju, K. Svensson, H. Ferrari, A. Döpp, G. Genoud, F. Wojda, M. Burza, A. Persson, O. Lundh, C.-G. Wahlström, & B. Cros.
Phys. Plasmas **20**, 083106 (2013).

VII **Analysis of X-Ray Emission and Electron Dynamics in a Capillary-Guided Laser Wakefield Accelerator**
J. Ju, G. Genoud, H. E. Ferrari, O. Dadoun, B. Paradkar, K. Svensson, F. Wojda, M. Burza, A. Persson, O. Lundh, N. E. Andreev, C.-G. Wahlström, & B. Cros.
Phys. Rev. ST Accel. Beams **17**, 051302 (2014).

VIII **Enhancement of X-Rays Generated by a Guided Laser Wakefield Accelerator inside Capillary Tubes**
J. Ju, K. Svensson, A. Döpp, H. E. Ferrari, K. Cassou, O. Neveu, G. Genoud, F. Wojda, M. Burza, A. Persson, O. Lundh, C.-G. Wahlström, & B. Cros.
Appl. Phys. Lett. **100**, 191106 (2012).

IX **A Setup for Studies of Laser-Driven Proton Acceleration at the Lund Laser Centre**
B. Aurand, M. Hansson, L. Senje, K. Svensson, A. Persson, D. Neely, O. Lundh, & C.-G. Wahlström.
Laser Part. Beams **33**, p. 59 (2015).

X **Manipulation of the Spatial Distribution of Laser-Accelerated Proton Beams by Varying the Laser Intensity Distribution**
B. Aurand, L. Senje, K. Svensson, M. Hansson, A. Higginson, A. Gonoskov, M. Marklund, A. Persson, O. Lundh, D. Neely, P. McKenna, & C.-G. Wahlström.
Phys. Plasmas **23**, 023113 (2016).

XI **Transverse Expansion of the Electron Sheath during Laser Acceleration of Protons**
K. Svensson, L. Senje, F. Mackenroth, A. Gonoskov, C. Harvey, B. Aurand, M. Hansson, A. Higginson, M. Dalui, O. Lundh, P. McKenna, A. Persson, & C.-G. Wahlström.
Manuscript.

XII **Hollow Microspheres as Targets for Staged Laser-Driven Proton Acceleration**
M. Burza, A. Gonoskov, G. Genoud, A. Persson, K. Svensson, M. Quinn, P. McKenna, M. Marklund, & C.-G. Wahlström.
New J. Phys. **13**, 013030 (2011).

Contents

Chapter 1

Introduction

Particle acceleration is central to many fields of research, for example, in medicine [1–3], biology [4, 5], chemistry [6, 7], materials science [8], and the development of new energy sources [9, 10]. It is also the basis for the ground breaking fundamental research conducted at facilities such as the Large Hadron Collider (LHC), which in 2012 finally enabled researchers to present experimental evidence of the existence of the Higgs Boson [11, 12].

Conventional accelerators are used to increase the kinetic energy of charged particles utilizing mean electric fields on the order of $\sim$10 MV m^{-1}, and the resulting energy of the particles is simply the product of the accelerator field strength, the acceleration length, and the particle charge. Thus, to attain higher energies, it is necessary to either increase the accelerating field, or the acceleration length, which is associated with very high costs. However, the maximum field strength is limited by electrical breakdown. Thus, in order to reduce the size of an accelerator, the physical limits of traditional accelerating cavities must be overcome.

Numerical example

To reach an energy of 1 GeV, particles with one elementary charge must be accelerated for 100 m in an electric field strength of 10 MV m^{-1}. To reach the same energy in a field strength of 100 GV m^{-1}, which is achievable in laser-produced plasmas, the acceleration distance needed is only 1 cm.

In 1979, Tajima and Dawson proposed the use of lasers to excite waves in underdense plasmas, and to then use these waves as accelerating structures [13]. They predicted that electric fields on the order of 100 GV m^{-1} could be sustained. This technique

is now known as laser wakefield acceleration (LWFA) [14], and the fields inside the plasma wave are several orders of magnitude higher than those possible in conventional accelerators. However, the technique relies on very short and very intense laser pulses, which were not as readily available at that time. The high laser powers required would have damaged the gain media in the laser systems, and prior to the advent of chirped pulse amplification (CPA) [15] very large beam sizes had to be used in laser amplification to reach peak powers above 1 TW. With the advent of the CPA technique, however, it became possible to achieve the focused intensities needed for LWFA, and the first laser wakefield accelerated electrons were experimentally observed in 1998 [16]. In that experiment, performed at Laboratoire pour l'Utilisation des Lasers Intenses (LULI) in France, an energy gain of 1.6 MeV was observed for externally injected electrons. At the beginning of this millennium, observations were made of the energetic protons and heavy ions emitted from the interaction between high-intensity lasers and solid materials [17–19]. The mechanism responsible for this effect was later named target normal sheath acceleration (TNSA) [20, 21], where protons are accelerated up to energies of several MeV in strong electric fields (on the order of TV m^{-1}) over very short distances. During the past decade, many improvements have been made regarding the quality and stability of beams of laser-accelerated electrons and protons. Examples of this are the production of quasi-monoenergetic electron beams [22–24], and GeV electron energies [25]. However, when the work on this thesis started, the reproducibility and stability, in terms of energy and charge, of both electron and proton acceleration, was rather poor.

This thesis describes experimental work on both electron and proton acceleration using laser-generated plasmas. The techniques used share a common theoretical background, which is presented in Chapter 2, as well as similar experimental setups and diagnostics, which are presented in Chapter 3. In principle, the main difference between electron and proton acceleration lies the type of target used. Gas targets are usually employed in LWFA, while thin solid foils are used in TNSA. However, the experimental setup is usually affected when changing target type, and in practice, LWFA and TNSA require two different experimental setups, with their own requirements on detectors and laser pulse focusing. For this reason, LWFA and TNSA are mostly described separately in this thesis. However, the experience gained from one technique can often be applied to the other. One example of this is the magnetic spectrometers described in Section 3.3.3, which work according to the same principle regardless of whether the accelerated particles are electrons or protons.

The details of the studies are given in Papers I to XII, which are appended at the end of this thesis. The experiments themselves, and the results obtained are summarized in Chapter 4. The experimental studies using LWFA in the thesis work are summarized in Section 4.1. The effects of basic parameters such as the target gas and backing pressure, and laser pulse properties such as focal spot quality and pulse length, on the process of self-injection, and therefore the accelerated electron beams, were investigated (Papers I and II). The quality of the focal spot was found to be especially important, since the energy outside the central part of the laser focus does

not couple to the plasma wave, and is essentially lost (Paper III). This knowledge is also important in LWFA experiments where more advanced injection mechanisms are used, since these mechanisms preferably act in a regime where the electron number density is lower than the threshold for self-injection. Density gradient injection was used to create electron beams with reduced divergence and increased charge, compared to electron beams created using self-injection (Paper IV). The setup described in Paper V is more configurable, since it is based on two individual gas sources, which enables more detailed tailoring of the gas density profile. Experiments using gas-filled dielectric capillary tubes as targets, instead of gas jets, are discussed in Papers VI, VII, and VIII. The acceleration process can be enhanced by collecting the laser pulse energy outside the central part of the laser focus, and recoupling it to the plasma wave. Another benefit of using gas-filled dielectric capillary tubes is the stability of the density profile, which is free of the shock waves that are present in gas jets.

The proton acceleration experiments using TNSA, described in Section 4.2, started with studies on how the laser intensity distribution on the front of a flat target affects the accelerated proton beams leaving the target (Paper X). The intensity distribution can be varied by either defocusing the laser beam, or by incorporating a split-mirror setup (described in Paper IX), capable of creating two synchronized laser pulses. The spatial proton beam divergence can be reduced by increasing the size of the laser focal spot, and is a consequence of the flatter electron sheath shape on the rear of the target. When using double laser pulses, it was found that the proton beam profile could become elliptic, with its major axis in the direction perpendicular to the axis of separation. In an ongoing study, the relative energy content of two spatially separated laser pulses is being varied (manuscript draft in Paper XI). This causes the elliptical proton beam profile to rotate, as a consequence of the relation between the transverse expansion speed of the electron sheath and the intensity and angle of incidence of the laser pulse. More advanced targets were also studied, for example, a hollow spherical target (Paper XII). In this case, the transverse sheath expansion can be used to facilitate staged proton acceleration. Flat targets with surface structure, such as nanospheres and gratings, have also been used as targets. Structures on the back of the target were to greatly affect the divergence of the proton beam.

Chapter 5 presents the conclusions together with comments on future research in this field.

Chapter 2

Theoretical Background

The aim of this chapter is to present the theoretical background necessary for the work presented in this thesis, in particular the concepts and terms used in the papers. Section 2.1 presents short introductions to high-power lasers and Gaussian laser beams, together with some important definitions, while in Section 2.2 the first stages of the interaction between high-intensity laser light and matter are described. Sections 2.3, 2.4, and 2.5 then provide short introductions to the definitions and concepts involved in laser-plasma interactions, and the two acceleration techniques studied in this work.

2.1 High-Power Lasers

In general, lasers [26] can be divided into two kinds: continuous wave (CW) and pulsed lasers. The intensities required for the work presented in this thesis are higher than those provided by a CW laser. However, many CW lasers can be operated in pulsed mode through techniques such as mode locking, q-switching, or gain switching. In contrast to CW lasers, pulsed lasers have broad spectral widths ($\Delta\lambda$), and the shortest possible pulse duration is given by:

$$\tau_{\text{min}} = K\frac{\lambda^2}{c\Delta\lambda}, \tag{2.1}$$

where K is a constant related to the pulse shape, λ is the central wavelength, and c is the speed of light.

Numerical Example

The shortest possible duration of a Gaussian pulse ($K = 0.441$) with a central wavelength of 0.8 µm and a spectral width of 30 nm is 30 fs.

Depending on the type of laser, energy can be supplied to the system in a number of different ways, for example, using flash lamps or pump lasers. However, if the laser beam is too highly amplified it will damage the optical components in the system, and the laser breaks down. Therefore, prior to the advent of chirped pulse amplification (CPA) large optical components were used to achieve high laser intensities [15]. After amplification, the laser pulse is compressed into a short pulse. This allows the intensity of the pulse to be reduced during amplification without increasing the beam diameter.

High-power laser systems, such as the multi-terawatt laser system in Lund (see Section 3.1), usually have several amplification stages, each with a gain medium that is supplied with energy. Spontaneous emission also takes place in these stages and, in some cases, the emitted radiation passes through subsequent amplifiers, leading to amplified spontaneous emission (ASE). ASE is almost always present in high-power laser systems, and its intensity is directly correlated to the energy supplied to the gain medium. The laser pulse generated in high-power systems is thus situated on top of an ASE pedestal of lower intensity.

2.1.1 Gaussian Laser Beams

In reality, the laser pulses produced by high-power laser systems are not exactly Gaussian in time or space. However, this is a good approximation that can be used to gain an understanding of the central concepts governing laser beams. Mathematically, laser beams are often represented by plane waves. However, this is an idealization, since a plane wave exists over all space. A wave confined in space can be described by a complex Gaussian function, $\mathbf{E}(t, \rho, z)$, where t is time, ρ is the radial distance from the optical axis, and z is the position along the propagation axis. It is also assumed that the laser is linearly polarized, so $\mathbf{E}/E = \mathbf{e}_x$, and that the beam is propagating in the positive z-direction. In the experiments described in this thesis, the laser pulse was compressed to ultra-short durations, which means that the Gaussian function describing the laser pulse also must be confined in time. This is done by multiplying $\mathbf{E}$ by:

$$\Gamma(t, z) = \exp\left[-2\ln 2\left(\frac{t - z/c}{\tau}\right)^2\right], \tag{2.2}$$

which is also a Gaussian function, where τ is the duration of the pulse at half the maximum height of the peak. The duration of a laser pulse can be defined in several ways, and throughout this thesis, the full width at its half maximum intensity (FWHM) will be used. The radius of the laser beam waist at focus, w_0, can also be defined in several ways, and is here defined as the radius at which the intensity has decreased by a factor of $\exp(2)$. The relation between w_0 and FWHM spot size is $w_0 = \mathrm{FWHM}/\sqrt{2\ln 2} \approx 0.85\mathrm{FWHM}$.

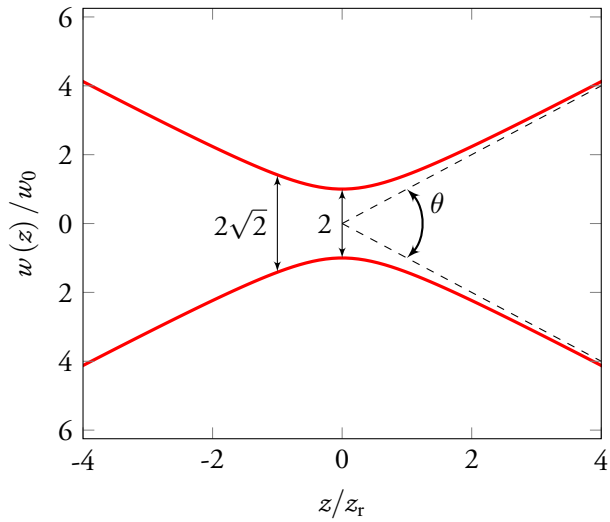

Figure 2.1 Waist of a Gaussian Beam
The minimum diameter is $2w_0$, which has increased to $2\sqrt{2}w_0$ after one Rayleigh length z_r. The far-field ($z \gg z_r$) divergence of the beam is $\theta = 2\lambda/\pi w_0$.

When focusing a Gaussian beam, the radius of the focal spot is given by:

$$w_0 = \frac{2\lambda}{\pi} f_n, \tag{2.3}$$

where f_n is the focal length divided by the beam diameter at the focusing optic. The beam radius at any position z can be calculated from:

$$w(z) = w_0 \sqrt{1 + \left(\frac{z}{z_r}\right)^2} \tag{2.4}$$

and is shown in Fig. 2.1. In Eq. 2.4, z_r is the Rayleigh length, which is defined as the distance from the beam waist to the point at which the cross-sectional area of the beam has increased by a factor of two relative to the beam waist. The Rayleigh length is given by:

$$z_r = \frac{\pi w_0^2}{\lambda}. \tag{2.5}$$

Knowing the laser pulse energy, $\mathcal{E}_{pulse}$, it is possible to determine the laser pulse peak power:

$$P_0 = 2\sqrt{\frac{\ln 2}{\pi}} \frac{\mathcal{E}_{pulse}}{\tau}, \tag{2.6}$$

and the intensity distribution can be determined from the focal spot size,

$$I(t, \rho, z) = I_0 \left(\frac{w_0}{w(z)}\right)^2 \exp\left[-\frac{2\rho^2}{w^2(z)}\right] \Gamma^2(t, z), \tag{2.7}$$

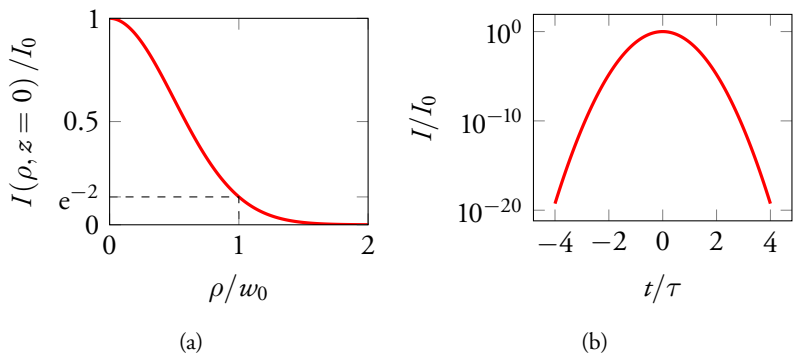

Figure 2.2 Intensity Distribution of a Gaussian Beam
(a) The intensity distribution of a Gaussian beam at the plane of the beam waist. The spot radius, w_0, is the transverse distance from the optical axis to the point where the intensity has decreased by a factor $\exp(2)$. (b) Logarithmic plot of the temporal intensity profile of a laser pulse at $\rho = 0$ and $z = 0$, where τ is the FWHM pulse duration.

where the peak intensity, I_0, is:

$$I_0 = \frac{2P_0}{\pi w_0^2} \approx 0.598 \times \frac{\mathcal{E}_{\text{pulse}}}{w_0^2 \tau}. \tag{2.8}$$

The temporal profile of the laser pulse at the beam waist is shown in Fig. 2.2(b).

> **Numerical example**
> The peak power of a laser pulse with $\mathcal{E}_{\text{pulse}} = 1\,\text{J}$ and $\tau = 40\,\text{fs}$ is 23 TW. If $w_0 = 10\,\mu\text{m}$, the peak intensity, I_0, is $15 \times 10^{18}\,\text{W cm}^{-2}$.

Light can also be described by its vector and scalar potentials, $\mathbf{A}$ and ϕ respectively, where $\mathbf{B} = \nabla \times \mathbf{A}$ and $\mathbf{E} = -\nabla\phi - \frac{\partial \mathbf{A}}{\partial t}$. The normalized vector potential, $\mathbf{a}$, is a useful quantity:

$$\mathbf{a} = \frac{q_e \mathbf{A}}{m_e c}, \tag{2.9}$$

where q_e is the elementary charge and m_e is the electron mass. The maximum amplitude of $\mathbf{a}$ in Eq. 2.9 is often used to characterize the strength of the laser pulse, and can be expressed as:

$$a_0 \approx 0.86\lambda\,[\mu\text{m}] \sqrt{I_0\left[10^{18}\,\text{W cm}^{-2}\right]}, \tag{2.10}$$

by noting that $\mathbf{A} = A_0 \cos(kz - \omega_0 t)\,\mathbf{e}_x$ with a laser angular frequency ω_0, $k = 2\pi/\lambda$, and intensity:

$$I = \frac{c\,\varepsilon_0}{2}\,|\mathbf{E}|^2\,, \tag{2.11}$$

where ε_0 is the permittivity of free space.

In the experiments described in this thesis, the intensities corresponded to $a_0 > 1$, or $I_0 > 2 \times 10^{18}\,\mathrm{W\,cm^{-2}}$. When $a_0 \gtrsim 1$, electrons in the laser field will oscillate with a speed $v_\perp \approx c$, which means that relativistic effects must be taken into account for an accurate physical description.

2.2 Ionization

The electric field in a laser pulse with an intensity $\sim 10^{18}\,\mathrm{W\,cm^{-2}}$ is so strong that it will drastically perturb the Coulomb potential experienced by the electrons in an atom at the laser focus, and the electrons will be able to spontaneously escape due to over-the-barrier-ionization (OTBI). The critical field needed to perturb the potential to this point is given by $E_\mathrm{c} = \pi\varepsilon_0\mathcal{E}_\mathrm{ion}^2/Zq_\mathrm{e}^3$ [27] which, according to Eq. 2.11, yields an effective ionization intensity of:

$$I_\mathrm{ionisation}\left[\mathrm{W\,cm^{-2}}\right] \approx 4 \times 10^9\,(\mathcal{E}_\mathrm{ion}\,[\mathrm{eV}])^4\,Z^{-2}, \tag{2.12}$$

where $\mathcal{E}_\mathrm{ion}$ is the energy required to create the ion, and Z is the charge state of the resulting ion. Assuming $I_0 = 1 \times 10^{18}\,\mathrm{W\,cm^{-2}}$, the laser pulse reaches an intensity of $I = 1 \times 10^{16}\,\mathrm{W\,cm^{-2}}$ at $t/\tau \approx 1.3$ (see Fig. 2.2(b)). This is the intensity needed to fully ionize gases such as hydrogen and helium, which means that the peak of the laser pulse interacts with a completely ionized plasma in these gases. Other atoms, such as aluminum (Al), although highly ionized, will not become completely ionized, even at the laser peak. At an intensity of $1 \times 10^{16}\,\mathrm{W\,cm^{-2}}$ aluminum will only reach Al^{3+}. Equation 2.12 is plotted against Z for a number of atoms in Fig. 2.3, where it can be seen that the intensity required to obtain Al^{1+} ions is approximately $10^{13}\,\mathrm{W\,cm^{-2}}$. However, Eq. 2.12 assumes free atoms, which is not the case in a metallic foil, and the ionization process is thus more complex. The process of laser-induced damage differs depending on the duration of the laser pulse. For long pulses (µs) or CW lasers, damage is caused by melting. For pulse lengths shorter than ns, laser-induced damage is due to electric breakdown in the material, and usually depends on the laser fluence. For light pulses with a short duration, τ_l, and a fluence damage threshold, F_LIDT, the intensity at which damage occurs can be determined from:

$$I_\mathrm{LIDT} = \frac{F_\mathrm{LIDT}}{\tau_l}, \tag{2.13}$$

where F_LIDT depends on the target material and the duration of the light. Note that τ_l is not necessarily the laser pulse length, τ, but can be related to ASE or prepulses. In general, I_LIDT is usually lower than that resulting from OTBI, but for the work

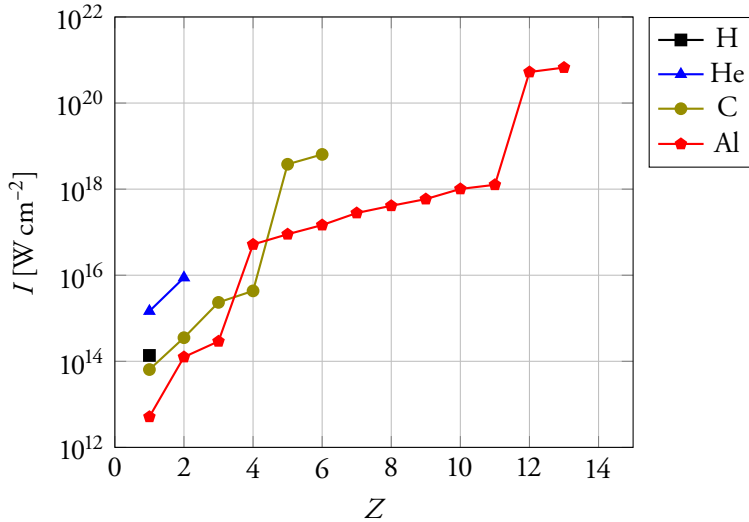

Figure 2.3 Over-the-Barrier-Ionization Intensities
Ionization intensity, I, for four different elements plotted against the charge state, Z, produced. It is apparent that atoms such as H and He, where OTBI can be used to describe the ionization process, are completely ionized by the front of the laser pulse.

described in this thesis, it is usually sufficient to assume that the plasma produced by the interaction between a high-intensity laser pulse and a solid has an increasing number density ramp and eventually becomes overdense (see Section 2.5.1).

As will become clear later in this section, an important parameter is the electron number density, n_e, in the plasma, which depends on both Z and the neutral number density, N. For gases, the value of n_e can be adjusted by changing the static gas pressure, since $N = p/k_B T$, where k_B is Boltzmann's constant and T the temperature. For solid materials, N can be estimated from the mass density, ρ_{mass}, and the atomic mass, m_{atom}. For Al, this yields a neutral number density on the order of 10^{22} cm^{-3}.

> **Numerical example**
>
> An ideal gas at $p = 1\,\text{bar}$ and $T = 300\,\text{K}$ has the number density $N = 2 \times 10^{19}\,\text{cm}^{-3}$. Solid Al at room temperature has $\rho_{\text{mass}} = 2.70\,\text{g cm}^{-3}$ and $m_{\text{atom}} = 26.98\,\text{u}$, yielding a number density of $N_{\text{Al}} = 6 \times 10^{22}\,\text{cm}^{-3}$.

There are other ionization processes, but these are not described in this thesis. For gases, OTBI guarantees ionization, and the plasma is often underdense. For solids, on the other hand, it can be assumed that the resulting plasma has a number density gradient, as the plasma that is produced expands into vacuum and eventually becomes overdense.

2.3 Laser–Plasma Interaction

A plasma can be modeled as a fluid consisting of free electrons and ions. However, on the timescale of an ultra-short laser pulse, only the motion of electrons needs to be considered as the ions have much larger masses, and they can thus be treated as a stationary, positively charged background. The motion of an electron in external electric and magnetic fields is described by the Lorentz equation, and when the time duration of the laser pulse is very short, the result is a time-averaged force called the ponderomotive force, $\mathbf{F}_p$. The important characteristic of the ponderomotive force is that [27]:

$$\mathbf{F}_\mathrm{p} \propto -\frac{q^2}{m}\nabla I, \tag{2.14}$$

where q and m are the particle charge and mass, respectively. This means that charged particles are pushed away from regions of high intensity irrespective of the sign of q, and the force is greatest for the lightest particles, i.e. electrons. The resulting charge separation creates electrostatic fields, and displaced electrons behind the laser pulse will start to oscillate. Globally, a plasma has no net charge, so $n_\mathrm{e} = Zn_\mathrm{i}$, where n_i is the ion number density. The local charge displacement introduced by the laser pulse is shielded by plasma electrons over a characteristic distance called the Debye length, given by:

$$\lambda_D = \sqrt{\frac{\varepsilon_0 k_B T_\mathrm{e}}{q_\mathrm{e}^2 n_\mathrm{e}}}, \tag{2.15}$$

where T_e is the electron temperature. Physically, the Debye length decreases with increasing electron number density, since more electrons are available for shielding. It is also reasonable that λ_D increases with T_e, since the electrons become more spread out at higher temperatures. The plasma response to an external electric field is not instantaneous, and is given by $t_D = \lambda_D / v_t$, where $v_t = \sqrt{k_B T_\mathrm{e}/m_\mathrm{e}}$ is the thermal velocity of the electrons. This can also be regarded as a characteristic plasma frequency, given by:

$$\omega_p = t_D^{-1} = \sqrt{\frac{q_\mathrm{e}^2 n_\mathrm{e}}{\varepsilon_0 m_\mathrm{e}}}. \tag{2.16}$$

It is also possible to derive a wave equation that describes the collective motion of electrons in a plasma. For small charge density displacements, Δn_e, its solution yields a dispersion relation for the propagation of an electromagnetic wave with frequency ω_0 in the plasma:

$$\omega_0^2 - \omega_p^2 = k^2 c^2, \tag{2.17}$$

where ω_p is given in Eq. 2.16. It is also possible to determine the corresponding refractive index, η, of the plasma from $\omega_0/k = c/\eta$, where:

$$\eta = \sqrt{1 - \frac{\omega_p^2}{\omega_0^2}}. \tag{2.18}$$

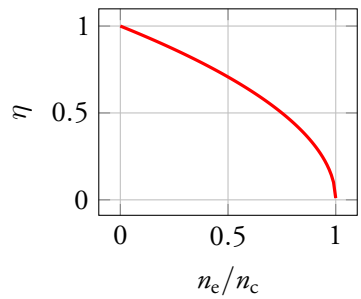

Figure 2.4 Refractive Index of Plasmas
Plasma refractive index, η, as a function of plasma electron number density, n_e, normalized to the critical number density, n_c, defined in Eq. 2.20.

It is worth noting that η is a function of n_e, as shown in Fig. 2.4. It is clear that for non-zero values of n_e, $\eta < 1$, and the phase velocity, $v_p = c/\eta$, is higher than the speed of light in vacuum. However, the group velocity,

$$v_g = \frac{\partial \omega_0}{\partial k} = \eta c, \tag{2.19}$$

is not. As can be seen in Fig. 2.4, η decreases with increasing n_e. According to Eq. 2.7, the laser intensity peaks at its center and falls off towards the wings. For a laser pulse with an intensity within the range where it can ionize the medium but not produce a fully ionized plasma, n_e varies radially over the laser beam profile; its maximum coinciding with the maximum laser intensity. According to Fig. 2.4, η should therefore be lowest at the laser beam center. Thus, ionization affects laser propagation and the forming plasma acts as a negative lens, causing the laser to defocus, i.e., ionization defocusing. However, for a fully developed plasma, the radial variation in the laser pulse intensity implies that the ponderomotive force is higher at the beam center, thus pushing electrons away and reducing n_e, with a corresponding increase in η, on-axis. Thus, the situation is now reversed, and the plasma acts as a positive lens, which can guide the laser pulse.

From Eq. 2.17 it is possible to define two different types of plasmas. The first is $\omega_0 < \omega_p$, for which k becomes imaginary. In this case, the plasma is called *overdense*, and the electrons are able to move together with the electric field in the laser pulse, which means that the laser field is effectively stopped and the pulse cannot propagate through the plasma. The second case is when $\omega_0 > \omega_p$, and the plasma is transparent to the incoming laser pulse. This is called an *underdense* plasma, and arises from low-density targets, such as gases and plasmas expanding into vacuum. It is possible to determine a critical density, n_c, at which the laser frequency is equal to the plasma frequency, which defines the boundary between these two types of plasma:

$$n_c = \frac{\varepsilon_0 m_e \omega_0^2}{q_e^2}. \tag{2.20}$$

Overdense plasmas are often formed when an intense laser pulse interacts with a solid target. This type of plasma can be used for ion acceleration, and the technique used here was target normal sheath acceleration [17, 18, 28]. From now on, the two types of plasmas, and their corresponding acceleration techniques will be treated separately.

Numerical Example

For a laser wavelength of 0.8 µm, the critical density is $1.74 \times 10^{21}\,\mathrm{cm}^{-3}$. To achieve this by fully ionizing neutral He at $T = 300\,\mathrm{K}$, a static pressure of 36 bar would be required.

2.3.1 Relativistic Effects

In the previous section, the relativistic nature of the electron oscillation was neglected. This approach is not sufficiently accurate for high field strengths (corresponding to $a_0 > 1$). For high laser field strengths, the speed of the electron oscillation will start to approach the speed of light, which means that the particles will experience an increase in mass. This will alter the value of ω_p (given in Eq. 2.16) by the transverse relativistic factor $\langle\gamma_\perp\rangle = \sqrt{1 + a^2(\rho)/2}$, where $a(\rho) = a_0 \exp\left[-\rho^2/2w_0^2\right]$ is the laser strength parameter at a distance ρ from the axis in the radial direction. Equation 2.17 now becomes:

$$\omega_0^2 - \frac{\omega_p^2}{\langle\gamma_\perp\rangle} = k^2 c^2. \tag{2.21}$$

In a plasma where the electron density is much lower than the critical density defined in Eq. 2.20, i.e. $n_\mathrm{e} \ll n_\mathrm{c}$, then $\omega_p \ll \omega_0$. In the relativistic case, the plasma frequency is $\omega_p/\sqrt{\langle\gamma_\perp\rangle}$, which means that the refractive index of the plasma can be written:

$$\eta(\rho) - 1 \approx -\frac{n_\mathrm{e}}{2n_\mathrm{c}}\left(1 - \frac{a^2(\rho)}{4}\right). \tag{2.22}$$

Since $a(\rho)$ has a Gaussian shape, η will be peaked at the center of the beam and fall off towards the wings of the pulse. This means that the plasma acts as a positive lens and focuses the beam, counteracting diffraction over several Rayleigh lengths. The power threshold for this type of relativistic self-focusing to occur is given by [29, 30]:

$$P_\mathrm{c} = \frac{8\pi\varepsilon_0 m_\mathrm{e}^2 c^5 n_\mathrm{c}}{q_\mathrm{e}^2 n_\mathrm{e}} \approx 17.4\,\mathrm{GW} \times \frac{n_\mathrm{c}}{n_\mathrm{e}}. \tag{2.23}$$

2.3.2 Laser Pulse Compression

There is also a difference in the refractive index of the plasma in the longitudinal direction, such that the front of the laser pulse will be propagating through a higher

refractive index than the back of the pulse, since the front is ionizing atoms as well as pushing away electrons. Under certain conditions, the back of the laser pulse will be propagating in an electron void. This means that the pulse will be compressed in time, and a simple estimate of this compression, after a length l, is given by [31]:

$$\tau_f(l) = \tau_0 - \frac{n_e l}{2cn_c}, \tag{2.24}$$

where τ_0 is the initial pulse length.

2.3.3 Pump Depletion

The laser pulse energy does not remain constant as it propagates through the medium, since ionization and plasma wave excitation require energy. This means that after a certain length, L_{pd}, the laser pulse cannot drive a plasma wave, and is considered depleted. This length is called the pump depletion length, and in the 3D nonlinear case it is given by [32]:

$$L_{pd} = \frac{c\tau_0\omega_0^2}{\omega_p^2} = \frac{c\tau n_c}{n_e}. \tag{2.25}$$

The pump depletion length is shorter for higher electron densities, since more energy is needed to both ionize and displace more electrons. According to Eq. 2.24, when the laser pulse reaches pump depletion, its final pulse length, τ_f, will be $\tau_f\left(l = L_{pd}\right) = \tau_0/2$.

2.4 Laser Wakefield Acceleration of Electrons

Before discussing the experiments on electron acceleration in underdense plasmas, a phenomenological picture of the process and the most important expressions used in the papers will be given. A more complete description of the theory behind LWFA is given by Esarey, Schroeder, and Leemans [14].

As described in Section 2.2, the leading edge of the laser pulse completely ionizes gases such as H_2 and He, and the main part of the laser pulse then propagates through a fully developed plasma, expelling electrons from regions of high intensity, due to the ponderomotive force, $\mathbf{F}_p$. Compared to electrons, the nuclei can be assumed to remain essentially stationary due to their larger mass, and can be regarded as a positively charged background. After the electrons have been displaced, they will start to oscillate due to the space charge introduced. For Gaussian pulses with moderate pump strengths, the longitudinal and radial electric fields of the resulting plasma waves are given by [33]:

$$E_z(\rho,\zeta) = f(\rho)\,\omega_p \cos\left(k_p\zeta\right) \tag{2.26}$$

and

$$E_\rho(\rho,\zeta) = -f(\rho)\,\frac{4\rho v_g}{w_0^2}\sin\left(k_p\zeta\right), \tag{2.27}$$

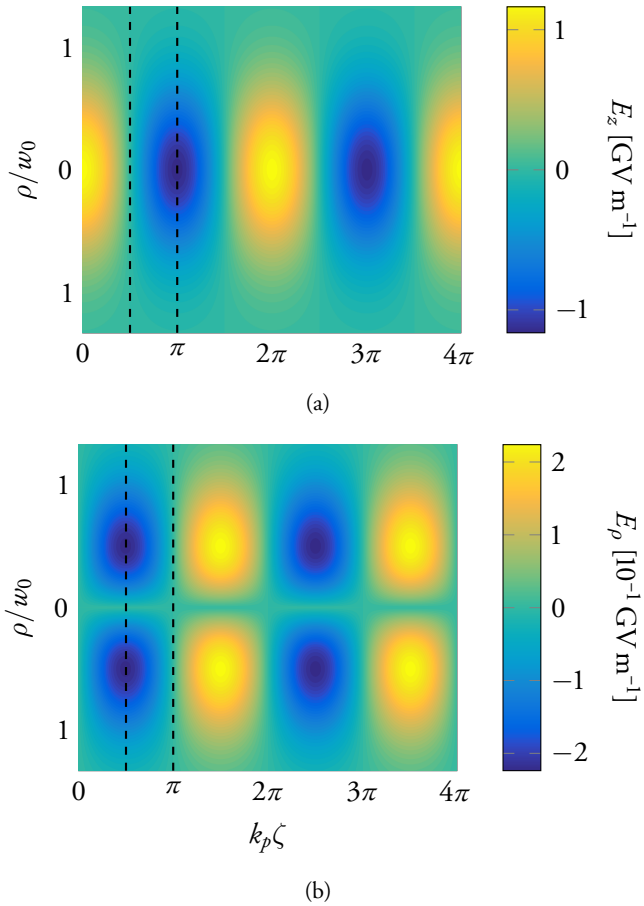

Figure 2.5 Electric Fields of a Plasma Wave
Longitudinal (a) and radial (b) electric fields calculated for $a_0 = 0.2$, $w_0 = 15\,\mu\text{m}$, $\tau = 40\,\text{fs}$, and $n_e = 5 \times 10^{18}\,\text{cm}^{-3}$. Note that there are phases where, for negatively charged particles, E_z is accelerating and E_ρ drives them towards the central axis. This is the case when $k_p\zeta$ takes values from $\pi/2$ to π (indicated by the dashed lines), and repeats with a period 2π. It can also be seen that the radial fields are zero on-axis, whereas the longitudinal fields reach their maximum values there.

where $k_p = \omega_p/c$, $\zeta = z - v_g t$ is the longitudinal coordinate in a reference frame moving with the laser pulse, and

$$f(\rho) = \frac{m_e v_g}{q_e}\sqrt{\frac{\pi}{2}}a_0^2\frac{\omega_p\tau}{2\sqrt{2\ln 2}}\exp\left[-\frac{\omega_p^2\tau^2}{16\ln 2}\right]\exp\left[-\frac{2\rho^2}{w_0^2}\right]. \tag{2.28}$$

The electric fields described by Eq. 2.26 and 2.27 are plotted in Fig. 2.5 for $a_0 = 0.2$, $w_0 = 15\,\mu\text{m}$, $\tau = 40\,\text{fs}$, and $n_e = 5 \times 10^{18}\,\text{cm}^{-3}$.

A negatively charged particle placed inside this electron void will experience very strong electrical fields, acting both longitudinally and radially, as shown in Fig. 2.5.

These fields will give the particle additional longitudinal and transverse momentum. As the electrons are accelerated, they will start to catch up with the laser pulse, and as they outrun the plasma wave, they will start to decelerate (between $k_p\zeta = \pi$ and $k_p\zeta = 2\pi$). This is called dephasing[1], and will take place after an acceleration length of [32]:

$$L_{\mathrm{d}} = \frac{4c\omega_0^2}{3\omega_p^3}\sqrt{a_0}. \tag{2.29}$$

If all the electrons are expelled behind the laser pulse, the result is a positively charged ion channel, which is called the blow-out regime or bubble regime [34]. When the restoring force and the ponderomotive force are balanced, the laser pulse drives the plasma wave very efficiently. Under these *matched conditions*, the transverse size, r, of the bubble is given by the force balance. Simulations have shown that these conditions are fulfilled when $r \approx w_0$ [35] yielding a matched laser pulse spot size:

$$w_0 = \frac{\sqrt{a_0}}{\pi}\lambda_p, \tag{2.30}$$

where λ_p is the plasma wavelength defined in Eq. 2.31.

From Eq. 2.16 it is possible to determine the plasma wavelength:

$$\lambda_p = \frac{2\pi v_p}{\omega_p}, \tag{2.31}$$

where v_p is the phase velocity of the plasma wave, which equals the group velocity of the laser pulse, given in Eq. 2.19, i.e. close to c. It is therefore possible to resonantly drive the plasma wave by matching the length of the laser pulse to the plasma wavelength. Assuming a Gaussian pulse, and a small relative electron density perturbation, the resonance condition is given by [27]:

$$c\tau = \frac{\sqrt{2\ln 2}}{\pi}\lambda_p \approx 0.4\lambda_p. \tag{2.32}$$

This resonance condition is also valid for large charge separations, but then the plasma wavelength must be changed to its relativistic counterpart, as is described in Section 2.3.1. This means that the plasma wavelength in the relativistic case becomes:

$$\lambda_p^{(r)} = \lambda_p\sqrt{\langle\gamma_\perp\rangle}, \tag{2.33}$$

instead of the expression given in Eq. 2.31.

The expressions given in Eq. 2.26 and Eq. 2.27 are only valid for $a_0 \ll 1$, and for high pump strengths it is not possible to derive analytical expressions in the three-dimensional case. However, it is possible in one dimension, and the wake potential is then given by [36]:

$$\frac{\partial^2\phi}{\partial\zeta^2} = \frac{k_p^2}{2}\left[\frac{1+a^2}{(1+\phi)^2} - 1\right], \tag{2.34}$$

[1]Dephasing can also occur in the linear regime. In this case the dephasing length is given by $L_{\mathrm{d}} = c\omega_0^2/\omega_p^3$ [32].

which can be solved for specific pulse shapes. The electron density modulation can then be found from:

$$\Delta n/n_e = \frac{1}{2}\left[\frac{1+a^2}{(1+\phi)^2} - 1\right], \tag{2.35}$$

and the electric field from $E_z = -(m_e c^2/q_e) \times \partial\phi/\partial\zeta$. In Fig. 2.6, Eq. 2.35 and E_z are shown for Gaussian pulse shapes with varying τ and a_0 for $n_e = 5 \times 10^{18}\,\mathrm{cm}^{-3}$.

It is possible to efficiently drive plasma waves by increasing the laser pulse intensity and decreasing its duration, as shown in Fig. 2.6. The density peaks are separated by roughly a plasma wavelength in each case, which increases with increasing a_0, as described in Section 2.3.1. The intensity of a real laser pulse varies over the transverse plane, see, for example, Eq. 2.7, which means that λ_p also varies transversally. This results in the characteristic plasma wave shape seen in Fig. 2.7(a).

2.4.1 Injection Mechanisms

If electrons are continuously injected into the plasma wave behind the laser pulse, the resulting electron spectrum will have a large energy spread. However, if a small number are injected locally, all the electrons in the bunch will experience the same acceleration force over the same distance, and thus attain the same energy after acceleration. To achieve this, a small number of electrons must be injected at one position over a very short time. There are several methods of injecting electrons into the accelerating part of the plasma wave, such as self-injection [37–39], density gradient injection [40–42], colliding pulse injection [43–45], and ionization injection [46–48]. In the LWFA experiments performed in this work, self-injection (Papers I, II, III, VI, VII, and VIII) and density gradient injection (Papers IV and V) were used.

Self-Injection

When the intensity of the laser pulse is very high (corresponding to $a_0 > 1$), the speed of the displaced electrons will approach the phase velocity of the plasma wave, v_p. The result is that the wave breaks and its growth is effectively stopped. It is also possible for electrons to enter the accelerating phase behind the laser pulse, and be accelerated by the extremely high electric fields generated by the charge separation. It has been shown that just above the injection threshold density, which is the lowest density at which electrons are self-injected, the accelerated electron beams have attractive properties such as low spatial divergence and a small energy spread [22–24]. This is an effect due to beam loading [49], which means that the electric field of the injected electrons shields the accelerating field and prevents any further injection.

Density Gradient Injection

Instead of relying on a stochastic process such as self-injection, electrons can be injected into the accelerating part of the plasma wave by locally altering the plasma

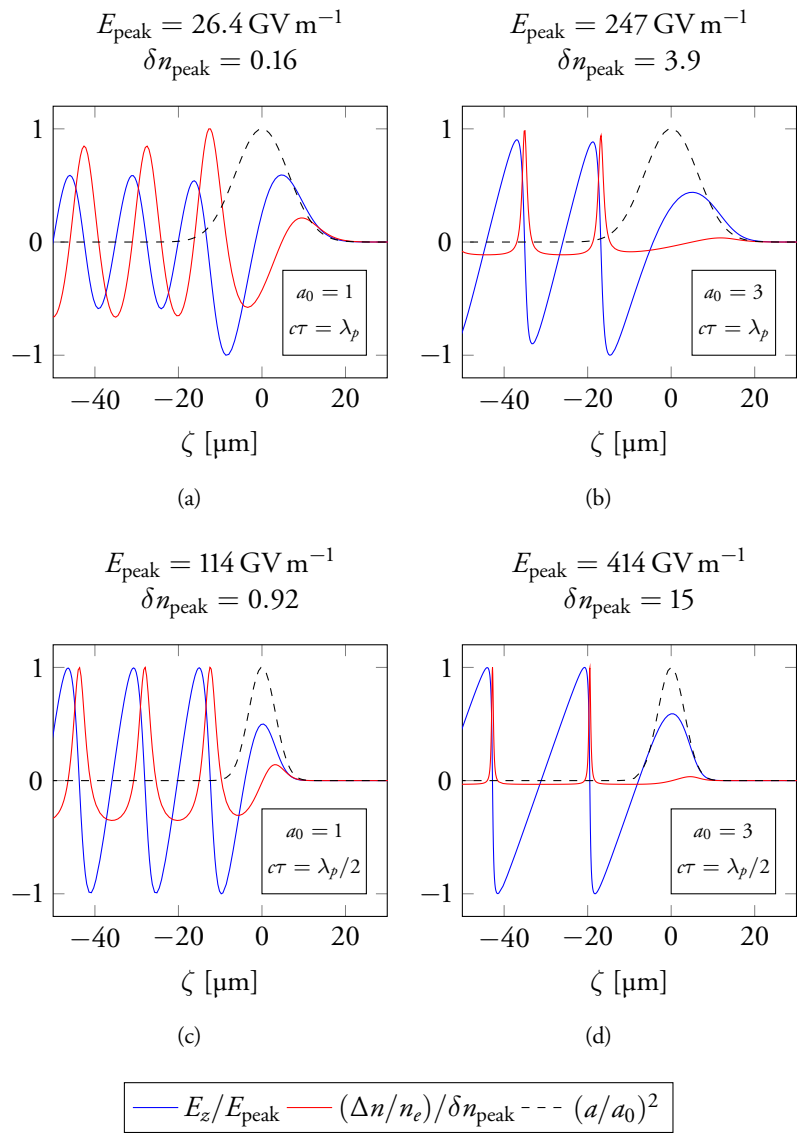

Figure 2.6 Nonlinear Plasma Waves
Normalized longitudinal electric fields (blue lines), electron density perturbations (red lines), and laser pulse envelopes (black dashed lines) in a plasma with $n_e = 5 \times 10^{18}$ cm^{-3} for (a) $a_0 = 1$, $c\tau = \lambda_p$, (b) $a_0 = 3$, $c\tau = \lambda_p$, (c) $a_0 = 1$, $c\tau = \lambda_p/2$, and (d) $a_0 = 3$, $c\tau = \lambda_p/2$. In the long-pulse, low-intensity case shown in (a), the density perturbation and electric field have a sinusoidal shape. Decreasing the pulse length closer to matching, as in (c), causes the density perturbation to become more peaked with stronger electric fields. This behavior is even more pronounced when the intensity is increased, instead of decreasing the pulse length (b). As can be seen in (d), a combination of short laser pulse length and high intensity results in very narrow density peaks, which create sawtooth-shaped electric fields.

wavelength. If we assume that a plasma wave has formed, with λ_p given by Eq. 2.31; then if λ_p is rapidly increased, the electrons at the back of the first plasma wave period can be trapped, as shown in Fig. 2.7. To achieve this rapid change in plasma wavelength it can be noted that combining Eq. 2.31 with Eq. 2.16 gives $\lambda_p \propto n_e^{-1/2}$. Thus, decreasing n_e, causes λ_p to increase, which allows for electron injection without breaking the plasma wave. The spectral features of the accelerated electron beams then depend on the duration of injection, which in this case translates into the length of the density gradient. In Fig. 2.7(a) the electron number density is $n_e = 6 \times 10^{18}$ cm^{-3} and is reduced to 3×10^{18} cm^{-3} in Fig. 2.7(c).

2.4.2 Generation of Betatron Radiation

Strong radial focusing forces exist inside the plasma wave, where the electrons are accelerated, due to the positively charged background of the stationary ions. Thus, if an electron is injected off-axis, it will gain transverse momentum and oscillate about the optical axis. As for all charged particles, acceleration will cause the particle to emit radiation. This radiation is called betatron radiation, and due to the relativistic velocity of the electrons in the forward direction, the emitted radiation extends to x-ray energies and forms a collimated beam in the forward direction. It has been shown that the spectrum is synchrotron-like [50, 51] with keV critical energy ($\mathcal{E}_c$). Since the properties of the emitted radiation are closely related to the electron acceleration and injection processes, the characteristics of the radiation can be studied and used as diagnostic tools, as was done in two of the current studies (Papers VI and VII). The longitudinal position of the x-ray source was determined from the spatial profile of the x-rays, which was possible since the capillary exit rim casts a shadow with a diameter depending on the position of the x-ray emission. The number of betatron oscillations was also inferred by studying the relation between electron beam charge and x-ray fluence. The amplitude of electron oscillation (r_β) can also be determined by measuring $\mathcal{E}_c$ and the mean electron energy, since [50]:

$$\mathcal{E}_c = \frac{3\hbar}{2c}\gamma^2\omega_p^2 r_\beta. \tag{2.36}$$

In Eq. 2.36, $\hbar$ is the reduced Planck's constant, and γ is the relativistic factor associated with the electrons emitting betatron radiation, which can be estimated from the mean electron energy.

Paper VIII reports on the enhancement of the x-ray signal when using gas-filled dielectric capillary tubes (see Section 3.2.1) instead of supersonic gas jets (see Section 3.2.2) as the target.

2.5 Target Normal Sheath Acceleration of Protons

As in Section 2.4, a brief description of the theory behind the acceleration process will be given before discussing the experiments. A more complete description of

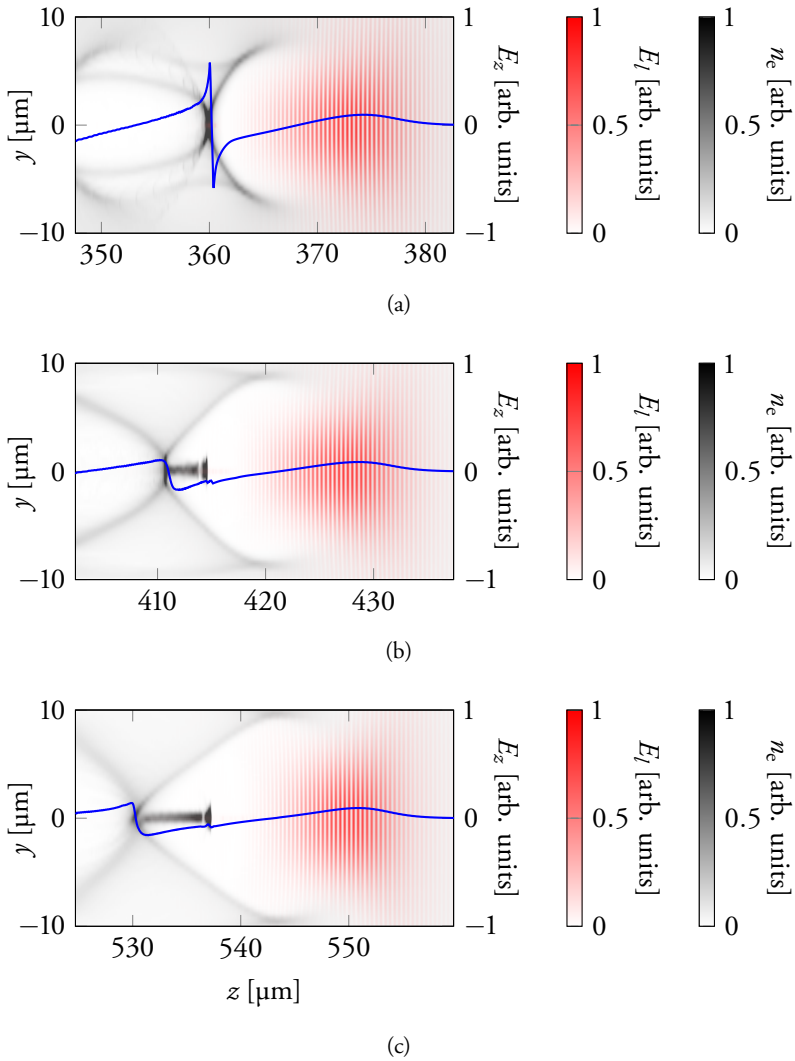

Figure 2.7 Density Gradient Injection
In the high-density region (a), there are no electrons inside the accelerating phase of the first period of the plasma wave, while in the density gradient (b), the plasma wavelength increases as the plasma electron number density is decreased, allowing the injection of electrons. In (c) the number density is again constant, but is lower, corresponding to a longer plasma wavelength. The longitudinal electric field strength is shown by the blue line.

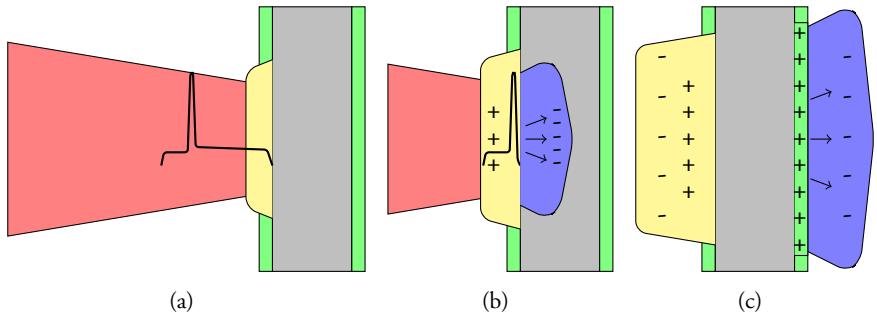

Figure 2.8 Target Normal Sheath Acceleration
(a) The front part of the incident laser pulse (red in figure) instantly ionizes the atoms or molecules (green in figure) present on the front of the target foil (gray in figure), creating an expanding plasma (yellow in figure). (b) As the main part of the laser pulse arrives at the target it starts to heat and push electrons (blue) into the target foil. (c) The electrons exit the rear of the target and form an electron sheath, which induces a strong electrostatic field (TV m^{-1}) that ionizes contaminants on the rear of the target. Positively charged particles are then accelerated in this field over a distance of several µm. If the accelerated particles are protons, they will reach energies of a few MeV.

TNSA is given by Daido, Nishiuchi, and Pirozhkov [20].

As was found from Eq. 2.17, if $\omega_0 < \omega_p$, the laser pulse cannot propagate through the plasma, and is therefore reflected. Since $n_e > n_c$, this means that the target material has a high number density. In practice, overdense plasmas are created by the ionization of solid targets, often thin foils. The concept of TNSA is illustrated in Fig. 2.8. In the first stage, the ASE pedestal (see Section 2.1) on the leading edge of the laser pulse creates a preplasma, which expands towards the main part of the laser pulse. The main part of the laser pulse then interacts with and heats the expanding plasma, and penetrates it until the laser pulse is eventually reflected. The ponderomotive force pushes electrons through the overdense region of the plasma and they exit from the rear of the foil, whose structure remains intact during this time span. When the electrons have traversed the foil, they expand into vacuum and set up a strong electric field, which ionizes the atoms or molecules present on the rear surface. Under normal experimental conditions, water molecules and hydrocarbons will be present on the rear surface. This means that mainly protons will be accelerated by the electrons, in the direction normal to the target, hence the name of the acceleration process. The resulting particle beam is actually quasi-neutral, since electrons and protons copropagate after acceleration. However, since the proton rest mass, $m_p c^2 = 938\,\text{MeV}$, is much larger than the kinetic energy gained during acceleration, the resulting proton beam is inherently non-relativistic. This means that the speed of the particle is determined by its energy, in contrast to the acceleration of electrons by LWFA, where all the electrons are traveling close to the speed of light. As a result, an initially short proton pulse becomes longer with increasing distance from the target foil, provided the proton pulse has a broad energy spectrum.

As can be seen in Fig. 2.8(c), the protons are emitted from an area on the rear of the foil that is larger than the laser spot size [52], and the emitted proton flow is highly laminar [53]. This means that the beam has imaging properties, and the protons can be regarded as having been emitted from a virtual source somewhere in front of the target.

2.5.1 Laser Absorption & Plasma Heating

The conversion of laser energy to hot electrons can be understood through a number of mechanisms, all of which are most efficient at the boundary where $n_e = n_c$. The interplay between these processes is complex, and a complete description of plasma heating requires detailed numerical simulations. However, some physical insight can be gained through a brief introduction to the main processes involved. It should first be mentioned that the absorption will either be collisional or collisionless, depending on the plasma temperature, T_e, and the electron number density. For most of the experimental conditions used in this work, absorption is expected to be mainly collisionless. Collisional absorption dominates for intensities between $10^{12}\,\mathrm{W\,cm^{-2}}$ and $10^{14}\,\mathrm{W\,cm^{-2}}$ [27], and for long plasma scale lengths, L, *inverse Bremsstrahlung* is the main laser absorption process. Here, the laser directly accelerates electrons in the underdense part of the expanding plasma, and T_e is increased through electron–ion collisions.

At higher laser intensities, where the resulting plasma can be considered collisionless, various absorption processes can occur. For instance, let us consider the case of an expanding plasma, with $L/\lambda \gg 1$, and an electron number density given by:

$$n_e(z) = \begin{cases} n_c\,(1 + z/L) & \text{for } z/L > -1 \\ 0 & \text{for } z/L < -1 \end{cases}. \tag{2.37}$$

For an angle of incidence, α, greater than zero, the pulse propagates through the underdense part of the plasma, and is continuously refracted in the density gradient. It is eventually reflected at the plane where $n_e = n_c \cos^2\alpha$ [54], as indicated in Fig. 2.9. At the plane of reflection, the electric field of a p-polarized laser pulse is parallel to the density gradient, and part of the electric field can tunnel through to the critical density plane. The electric field will resonantly induce a plasma wave, oscillating at the plasma frequency, since $n_e = n_c$ and thus $\omega_0 = \omega_p$. The amplitude of the wave increases during the duration of the laser pulse, and the plasma temperature is increased as the wave is attenuated by processes such as wave breaking (see Section 2.4.1) or electron–ion collisions. The damping process that dominates also depends on T_e and n_e. This process is called *resonance absorption*, and a numerical example for a linear plasma density gradient, its corresponding refractive index (see Eq. 2.18), and the resulting refractive angle for incidence angle of 45° are shown in Fig. 2.10. The above reasoning does not hold for s-polarized light, since the electric

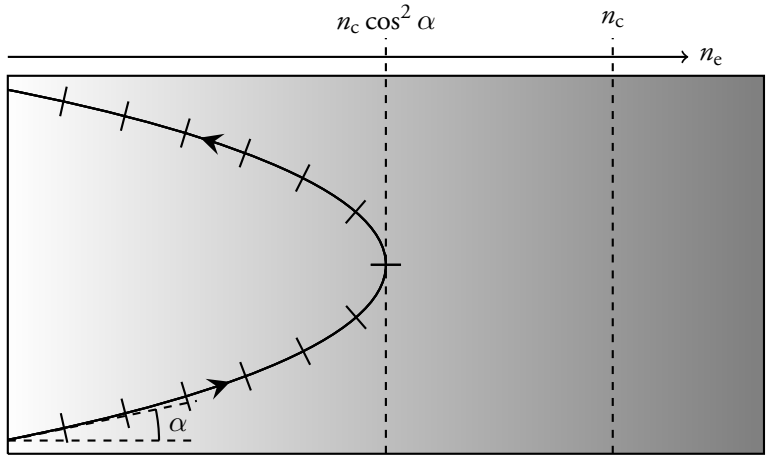

Figure 2.9 Resonant Absorption
Schematic illustration of resonant absorption of p-polarized laser light in a plasma with an increasing density gradient. The light is continuously refracted as it propagates through the linear density ramp, and is eventually reflected. At the point of reflection, the electric field of the laser is parallel to the density gradient, and part of the field can tunnel through to the plane of critical density and resonantly drive a plasma wave.

field will never be directed along the density gradient, and cannot tunnel through to the plane of critical density.

In the case of short plasma gradient lengths, or $L < v_{osc}/\omega_0$ [55], where v_{osc} is the oscillation velocity and ω_0 the laser angular frequency, *vacuum heating* becomes important. Here, the electrons are transported out into vacuum and then sent back into the plasma by the laser field [56]. Close to the vacuum–plasma boundary, an electron can be forced to exit the plasma by the electric field of the laser. Halfway through the laser cycle, the electric field changes direction, and the electron is accelerated back towards the plasma gradient. Since the gradient is steep, the plasma quickly becomes overdense, effectively stopping the laser. The electron, however, is free to continue into the plasma, where it can be absorbed through collisions.

For steep density gradients and very high intensities ($>10^{19}\,\mathrm{W\,cm^{-2}}$), plasma heating can also occur through a process called *J x B heating*. This is driven by the oscillating part of the ponderomotive force exerted by the laser field on the electrons [57]. These electrons are driven into the plasma, thus increasing the temperature. This acceleration is directed along the axis of laser propagation, and is therefore most efficient for normal incidence.

In the collisionless processes described above, some of the resulting energetic electrons are absorbed by the plasma, while others are converted into hot electrons, with a temperature T_h, that retain energies higher than the bulk plasma electrons. The direction of the hot electrons depends on the heating mechanism. In resonance absorption and vacuum heating the heating is isotropical, and, as stated previously,

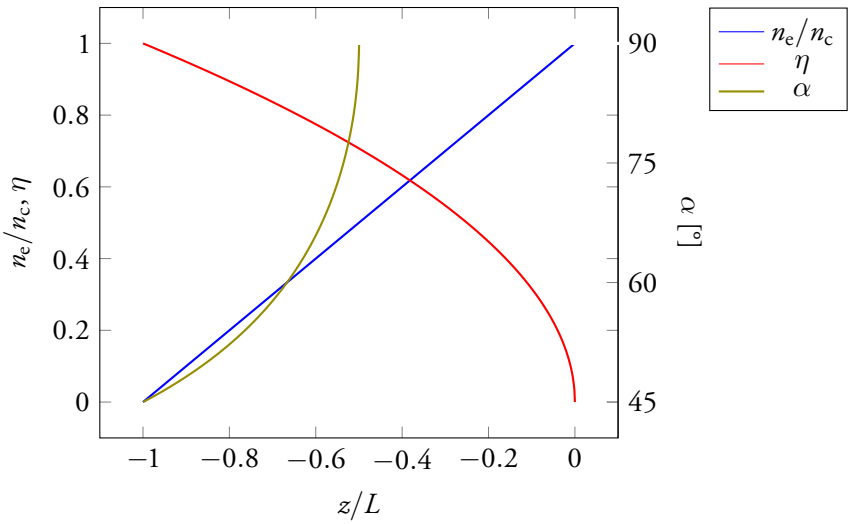

Figure 2.10 Resonant Absorption
The refractive index (red line) of an expanding plasma with a linear density ramp (blue line). The refraction angle of the laser beam, incident at an angle of 45°, is shown in green, and it can clearly be seen that reflection occurs before the critical number density is reached.

along the laser propagation axis in J x B heating.

Experiments have shown that there are different regimes of T_h scaling [27, p. 179]. For intensities $I\lambda^2 > 10^{18}\,\mathrm{W\,cm^{-2}\,\mu m^2}$, T_h scales as [58–60]:

$$T_h \approx \frac{m_e c^2}{k_B}\left(\sqrt{1+a_0^2}-1\right), \tag{2.38}$$

while the number density of hot electrons on the front of the target is given by [61]:

$$n_h = \frac{\chi\,\mathcal{E}_{\mathrm{pulse}}}{c\tau\pi w_0^2 k_B T_h}, \tag{2.39}$$

where χ is the conversion efficiency, which scales as [61]:

$$\chi = 1.2\times10^{-15}\left(I\left[\mathrm{W\,cm^{-2}}\right]\right)^{0.74}, \tag{2.40}$$

up to $\chi = 50\,\%$. However, measurements have shown that for $\alpha = 45°$ the conversion efficiency can be as high as 80 % to 90 % for $I_0 \geq 10^{20}\,\mathrm{W\,cm^{-2}}$ [62], but this is not expected to be the case in the experiments presented in this thesis.

2.5.2 Electron Transport & Sheath Expansion

A fraction of the hot electrons will propagate through the target, and these are characterized by their temperature. The resulting hot-electron current, $\mathbf{j}_h$, can be

extremely high (∼50 MA [27, p. 193]), and cold return currents, $\mathbf{j}_c$, thus arise [63]. As the return currents have a lower temperature (T_c) than the hot currents, the return current number density, n_c, must be increased to balance $\mathbf{j}_h$. The resulting total current is therefore close to zero [63], or $\mathbf{j}_h + \mathbf{j}_c \approx 0$. The hot electrons are reflected from the rear surface due to self-induced sheath fields [64], and if the target thickness, d, is smaller than half the laser pulse length, i.e.:

$$d < \frac{c\tau}{2}, \tag{2.41}$$

the electrons can be recirculated and reheated in the target, which enhances the hot electron density, n_s, on the rear of the target:

$$n_s = \left(\frac{w_0}{r_s}\right)^2 n_h, \tag{2.42}$$

where r_s is defined in Eq. 2.43. The increase in n_s in turn increases the accelerating electric field, and thus the resulting maximum proton energy, depending on target thickness [65].

Numerical Example

For a laser pulse with a duration of 35 fs, the corresponding laser pulse length is 10 µm. Thus, hot-electron recirculation and reheating are expected for targets thinner than 5 µm.

In general, the maximum proton energy increases with decreasing target thickness. For moderately thick targets ($d > c\tau/2$) this is mainly due to a geometric effect [66], which is illustrated in Fig. 2.11. Since r_s is small for small values of d, the hot-electron density on the rear of the target is high, thus allowing higher accelerating field strengths. The beam of hot electrons diverges by the half angle θ, and the initial sheath radius is given by:

$$r_s = w_0 + d\tan\theta. \tag{2.43}$$

However, it is difficult to determine θ, since it depends on variables such as the laser energy, laser intensity, and target material. In fact, θ has been reported to be ∼15° for $d > 40$ µm and as low as 8° for $d \leq 10$ µm [67, p. 308]. It is therefore difficult to determine r_s, but a general dependence on w_0 and d, as stated in Eq. 2.43, can be expected.

The initial electric field strength is given by [67, p. 311]:

$$E(z) = \frac{2k_B T_h}{q_e} \times \frac{1}{z + \sqrt{2\exp(1)}\lambda_{D0}}, \tag{2.44}$$

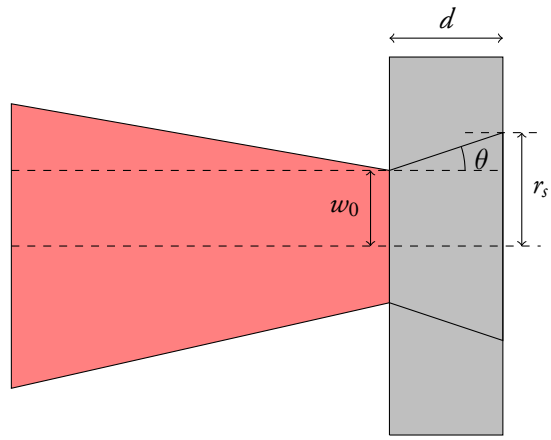

Figure 2.11 Transverse Sheath Size
The transverse size of the electron sheath depends on the target thickness and the electron divergence inside the target. The sheath size decreases with decreasing target thickness, which means that the resulting sheath electron density is increased.

where

$$\lambda_{D0} = \sqrt{\frac{\varepsilon_0 k_B T_\mathrm{h}}{q_\mathrm{e}^2 n_\mathrm{s}}} \tag{2.45}$$

is the local Debye length on the rear of the target. The maximum electric field is found by setting $z = 0$ in Eq. 2.44, and combining with Eq. 2.45:

$$E_\mathrm{max} = \sqrt{\frac{2 k_B T_\mathrm{h} n_\mathrm{s}}{\exp(1)\,\varepsilon_0}} \tag{2.46}$$

from which it is clear that increasing T_h or n_s results in a higher field strength. Also, a small r_s also increases E_max, which simply means that the hot-electron density on the rear of the target is higher for smaller sheath radii. Typically, E_max is on the order of TV m^{-1}, which is large enough to instantly ionize atoms or molecules on the rear of the target.

Numerical example

For an electron temperature of 1 MeV, a laser energy of 1 J, a pulse duration of 35 fs, and a FWHM spot size of 5 µm, the resulting hot-electron density is 2×10^{21} cm^{-3} for a 50 % conversion efficiency. The maximum electric field strength is then 9 TV m^{-1} with a local Debye length of 0.1 µm for $\theta = 8°$ and a 3 µm target thickness.

For target materials without return currents [68], strong electric fields induced within the target effectively stop the hot-electron current. In fact, it has been shown that without any return currents at all, $\mathbf{j}_\mathrm{h}$ is stopped after $\sim$1 nm [69]. This means that in materials where the current is restricted, such as insulators, the target must first be ionized before being able to carry the necessary return currents. Thus, electron transport and the resulting proton beam are affected by the target material. There may also be spatial separations between $\mathbf{j}_\mathrm{h}$ and $\mathbf{j}_\mathrm{c}$, causing large magnetic fields to be induced. These magnetic fields will affect the propagating electrons, and can cause pinching and even filamentation due to the Weibel instability [70]. The timescale for filament formation is given by [71]:

$$t_w = \omega_{ph}^{-1} \sqrt{\frac{\gamma n_\mathrm{e}}{n_\mathrm{h}}} \frac{c}{v_h}, \tag{2.47}$$

where ω_{ph} and $v_h \approx c$ are the plasma frequency and the velocity of the hot-electron beam, respectively.

Numerical Example

Consider a hot electron beam of density $n_\mathrm{h} = 0.1 n_\mathrm{c}$ and temperature $k_B T_\mathrm{h} = 5\,\mathrm{MeV}$, propagating through an overdense plasma of density $n_\mathrm{e} = 30 n_\mathrm{c}$. The filament formation timescale is $t_w \approx 80\,\mathrm{fs}$, and significant electron beam filamentation is thus not expected for target thicknesses smaller than $c\,t_w \approx 20\,\mu\mathrm{m}$.

A portion of the hot electrons will exit through the rear of the target, and will start to form an electron sheath. The initial transverse shape of the electron sheath depends on the electron transport through the target. If θ decreases linearly with electron energy, the sheath profile will be parabolic [72]. Initially, the sheath mainly expands longitudinally, but gradually starts to expand transversely [73]. The speed of the longitudinal expansion, v_z, is approximately equal to the proton sound speed, thus:

$$v_z(t) = \sqrt{\frac{k_B T_\mathrm{h}(t)}{m_\mathrm{p}}}, \tag{2.48}$$

where m_p is the proton mass. The transverse expansion can be seen as a consequence of the initial transverse velocity component of the electrons, which remains largely unchanged. As these electrons are reflected by the sheath fields at the rear surface, they will recirculate and spread out transversely at a velocity that can be estimated as $v_\perp \approx \cos(\alpha) \times v_h$ [74, 75]. The transverse expansion can also be understood from the self-generated magnetic fields on the rear of the target. Electrons with relativistic

energies, $\mathcal{E}_\mathrm{h}$, in a magnetic field of length l and strength B attain transverse speeds according to [76]:

$$v_\perp = \frac{c^2\, l\, q_\mathrm{e} B}{\mathcal{E}_\mathrm{h}}. \tag{2.49}$$

2.5.3 Effect of Laser Pulse Temporal Contrast

In Section 2.5.1, it was stated that different laser absorption mechanisms will dominate depending on the laser intensity and the on plasma scale length (L). To achieve a short scale length, it is necessary for the laser pulse to have a high temporal contrast ratio (see Section 3.1.1). The highest laser intensity that will not affect the front of the target can be estimated from the laser-induced damage threshold fluence, F_LIDT (see Eq. 2.13). Thus, the limiting intensity can be estimated as $I = F_\mathrm{LIDT}/\tau_\mathrm{pre}$ for light with a duration τ_pre. This can be expressed in terms of the contrast ratio as:

$$C = \frac{I_0 \tau_\mathrm{pre}}{F_\mathrm{LIDT}}. \tag{2.50}$$

In Eq. 2.50, there only seems to be a weak dependence on τ_pre. However, F_LIDT is implicitly dependent on light duration, and generally varies with both the laser pulse duration and the target material.

It is also important to have a sharp plasma boundary on the rear of the target to achieve high proton energies, since the local Debye length, defined in Eq. 2.45, is then equal to the charge separation distance. If there is plasma expansion prior to the main laser pulse, and the scale length on the rear of the target, L_rear, is greater than λ_{D0}, L_rear replaces the local Debye length in Eq. 2.44, thus reducing $E(z)$. As soon as a light pulse hits the target, it will induce a shock wave traveling at the speed v_s given by [77]:

$$v_s = \frac{c_0}{2}\left(\sqrt{1+x}+1\right), \tag{2.51}$$

where c_0 is the speed of sound in the unperturbed target, and:

$$x = \frac{4\alpha_\mathrm{n}}{\rho_0 c_0^2} P, \tag{2.52}$$

α_n is a material constant, ρ_0 the unperturbed target mass density, and $P = \xi I^{(2/3)}$ is the pressure associated with light of intensity I. Here, ξ is a material parameter, with the value $\approx 1\,\mathrm{kg}^{1/3}\,\mathrm{m}^{-1}$ for laser light with a wavelength of 0.8 µm. The shock wave takes a time $\tau_s = d/v_s$ to traverse a target of thickness d, and thus τ_s is the limiting time duration between the light initiating the shock wave and the main laser pulse. Using this expression together with Eq. 2.51 and Eq. 2.52 to find the limiting intensity, I, yields:

$$I = \left[\frac{\rho_0 d}{\alpha_\mathrm{n}\xi\tau_s^2}\left(d - c_0\tau_s\right)\right]^{3/2}. \tag{2.53}$$

Table 2.1 Material Parameters
Material parameters for materials often used as targets in TNSA experiments [77]

Material	ρ_0 [g cm^{-3}]	c_0 [µm ns^{-1}]	α_n
Aluminum	2.70	5.24	1.40
Gold	19.30	3.08	1.56
Mylar	0.92	2.76	1.59

Relating this expression to I_0 by $I_0 = CI$, where C is the contrast ratio gives:

$$C = I_0 \tau_s^3 \times \left[\frac{\alpha_n \xi}{\rho_0 d (d - c_0 \tau_s)} \right]^{3/2}. \tag{2.54}$$

This contrast ratio is the limit at which the rear of the target is affected by light reaching the target before the main laser pulse. As can be seen in Eq. 2.54, it is strongly dependent on τ_s. It is therefore important to control the duration of the light prior to the main pulse. The temporal contrast ratio in Eq. 2.54 is also strongly dependent on d. Since the shock waves must traverse the target, a higher contrast ratio will be required with thin targets than with thick ones. Parameters for some of the materials often used as targets in TNSA experiments are given in Table 2.1.

Numerical Example

Consider laser light focused to an intensity of 5×10^{19} W cm^{-2} on an aluminum target of thickness 3 µm. Assuming that the light preceding the main laser pulse has a duration of 150 ps, a temporal contrast ratio better than 10^6 is needed to avoid effects on the rear of the target. To avoid effects on the front of the target, and assuming that the induced damage threshold fluence for picosecond pulses on aluminum is 200 mJ cm^{-2}, the temporal contrast ratio must be greater than 4×10^{10}.

2.5.4 Spectral and Spatial Proton Beam Properties

Beams of laser-accelerated ions have several attractive features, such as high laminarity, a sharp maximum energy cut-off, and a high number of particles. In the experiments performed in this work, the main accelerated ion species was protons, since they have the highest charge-to-mass ratio. These protons originate from water or hydrocarbons on the rear surface of the target, and are accelerated in the electrostatic sheath field. As they leave the target they will screen the heavier

ions at the target surface from the electric field. This means that the protons that are accelerated first will experience the highest accelerating field, and thus attain the highest energies. The maximum proton energy as a function of time during acceleration can be expressed as [78]:

$$\mathcal{E}_{\max} = 2k_B T_{\mathrm{h}} \ln^2 \left(\tau_{\mathrm{n}} + \sqrt{1 + \tau_{\mathrm{n}}^2} \right), \tag{2.55}$$

where $\tau_{\mathrm{n}} = \omega_{pi} t / \sqrt{2 \exp(1)}$, and ω_{pi} is the plasma ion frequency given by:

$$\omega_{pi} = \sqrt{\frac{n_s Z q_{\mathrm{e}}^2}{m_i \varepsilon_0}}, \tag{2.56}$$

where n_s is the electron density on the rear of the target (given in Eq. 2.42). It has been found [61, 79] that the acceleration time for intensities $> 3 \times 10^{19}\,\mathrm{W\,cm^{-2}}$ is given by:

$$\tau_{\mathrm{acc}} \approx 1.3 \left(\tau + t_{\min} \right), \tag{2.57}$$

where $t_{\min}$ is 60 fs. In order to determine how the maximum proton energy scales with peak laser intensity (I_0), it can be seen in Eq. 2.55 that $\mathcal{E}_{\max} \propto T_{\mathrm{h}}$, and combining with Eq. 2.10 and Eq. 2.38 it is found that $\mathcal{E}_{\max} \propto \sqrt{I_0}$.

Using Eq. 2.55 together with expressions for τ_{n}, ω_{pi}, n_s, and n_{h} (see Eq. 2.39), $\mathcal{E}_{\max}$ is found to be a function of the laser parameters $\mathcal{E}_{\mathrm{pulse}}$, FWHM, and τ, as shown in Fig. 2.12. It is expected that the highest proton energies will be achieved for the highest value of $\mathcal{E}_{\mathrm{pulse}}$ in combination with the smallest FWHM and τ, which can also be seen in Fig. 2.12. By combining Eq. 2.56 and Eq. 2.42, it is also found that $\mathcal{E}_{\max}$ increases with decreasing target thickness, d. However, this assumes that the temporal contrast of the laser pulse is sufficiently high.

The number of protons decreases exponentially as their energy increases with a rapid decrease at $\mathcal{E}_{\max}$, and since the relevant energies are well below the proton rest mass ($m_{\mathrm{p}} c^2 = 938\,\mathrm{MeV}$), the beam is inherently non-relativistic. The particle speed, v_i, can therefore be determined from:

$$\beta_i \approx \sqrt{\frac{2\mathcal{E}}{m_{\mathrm{p}} c^2}}, \tag{2.58}$$

where $\beta_i = v_i / c$ (see Fig. 2.13). This means that the length of the proton bunch increases as it propagates from the target.

The energy of the beams of accelerated protons affects the divergence angle, θ_D, which increases with decreasing energy [80]. The maximum energy, given by setting $t = \tau_{\mathrm{acc}}$ (see Eq. 2.57) in Eq. 2.55, is therefore expected at the beam center. This property is an effect of the shape of the electron sheath [81], which has been shown to be parabolic initially [82]. As acceleration occurs predominantly normal to the density gradient, this causes an energy-dependent divergence angle, as described

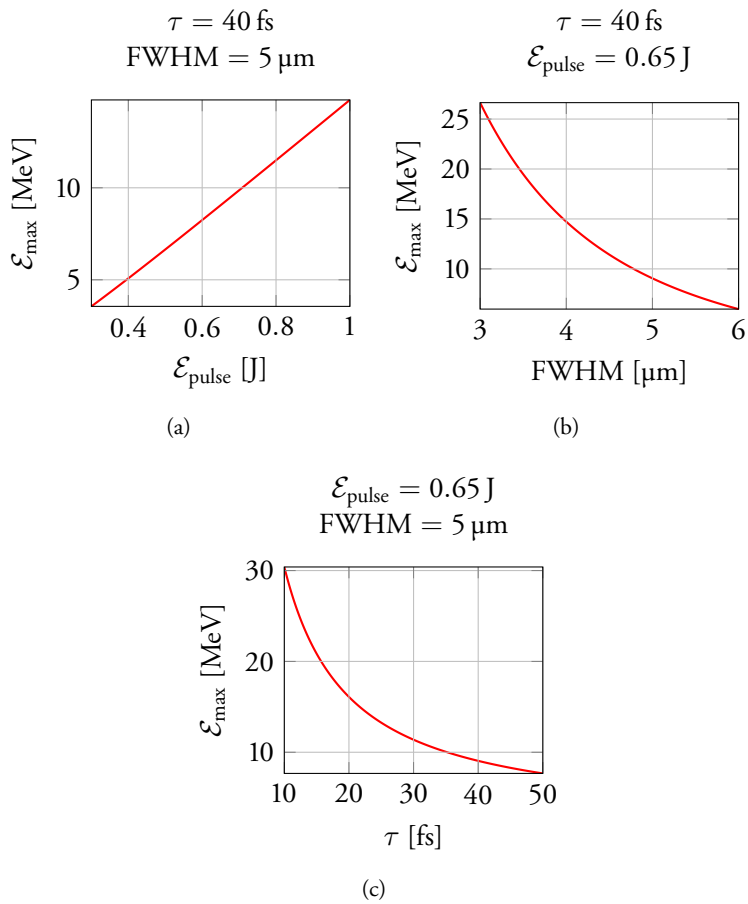

Figure 2.12 Maximum Proton Energy
The maximum proton energy as described by Eq. 2.55, with the acceleration duration given in Eq. 2.57 for $d = 3\,\text{mm}$ and $\theta = 8°$ when varying (a) laser pulse energy with FWHM $= 5\,\mu\text{m}$ and a pulse duration of 40 fs (giving $\tau_{acc} = 130\,\text{fs}$), (b) laser spot size with an energy of 650 mJ and a pulse duration of 40 fs, and (c) laser pulse duration with a spot size of 5 µm and a pulse energy of 650 mJ. It can clearly be seen that the maximum proton energy is strongly dependent on the laser spot size and pulse duration.

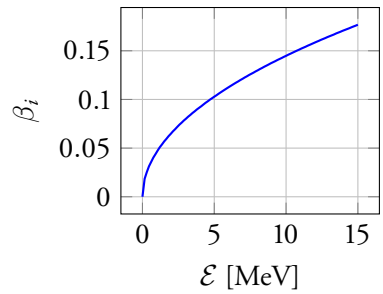

Figure 2.13 Proton Speed
Since the protons have non-relativistic energies, their speeds vary significantly with kinetic energy. The proton bunch length therefore increases with propagation distance from the target if the protons have a broad energy distribution, as is the case in TNSA.

above. It should also be mentioned that this relationship was utilized in the studies described in Papers X and XI, where altering the laser pulse intensity distribution on the front of the target directly affected the shape of the electron sheath, which in turn affected the spatial profile of the proton beam produced. The source size on the rear of the target can be many times greater than the diameter of the impinging focal spot; up to 500 µm for low-energy particles [52]. The source diameter for high-energy protons, on the other hand, can be less than 10 µm [67, p. 325].

The number of accelerated particles can also be estimated. In a previous experiment [83], the contamination layer on the rear of the target was determined to be approximately 12 Å thick, with an estimated hydrogen atom density of $2.24 \times 10^{23}\,\mathrm{cm}^{-3}$. Thus, for a source with 200 µm diameter, as was estimated in that experiment, the number of protons available for acceleration was 8.4×10^{12}. This is approximately the same order of magnitude as that observed in experiments, showing that the protons on the rear surface of the target can actually be depleted.

Chapter 3

Experimental Methods

In the first part of this chapter, the Lund multi-terawatt laser system is presented, including the diagnostics used to characterize the laser pulses. The targets used to create underdense and overdense plasmas are then presented in Sections 3.2 and 3.2.3, respectively. Finally, the most important diagnostics used during the laser–plasma acceleration experiments are briefly explained.

3.1 Laser System & Laser Pulse Diagnostics

The multi-terawatt laser system at the Lund Laser Centre is shown in Fig. 3.1. The lasing medium is a sapphire crystal doped with titanium [84]. Short, high-intensity laser pulses are generated using CPA [15]. The Kerr-lens mode-locked oscillator [85] emits pulses at a rate of 80 MHz. The laser pulses have a central wavelength of 0.8 µm

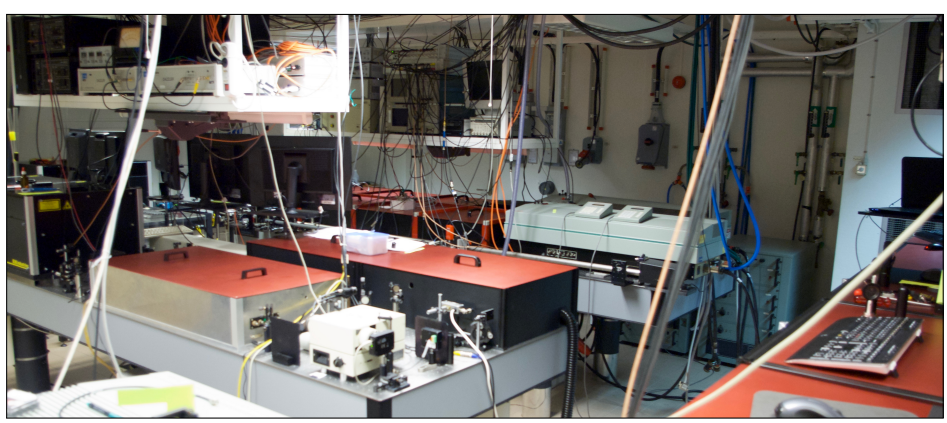

Figure 3.1 Lund Multi-Terawatt Laser System
The multi-terawatt laser at the Lund Laser Centre.

Table 3.1 Laser Parameters
Typical parameters of the Lund multi-terawatt laser system used in the experiments described in this thesis

Central wavelength	0.8 µm
Pulse energy	1 J
Pulse length	40 fs
Repetition rate	10 Hz
Beam diameter	5 cm
Contrast ratio	$> 10^8$
Peak power	40 TW

and a bandwidth of approximately 50 nm. The pulse train exits the oscillator through an output coupler and enters a Pockels cell, which, together with a polarizer, selects ten pulses per second. An acousto-optic device (Fastlite, Dazzler) in the beam path shapes the light spectrally to precompensate for gain narrowing [86] and higher-order dispersion, which occur later in the optical system.

The first part of the CPA setup, a stretcher immediately after the acousto-optic device, increases the pulse length to hundreds of picoseconds by introducing path length differences between different spectral components of the pulse. There are several ways of introducing this temporal broadening, and in this setup diffraction gratings were used. A long pulse length is needed when amplifying to high pulse energies, to prevent damage to the gain media in the amplifiers and other optical components due to nonlinear effects, such as self-focusing [87, 88].

The amplification chain consists of three or four different stages. The first is an optional six-pass preamplifier situated before the stretcher with a gain between 10^3 and 10^4 which, when active, reduces the gain required in the regenerative amplifier [89], which is the next amplification stage. The laser pulses make 10 or 15 round-trips in the regenerative amplifier, depending on whether the preamplifier is active or not, before being switched out from the closed cavity. The laser pulses are then sent through two separate multipass amplifiers [90]. After five passes in the second stage, the pulse energy reaches 400 mJ. The beam is then split into two parts, such that 200 mJ is sent to the last amplifier stage. In preparation for the third, and final, amplifier, a spatial filter removes high-frequency noise from the beam, to prevent damage to the final amplification crystal (which is cryogenically cooled) or the compressor gratings. Finally, pulse compression, which reduces the pulse duration to about 40 fs, takes place under vacuum, since the pulses would otherwise be destroyed by nonlinear effects in air. As stated above, the pulses are optimized by both an acousto-optic device and a spatial filter, however, other polarizers and Pockels cells are used to remove pre-pulses and reduce the amplified spontaneous emission by time gating. The amplification of spontaneous emission is inevitable when using high-power lasers, as in a hard-pumped, closed cavity, the gain medium will spontaneously emit radiation. If this light starts to make round-trips in the

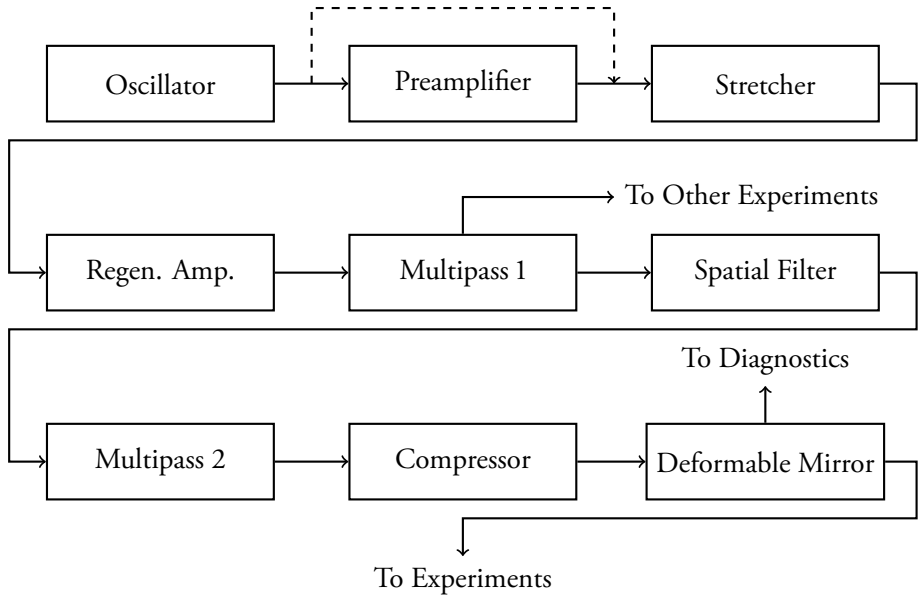

Figure 3.2 Flowchart of the Lund Multi-Terawatt Laser System
The laser pulse originates in the oscillator, and is then sent through an optional preamplifier. The laser pulse is then passed through the stretcher, where the pulse length is increased to several hundreds of picoseconds. The number of round-trips in the regenerative amplifier (Regen. Amp.) is 10 if the preamplifier is used and 15 if it is not. After the first multipass amplifier, the pulse energy is 400 mJ and the beam is split into two parts. One part, containing 200 mJ, is sent to a different lab, while the other passes through a spatial filter before entering the second multipass amplifier, where the pulse energy is increased to 2 J. The laser pulse is then sent to a compressor with 65 % transmission, where the pulse length is decreased to about 40 fs, before it is reflected by a deformable mirror placed in the beam line. From this point, the laser pulse can either be sent to a diagnostics table or to the experimental setup.

cavity, it will be amplified. The temporal contrast ratio can be determined by measuring the intensity at different times relative to the main pulse. When irradiating solid targets, it is of the utmost importance to have a sufficiently high temporal contrast ratio (as described in Section 2.5.3). In the experiments on solid targets described in this thesis (Papers IX to XII), temporal contrast ratios higher than 10^9 on the 100 ps timescale were achieved. It is also possible to enhance the contrast by introducing a plasma mirror in the experimental setup, as will be described in Section 3.1.2.

After amplification and compression, each laser pulse has an energy of about 1 J, and the beam diameter is 5 cm. For a pulse duration of 35 fs, the laser pulse has a spatial extension along its direction of propagation of only 10 µm, which means that the laser pulse can be regarded as a propagating ultra-thin disc of light with a diameter of 5 cm. A schematic overview of the laser system is given in Fig. 3.2, and important experimental laser parameters are summarized in Table 3.1.

The quality of the focal spot is important, as was clearly shown in this work

Table 3.2 Focusing Optics
The focal lengths of the off-axis parabolic mirrors used in the various experiments and the diffraction-limited FWHM spot sizes they can produce assuming a central wavelength of 0.8 μm and beam diameter of 3.5 cm

Focal Length [cm]	FWHM [μm]	Papers
76.5	13	I, V, IV, VI, VII, & VIII
45	7.7	II & III
15.2	2.6	IX, X, XI, & XII

(Papers II and III). One way to optimize the focus of a laser beam is to use an adaptive optics system to correct the wavefront of the light to reduce optical aberrations. Our system consists of a deformable mirror and a wavefront-sensitive detector (Phasics SID 4). The mirror itself has a reflectivity greater than 99.9 % for 0.8 μm wavelength light, and the surface can be deformed by applying high voltages over 32 different control electrodes, employing the inverse piezoelectric effect. One of the 32 electrodes changes the overall curvature of the mirror, which makes it possible to fine-tune the position of the focal plane inside the experimental target chamber. One of the key elements in the studies described in Papers II and III is the deformable mirror's ability to add spherical aberration to the laser pulse in a controlled manner, which alters the energy within the FWHM of the focal spot.

Three different focusing optics, all silver-coated, off-axis parabolic (OAP) mirrors, were used during the experimental work. Information on the focal length of the OAP mirrors and the diffraction-limited FWHM spot size is given in Table 3.2, together with information on which mirror was used for the various studies. Note that the measured FWHM spot sizes were always slightly larger than the diffraction-limited sizes given in Table 3.2 (more detailed information can be found in the respective papers).

Since the intensity of the light is very high, the experiments must be performed under vacuum. The chamber used is an aluminum cylinder with a radius of 60 cm. An extra compartment attached underneath the chamber floor houses three orthogonal translation stages, enabling the target to be moved in three dimensions under vacuum. A number of ports on the top and the side of the chamber enable external equipment to be mounted for diagnostics (see Section 3.3) or other purposes. An example of this is motorized mirrors, which are part of the laser alignment system. They are powered and controlled by cables connected via feed-throughs that do not break the vacuum. A wide range of flanges, pipes and cubes are available that can be connected to the ports, making this a versatile vacuum chamber that can be adapted to very different types of experiments.

A typical setup for LWFA experiments is shown in Fig. 3.3. More equipment is used in a typical experiment, but this has been left out for clarity. As the beam enters the chamber, it is guided by mirrors onto the off-axis parabolic mirror, which focuses

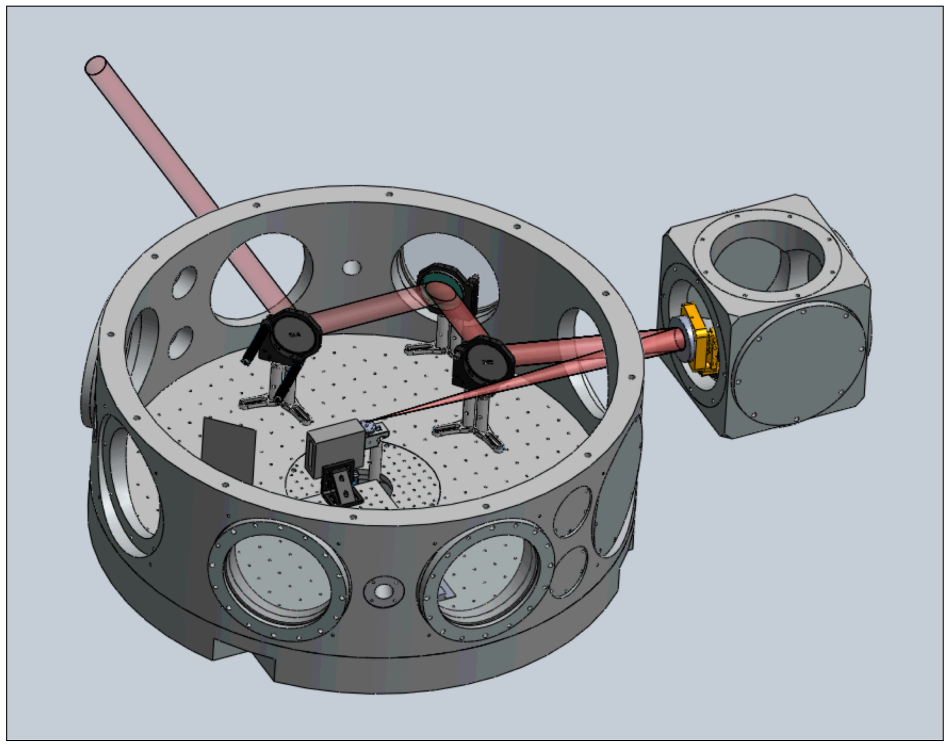

Figure 3.3 Typical Laser Wakefield Acceleration Setup
Typical experimental setup for electron acceleration using LWFA. The off-axis parabolic mirror focuses the incoming laser beam into the gas jet. Directly after the gas jet, a permanent dipole magnet is mounted on a slide, which allows it to be moved away from the optical axis. A scintillating screen is also visible after the magnet. Equipment used for the alignment of the laser, the top-view camera, interferometer, the 16-bit CCD camera, and the x-ray-sensitive CCD camera are not shown for the sake of clarity.

it to a spot size according to Table 3.2, and a pulsed gas jet, a gas-filled capillary tube, or a solid target is placed in the focal plane.

3.1.1 Laser Diagnostics

After the compressor, the laser pulse (or a small fraction of it) can be extracted to a diagnostics table, where the duration and temporal contrast of the laser pulse can be measured.

The pulse duration is determined using a single-shot, second-order autocorrelator [91, 92]. A schematic representation of this device is shown in Fig. 3.4. The laser pulse is first sent through a beam splitter, which divides the incoming pulse into two parts with the same intensity. One arm has a constant optical path length, whereas it is possible to adjust the other. The pulses are then overlapped in a second-harmonic-generation crystal at a small angle, ϕ, relative to each other. When

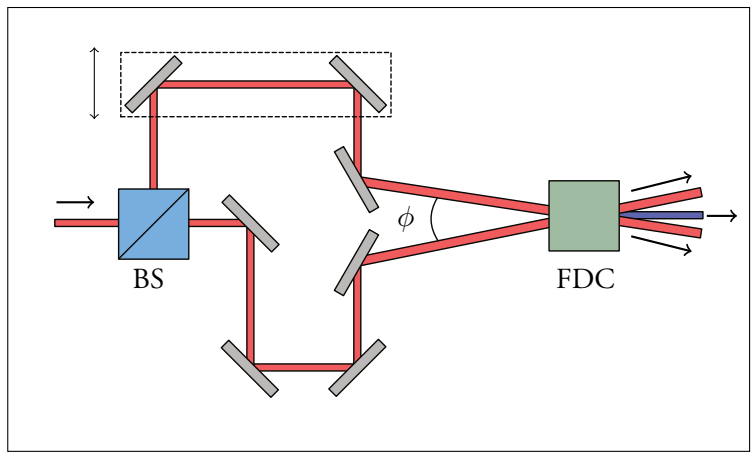

Figure 3.4 Second-Order Autocorrelator
The fundamental beam is sent to a beam splitter (BS) and the two components travel along different paths. One path has constant length, and the other can be varied. The two beams are then overlapped in a frequency-doubling crystal (FDC) at an angle relative to each other. The second-order harmonic is only generated when the two fundamental beams are overlapped, and thus the spatial width of the second harmonic trace is proportional to the duration of the fundamental pulse.

the pulses are overlapped in time and space, light will be generated at the second harmonic frequency, in a direction between the two fundamental arms, as shown in Fig. 3.4. This light is recorded by a CCD camera, and its intensity, I_{SH}, depends on the product of the two incoming intensities $I_1(t)$ and $I_2(t)$. Since second-harmonic generation is only active during the duration of the pulse, τ, it is possible to determine τ from ϕ and the width of the recorded second-harmonic trace:

$$\tau = \frac{k\Delta x \sin(\phi/2)}{c}, \tag{3.1}$$

where Δx is the spatial FWHM of the second-harmonic trace, and k is a number related to the pulse shape. For a Gaussian pulse shape, $k = \sqrt{2}$ and for sech^2 $k \approx 1.55$ [93].

A second-order autocorrelator is not useful in determining the temporal contrast ratio of the laser pulse, since its correlation signal is symmetric, and it is therefore not be possible to distinguish between post- and prepulses, which is essential in TNSA experiments. The temporal contrast is instead determined with a third-order autocorrelator [94] (Amplitude Technologies, Sequoia), which correlates the original signal with its second harmonic, yielding an asymmetric signal. This device has a high dynamic range, since the wavelength of the resulting signal differs from that of the two input signals, or their harmonics. This method can thus be used to measure high temporal laser contrast ratios.

In many of the experiments described in this thesis, knowledge about the ASE level is very important, and the mean ASE intensity, I_{ASE}, between 150 and 110 ps

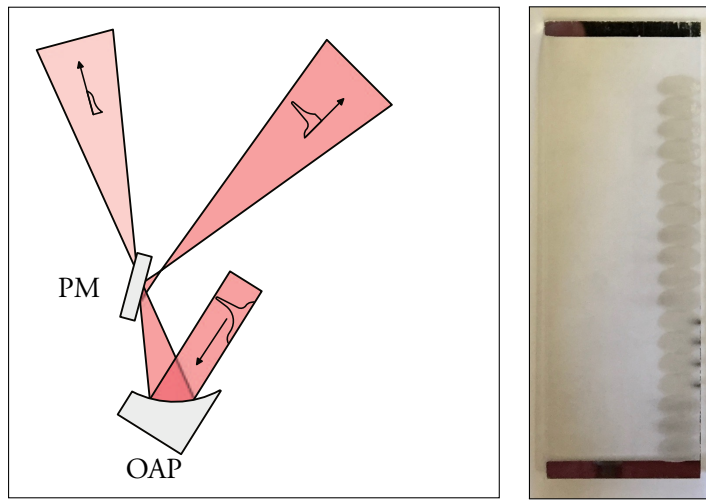

Figure 3.5 Plasma Mirror
(a) Schematic overview of the plasma mirror setup. The p-polarized laser pulse is incident on an off-axis parabolic (OAP) mirror, and a glass plate at Brewster's angle, acting as a plasma mirror (PM), is situated close to the laser focus. The low-intensity leading part of the laser pulse is transmitted through the plasma mirror, but as the intensity increases, a plasma forms, and the rest of the laser pulse is reflected. (b) A photograph of the plasma mirror. The two ends are coated with a thin layer of silver allowing for characterization and optimization of the focal spot at laser intensities lower than that required to activate the plasma mirror. The ellipses visible on the right-hand side are damage resulting from the use of the plasma mirror.

prior to the main pulse is therefore regularly measured, together with I_0. The temporal contrast is then simply given by:

$$C = \frac{I_0}{I_{\mathrm{ASE}}}. \tag{3.2}$$

3.1.2 Plasma Mirror Setup

In experiments where the temporal contrast of the laser is most important, such as those presented in Paper XII, a plasma mirror [95, 96] can be used. As was discussed in Section 2.5.3, high temporal contrast ratios are very important in TNSA experiments, but are not as crucial in LWFA. As part of the work described in this thesis, a plasma mirror setup was designed and implemented, a schematic of which is shown in Fig. 3.5(a).

The mirror itself consists of a flat transparent piece of glass (see Fig. 3.5(b)), in this case a common microscope slide, which is placed in the converging p-polarized laser beam in the plane where the peak intensity reaches 5×10^{15} W cm^{-2}. To increase the efficiency of the plasma mirror, the laser incidence angle is set to Brewster's angle, since the central rays of p-polarized light are comletely transmitted at this angle. The

intensity of the ASE preceding the laser pulse is sufficiently low at this position to be transmitted through the glass slide. As the intensity increases, a plasma starts to form on the plasma mirror, and when $n_e = n_c$ the rest of the laser pulse is reflected. This allows a plasma mirror to function as an ultra-fast optical switch that can filter out the ASE from the temporal structure of the laser pulse. This technique can be used to enhance the temporal contrast ratio by more than two orders of magnitude [97], although at the expense of laser energy. The reflectivity of this setup was measured in one of the experiments described in this thesis (see Section 4.2.3), and found to be 60 %, which was as expected for the laser pulse intensity used [98]. A plasma mirror is a single-shot device, since the glass is damaged upon plasma creation and the reflection of the laser pulse. The glass plate must therefore be moved after each laser pulse.

Since the plasma mirror only functions for high-intensity laser pulses, it can be difficult to use the setup for laser focus imaging and optimization (see Sections 3.1.1 and 3.1.4), since the optical system used for focal spot characterization cannot withstand the full intensity of the amplified laser pulse. It is therefore convenient to use glass slides such as the one shown in Fig. 3.5(b), where the two ends are coated with silver, which can act as normal mirrors for low-intensity pulses.

3.1.3 Split Mirror

In some of the TNSA experiments described in this thesis, a setup with a split mirror was used, which is illustrated in Fig. 3(a) in Paper IX. This splits incoming laser pulses into two parts before the focusing optics. Using the translation stages attached to the mirror, it is possible to create two foci, which can be spatially separated in two dimensions by slightly tilting one of the mirrors. The relative intensity between the foci can also be adjusted by moving the entire split mirror setup sideways, thus changing the laser energy on each mirror. Furthermore, it is possible to introduce a time delay between the two foci by moving one mirror along its normal. Thus, this setup can create two synchronized laser pulses with variable separation in space and time. During this work, experiments were carried out in which the effects of spatially separated foci on accelerated proton beams were studied (Paper IX). The effects on accelerated protons when varying the laser energy ratio (Paper XI), as well as the time delay between the two laser pulses, were also studied.

3.1.4 Alignment System for Solid Targets

In TNSA experiments, it is very important to position the targets at the laser focus with high precision. For proton acceleration, tight focusing ($f_n = 3$) is used to attain high intensities. According to Eq. 2.5 the Rayleigh length is approximately 70 µm for a FWHM of 5 µm, which is a typical spot size in the TNSA experiments described in this thesis. Thus, the target must be positioned with an accuracy better than this. For the experimental setups described in Papers IX to XI, an optical system, which

included a microscope objective, was used. The objective was positioned such that it could image the focal plane of the laser pulse onto a CCD camera. The camera used to image the focal spot was also used when positioning the target foil, which enabled very precise overlap of the target foil and the laser focal plane.

3.2 Targets

Two different types of gas targets were used in the LWFA experiments. In the experiments presented in Papers I to IV gas jets capable of producing supersonic flows were used, while in later studies (Papers VI to VIII) gas-filled glass capillary tubes were used as targets. Several different types of solid targets were used for proton acceleration experiments. In the studies presented in Papers XI to IX, thin foils of aluminum and Mylar were the main target materials. Experiments were also carried out using targets with surface structures, but these results have not yet been published. These targets will, however, be described in this section, and the results of the experiments are given in Section 4.2.3. In the experiment described in Paper XII, a more complex geometry was investigated by using small hollow spheres as targets.

3.2.1 Gas Jets

The pulsed valves used in the gas-jet experiments have fast opening times, and are opened a few milliseconds before the laser pulse arrives, to ensure a stable gas flow. The nozzle has a conic shape, and is detachable, which makes it possible to adjust the length of the gas medium by using alternative nozzle orifices. During the experimental work described later in this thesis, nozzle diameters of 2 mm (Papers I, II, III, V, & VIII) and 3 mm (Paper IV) were used. To ensure efficient plasma wave generation, laser propagation depends on relativistic self-focusing (as described in Section 2.3.1). Experimentally, a density threshold for self-injection is observed, which places a lower limit on the electron number density in the plasma, below which injection stops and no electrons are accelerated. The plasma density is varied by changing the pressure behind the nozzle. The resulting number density in supersonic gas flows can be determined from the nozzle dimensions, gas species, and backing pressure, and is described later in this section.

Great care must be taken to ensure that the focal plane lies close to the edge of the supersonic gas flow, since effects such as ionization defocusing (Section 2.3) would otherwise prevent the laser pulse from reaching the intensities required for LWFA. Thus, the gas jet must have a sharp edge, which is why the gas flow should preferably be supersonic, since such flows have sharp boundaries defined by their Mach cone [99].

Typically, the diffraction length of a focused laser beam is taken to be the Rayleigh length, z_r in Eq. 2.4, which would be the acceleration length limit without relativistic self-focusing (Section 2.3.1), which counteracts diffraction. The result of this is that

Table 3.3 Gas Properties
Phase differences ($\Delta\varphi$), relative to vacuum, for light with a wavelength of 0.6328 μm that has traveled 3 mm through different gases at standard pressure and temperature. The refractive indices ($\eta - 1$) relative to vacuum, and K, which is a constant relating refractive index to number density, are also included.

Gas	$\Delta\varphi$ (rad)	$\eta - 1$	$K\,(10^{-24}\ \mathrm{cm}^3)$
H_2	4.1	1.3888×10^{-4}	5.186
He	1.0	3.4879×10^{-5}	1.302
Ar	8.4	2.8106×10^{-4}	10.49

the acceleration of electrons is usually limited by either pump depletion or dephasing, which are described in Sections 2.3.3 and 2.4, respectively.

Density Measurements

Consider two monochromatic plane waves that are represented by their complex wave functions: $U_1 = \sqrt{I_0}\exp\left[-i\left(\mathbf{k}\cdot\mathbf{r} - \omega t + \varphi_1\right)\right]$ and U_2 defined similarly. The intensity, I, of their superposition is given by:

$$I = |U_1 + U_2|^2 = 2I_0\left[1 + \cos\left(\Delta\varphi\right)\right], \tag{3.3}$$

where $\Delta\varphi = \varphi_1 - \varphi_2$. Thus, the intensity of the superposition will be modulated by the phase difference.

If the two waves travel along paths with different refractive indices, η_1 and η_2, a phase difference will be introduced between them. Assuming that the two different media are homogeneous and that the paths of the waves are parallel, the phase difference after a length d can be expressed as:

$$\Delta\varphi = \frac{2\pi\Delta s}{\lambda}, \tag{3.4}$$

where λ is the wavelength, and

$$\Delta s = \int \left[\eta_1\left(s'\right) - \eta_2\left(s'\right)\right] \mathrm{d}s' \tag{3.5}$$

is the difference in the optical path lengths. Therefore, by measuring $\Delta\varphi$ and knowing Δs and λ, as well as one of the refractive indices, it is possible to determine the integrated value of the other. The phase differences relative to propagation in vacuum, calculated for $\lambda = 0.6328\,\mu\mathrm{m}$, $d = 3\,\mathrm{mm}$, and uniform standard pressure and temperature for typical gases, together with their corresponding refractive indices, and K, which is defined in Eq. 3.6, are given in Table 3.3.

Since the refractive index of a medium varies with number density, n, as

$$\eta - 1 \approx Kn, \tag{3.6}$$

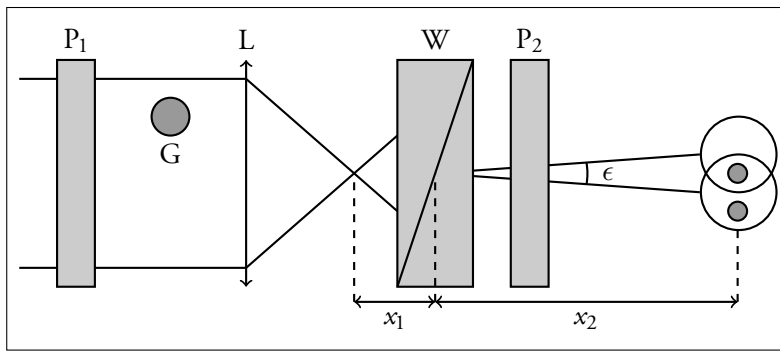

Figure 3.6 Wollaston Interferometer
An expanded beam enters from the left, and is linearly polarized after the first polarizer (P_1). The upper part acquires a phase shift as it propagates through the gas (G), while the reference part does not. The beam then passes through the imaging lens (L). The beam is split in the Wollaston prism (W), into an ordinary and an extra-ordinary ray. A second polarizer (P_2) is needed to obtain an interference pattern. The overlap of the two circles on the right represents the area where interference occurs. Note that the imaging plane has been rotated for viewing purposes.

where K is a constant that depends on the medium, it is possible to determine n by measuring $\Delta\varphi$ and combining with Eq. 3.4 to obtain:

$$n \approx \frac{\lambda}{2\pi K d} \times \Delta\varphi \tag{3.7}$$

where $\Delta\varphi$ is the phase shift relative to vacuum.

An interferometer setup based on a birefringent Wollaston prism [100] was used in the study described in Paper IV. A schematic of this type of interferometer is shown in Fig. 3.6. Interference is achieved by using an expanded polarized laser beam, and letting one part of it travel through a medium (in this case a gas), while the rest travels through a reference material, which in this case is vacuum. The beam is then led through a Wollaston prism, which divides it into two parts orthogonally polarized and separated by an angle ϵ in space. Since the two parts of the beam now have orthogonal polarizations, they must propagate through a polarizer that is oriented at an angle of 45° to both of them. The resulting interference pattern has a fringe separation of:

$$\Delta = \frac{\lambda x_2}{\epsilon x_1}, \tag{3.8}$$

where ϵ, x_1, and x_2 are defined in Fig. 3.6. This means that the fringe separation can be changed by adjusting x_1 and x_2. The resulting density can then be obtained from the Abel inversion of the interferogram, since the gas jet is cylindrically symmetric.

The nature of this setup places some restrictions on the illumination laser. Mainly, there is need for a high spatial coherence and uniform intensity of the laser beam, since different areas of the same wavefront interfere. Assuming that the smallest resolvable optical path difference of the setup is $\lambda/4$, which means

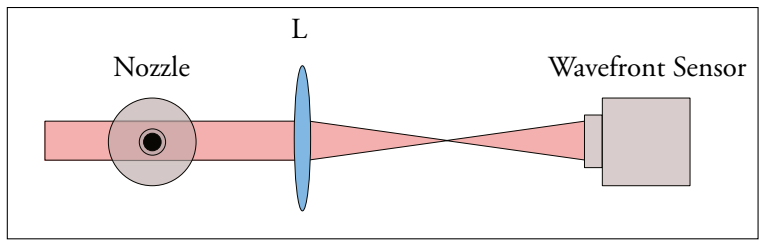

Figure 3.7 Density Measurement with a Wavefront Sensor
An expanded HeNe beam passes through a gas jet released from a supersonic nozzle. The flow is imaged by a lens (L) onto a wavefront sensor, where the phase of the HeNe laser is measured. The additional optical path length introduced by the gas can be determined by comparing the phase inside the gas flow, with the phase outside it.

that $(\eta_{\text{min}} - 1) = \lambda/4d$ for a homogeneous medium of thickness d, the smallest detectable density is then given by Eq. 3.6:

$$n_{\text{min}} \approx \frac{\eta_{\text{min}} - 1}{K}. \tag{3.9}$$

If the refractive index is known for a certain temperature and pressure, and ideal gas behavior is assumed, it is possible to determine K for different gases. Using the values of K presented in Table 3.3 together with Eq. 3.9 and $d = 3$ mm yields:

$$n_{\text{min}} \approx \begin{cases} 10 \times 10^{18}\,\text{cm}^{-3} & \text{for } H_2 \\ 40 \times 10^{18}\,\text{cm}^{-3} & \text{for He} \\ 5 \times 10^{18}\,\text{cm}^{-3} & \text{for Ar} \end{cases}. \tag{3.10}$$

Gas densities can also be measured using an expanded laser beam together with a wavefront sensor, with a setup such as that shown in Fig. 3.7.

Again, an expanded laser beam passes through a gas medium, where phase shifts are introduced, which can be detected by the sensor. By comparing the phase relative to vacuum and using Eq. 3.4, it is again possible to determine the refractive index of the gas. A phase map obtained from the wavefront sensor for a supersonic jet of H_2 released from a 2 mm nozzle backed by 10 bar is shown in Fig. 3.9. It is again possible to use an inverse Abel transformation to obtain the density profile. However, a more robust method is to first assume a general shape of the density profile and to determine its Abel transform. It is then possible to determine the density profile that best fits the measured phase map by using n_0, l_x, and l_g (see Fig. 3.8 for definitions of the parameters) as fitting parameters. This method proved much more sensitive than that based on the Wollaston interferometer, and this setup was of vital importance in the studies reported in Paper I. A similar method can be used to measure plasma electron number densities directly during laser–matter interactions [101].

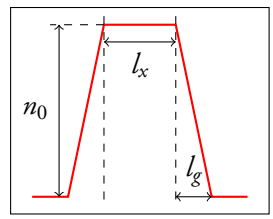

Figure 3.8 Density Profile
Instead of determining the density profile from an inverse Abel transform, a more robust method is to first assume a general shape of the profile. The density profile that best describes the measured phase map can then be determined using the peak density, plateau length, and gradient length as fitting parameters.

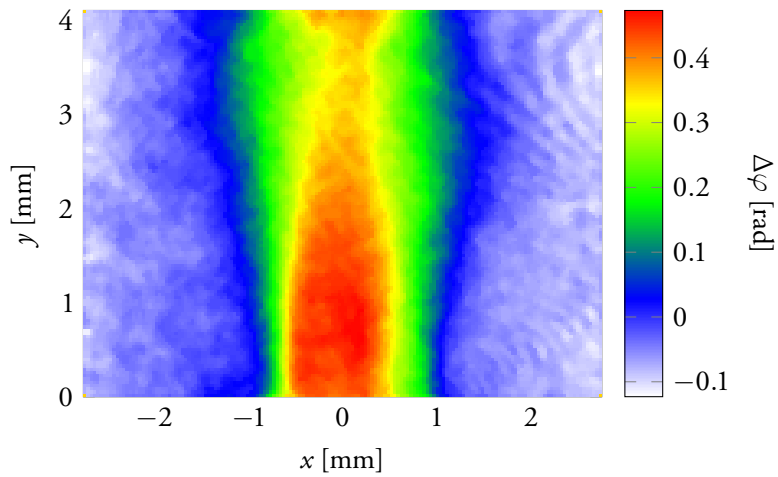

Figure 3.9 Phase Map
Phase map obtained from a measurement in a supersonic hydrogen jet released from a 2 mm diameter nozzle, backed by 10 bar pressure.

Number Density in Supersonic Gas Jets

The conventions used by F. M. White [102] are used throughout this section. A schematic representation of a supersonic nozzle is shown in Fig. 3.10. In a converging-diverging region of a gas flow the relation between the nozzle throat radius and Mach number, Ma, of the jet is given by:

$$\left(\frac{r_0}{r_c}\right)^2 = \frac{1}{\mathrm{Ma}}\left[\frac{1+(k-1)\mathrm{Ma}^2/2}{(k+1)/2}\right]^{\frac{k+1}{2(k-1)}}, \tag{3.11}$$

where r_0 is the nozzle exit radius, r_c the critical radius where the flow reaches sonic speeds, and k is the heat capacity ratio of the gas. By calculating the local temperature, T, at the exit of the nozzle according to:

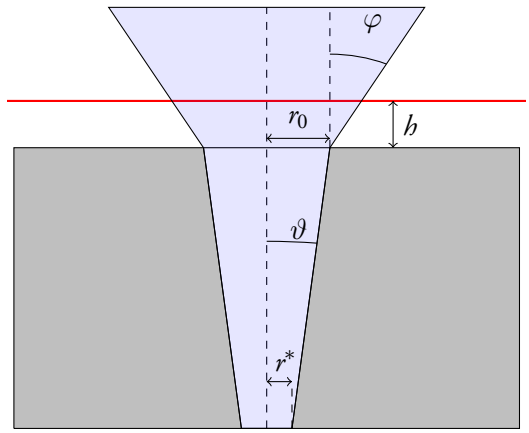

Figure 3.10 Supersonic Gas Flow
Schematic illustration of the divergent region of a converging-diverging nozzle producing a supersonic gas jet. The critical radius (r_c) for choking conditions, ϑ the expansion angle of the nozzle, r_0 the nozzle exit radius, h the distance between the nozzle exit and the laser axis, and φ the divergence half-angle of the resulting gas jet. Note that φ depends on the Mach number of the flow.

$$\frac{T_0}{T} = 1 + \frac{k-1}{2}\mathrm{Ma}^2, \tag{3.12}$$

where $T_0 \approx 300\,\mathrm{K}$ is the temperature at stagnation conditions, it is possible to determine the local speed of sound, c_s, as:

$$c_s = \sqrt{\frac{kRT}{M}}, \tag{3.13}$$

where $R \approx 8.31\,\mathrm{J\,mol^{-1}\,K^{-1}}$ is the gas constant, and M is the molecular mass of the gas. At choking conditions, which is a requirement for supersonic jets, the mass flow is given by:

$$\dot{m} = \sqrt{k} \times \left(\frac{2}{k+1}\right)^{\frac{k+1}{2(k-1)}} \times \pi\,(r_c)^2\,\frac{p_0}{\sqrt{RT_0/M}}, \tag{3.14}$$

where p_0 is the stagnation pressure. The mass flow can then be rewritten as:

$$\dot{m} = m_u n_{\mathrm{exit}} \pi r_0^2 v, \tag{3.15}$$

where m_u is the mass of a single atom or molecule in the gas, v the speed of the flow, and n_{exit} is the particle number density in the flow at the exit of the nozzle. Setting Eq. 3.14 and 3.15 equal and solving for n_{exit} gives:

$$n_{\mathrm{exit}} = \sqrt{k} \times \left(\frac{2}{k+1}\right)^{\frac{k+1}{2(k-1)}} \times \left(\frac{r_c}{r_0}\right)^2 \times \frac{p_0}{v\sqrt{k_B T_0 m_u}}, \tag{3.16}$$

where k_B is Boltzmann's constant. Equation 3.11 must be solved numerically to obtain Ma, and using this result together with Eq. 3.12 and 3.13, it is possible to determine the flow number density at the nozzle exit from Eq. 3.16.

As the supersonic jet exits the nozzle, the divergence half-angle of the flow, α, will depend on Ma as $\sin\alpha = \mathrm{Ma}^{-1}$. If the nozzle itself is diverging with a half-angle ϑ, the total half-angle of the flow, φ, is given by $\alpha + \vartheta = \arcsin\left(\mathrm{Ma}^{-1}\right) + \vartheta$. This means that the flow radius, r_{flow}, will be a function of the distance from the nozzle orifice, h, and assuming that φ is constant, the number density in the supersonic gas jet is given by:

$$n(h) = \left[\frac{r_0}{r_0 + h\tan\varphi}\right]^2 n_{\mathrm{exit}}. \tag{3.17}$$

Number Density Gradients

Several different ways of introducing density gradients into the gas jet were used during the course of this work (Section 2.4.1). In the experiment presented in Paper V a setup consisting of two independent gas nozzles was used, while in the study described in Paper IV a thin steel wire in the gas flow created the density perturbation.

Schematic illustrations of the twin-nozzle setup are shown in Figures 3.11(a) and 3.11(b). The main flow is released from a 2 mm supersonic nozzle, and the other from a 400 µm diameter needle producing a subsonic flow. The two nozzles are connected to separate gas feeding systems, making it possible to change their backing pressures, p_0 (main) and p_{n} (needle), as well as gas types, independently. The nozzles are also mounted on separate translation stages. This setup allowed for precise control of the density profile, an example of which is shown in Fig. 3.11(c).

In the experiment where density modulation was created by inserting a thin steel wire into the gas jet, the supersonic gas jet was released from a 3 mm nozzle. The height of the wire and its position along the laser axis could be controlled, allowing for precise positioning. The resulting density profile was similar to that shown in Fig. 3.12. The advantage of this setup is that very steep gradients can be created in the density profile.

3.2.2 Gas-Filled Dielectric Capillary Tubes

One way of increasing the acceleration length is to use gas-filled dielectric capillary tubes, which act as waveguides for the laser pulse. In addition to guiding the pulse, the capillary also couples the laser energy outside the pulse FWHM to the interaction [103], which was shown not to be the case with gas jets operating in the self-injection regime (Paper II). The intensity of the laser pulse will increase even further as it propagates through the capillary due to nonlinear pulse evolution, which makes it possible to use lower intensities to accelerate electrons than when using gas jets utilizing self-injection [104]. It has been shown previously in our laboratory that

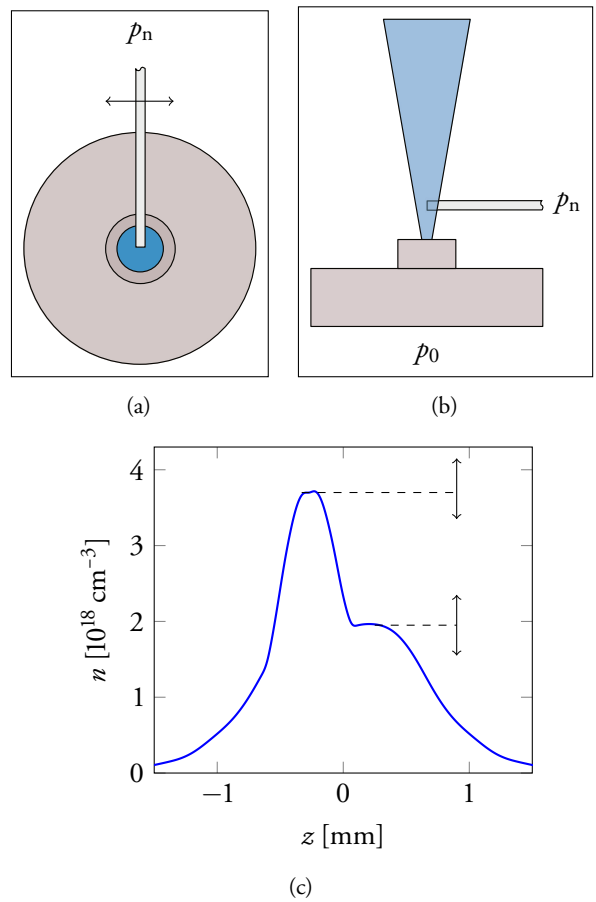

Figure 3.11 Schematic of Twin-Nozzle Setup
(a) Top and (b) side view of the twin-nozzle setup used to produce the density gradients for the experiment presented in Paper V. An example of the density profile produced is shown in (c), with arrows indicating how it can be altered.

plasma waves can be excited and driven by focusing laser pulses into capillaries with lengths up to 8 cm [105]. Gas-filled capillary tubes are thus good candidates as a means of increasing the acceleration length. Compared to a supersonic gas jet, a uniform density distribution free of shock waves can be maintained in gas-filled capillary tubes [106]. Thus, these provide a target well suited for systematic studies of electron acceleration and x-ray production.

In the experiments presented in Papers VI to VIII, the capillary tubes had outer diameters of 5.5 mm and inner diameters ranging from 152 µm to 254 µm. For inner diameters in this range, multimode guiding of the laser pulse is expected [107]. The tube lengths were 1 cm and 3 cm. Prior to the arrival of the laser pulses, gas was pumped into the tubes in pulses through two 270 µm wide slits, situated 2.5 mm from each end of the capillary tubes. The gas pulses are longer when filling capillary

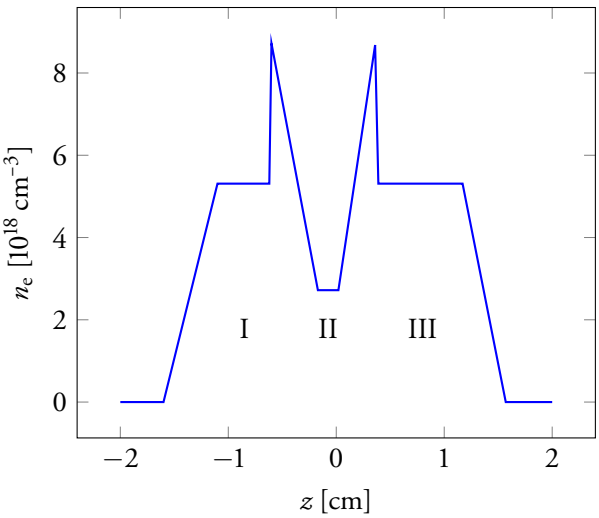

Figure 3.12 Modulated Density Profile
The modulated density profile used for the simulations presented in Paper IV is a simplification of the measured density profile. Region I is where the laser pulse evolves to matched conditions before entering the density-modulated region (II), where electrons are trapped in the plasma wave. After trapping, the plasma wave contracts as it enters region III, where additional acceleration can occur.

tubes than in the case of gas jets.

One drawback of gas-filled capillary tubes, compared to gas jets, is the requirement of precise target alignment and stable laser beam pointing [108]. If the propagation axis of the impinging laser pulse is not properly aligned with the capillary tube, the tube will be damaged and must be replaced.

3.2.3 Solid Targets

Thin Foils

When accelerating protons, the main target used in this work was 3 µm thick aluminum foils. The foil was mounted in a sandwich structure with 300 individual target sites, which enabled long systematic scans without opening the target chamber. Other materials were also used, such as plastic foils (Mylar®). The main differences between Al and Mylar foils are their ability to sustain the return current, as described in Section 2.5.2, and the number of protons available for acceleration. However, if the Mylar targets are sufficiently thin (see Eq. 2.47), there will be no electron beam instability inside the target that could affect the resulting proton beam. In general, the number of accelerated protons was higher when using Mylar foils as the target, than in the corresponding experiment performed with Al foils. However, Al foils were chosen as they have fine surface structures that aid target alignment.

Structured Targets

During one of the experimental campaigns in this work, targets to which very small surface structures had been added were investigated. Two different structures were used; nanospheres and gratings. Experiments were carried out with the structures on the front or the back of the target. One type of target consisted of 0.5 µm thick Mylar foils with nanospheres of 0.4 µm diameter in a monolayer on the surface. Thus, the overall thickness was 0.9 µm. The other type, with grating structures, had groove widths of 0.5 µm, 1 µm, or 2 µm, and they were placed on a membrane with a thickness of 0.2 µm. The overall thickness of this type of target was 0.7 µm, so each groove had a depth of 0.5 µm. The results of these experiments have not yet been published, but are briefly presented in Section 4.2.3.

As was discussed in Section 2.5.3, good temporal contrast of the laser pulse is required when short plasma scale lengths are important. For structured targets, an expanding plasma on the front of the target can wash out the structures if the plasma scale length is too large. Therefore, a plasma mirror (see Section 3.1.2) was used with these targets.

Hollow Microspheres

During the experiments described in Paper XII, protons were accelerated using hollow glass microspheres covered with silver. These spheres are commercially available with a 50 µm diameter. The shell of each sphere is between 0.5 and 1 µm thick, and they were covered with a layer of silver approximately 50 nm thick. Before being used as a target, a small hole was made, by laser machining, at what is called the sphere 'north pole'. The idea of this target configuration is to allow for TNSA on the 'south pole', and to take advantage of electrons traveling laterally [74] inside the target by bending the surface towards propagating protons. When the electrons reach the north pole, they exit the shell and induce strong electric sheath fields where protons can gain additional energy under the appropriate conditions, which are determined by the proton energy, the lateral expansion speed of the electrons, and the sphere diameter.

3.3 Particle & X-Ray Diagnostics

The laser–plasma interactions studied during this work give rise to interesting physical phenomena, which were described in Sections 2.4 and 2.5. In this section, some important diagnostic tools used to detect electrons, protons, and x-rays are presented.

3.3.1 Electron Detection

The setup used for electron detection in the LWFA investigations consisted of three independent parts: a permanent dipole magnet, a scintillating screen and a CCD camera. The scintillating screen (Kodak Lanex Regular) starts to fluoresce when electrons hit it. Any residual laser light was stopped by an aluminum plate in front of the scintillator, while the energetic electrons of interest could pass through this plate. A CCD camera was used to collect the light generated in the Lanex screen. The interactions inside the vacuum chamber create a large amount of light and the laser beam was very intense, so an interference filter, in combination with a light shield, was placed in front of the camera lens to protect the camera. The setup could be operated in two different modes, either with a magnet to disperse the electrons according to their energy, or without the magnet, to measure beam pointing and divergence. When operating without the magnet, simple trigonometry was used to obtain the pointing and divergence of the electron beam, since the source is very small and can be considered to be point-like.

3.3.2 Proton Detection

The main diagnostic tool used in most of the TNSA experiments was a scintillating screen (Saint-Gobain BC-408) that emits light at a wavelength of 0.43 µm when it is hit by charged particles or x-rays. A 13 µm thick aluminum foil was used to prevent laser light and low-energy electrons from reaching the scintillator. This also stops protons with energies below 0.9 MeV. The scintillator is 1 mm thick, and protons with energies up to approximately 9 MeV are stopped inside it. This means that the scintillation signal depends on the particle energy, and this must be taken into account when the proton number is of interest. Two scintillators are usually incorporated into the setup, one monitoring the spatial profile of the proton beam, and the other after the particles have been dispersed according to their energy by a magnetic field.

Another type of detector, a plastic polymer called CR-39, can also be used for proton detection. When protons impinge on this material, its molecular bonds are broken, leading to damage in the material. The detector is then placed in a chemical solution that etches the plastic. Etching is more rapid where the molecular bonds have been broken, revealing the proton tracks. These tracks are identified and counted using a microscope, giving the absolute number of protons.

It is also possible to use radiochromic film (RCF) as a proton detector. As RCF absorbs radiation, it changes color without the need for photographic development. RCF is not only sensitive to protons, but also to electrons and x-rays, which may lead to problems in calibration.

Since the proton beam is highly laminar, it can be regarded as emerging from a virtual source in front of the target foil. The position of this virtual source can be determined by projecting a fine mesh at a set distance from the rear of the target

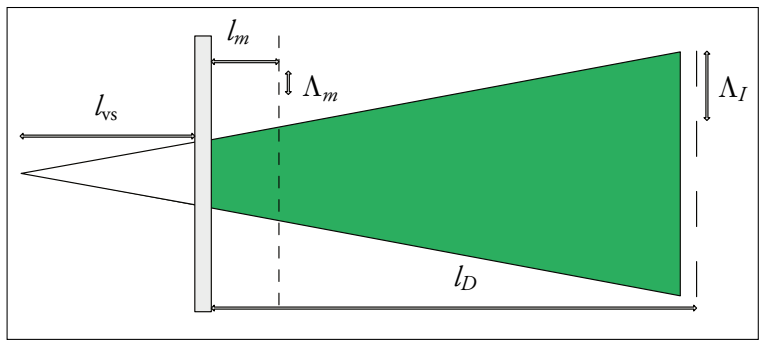

Figure 3.13 Virtual Source
The virtual proton source is positioned in front of the target, and can be found by making a shadow of a fine mesh with the proton beam.

[109]. By considering the definitions in Fig. 3.13, simple geometry yields:

$$l_{vs} = \frac{\Lambda_m l_D - \Lambda_I l_m}{\Lambda_I - \Lambda_m}. \tag{3.18}$$

Although this calculation implies a point source, it is also possible to determine the size of the virtual source by imaging a sharp edge. The blurriness of the edge shadow gives an indication of the size of the virtual source.

3.3.3 Particle Spectrometers

A particle with a rest mass m_0 and charge q traveling at a velocity $\mathbf{v}$ through a magnetic field $\mathbf{B}$ will, due to the Lorentz force, experience a change in momentum $\dot{\mathbf{p}} = q\mathbf{v}\times\mathbf{B}$, assuming that no electric field is present. The work done on the particle by the magnetic field over a curve C is $W = \int_C \dot{\mathbf{p}} \cdot \mathrm{d}\mathbf{s} = 0$, since $\mathrm{d}\mathbf{s}$ is parallel to $\mathbf{v}$ and therefore orthogonal to $\dot{\mathbf{p}}$. Thus, there is no change in particle energy due to the magnetic field.

If $\mathbf{B}$ is constant and perpendicular to $\mathbf{v}$, the particle will travel in a circular arc since the force is orthogonal to both $\mathbf{B}$ and $\mathbf{v}$. The acceleration due to circular motion is $\dot{\mathbf{v}} = -\hat{\mathbf{e}}_v v^2/R$, where:

$$R = \frac{\beta\left(\mathcal{E}_0 + \mathcal{E}_k\right)}{qcB} \tag{3.19}$$

is the radius of the circle traced by the moving particle, and $\hat{\mathbf{e}}_v = \mathbf{v}/|\mathbf{v}|$. In Eq. 3.19 $\beta = v/c$, and $\mathcal{E}_0$ and $\mathcal{E}_k$ are the rest and kinetic energy, respectively. At non-relativistic speeds, $\mathcal{E}_0 \gg \mathcal{E}_k$, and Eq. 3.19 becomes $R_{\mathrm{nr}} = m_0 v/qB$. Similarly, at relativistic speeds, or $\beta \approx 1$ and $\mathcal{E}_0 \ll \mathcal{E}_k$, the bending radius becomes $R_{\mathrm{rel}} = \mathcal{E}_k/qcB$. The kinetic energy is given by $\mathcal{E}_k = m_0 v^2/2$ for non-relativistic particles,

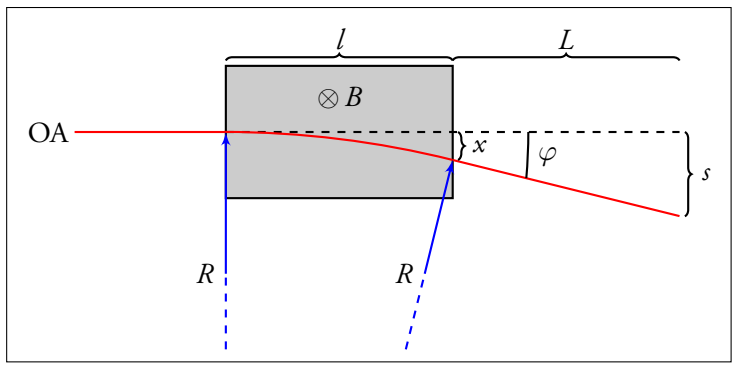

Figure 3.14 Magnetic Spectrometer
The red line shows the electron trajectory, with bending radius R inside the magnetic field. OA denotes the optical axis, which is also the initial path of the electron. The gray area represents a magnetic field pointing into the paper. l is the length of the magnetic field in the propagation direction, and s is the distance the electron has been deflected from OA after a distance $l + L$.

and R can then be approximated by:

$$R = \begin{cases} \sqrt{2m_0\mathcal{E}_k}/qB & \text{for non-relativistic particles} \\ \mathcal{E}_k/cqB & \text{for relativistic particles} \end{cases} \tag{3.20}$$

To determine the distance, s, a particle has been deflected after a distance $l + L$, it is helpful to consider Fig. 3.14. From this figure, it can be seen that $R^2 = l^2 + (R - x)^2$, or $x = R - \sqrt{R^2 - l^2}$. After leaving the magnetic field, the particle will follow a straight trajectory, since it does not experience any forces. This means that $\tan(\varphi) = (s - x)/L$, and with some simple trigonometry, it can be shown that $\tan(\varphi) = l/(R - x)$. The combination of these equations yields:

$$s = R - \sqrt{R^2 - l^2} + \frac{lL}{\sqrt{R^2 - l^2}}, \tag{3.21}$$

where R is given by Eq. 3.19.

Based on Eq. 3.21, two different types of magnets can be defined. One where $l > R$, which yields an imaginary solution for s. This is the case when an electron entering the magnetic field has an energy that is so low that its motion is reversed and it travels back towards the target. This can be called a strong magnet, since $R \propto B^{-1}$. In the other case, when $R \gg l$, $s \approx lL/R$. Often, $L \approx l$ which implies that s is very small. This is reasonable since a large bending radius indicates a low magnetic field strength or high particle energy. This is thus a weak magnet for particles of energy E.

The influence of L on s can be deduced by calculating:

$$\frac{\partial s}{\partial L} = \frac{l}{\sqrt{R^2 - l^2}}. \tag{3.22}$$

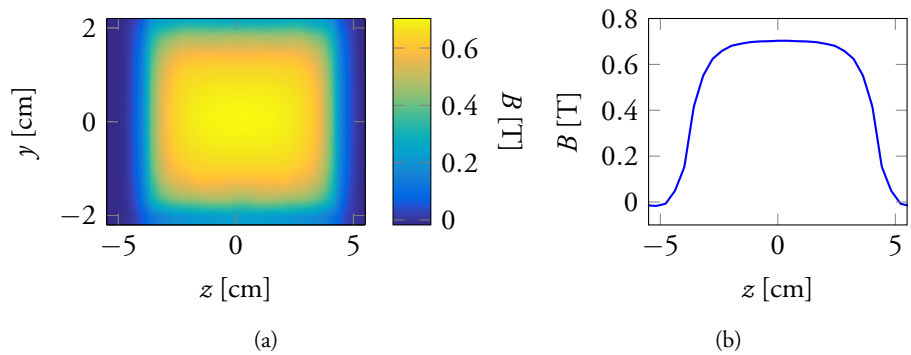

(a) (b)

Figure 3.15 Magnetic Field Strength
(a) The magnetic field strength of the magnet used in the studies described in Papers I to VIII. Note that the actual size of the magnet is 12 cm including the iron cladding, but the map indicates an effective length of approximately 10 cm. The size of the Hall probe used to map the field also limits the height of the map to 4.4 cm, despite the fact that the height of the actual magnet is 5 cm. (b) Line-out of the magnetic field shown in (a). Gradients are visible on both sides of the maximum field strength.

For a magnetic field strength of 0.65 T and an electron energy of 100 MeV, the bending radius is 0.5 m. If the length of the magnet is 10 cm, then $\partial s/\partial L = 0.25$. Thus, altering L by 1 cm changes s by 2.5 mm for this particular electron energy. This example is replicated in the non-relativistic case for a proton of energy 5.1 MeV.

A map showing the magnetic field strength of the magnet used in the LWFA experiments is shown in Fig. 3.15(a), and is similar to the magnet used for TNSA experiments. The magnetic field is not constant over the entire length of the magnet, and the line-out in Fig. 3.15(b) shows that there are gradients several centimeters long in the field. It is possible to calculate an average effective magnetic field, but the best solution is to simulate the electron trajectories through this magnetic field. In this way it is also possible to include the effect of the magnet on highly divergent particle beams.

A comparison between a simulated dispersion and a constant-field approximation for electrons is shown in Fig. 3.16. The simulation is based on the actual map of the magnet shown in Fig. 3.15(a), while the constant-field approximation assumes $l = 10$ cm and a mean magnetic field of 0.52 T over that length. The difference in s for 100 MeV electrons is about 0.5 mm. This means that the energy of the electrons determined using the constant-field approximation is 100 MeV, while the simulation predicts that they have an energy of 98.8 MeV. The agreement is thus good for on-axis electrons. However, it is important to use an appropriate length and mean field in the constant-field approximation, which may be difficult to determine. Another important aspect of the constant-field approximation is that the magnetic field must be centered around the optical axis, if it is not, the mean magnetic field must be adjusted.

The lowest energy displayed in Fig. 3.16 is ∼40 MeV, which is the lowest

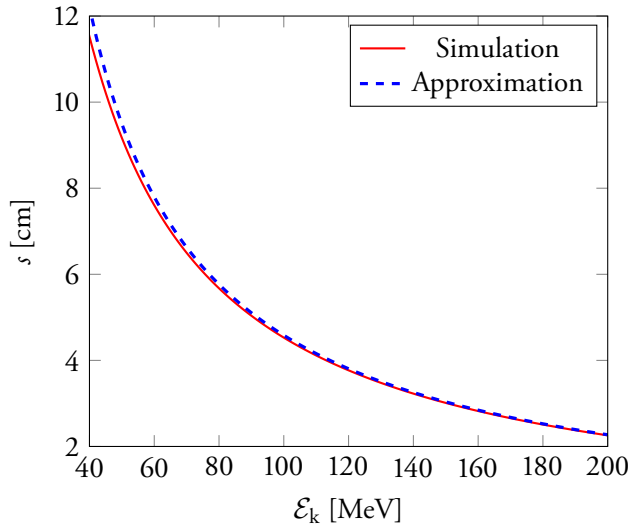

Figure 3.16 Dispersion Curves
Comparison between the simulated and constant-field approximated deflection. The approximation is based on a mean field strength of 0.52 T and length of 10 cm.

detectable energy for the setup used during these simulations. In this case, the cut-off arises because the height of the magnet is smaller than its length, l, so electrons with $R \approx l$ hit the magnet or its iron cladding and are stopped. A cut-off can also arise when L is very large. In this case, an electron that exits the magnet with a bending radius just large enough not to hit it, could still be deflected too much and miss the detector.

The resolution of the spectrometer is mainly limited by the beam divergence and pointing instabilities. A typical resolution is shown in Fig. 3.17. An electron beam with an uncertainty of 5 mrad is plotted in the figure, and $\Delta\mathcal{E}$ is the energy range the beam can be interpreted as due to its uncertainty. As expected, the resolution is better at lower energies than at higher ones. The reason for this can be seen in Fig. 3.16. Since the dispersion is greater for lower energies, the resolution is higher compared to higher electron energies. Since the electron beam has a small divergence, an entrance slit is usually not needed before the magnet. It is also undesirable to use a slit in an electron spectrometer, since it must be about 4.4 cm thick in order to stop 200 MeV electrons, and as the electrons are stopped, Bremsstrahlung will be produced, increasing the background noise in the images obtained.

The proton beams studied in the TNSA experiments included in this thesis generally had large divergence angles. Therefore, an entrance slit was used, and only a small fraction of the proton beam was sampled and sent through the spectrometer.

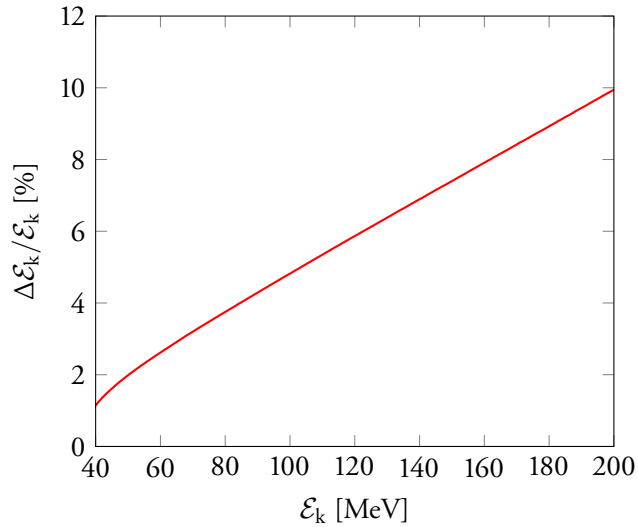

Figure 3.17 Resolution of the Magnetic Spectrometer
Resolution of one spectrometer setup used in this work. In this simulation, an electron beam with a divergence of 5 mrad was evaluated using the same setup parameters as in Fig. 3.16.

Numerical Example

After a distance of 40 cm, an electron beam with a divergence of 5 mrad will have a diameter of 2 mm. For a proton beam with a divergence similar to that reported in Paper X (450 mrad), the beam diameter will instead be 18 cm.

One potential problem associated with the spectrometer used in the TNSA experiments during this work, apart from large beam divergences, is the acceleration of heavier ions, such as carbon. In Section 2.5 it was mentioned that protons are predominantly accelerated if water or hydrocarbons are present on the rear of the target. However, at sufficiently high laser intensities, carbon may also be accelerated. The scintillator placed after the spectrometer magnet was therefore covered with a 13 µm thick Al foil, which stops carbon ions with $\mathcal{E}_k < 14.5$ MeV.

The energies of the carbon ions can be estimated from the observed proton energies. Assuming that all the charged particles are accelerated in the same field strength, and over the same length, the energies of the carbon ions will be increased by a factor of Z compared to protons. Under the experimental conditions used in this work, the highest proton energies were approximately 8 MeV, which means that carbon ions, with $Z \geq 2$, can have energies high enough to penetrate the aluminum foil in front of the scintillator. Carbon ions with such high energies would pass almost straight through the magnetic spectrometer, according to Eq. 3.21. However,

no signal was observed at this s position, and it is therefore believed that no carbon ions reached the scintillator, removing the need to distinguish heavier ion species from protons. Thus, a Thomson parabola, which simultaneously disperses particles according to their energy and charge-to-mass ratio, was not needed for the TNSA experiments presented in this thesis.

Absolute Calibration of Electron Spectrometers

In Papers I to VIII, the absolute accelerated charge is given in picocoulombs. This charge was determined by measuring the quantum efficiency of the camera and estimating the solid angle of collection of the optical system. The conversion from CCD counts to absolute charge is energy-dependent [110]:

$$\frac{\mathrm{d}Q}{\mathrm{d}\mathcal{E}}(\mathcal{E}') = N(\mathcal{E}') \times \left(\Lambda\,\Omega\,T_{\mathrm{total}}\cos\theta_{\mathrm{CCD}}\,\delta s_{\mathrm{pixel}}\right)^{-1} \times \\ \times \left(\kappa \exp\left[-\frac{\tau_d}{\tau_l}\right]\right)^{-1} \times \cos\theta_{\perp}\frac{\mathrm{d}s}{\mathrm{d}\mathcal{E}}, \tag{3.23}$$

where Q denotes charge and $\mathcal{E}$ the electron energy. The first factor on the right-hand side of Eq. 3.23 is the number of counts[1] on the CCD chip corresponding to an energy $\mathcal{E}'$, which is the actual signal in the measurement. The second factor depends on the geometry of the optical setup, where Λ is the number of CCD counts per recorded photon, Ω is the solid collection angle, T_{total} is the total transmission through all optics, θ_{CCD} is the viewing angle of the CCD camera, and $\delta s_{\mathrm{pixel}}$ is the pixel size in the dispersion direction. The third factor depends on the scintillator type (κ and τ_l), and the delay time, τ_d, that determines how much of the signal is cut off if the camera is time-gated. For a Kodak Lanex Regular screen, $\kappa = 6.95 \times 10^9\ \mathrm{pC^{-1}\,sr^{-1}}$ [111], and $\tau_l = 660\ \mu\mathrm{s}$ [112]. The last factor depends on the electron energy, where $\theta_{\perp}$ is the angle at which the electrons hit the scintillating screen, and $\mathrm{d}s/\mathrm{d}\mathcal{E}$ is the energy dispersion. Dividing $\mathrm{d}s/\mathrm{d}\mathcal{E}$ by $\delta s_{\mathrm{pixel}}$ yields the conversion between pixel size and energy range. The setup-specific variables necessary for the absolute charge calibration performed in some of the studies are listed in Table 3.4.

A peaked spectrum with a tail of lower-energy electrons is typical for LWFA experiments. The noise seen in the tail arises from three different sources. First, all CCDs suffer from thermal noise, which means a cooled camera is preferable. The second source is residual light from laser–matter interactions or from the laser itself. To avoid this, time gating, where the camera is triggered after the laser pulse has passed (Papers II, III, VI, VII, and VIII), or a light-tight shield was used (Papers I, IV, V, IX, X, and XI). The advantage of using time gating is that the experimental

[1] It is important to distinguish between the number of counts on the CCD chip and the number of counts in the image. It is common for images to be saved in a 16-bit format, while the raw data are not. For such images, rescaling is needed, such that one count on the CCD chip corresponds to one count in the image.

Table 3.4 Characteristics of the Optical Detection Systems
The characteristics of the optical detection systems used in some of the studies described in this thesis, where Ω is the solid collection angle, T_{total} is the total transmission through the system, θ_{CCD} is the viewing angle of the CCD camera, τ_d is the camera delay time, and δs_{pixel} is the size of a pixel in the dispersion direction

Paper	Ω [msr]	T_{total}	θ_{CCD} [°]	τ_d [µs]	δs_{pixel} [µm]
IV	0.963	0.49	43	0	13
VI, VII, & VIII	0.840	0.45	40	76.5	4.65

setup is much simpler. However, the disadvantage is that the most intense part of the signal will be lost, which is not the case when a light shield is used. The third, and probably largest, contribution to the noise is light reflected into the scintillator. Since the experiment takes place under vacuum, the light from the scintillator must pass through an experimental chamber window where it can be reflected. This means that a window of good optical quality, with anti-reflection coating, should be used to minimize the noise. However, light can also be reflected from other components. One way of reducing the influence of reflected light on the resulting signal is to identify an area of the raw image where the main signal is not present. This area can then be used as a measure of the reflected light, as well as the background noise, and subtracted from the raw image. This assumes that the background is uniform, and it may be necessary to use more elaborate background subtraction routines to improve the detected signal.

Absolute Calibration of Proton Spectrometers

As in the case of the electron spectrometer described in the previous section, it is possible to calibrate the proton spectrometer, allowing the absolute proton charge to be determined. However, instead of using published data for the scintillator response, this was measured directly by comparison with a CR-39 detector. During calibration, a CR-39 plate was mounted next to the scintillator, and spectra were recorded simultaneously by both detectors. The conversion function could then be determined by counting the number of protons recorded on the CR-39 as a function of position in the dispersion direction.

3.3.4 X-Ray Detection

X-ray detection, together with the electron spectrometer, was the main diagnostic tool used in the studies described in Papers VI to VIII. As the electrons wiggle during acceleration in the plasma they produce x-ray radiation, as described in Section 2.4.2. A simple way to detect the spatial features of the x-ray beam is to use an x-ray-sensitive CCD camera placed in the beam path. However, it is important to deflect the

electron beam so that it does not hit the CCD, as the x-ray signal would be completely hidden by the electrons, and the chip itself may be damaged. The quantum efficiency of a CCD chip depends strongly on the photon energy, so in this rather simple setup, no information is available on the photon number. This means that it is necessary to obtain information on the photon energy. Placing a filter array of different materials in front of the camera, together with knowledge of the energy-dependent x-ray transmission through each filter, gives rough information on the spectral distribution of the x-ray beam. Assuming a synchrotron-like spectrum, it is then possible to determine the critical energy, $\mathcal{E}_c$.

One problem associated with x-ray detection is the influence of noise. The electrons accelerated in the plasma are deflected by a magnet and stopped in the chamber wall. During this deceleration, the electrons produce Bremsstrahlung, which can hit the CCD camera. The most obvious way to reduce the influence of this radiation is to use a dedicated electron beam dump, which minimizes the amount of Bremsstrahlung that reaches the x-ray-sensitive CCD camera. Another way is to utilize the fact that betatron radiation is a collimated beam, whereas the Bremsstrahlung will decrease as L^{-2}, where L is the distance between the CCD camera and the beam dump. As long as the size of the x-ray beam is smaller than the CCD chip, the total amount of betatron radiation detected will be the same as L increases. However, at large values of L the beam will be larger than the CCD chip, and the amount of betatron radiation detected will start to decrease at the same rate as the Bremsstrahlung. A third way of increasing the signal-to-noise ratio is to place the x-ray camera inside a lead enclosure with a small hole on the optical axis to allow the betatron radiation to pass through and be detected by the CCD camera. In the experiments described in this thesis, combinations of these different measures were frequently utilized depending on the experimental conditions.

Chapter 4

Experiments & Results

Since the experiments described in this thesis were performed in different plasma density regimes, this chapter is divided into two main parts. In Section 4.1, the experiments and main results obtained using electron acceleration via laser wakefields are presented, while in Section 4.2, the experiments, and their results, regarding target normal sheath acceleration of protons are described. More details are given in the respective papers.

4.1 Laser Wakefield Acceleration

In this section, the experiments presented in Papers I to VIII are discussed, and the most important experimental results are presented.

4.1.1 Self-Injection in Supersonic Gas Jets

Many LWFA experiments today rely on advanced injection mechanisms, such as density gradient injection, ionization injection, and colliding pulses. All these mechanisms should preferably be employed in a regime where self-injection does not occur. It is therefore important to be able to predict the conditions under which self-injection will occur during the experimental design stage. In the first study (Paper I), the way in which the choice of gas affects the resulting electron beams emerging from supersonic jets was investigated. This study was performed following the experimental observation that, at the same nozzle backing pressure, very stable electron beams were produced when using hydrogen gas, but not when using helium. Early data, not included in the final paper, showed significant differences in the electron beam divergence as well as beam pointing. These results are shown in Fig. 4.1 for electron beams accelerated in a 3 mm gas jet with *the same* backing pressure (9.5 bar), which corresponds to a plasma density of 7.5×10^{18} cm^{-3} when determined for hydrogen using the Wollaston-based interferometer described in

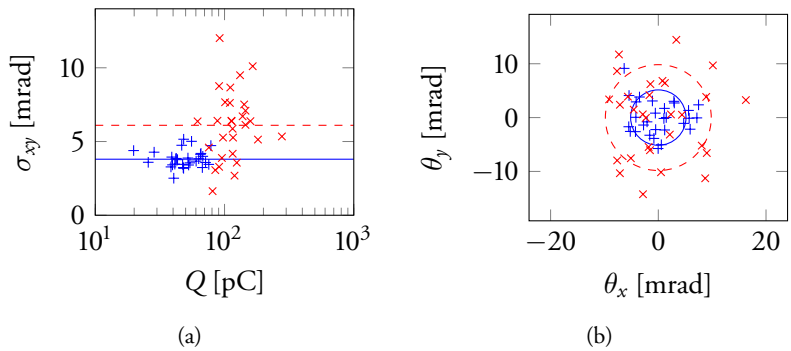

Figure 4.1 Electron Beam Stability
(a) The divergence of the recorded electron beam profiles for He (red symbols) and H_2 (blue symbols) gas at the same backing pressure. The average divergence of the beams are shown for He (red dashed line) and H_2 (blue solid line). (b) The pointing of the electron beams emerging from He (red symbols) and H_2 (blue symbols). The standard deviations in the two series of measurements are indicated by the red dashed line and the blue solid line for He and H_2, respectively. The differences in the results obtained for the two gases are due to different gas flow dynamics in supersonic jets, resulting in different plasma electron number densities.

Section 3.2.1. Both H_2 and He result in two electrons when completely ionized, and a similar value of n_e was therefore expected. However, neutral gas number density measurements performed with the wavefront-based setup showed that, at the same backing pressure, the two gases resulted in different number densities. Helium consistently produced number densities 30 % higher than H_2. A theoretical analysis of gas dynamics in supersonic gas jets confirmed the experimental findings. The results in Fig. 4.1 show the differences in electron beam stability when increasing the plasma density by 30 %. More stable beams are produced close to the threshold for self-injection than at higher values of n_e. This difference can be explained by longitudinal and transverse self-injection [113], as explained in Paper I.

A systematic study of the threshold for self-injection in supersonic gas jets was then performed (Paper II). Prior to this study, the threshold for self-injection has been reported to occur at a fixed value of $\alpha' P/P_c$ [114], where α' is the energy fraction within the FWHM of the focal spot, P the laser pulse power, and P_c the critical power for relativistic self-focusing, as defined in Eq. 2.23. In the present study, key variables such as α', laser pulse energy, plasma density, and pulse duration were varied, and it was found that self-injection in laser wakefield accelerators depended on both the laser pulse compression in the plasma, and the focal spot quality through the fraction α'. A useful expression for the minimum pulse energy required to reach wave breaking is given in Eq. 3 in Paper II. The importance of the focal spot quality was further investigated (Paper III), and it was found that only the energy within the FWHM couples to, and therefore drives, the plasma wave.

4.1.2 Density Gradient Injection

Two different methods were used to create density modulations, either with the thin wire (Paper IV), or with the twin-nozzle setup (Paper V), allowing for density gradient injection. The gradients produced were between 200 µm and 300 µm long in both cases. Paper IV describes the comparison of gradient injection and self-injection with regard to important electron beam properties. The results showed that using a wire, instead of relying on self-injection, had clear advantages, including increased injected charge, smaller beam divergence, and quasi-monoenergetic spectral features. The reduced divergence was attributed to acceleration in the second plasma wave period, where the electron bunch does not interact directly with the laser pulse. It was also found to be possible to tune the electron energy by moving the wire along the laser propagation axis.

The advantage of the twin-nozzle setup (Paper V) over the wire, is the ability to actively tailor the number density ramp, allowing its influence on the electron beams to be studied. The ability to alter the peak electron energy, by either increasing the number density from the main nozzle or increasing the acceleration length after the density peak, was demonstrated. The amount of charge could also be controlled by changing the number density in the density peak. However, at an electron density of 1×10^{19} cm^{-3} in the peak additional charge resulting from self-injection was also observed.

4.1.3 Gas-Filled Capillary Tubes

In the experiments presented in Papers VI to VIII, gas-filled capillary tubes were used, instead of gas jets, as tubes provide stable gas targets. The tubes can also collect the energy present in the wings of the laser pulse, which would otherwise not contribute to driving the plasma wave, and they also guide the laser pulse over longer distances than in a gas jet under similar experimental conditions. These properties, together with the increased plasma length, allow for electron injection at lower densities than for gas jets under similar experimental conditions. This also means that higher mean electron energies can be attained with capillary tubes than when using gas jets. In addition, the production of x-rays is enhanced using gas-filled capillary tubes, as is discussed in Paper VIII. Since the properties of x-ray emission depend on the characteristics of the accelerated electrons, the x-rays can also be used as a diagnostic tool for electron dynamics, as well as the acceleration process, as described in Papers VI and VII.

The results showed that the acceleration process was stable and similar for different laser shots, and that the variation in x-ray intensity was a consequence of the injected charge, probably due to the stochastic nature of self-injection. The transverse profile of the detected x-rays also showed signs of some kind of secondary emission, and the detailed analysis presented in Paper VII revealed that this was due to a combination of x-ray reflection on the inner walls of the capillary tubes, and

Bremsstrahlung. Bremsstrahlung is created as accelerated electrons are scattered by the laser pulse and decelerate in the capillary walls.

4.2 Target Normal Sheath Acceleration

In this section, the experiments and the most important results presented in Papers IX to XII are discussed.

4.2.1 Double Laser Pulses

Paper IX describes in detail the experimental setup used in two subsequent studies (Papers X and XI). The split mirror described in Section 3.1.3 enabled systematic studies of the effects of the laser intensity distribution on the front of the target on the accelerated proton beams. It was shown in the study presented in Paper X that the proton beam divergence could be reduced by increasing the laser spot size on the front of the target, either in two dimensions by defocusing, or in one dimension by using the split mirror to obtain two laser foci, as shown in Fig. 4.2. When defocusing, the proton beam divergence was decreased in two dimensions (see Fig. 4.2(a)), while using two laser foci separated by approximately one spot diameter resulted in an elliptical proton beam shape, as shown in Fig. 4.2(d). Upon increasing the spatial separation to several spot sizes, the elliptical beam shape disappeared and the profile became circular again.

In both Fig. 4.2(b) and 4.2(d), the laser intensity was reduced which, according to Eq. 2.38, leads to lower hot-electron temperatures. This, in turn means that the maximum attainable proton energy (see Eq. 2.55) is lower than when using a small laser focus, which was confirmed in this study. However, the number of protons detected with energies lower than 2 MeV (Fig. 4.2(b)) and 3 MeV (Fig. 4.2(d)) was increased, but not when spatial separation between the laser foci became too large, showing that the observed decrease in spatial divergence of the proton beam profiles was actually due to collimation of low-energy protons.

4.2.2 Transverse Electron Expansion

In an ongoing study (manuscript in Paper XI), the effect of using two foci with a fixed vertical separation while changing their relative intensities is being investigated. Upon introducing a small energy difference between the foci (45/55), a rotated proton beam ellipse was observed as shown in Fig. 4.3. Swapping the identity of the two foci changed the orientation of the rotated ellipse. However, no such effect was seen when the foci were separated horizontally, and the ellipses were always oriented vertically. The observed effect could be explained if the transverse expansion speed of the electron sheath depends on laser intensity, and also has a preferred expansion direction along the incident laser axis. The resulting shape of the electron sheath then affects the proton beam profile.

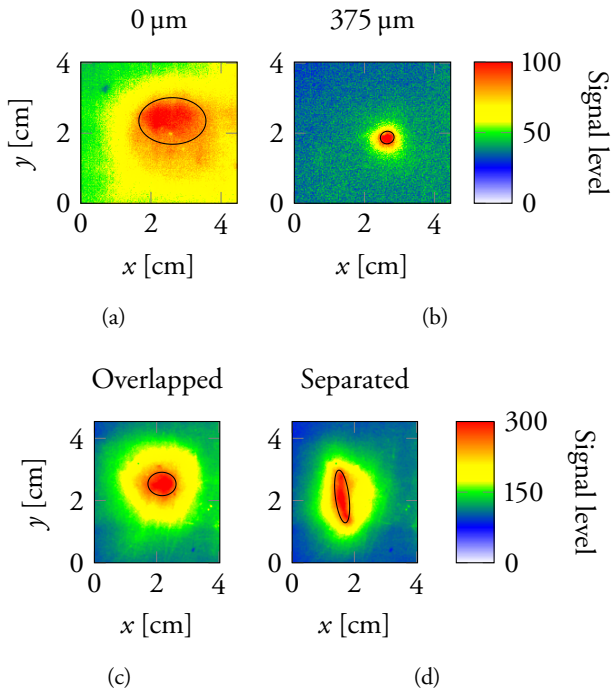

Figure 4.2 Reduced Proton Beam Divergence
Spatial proton beam profiles recorded 6.4 cm from the rear of the target in four cases: (a) one laser pulse and target at the focus, (b) one laser pulse and target placed 375 µm after the focal plane, (c) two overlapping laser foci, and (d) two laser foci separated along x by three focal spot sizes.

Another way of using transverse electron expansion is to employ a hollow spherical target with a small opening in TNSA (as described in Section 3.2.3). When using a flat target, the charge wave associated with the transverse expansion only acts to spread out the sheath. However, when using a curved target, the charge wave can be redirected back towards the propagating proton beam, allowing for staged acceleration. In Paper XII the feasibility of using this type of target was demonstrated. An increase in the proton number for particle energies between 5.5 MeV and 6.5 MeV, compared to using a flat target, was observed. Since the protons in this experiment was non-relativistic, the particles reached the opening at the opposite side of the sphere at different times. The charge wave produced by the transversely spreading electrons set up a strong electric sheath field at that opening, but the time taken for the wave to reach this point depends on the dimensions of the sphere and the surface wave velocity. In this experiment the time required for the charge wave to reach the opening was significantly shorter (by a factor 3-4) than for the fastest protons passing straight through the sphere. Further work is required to fully explore the potential of this type of target, for example, ways of slowing down the surface waves or increasing their propagation distance using other shapes (e.g.

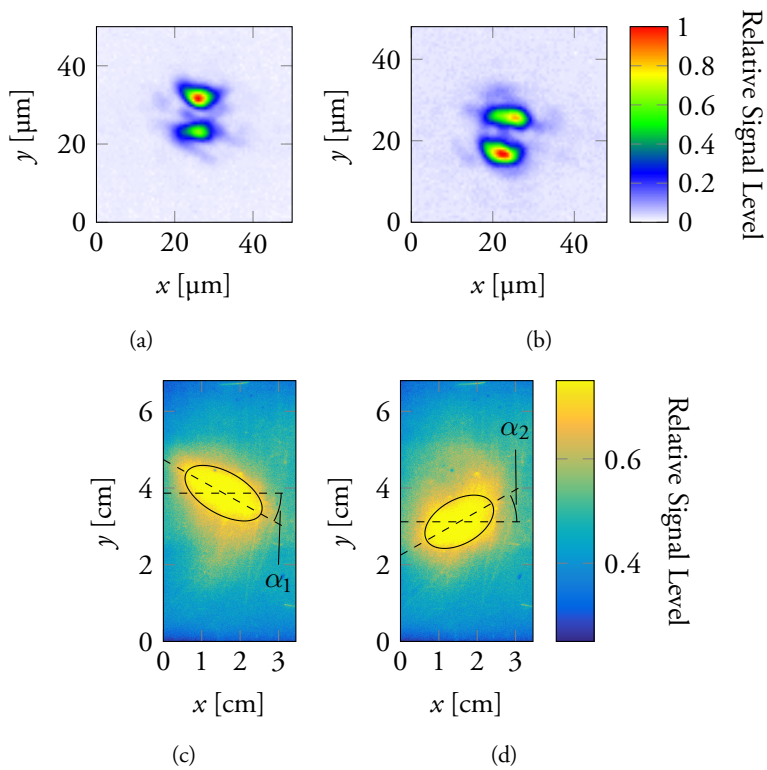

Figure 4.3 Rotation of Elliptical Proton Beam Profiles
Separated laser foci where 55 % of the total energy is (a) in the upper, and (b) in the lower focal spot. The resulting proton beam profiles recorded 6.4 cm from the target are shown in (c) and (d).

oblate).

4.2.3 Structured Targets

The structured targets described in Section 3.2.3 were also investigated. When comparing the results obtained with those from a flat target of the same overall thickness (0.9 µm), it was found that the maximum proton energy was slightly increased when using a target with nanospheres on the front, which could indicate an increase in laser absorption. No energy increase was seen when using targets with nanospheres on the rear surface, but this target resulted in increased divergence and a more homogeneous spatial profile of the proton beam, as shown in Fig. 4.4. These results are not surprising, since acceleration takes place in the direction normal to the target. Thus, a curved surface much smaller than the size of the proton source, should increase the beam divergence.

Experiments were also carried out using the grating structured targets described in Section 3.2.3. Experiments with grating structures on the front of the target

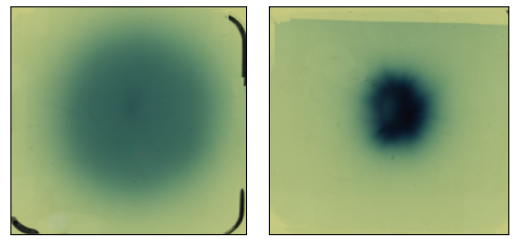

(a) (b)

Figure 4.4 Proton Beam Profiles Obtained using Flat Targets with Nanosphere Structures

Radiochromic films showing typical beam profiles obtained with 0.5 µm thick flat Mylar foils with 0.4 µm diameter spheres on (a) the rear and (b) the front of the target. It is clear that the overall proton beam divergence is greater when the spheres are on the rear of the target.

showed a decrease in maximum proton energy, as well as proton number. When the grating structures were placed on the rear of the target, low proton energies (1.5 MeV to 2.5 MeV) were observed. An explanation of this can be found by examining the spatial profiles of the sampled proton beams, which are shown in Fig. 4.5. Very large increases in divergence in one direction (perpendicular to the grating groove orientation), and a reduction in the other can clearly be seen. The reduction in energy could be an effect of the reduced divergence, as the particle spectrometer could thus be sampling a non-central part of the proton beam. An explanation of the proton beam divergence can be found by again considering the electron sheath expansion. The hot-electron charge wave can propagate unhindered along the grating grooves, whereas in the orthogonal direction the grating structure prevents expansion, thus resulting in a smaller sheath. Similarly to the case reported in Paper X, an electron sheath with this shape would give rise to proton beam profiles such as those shown in Fig. 4.5.

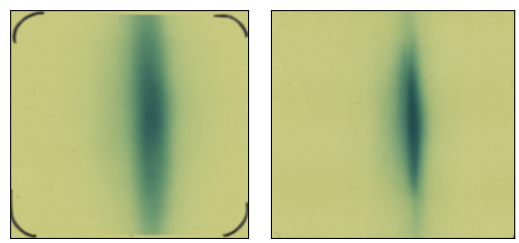

(a) (b)

Figure 4.5 Proton Beam Profiles Obtained using Flat Foil Targets with Grating Structures

Radiochromic films showing the spatial profiles of proton beams accelerated from targets with (a) 1 µm and (b) 2 µm gratings on the rear of the target. The profile shown in (a) is the accumulation of two individual proton beams, while in (b) only a single proton beam was recorded. In both cases, the proton beam profiles are stretched perpendicular to the grating structure orientation.

Chapter 5

Summary & Outlook

This thesis describes experiments performed within the field of laser plasma acceleration of electrons and protons.

Some of the laser wakefield acceleration (LWFA) experiments were dedicated to studying the basic principles of wave breaking, and the conditions required for electron self-injection. Basic studies on the effect of the choice of gas on number densities in supersonic gas jets are presented in Paper I, which provided important information for more advanced studies. The quality of the laser focus spot was then studied (Papers II and III), and it was found that only the energy within the FWHM drives the plasma wave. It was also found that compression of the laser pulse in space and time is important in the self-injection process. More advanced and better controlled injection mechanisms, such as density gradient injection, are preferably used at plasma densities lower than the threshold for self-injection.

Changes in plasma wavelength with electron number density in controlled gradients were thus used to inject electrons in a controlled manner into the accelerating part of the plasma wave (Papers IV and V). This resulted in controllable increases in beam charge compared to self-injection. In the experiments presented in Paper IV, the electron beams were highly reproducible with very low spatial divergence, and quasi-monoenergetic features, which were attributed to the increased stability when using gradient injection rather than relying on self-injection.

A different method of creating stable and reproducible electron beams of high energy, utilizing gas-filled dielectric capillary tubes, was investigated in the experiments presented in Papers VI, VII, and VIII. These experiments showed an increase in the x-ray yield when using a 1 cm capillary tube compared to a 2 mm supersonic gas jet, under similar experimental conditions. The x-rays were also used as a diagnostic tool to analyze the electron acceleration process, as described in Papers VI and VII.

The target normal sheath acceleration (TNSA) setup described in Paper IX enabled studies of the effects of different laser intensity distributions on the front

of the target on the proton beams generated. The study described in Paper X showed that the shape of the electron sheath on the rear of the target could be altered using two laser foci spatially separated by a small distance or by defocusing, affecting the resulting proton beam divergence in one or two dimensions, respectively. The decrease in one-dimensional divergence led to an elliptical beam shape, which could in turn be affected by changing the relative intensities at the two laser foci. The ongoing study, described in Paper XI, shows that the elliptical proton beam profile is rotated by altering the intensity ratio. One explanation of this could be different transverse expansion speeds of the electron sheath and its associated charge wave.

Hollow microspheres offer a different type of target that makes use of transverse electron transport. These were investigated as targets in the studies presented in Paper XII. The hollow spherical target redirects the charge wave back towards an opening on the opposite side of the sphere, which can affect parts of the propagating proton beam. During this study, an increase in proton number between 5.5 MeV and 6.5 MeV was seen compared to flat targets.

Microstructured flat targets were also investigated, and it was found that the spatial profile of the proton beam was greatly affected by structures on the rear of the target. When nanospheres were attached to the rear of the target, an increase in proton beam divergence was seen together with a more homogeneous transverse spatial particle distribution, compared to a flat Mylar foil. When a grating structure was placed on the rear of the target the proton beam divergence was reduced along the groove direction and greatly increased in the perpendicular direction.

During the course of this work, tremendous progress has been made internationally within these fields. Electron beams with energies up to 4.2 GeV have been reported using LWFA [25], and new injection mechanisms have greatly increased the reproducibility and stability of the electron beams. In TNSA, more powerful laser systems have increased maximum proton energies towards 85 MeV [115]. In the future, even higher laser intensities will enable the realization of new acceleration mechanisms such as radiation pressure acceleration [116], or new promising ideas such as chirped standing wave acceleration [117].

Conventional acceleration techniques still have many advantages over the laser-plasma-based techniques described in this thesis, such as high repetition rates, high attainable particle energies, and low energy spreads. However, the potential of new, compact accelerators that could result from this research should not be underestimated. Although the shot-to-shot fluctuations in LWFA and TNSA may seem large compared to conventional accelerators, their compactness is very attractive. For instance, small particle accelerators may find applications in hospitals, either in treating cancer patients with proton beams directly, or for the production of short-lived radioactive isotopes used in medical imaging and treatment or the sterilization of medical equipment. LWFA-generated electron beams have very short durations, shorter than those achievable at synchrotron radiation facilities today. The use of LWFA-based accelerators as injectors for conventional accelerators could therefore be interesting despite the difficulties involved in such techniques [118].

Both LWFA and TNSA are fairly new areas of experimental research, having only been studied for approximately 20 years, whereas conventional accelerators have been in use for almost 100 years. Despite their novelty, LWFA and TNSA are now rather well understood, and the work presented in this thesis has hopefully contributed to this understanding. As in many other areas of research, as they become more mature they have started to move from the understanding of basic principles to novel applications, and we will probably see many applications of laser-based particle accelerators in the future.

The Author's Contributions to the Papers

I **Supersonic Jets of Hydrogen and Helium for Laser Wakefield Acceleration**

This paper is based on a large number of experiments ranging over several years. I played a leading role in the first part of the experimental work, where I designed and implemented parts of the experimental setup. I also planned and executed all the experiments, and evaluated all the data from the initial experiments. I was also highly involved in the second experimental phase. I derived a theoretical model that can be used to predict the neutral number density in supersonic gas jets from variables such as backing pressure and gas species. I took part in numerous discussions regarding the interpretation of the data. I also wrote the manuscript.

II **Self-Injection Threshold in Self-Guided Laser Wakefield Accelerators**

III **Increasing Energy Coupling into Plasma Waves by Tailoring the Laser Radial Focal Spot Distribution in a Laser Wakefield Accelerator**

I took part in all phases of the experiment on which these two papers are based, ranging from the initial planning and design to the construction of the setup. I also designed and built a gas delivery system. I took an active part in discussions regarding the interpretation of the data, and gave constructive feedback on the manuscripts.

IV **Laser Wakefield Acceleration using Wire Produced Double Density Ramps**

I took part in all phases of the experimental work, including the design and construction of the setup. I was responsible for the construction of the electron spectrometer, and its calibration. I evaluated all the electron spectra to provide information on the charge and energy distribution of the electron beams. I also mounted and adjusted the gas nozzle for optimal performance. I participated in discussions regarding the experimental findings and gave constructive feedback on the manuscript, including crucial input to many of the figures. I did not contribute to the computer simulations, or their interpretation.

V **Down-Ramp Injection and Independently Controlled Acceleration of Electrons in a Tailored Laser Wakefield Accelerator**

I took part in the experimental phase, and participated in discussions regarding the interpretation of the data. I also gave feedback on the manuscript. I did not contribute to the simulations.

VI **Study of Electron Acceleration and X-Ray Radiation as a Function of Plasma Density in Capillary-Guided Laser Wakefield Accelerators**

VII **Analysis of X-Ray Emission and Electron Dynamics in a Capillary-Guided Laser Wakefield Accelerator**

VIII **Enhancement of X-Rays Generated by a Guided Laser Wakefield Accelerator inside Capillary Tubes**

I took an active part in the design and the construction of the experimental setup on which these three papers are based. My main contribution is related to the electron spectrometer, which I constructed and calibrated. Calibration of the spectrometer enabled the absolute charge to be determined. I was also highly involved during the collection of the experimental data and their interpretation. I evaluated all the electron spectra, which provided information on electron energies and beam charge. I also participated in discussions regarding the results, and contributed to the manuscript, including input to figures. I did not contribute to the computer simulations or their interpretation.

IX **A Setup for Studies of Laser-Driven Proton Acceleration at the Lund Laser Centre**

X **Manipulation of the Spatial Distribution of Laser-Accelerated Proton Beams by Varying the Laser Intensity Distribution**

These two papers are based on the same experimental setup, and I played an active role in many of the experiments leading up to them. I improved the spatial detector, which increased its resolution. I participated in discussions regarding the manuscripts, and gave feedback on both of them. I evaluated most of the experimental data in Paper X, including the proton spectra and spatial profiles, and produced many of the figures. I did not contribute to the computer simulations or their interpretation.

XI **Transverse Expansion of the Electron Sheath during Laser Acceleration of Protons**

This manuscript is based on several experiments and setups. One of the setups is partly my own design. I improved the ability to accurately adjust the energy ratio of the two foci, which was crucial for the experiments. I also constructed and aligned most of the experimental setup. I collected much experimental data on my own, and evaluated it. I also participated in discussions with researchers performing simulations, and I am writing the manuscript. I did not perform the simulations.

XII **Hollow Microspheres as Targets for Staged Laser-Driven Proton Acceleration**

I took part in the experimental work and participated in discussions regarding the collected data. I took part in discussions regarding the simulations, and gave constructive feedback on the manuscript. I did not perform the simulations.

Acknowledgments

First of all, I would like to thank my supervisor, Claes-Göran Wahlström, for giving me the opportunity, not only once but twice, to be part of his research group. The first time was in 2009, when I initially started my post-graduate studies, and the second was in 2014, when I had realized that I wanted to continue beyond my Licentiate degree and obtain a PhD. You have helped me believe and trust in myself. I would also like to thank my co-supervisors, Olle Lundh and Anders Persson, for all their help during my years at the Division.

I would also like to thank past and present PhD students and postdocs in the research group: Guillaume Genoud and Matthias Burza, for helping me when I started as a PhD student; Lovisa Senje for her help in the lab; Franck Wojda for his skills with capillaries, and Martin Hansson for interesting discussions on a wide range of subjects. I wish to acknowledge the contributions of Bastian Aurand to the TNSA experiments, and to thank Isabel Gallardo-Gonzales and Henrik Ekerfelt for helping me align OAPs and plasma mirrors. Additionally, I would like to thank, and wish good luck to, Malay Dalui and Jonas Björklund Svensson. Thanks to everyone at the Division of Atomic Physics for the pleasant working environment.

I also want to acknowledge the researchers involved in the PLIONA project, and I would particularly like to thank Tünde Fülöp, Mattias Marklund, Arkady Gonoskov, Felix Mackenroth, and Christopher Harvey. I have, of course, enjoyed the company of everyone in the PLIONA team.

During my time as a PhD student, I have also had the privilege to conduct experimental work with researchers and students from several international groups, and I would therefore like to thank the groups of Stuart Mangles, Brigitte Cros, David Neely, Paul McKenna, and Daniele Margarone for fruitful collaboration.

I also think it is appropriate to acknowledge the person who is responsible for my initial endeavors in physics, namely Patrik Norqvist at Umeå University. If it had not been for him, I would never have considered becoming a student in Engineering Physics in the first place.

My friends outside work are also important, and I want to acknowledge them here, and thank them for at least trying, to make me talk about things other than physics. They are, in no particular order: Tomas Weis, Mikael Nordqvist, Jonas

Thygesen, Martin Björklund, Mattias Alm, Erik Abrahamsson, Christofer Ryås, and Jimmy Lundqvist.

My mother and my sisters and their families have also played an important role in my academic studies, especially my sister, Malin, who convinced me to study natural sciences instead of economics.

It would not have been possible to complete this thesis without my lovely wife, Linda-Maria. Without her support during all the years in the lab, or her understanding and patience over the last couple of months when I was writing this thesis, things would have been very different. Finally, to my daughter Elisabeth who means the world to me —Thank you for being you.

References

1. S V Bulanov and V S Khoroshkov. *Feasibility of Using Laser Ion Accelerators in Proton Therapy*. Plasma Phys. Rep. **28**, 453–456 (2002).

2. P R Bolton *et al. Toward Integrated Laser-Driven Ion Accelerator Systems at the Photo-Medical Research Center in Japan*. Nucl. Instrum. Methods Phys. Res. Section A **620**, 71–75 (2010).

3. Oliver Jäkel *et al. State of the Art in Hadron Therapy*. In *Nuclear Physics Medthods and Accelerators in Biology and Medicine* pages 70–77. AIP (2007).

4. V Malka, J Faure, and Y A Gauduel. *Ultra-Short Electron Beams Based Spatio-Temporal Radiation Biology and Radiotherapy*. Mutat. Res. Rev. Mutat. Res. **704**, 142–151 (2010).

5. Kedar Narayan and Sriram Subramaniam. *Focused Ion Beams in Biology*. Nature Methods **12**, 1021–1031 (2015).

6. C T Dillon. *Synchrotron Radiation Spectroscopic Techniques as Tools for the Medicinal Chemist: Microprobe X-Ray Fluorescence Imaging, X-Ray Absorption Spectroscopy, and Infrared Microspectroscopy*. Aust. J. Chem. **65**, 204–217 (2012).

7. I G Gonzalez-Martinez *et al. Electron-Beam Induced Synthesis of Nanostructures: A Review*. Nanoscale **8**, 11340–11362 (2016).

8. F Watt *et al. Ion Beam Lithography and Nanofabrication: A Review*. Int. J. Nanosci. **04**, 269–286 (2005).

9. S Kawata, T Karino, and A I Ogoyski. *Review of Heavy-Ion Inertial Fusion Physics*. Matter Radiat. Extremes **1**, 89–113 (2016).

10. C Labaune *et al. Fusion Reactions Initiated by Laser-Accelerated Particle Beams in a Laser-Produced Plasma*. Nat. Commun. **4** (2013).

11. S Chatrchyan *et al. Observation of a New Boson at a Mass of 125 GeV with the CMS Experiment at the LHC*. Phys. Lett. B **716**, 30–61 (2012).

12. G Aad *et al. Observation of a New Particle in the Search for the Standard Model Higgs Boson with the ATLAS Detector at the LHC*. Phys. Lett. B **716**, 1–29 (2012).

13. T Tajima and J M Dawson. *Laser Electron Accelerator*. Phys. Rev. Lett. **43**, 267–270 (1979).

14. E Esarey, C B Schroeder, and W P Leemans. *Physics of Laser-Driven Plasma-Based Electron Accelerators*. Rev. Mod. Phys. **81**, 1229–1285 (2009).

15. D Strickland and G Mourou. *Compression of Amplified Chirped Optical Pulses*. Opt. Commun. **56**, 219–221 (1985).

16. F Amiranoff *et al. Observation of Laser Wakefield Acceleration of Electrons*. Phys. Rev. Lett. **81**, 995–998 (1998).

17. E L Clark *et al. Measurements of Energetic Proton Transport Through Magnetized Plasma From Intense Laser Interactions with Solids*. Phys. Rev. Lett. **84**, 670–673 (2000).

18. R A Snavely *et al. Intense High-Energy Proton Beams from Petawatt-Laser Irradiation of Solids*. Phys. Rev. Lett. **85**, 2945–2948 (2000).

19. A Maksimchuk *et al. Forward Ion Acceleration in Thin Films Driven by a High-Intensity Laser*. Phys. Rev. Lett. **84**, 4108–4111 (2000).

20. H Daido, M Nishiuchi, and A S Pirozhkov. *Review of Laser-Driven Ion Sources and Their Applications*. Rep. Prog. Phys. **75**, 056401 (2012).

21. M Borghesi *et al. Fast Ion Generation by High-Intensity Laser Irradiation of Solid Targets and Applications*. Fusion Sci. Technol. **49**, 412–439 (2006).

22. S P D Mangles *et al. Monoenergetic Beams of Relativistic Electrons From Intense Laser–Plasma Interactions*. Nature **431**, 535–538 (2004).

23. C G R Geddes *et al. High-Quality Electron Beams From a Laser Wakefield Accelerator Using Plasma-Channel Guiding*. Nature **431**, 538–541 (2004).

24. J Faure *et al. A Laser–Plasma Accelerator Producing Monoenergetic Electron Beams*. Nature **431**, 541–544 (2004).

25. W P Leemans *et al. Multi-GeV Electron Beams From Capillary-Discharge-Guided Subpetawatt Laser Pulses in the Self-Trapping Regime*. Phys. Rev. Lett. **113**, 245002 (2014).

26. T H Maiman. *Optical and Microwave-Optical Experiments in Ruby*. Phys. Rev. Lett. **4**, 564–566 (1960).

27. P Gibbon. *Short Pulse Laser Interactions with Matter*. An Introduction. Imperial College Press London (2005).

28. S C Wilks *et al. Energetic Proton Generation in Ultra-Intense Laser–Solid Interactions*. Phys. Plasmas **8**, 542 (2001).

29. P Sprangle, C-M Tang, and E Esarey. *Relativistic Self-Focusing of Short-Pulse Radiation Beams in Plasmas*. IEEE T. Plasma Sci. **15**, 145–153 (1987).

30. G-Z Sun *et al. Self-Focusing of Short Intense Pulses in Plasmas*. Phys. Fluids **30**, 526–532 (1987).

31. J Schreiber *et al. Complete Temporal Characterization of Asymmetric Pulse Compression in a Laser Wakefield*. Phys. Rev. Lett. **105**, 235003 (2010).

32. W Lu *et al. Generating Multi-GeV Electron Bunches Using Single Stage Laser Wakefield Acceleration in a 3D Nonlinear Regime*. Phys. Rev. ST Accel. Beams **10**, 061301 (2007).

33. L M Gorbunov and V I Kirsanov. *Excitation of Plasma Waves by an Electromagnetic Wave Packet*. Journal of Experimental and Theoretical Physics **66**, 290–294 (1987).

34. A Pukhov and J Meyer-ter Vehn. *Laser Wake Field Acceleration: the Highly Non-Linear Broken-Wave Regime*. Appl. Phys. B **74**, 355–361 (2002).

35. W Lu *et al. Nonlinear Theory for Relativistic Plasma Wakefields in the Blowout Regime*. Phys. Rev. Lett. **96**, 165002 (2006).

36. P Sprangle, E Esarey, and A Ting. *Nonlinear Interaction of Intense Laser Pulses in Plasmas*. Physical Review A **41**, 4463–4469 (1990).

37. A Modena *et al. Electron Acceleration From the Breaking of Relativistic Plasma Waves*. Nature **377**, 606–608 (1995).

38. M I K Santala *et al. Observation of a Hot High-Current Electron Beam From a Self-Modulated Laser Wakefield Accelerator*. Phys. Rev. Lett. **86**, 1227–1230 (2001).

39. V Malka. *Electron Acceleration by a Wake Field Forced by an Intense Ultrashort Laser Pulse*. Science **298**, 1596–1600 (2002).

40. S Bulanov *et al. Particle Injection Into the Wave Acceleration Phase Due to Nonlinear Wake Wave Breaking*. Phys. Rev. E **58**, R5257–R5260 (1998).

41. H Suk *et al. Plasma Electron Trapping and Acceleration in a Plasma Wake Field Using a Density Transition*. Phys. Rev. Lett. **86**, 1011–1014 (2001).

42. A J Gonsalves *et al. Tunable Laser Plasma Accelerator Based on Longitudinal Density Tailoring*. Nat. Phys. 7, 862–866 (2011).

43. D Umstadter, J K Kim, and E Dodd. *Laser Injection of Ultrashort Electron Pulses Into Wakefield Plasma Waves*. Phys. Rev. Lett. **76**, 2073–2076 (1996).

44. E Esarey *et al. Electron Injection Into Plasma Wakefields by Colliding Laser Pulses*. Phys. Rev. Lett. **79**, 2682–2685 (1997).

45. J Faure *et al. Controlled Injection and Acceleration of Electrons in Plasma Wakefields by Colliding Laser Pulses*. Nature **444**, 737–739 (2006).

46. A Pak *et al. Injection and Trapping of Tunnel-Ionized Electrons Into Laser-Produced Wakes*. Phys. Rev. Lett. **104**, 025003 (2010).

47. C McGuffey *et al. Ionization Induced Trapping in a Laser Wakefield Accelerator*. Phys. Rev. Lett. **104**, 025004 (2010).

48. M Chen *et al. Theory of Ionization-Induced Trapping in Laser-Plasma Accelerators*. Phys. Plasmas **19**, 033101 (2012).

49. C Rechatin *et al. Observation of Beam Loading in a Laser-Plasma Accelerator*. Phys. Rev. Lett. **103**, 194804 (2009).

50. E Esarey *et al. Synchrotron Radiation From Electron Beams in Plasma-Focusing Channels*. Phys. Rev. E **65**, 056505 (2002).

51. S Fourmaux *et al. Demonstration of the Synchrotron-Type Spectrum of Laser-Produced Betatron Radiation*. New J. Phys. **13**, 033017 (2011).

52. J Schreiber *et al. Source-Size Measurements and Charge Distributions of Ions Accelerated From Thin Foils Irradiated by High-Intensity Laser Pulses*. Appl. Phys. B **79**, 1041–1045 (2004).

53. F Nürnberg *et al. Radiochromic Film Imaging Spectroscopy of Laser-Accelerated Proton Beams*. Rev. Sci. Instrum. **80**, 033301 (2009).

54. J P Freidberg *et al. Resonant Absorption of Laser Light by Plasma Targets*. Phys. Rev. Lett. **28**, 795–799 (1972).

55. F Brunel. *Not-So-Resonant, Resonant Absorption*. Phys. Rev. Lett. **59**, 52–55 (1987).

56. S C Wilks and W L Kruer. *Absorption of Ultrashort, Ultra-Intense Laser Light by Solids and Overdense Plasmas*. IEEE J. Quant. Electron. **33**, 1954–1968 (1997).

57. W L Kruer and K Estabrook. *J×B Heating by Very Intense Laser Light*. Phys. Fluids **28**, 430–432 (1985).

58. S C Wilks *et al. Absorption of Ultra-Intense Laser Pulses*. Phys. Rev. Lett. **69**, 1383–1386 (1992).

59. S C Wilks. *Simulations of Ultraintense Laser–Plasma Interactions*. Phys. Fluids B **5**, 2603 (1993).

60. B F Lasinski *et al. Particle-in-Cell Simulations of Ultra Intense Laser Pulses Propagating Through Overdense Plasma for Fast-Ignitor and Radiography Applications*. Phys. Plasmas **6**, 2041–2047 (1999).

61. J Fuchs *et al. Laser-Driven Proton Scaling Laws and New Paths Towards Energy Increase*. Nat. Phys. **2**, 48–54 (2005).

62. Y Ping *et al. Absorption of Short Laser Pulses on Solid Targets in the Ultrarelativistic Regime*. Phys. Rev. Lett. **100**, 085004 (2008).

63. A R Bell *et al. Fast-Electron Transport in High-Intensity Short-Pulse Laser-Solid Experiments*. Plasma Phys. Control. Fusion **39**, 653–659 (1997).

64. A J Mackinnon *et al. Enhancement of Proton Acceleration by Hot-Electron Recirculation in Thin Foils Irradiated by Ultraintense Laser Pulses*. Phys. Rev. Lett. **88**, 215006 (2002).

65. Y Sentoku *et al. High Energy Proton Acceleration in Interaction of Short Laser Pulse with Dense Plasma Target*. Phys. Plasmas **10**, 2009–2015 (2003).

66. M Kaluza *et al. Influence of the Laser Prepulse on Proton Acceleration in Thin-Foil Experiments*. Phys. Rev. Lett. **93**, 045003 (2004).

67. P McKenna, R Bingham, and D A Jaroszynski, editors. *Laser-Plasma Interactions and Applications*. Springer International Publishing Heidelberg (2013).

68. F Pisani *et al. Experimental Evidence of Electric Inhibition in Fast Electron Penetration and of Electric-Field-Limited Fast Electron Transport in Dense Matter*. Phys. Rev. E **62**, R5927–R5930 (2000).

69. A R Bell *et al. Fast Electron Transport in Laser-Produced Plasmas and the KALOS Code for Solution of the Vlasov–Fokker–Planck Equation*. Plasma Phys. Control. Fusion **48**, R37–R57 (2006).

70. E S Weibel. *Anomalous Skin Effect in a Plasma*. Phys. Fluids **10**, 741–748 (1967).

71. R Jung *et al. Study of Electron-Beam Propagation Through Preionized Dense Foam Plasmas*. Phys. Rev. Lett. **94**, 195001 (2005).

72. X H Yuan *et al. Effect of Self-Generated Magnetic Fields on Fast-Electron Beam Divergence in Solid Targets*. New J. Phys. **12**, 063018–11 (2010).

73. O Jäckel *et al. All-Optical Measurement of the Hot Electron Sheath Driving Laser Ion Acceleration From Thin Foils*. New J. Phys. **12**, 103027 (2010).

74. P McKenna *et al. Lateral Electron Transport in High-Intensity Laser-Irradiated Foils Diagnosed by Ion Emission*. Phys. Rev. Lett. **98**, 145001 (2007).

75. S Buffechoux *et al. Hot Electrons Transverse Refluxing in Ultraintense Laser-Solid Interactions*. Phys. Rev. Lett. **105**, 015005–5 (2010).

76. E Brambrink *et al. Transverse Characteristics of Short-Pulse Laser-Produced Ion Beams: a Study of the Acceleration Dynamics*. Phys. Rev. Lett. **96**, 154801 (2006).

77. O Lundh *et al. Influence of Shock Waves on Laser-Driven Proton Acceleration*. Phys. Rev. E **76**, 026404 (2007).

78. P Mora. *Plasma Expansion Into a Vacuum*. Phys. Rev. Lett. **90**, 185002 (2003).

79. J Fuchs *et al. Comparative Spectra and Efficiencies of Ions Laser-Accelerated Forward From the Front and Rear Surfaces of Thin Solid Foils*. Phys. Plasmas **14**, 053105 (2007).

80. J Fuchs *et al. Spatial Uniformity of Laser-Accelerated Ultrahigh-Current MeV Electron Propagation in Metals and Insulators*. Phys. Rev. Lett. **91**, 255002 (2003).

81. D C Carroll *et al. Active Manipulation of the Spatial Energy Distribution of Laser-Accelerated Proton Beams*. Phys. Rev. E **76**, 065401 (2007).

82. E Brambrink *et al. Modeling of the Electrostatic Sheath Shape on the Rear Target Surface in Short-Pulse Laser-Driven Proton Acceleration*. Laser Part. Beams **24**, 163–168 (2006).

83. M Allen *et al. Direct Experimental Evidence of Back-Surface Ion Acceleration From Laser-Irradiated Gold Foils*. Phys. Rev. Lett. **93**, 265004 (2004).

84. P F Moulton. *Tunable Solid-State Lasers*. Proc. IEEE **80**, 348–364 (1992).

85. D E Spence *et al. Regeneratively Initiated Self-Mode-Locked Ti:Sapphire Laser*. Opt. Lett. **16**, 1762–1764 (1991).

86. D F Hotz. *Gain Narrowing in a Laser Amplifier*. Appl. Opt. **4**, 527–530 (1965).

87. R Y Chiao, E Garmire, and C H Townes. *Self-Trapping of Optical Beams*. Phys. Rev. Lett. **13**, 479–482 (1964).

88. P L Kelley. *Self-Focusing of Optical Beams*. Phys. Rev. Lett. **15**, 1005–1008 (1965).

89. J E Murray and W H Lowdermilk. *ND:YAG Regenerative Amplifier*. J. Appl. Phys. **51**, 3548–3556 (1980).

90. W H Lowdermilk and J E Murray. *The Multipass Amplifier: Theory and Numerical Analysis*. J. Appl. Phys. **51**, 2436–2444 (1980).

91. Yuzo Ishida, Tatsuo Yajima, and Akira Watanabe. *A Simple Monitoring System for Single Subpicosecond Laser Pulses Using an SH Spatial Autocorrelation Method and a CCD Image Sensor*. Opt. Commun. **56**, 57–60 (1985).

92. M Raghuramaiah *et al. A Second-Order Autocorrelator for Single-Shot Measurement of Femtosecond Laser Pulse Durations*. J. Sādhanā **26**, 603–611 (2001).

93. F Salin *et al. Single-Shot Measurement of a 52-Fs Pulse*. Appl. Opt. **26**, 4528–4531 (1987).

94. S Luan *et al. High Dynamic Range Third-Order Correlation Measurement of Picosecond Laser Pulse Shapes*. Meas. Sci. Technol. **4**, 1426–1429 (1993).

95. H C Kapteyn *et al. Prepulse Energy Suppression for High-Energy Ultrashort Pulses Using Self-Induced Plasma Shuttering*. Opt. Lett. **16**, 490–492 (1991).

96. B Dromey *et al. The Plasma Mirror - A Subpicosecond Optical Switch for Ultrahigh Power Lasers*. Rev. Sci. Instrum. **75**, 645–649 (2004).

97. G Doumy *et al. Complete Characterization of a Plasma Mirror for the Production of High-Contrast Ultraintense Laser Pulses*. Phys. Rev. E **69**, 026402 (2004).

98. Ch Ziener *et al. Specular Reflectivity of Plasma Mirrors as a Function of Intensity, Pulse Duration, and Angle of Incidence*. J. Appl. Phys. **93**, 768 (2003).

99. W A Mair. *Supersonic Gas Flow*. Br. J. Appl. Phys. **5**, 1–6 (1954).

100. R Benattar, C Popovics, and R Sigel. *Polarized Light Interferometer for Laser Fusion Studies*. Rev. Sci. Instrum. **50**, 1583–1586 (1979).

101. G R Plateau *et al. Wavefront-Sensor-Based Electron Density Measurements for Laser-Plasma Accelerators*. Rev. Sci. Instrum. **81**, 033108 (2010).

102. F M White. *Fluid Mechanics*. McGraw-Hill Education New York 6th edition (2008).

103. H E Ferrari *et al. Electron Acceleration by Laser Wakefield and X-Ray Emission at Moderate Intensity and Density in Long Plasmas*. Phys. Plasmas **18**, 083108 (2011).

104. G Genoud *et al. Laser-Plasma Electron Acceleration in Dielectric Capillary Tubes*. Appl. Phys. B **105**, 309–316 (2011).

105. F Wojda *et al. Laser-Driven Plasma Waves in Capillary Tubes*. Phys. Rev. E **80**, 066403 (2009).

106. M Hansson *et al. Enhanced Stability of Laser Wakefield Acceleration Using Dielectric Capillary Tubes*. Phys. Rev. ST Accel. Beams **17**, 031303 (2014).

107. B Cros *et al. Eigenmodes for Capillary Tubes with Dielectric Walls and Ultraintense Laser Pulse Guiding*. Phys. Rev. E **65**, 026405 (2002).

108. G Genoud *et al. Active Control of the Pointing of a Multi-Terawatt Laser*. Rev. Sci. Instrum. **82**, 033102 (2011).

109. M Borghesi *et al. Multi-MeV Proton Source Investigations in Ultraintense Laser-Foil Interactions*. Phys. Rev. Lett. **92**, 055003 (2004).

110. Y Glinec *et al. Absolute Calibration for a Broad Range Single Shot Electron Spectrometer*. Rev. Sci. Instrum. 77, 103301 (2006).

111. A Buck *et al. Absolute Charge Calibration of Scintillating Screens for Relativistic Electron Detection*. Rev. Sci. Instrum. **81**, 033301 (2010).

112. R Nowotny and A Taubeck. *A Method for the Production of Composite Scintillators for Dosimetry in Diagnostic Radiology*. Phys. Med. Biol. **54**, 1457–1468 (2009).

113. S Corde *et al. Observation of Longitudinal and Transverse Self-Injections in Laser-Plasma Accelerators*. Nat. Commun. **4**, 1501 (2013).

114. D H Froula *et al. Measurements of the Critical Power for Self-Injection of Electrons in a Laser Wakefield Accelerator*. Phys. Rev. Lett. **103**, 215006 (2009).

115. F Wagner *et al. Maximum Proton Energy Above 85 MeV From the Relativistic Interaction of Laser Pulses with Micrometer Thick CH_2 Targets*. Phys. Rev. Lett. **116**, 205002 (2016).

116. M Borghesi. *Laser-Driven Ion Acceleration: State of the Art and Emerging Mechanisms*. Nucl. Instrum. Methods Phys. Res. Section A 7**40**, 6–9 (2014).

117. F Mackenroth, A Gonoskov, and M Marklund. *Chirped-Standing-Wave Acceleration of Ions with Intense Lasers*. Phys. Rev. Lett. in Press (2016).

118. S Hillenbrand *et al. Study of Laser Wakefield Accelerators as Injectors for Synchrotron Light Sources*. Nucl. Instrum. Methods Phys. Res. Section A 7**40**, 153–157 (2014).

Papers

Paper I

Supersonic Jets of Hydrogen and Helium for Laser Wakefield Acceleration

K. Svensson, M. Hansson, F. Wojda, L. Senje, M. Burza, B. Aurand, G. Genoud, A. Persson, C.-G. Wahlström, & O. Lundh.

Phys. Rev. Accel. Beams **19**, 051301 (2016).

PHYSICAL REVIEW ACCELERATORS AND BEAMS **19,** 051301 (2016)

Supersonic jets of hydrogen and helium for laser wakefield acceleration

K. Svensson,* M. Hansson, F. Wojda, L. Senje, M. Burza, B. Aurand, G. Genoud, A. Persson, C.-G. Wahlström, and O. Lundh†

Department of Physics, Lund University, P.O. Box 118, SE-221 00 Lund, Sweden

(Received 1 December 2015; published 2 May 2016)

The properties of laser wakefield accelerated electrons in supersonic gas flows of hydrogen and helium are investigated. At identical backing pressure, we find that electron beams emerging from helium show large variations in their spectral and spatial distributions, whereas electron beams accelerated in hydrogen plasmas show a higher degree of reproducibility. In an experimental investigation of the relation between neutral gas density and backing pressure, it is found that the resulting number density for helium is ∼30% higher than for hydrogen at the same backing pressure. The observed differences in electron beam properties between the two gases can thus be explained by differences in plasma electron density. This interpretation is verified by repeating the laser wakefield acceleration experiment using similar plasma electron densities for the two gases, which then yielded electron beams with similar properties.

DOI: 10.1103/PhysRevAccelBeams.19.051301

The development of bright and ultrashort sources of particles and x rays is an important area of research. Such sources are of interest in many domains, including materials science, chemistry, biology, and medicine. Currently, emerging sources based on laser-plasma acceleration [1] are attracting significant attention. The accelerator can be very compact, and the particle beams have several unique characteristics. Recent achievements include the generation of electron beams with high energies (few GeV) [2], short pulse duration (few femtoseconds) [3], high peak current (few kA) [4], low energy spread ($< 1.5\%$) [5], and low emittance (few mm × mrad) [6]. For most demanding applications, however, the stability of the source is also very important. A critical issue for laser wakefield accelerator (LWFA) research is to find ways to decrease shot-to-shot fluctuations.

In a typical LWFA, an intense laser pulse is focused in a neutral gas medium and atoms, or molecules, are rapidly ionized by the leading edge of the laser pulse. The main part of the pulse interacts with a plasma, and free electrons are displaced by the laser ponderomotive force which leads to a significant charge separation and a copropagating plasma wave. Strong accelerating electric fields (∼100 GV/m) are present in the plasma wave, and copropagating electrons can be accelerated to high energies if they have sufficient initial kinetic energy and are located in an appropriate phase of the plasma wave. In the so-called bubble regime [7], the injection of electrons can be achieved by driving the plasma wave to such a high amplitude that the wave breaks. This occurs as the velocity of the electrons exceeds the phase velocity of the plasma wave and results in self-injection of electrons from the background plasma into the accelerating phase of the plasma wave.

The threshold for wave breaking can be described as a laser power threshold [8] as well as a laser energy threshold [9] for a given plasma electron density n_e. Thus, for a given set of laser parameters, the self-injection threshold can be found by adjusting n_e. Assuming ideal gas behavior, the neutral gas number density n in a supersonic jet is proportional to the pressure p_0 supplied to the nozzle and for a fully ionized gas $n_e = N_e n$, where N_e is the number of electrons per atom, or molecule, depending on the gas species. Thus, for fully ionized gases, $n_e \propto p_0$. In this article, we present, to our knowledge, the first comparative study of electron beams emerging from supersonic jets of H_2 and He. These gases were chosen since they will be fully ionized for the present experimental conditions.

The experimental investigations were conducted using the multiterawatt laser at the Lund Laser Centre. This Ti:sapphire-based system produced 37 fs duration laser pulses with 650 mJ of energy on target during the present study. An $f/15$ parabolic mirror focused the laser pulse to a 16 μm (FWHM) spot measured in vacuum, which yielded a peak intensity of 5.7×10^{18} W/cm^2. The beam waist was positioned, within one Rayleigh length, at the front edge of a supersonic gas flow released from a 2 mm diameter nozzle. Behind the interaction medium, along the laser propagation axis, a permanent dipole magnet dispersed the accelerated electrons according to energy. The dispersed electron beams impacted on a scintillating screen, imaged using a 16-bit digital camera. The integrated charge above

*kristoffer.svensson@fysik.lth.se
†olle.lundh@fysik.lth.se

the spectrometer threshold energy (40 MeV) was also estimated using the measured response of the scintillator screen [10,11].

In Fig. 1, two five-image sequences of electron beams accelerated in 2 mm gas jets of H_2 and He operated at $p_0 = 9.5$ bar are presented. It is apparent that electron beams originating from H_2 [Fig. 1(a)] were, compared to those accelerated in He plasmas [Fig. 1(b)], more stable in terms of maximum electron energy, position, and spatial divergence, as well as integrated beam charge. Most electron energy spectra contained a single peak with a relatively large energy spread, corresponding to the dispersed electron beams shown in Fig. 1(a). Also, the individual images shown in Fig. 1(a) are similar to the average of the full sequence, consisting of ten images, which is shown in Fig. 1(c). However, the electron beams emerging from He [Fig. 1(b)] fluctuated significantly and suffered from filamentation, which was not the case for beams from H_2. Most of the energy spectra of the beams originating in He had multiple peaks, each often having very small energy spreads. It is also apparent that the sequence average [see Fig. 1(d)] is not similar to any of the individual images shown in Fig. 1(b). When comparing the two series, it can also be deduced that the integrated charge of beams accelerated in He is significantly larger than those accelerated in H_2.

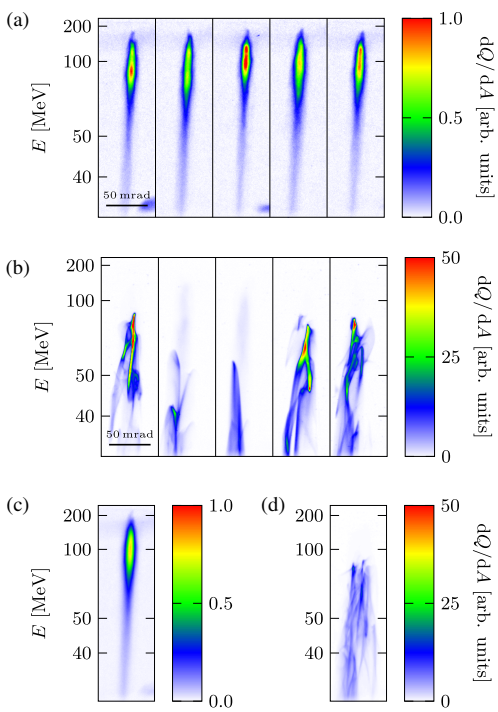

FIG. 1. False-color images of five electron beams emerging from (a) H_2 and (b) He dispersed by a permanent dipole magnet. In both cases, a 2 mm nozzle was used at a fixed backing pressure of 9.5 bar. The reproducibility of the data is shown by the average of ten individual images of electron spectra for beams emerging from (c) H_2 and (d) He. All color scales are normalized to the maximum signal in (a).

The integrated beam charge was measured in a sequence of pulses while varying the pressure in the range 3–15 bar, and the results are shown in Fig. 2. As can be seen, the threshold for self-injection, which is the point where beam charge increases rapidly, is at 9 bar for He but occurs at 11 bar for H_2, indicating differences between the two media.

We have evaluated several phenomena in order to explain our observations, such as differences in the neutral gas ionization and the corresponding ionization-induced defocusing [12]. However, the intensity needed [13] for $He \rightarrow He^+$ is 1.4×10^{15} W/cm^2, and for $He^+ \rightarrow He^{2+}$ is 8.8×10^{15} W/cm^2, which are at least 2 orders of magnitude below the peak laser intensity used in this experiment. Thus, this effect should have been noticeable only at the front of the laser pulse and in the wings. Simulations of the laser-pulse evolution performed using the code WAKE [14], which included ionization of neutral gases, did not show any significant differences in pulse characteristics when propagating through H_2 compared to He at identical n_e.

Another possible cause for the behavior in Fig. 2 could be weaker accelerating fields for H_2 than for He. Since H_2 is a molecular gas, the background of positively charged ions in the bubble behind the laser pulse might not be homogenous, as is expected for monatomic gases such as He. Assuming that the protons of the fully ionized H_2 ions

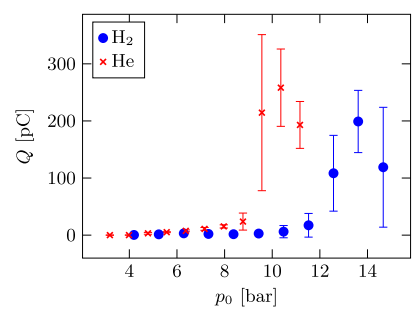

FIG. 2. Measured charge Q in the electron beams accelerated in a 2 mm gas jet over the scanned pressure range 3–15 bar in H_2 (blue circles) and He (red crosses) plotted as functions of the backing pressure. Each point represents the average of ten individual measurements with error bars indicating one standard deviation in each direction. Note that only electrons with an energy exceeding the cutoff (40 MeV) contributes to Q in this figure.

are separated by their molecular bond distance (0.074 nm), Coulomb repulsion will cause an explosion. However, in a H_2 plasma, the initial ion speed (~4.5 nm/fs) is too small to have a noticeable effect on the ion density in the bubble.

Finally, the differences between the gases seen in Figs. 1 and 2 can be due to fluid mechanical differences between the gases. To determine the magnitude of such an influence on the resulting n_e, a simple model of a converging-diverging nozzle was investigated. The relation between the nozzle throat sizes and flow Mach number M is [15]

$$\left(\frac{r_0}{r^*}\right)^2 = \frac{1}{\mathrm{M}}\left[\frac{2+(\kappa-1)\mathrm{M}^2}{(\kappa+1)}\right]^{\frac{\kappa+1}{2(\kappa-1)}}, \quad (1)$$

where r_0 is the nozzle exit radius, r^* is the critical radius where the flow reaches sonic speeds inside the nozzle, and κ is the ratio of specific heats of the gas with numerical values 1.41 for H_2 and 1.66 for He [16]. For the specified $r^* = 0.39$ mm of the 2.0 mm diameter nozzle used in the experiments, Eq. (1) yields $\mathrm{M} = 3.5$ and $\mathrm{M} = 4.2$, for H_2 and He, respectively. Assuming that the gas can be described as an ideal gas, it is also possible to express the density at the nozzle exit, n_{exit}, as [17]

$$n_{\mathrm{exit}} = \frac{p_0}{k_B T_0}\left[1+\frac{\kappa-1}{2}\mathrm{M}^2\right]^{-\frac{1}{\kappa-1}}, \quad (2)$$

where k_B is Boltzmann's constant and $T_0 = 293$ K the temperature. As the flow exits the nozzle, it will diverge with half-angle φ given by $\varphi = \alpha + \theta$, where $\alpha = \arcsin \mathrm{M}^{-1}$ is the Mach cone half-angle and θ the nozzle expansion angle. This means that, using cylindrical symmetry, the radius of the gas flow can be written as $r = r_0 + h\tan\varphi$, where h is the vertical distance from the nozzle exit. Assuming that φ remains constant, the gas density at a specific h close to the nozzle exit can be estimated as $n = n_{\mathrm{exit}}(r_0/r)^2$.

As is seen from Eqs. (1) and (2), there is a nontrivial relation between n_{exit} and the gas-species-dependent κ. Therefore, characterizing the relation between p_0 and n for both gases released from the nozzle was necessary and performed experimentally. The phase shift introduced by He at $n = 5\times10^{18}$ cm^{-3} over 2 mm for 633 nm light is 0.14 rad (corresponding to a 14 nm optical path length difference), which is difficult to measure with an ordinary interferometer. Therefore, n was measured as a function of p_0 with a setup consisting of an expanded HeNe-laser beam and a wave-front sensor [18], which is sensitive enough to determine the phase shift introduced by He. By assuming full ionization, n_e is then plotted as a function of p_0 for the two gases in Fig. 3, which clearly shows that they resulted in different n_e at all p_0. Using r^* as a fitting parameter in Eq. (1) to simultaneously fit the theoretical model to experimental results obtained for both H_2 and He yielded $r^* \approx 0.35$ mm, which is close to the specified critical radius

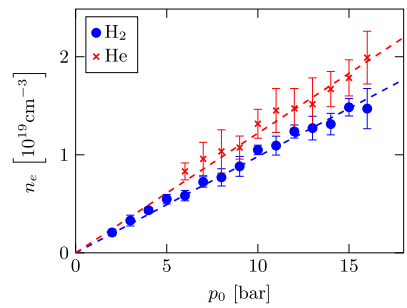

FIG. 3. The plasma electron number density n_e, 1 mm from the nozzle orifice (2 mm diameter) as a function of the applied backing pressure (p_0) for H_2 (blue circles) and He (red crosses). Assuming full ionization, the plateau electron number density n_e along the center axis in the laser propagation direction is determined from measurements of the neutral gas number density (n) using a setup consisting of an expanded HeNe beam and a wave-front sensor. Each point represents the average of 10–20 individual measurements, and the error bars indicate one standard deviation in each direction. The dashed lines are the theoretical results fitted with regards to r^*.

of the nozzle. The fitted results, shown as dashed lines in Fig. 3, are in excellent agreement with the experimental data.

From the theoretical model, it was found that $n_{\mathrm{He}} \approx 1.3 n_{\mathrm{H_2}}$. Thus, n_e in He is ~30% higher than for H_2 at any specific p_0. Compensating for this difference and plotting the data in Fig. 2 as a function of n_e instead of p_0 results in Fig. 4(a). Now it can be seen that the rapid increase in Q occurs at the same n_e for both gas species. The effect observed in Fig. 1 is therefore not significantly due to any of the previously discussed differences between the two gas species but can be explained by the relation between n_e and p_0 in Fig. 3. In Fig. 1, the electrons were accelerated in gas jets with $p_0 = 9.5$ bar which corresponds to $n_e = 9.3\times10^{18}$ cm^{-3} for H_2 and $n_e = 1.2\times10^{19}$ cm^{-3} for He. Using a similar n_e for He as for H_2 in Fig. 1(a) results in Fig. 4(b). Now, the accelerated electron beams emerging from He are very similar to the ones from H_2, which is also seen when comparing the averages of ten individual images in Figs. 1(c) (H_2) and 4(c) (He). Laser self-focusing inside the plasma becomes stronger with increasing n_e, resulting in a smaller spot size w_0 and a higher normalized vector potential a_0 for He than for H_2. For small w_0 and high a_0, it is expected that self-injection LWFA results in unstable, high charge electron beams, since transversal injection dominates over longitudinal injection [19]. When longitudinal injection is the dominant injection mechanism (large w_0 and small a_0), the accelerated electron beams becomes very stable, but with low charge. Thus, the differences seen in Fig. 1 can be explained by the differences in n_e between H_2 and He at

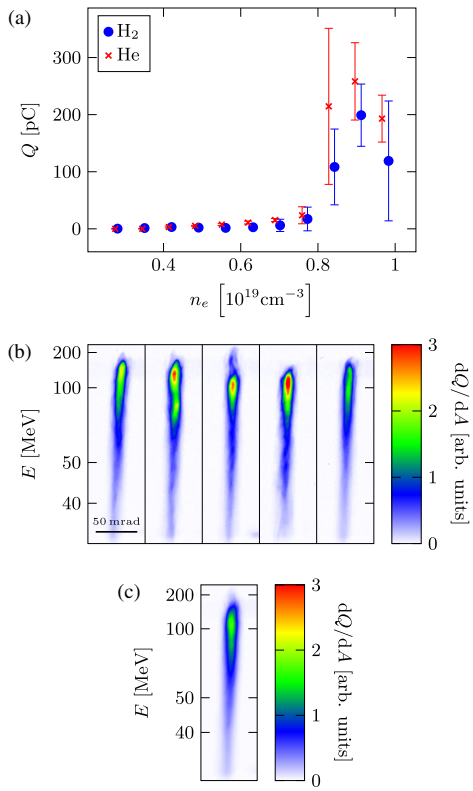

FIG. 4. (a) Measured charge Q from Fig. 2 plotted against plasma electron density n_e (assuming full ionization) instead of backing pressure p_0, by using the results of Fig. 3. Again, only electrons with energies exceeding the cutoff energy of the spectrometer setup contribute to Q. Each point represents the average of ten individual measurements with error bars indicating one standard deviation. (b) False-color images of five electron beams emerging from He at $n_e = 9.8 \times 10^{18}$ cm^{-3} dispersed by a permanent dipole magnet, showing a high resemblance to electron beams accelerated in H_2 at similar n_e. (c) Average of the full ten-image sequence which is partly shown in (b). The color scales are normalized to the maximum signal in Fig. 1(a).

identical p_0, since the two series have different injection mechanisms.

In this study, we have shown that electron beams emerging from H_2 and He at identical nozzle backing pressures have different properties. This is found to be primarily a result of the supersonic gas jet number density dependence on a specific heat ratio which, generally, differs between gas species. Repeating the experiment using similar n_e for both gases confirms these findings, since the resulting beams of accelerated electrons then showed similar properties regardless of gas species. Thus, both gases resulted in stable, low charge electron beams for $n_e < 8 \times 10^{18}$ cm^{-3}, which can be deduced from Fig. 4. It is also believed that this effect can have implications when using gas mixtures as an acceleration medium and should be studied further.

We acknowledge the support of the Swedish Research Council, the Knut and Alice Wallenberg Foundation, the Swedish Foundation for Strategic Research, Laserlab-Europe/CHARPAC (Grant Agreement No. 284464, EC's 7th Framework Programme) and EuCARD2/ANAC2 (Grant Agreement No. 312453, EC's 7th Framework Programme).

[1] T. Tajima and J. M. Dawson, Laser Electron Accelerator, Phys. Rev. Lett. **43**, 267 (1979).

[2] W. P. Leemans, A. J. Gonsalves, H. S. Mao, K. Nakamura, C. Benedetti, C. B. Schroeder, C. Toth, J. Daniels, D. E. Mittelberger, S. S. Bulanov, J. L. Vay, C. G. R. Geddes, and E. Esarey, Multi-GeV Electron Beams from Capillary-Discharge-Guided Subpetawatt Laser Pulses in the Self-Trapping Regime, Phys. Rev. Lett. **113**, 245002 (2014).

[3] A. Buck, M. Nicolai, K. Schmid, C. M. S. Sears, A. Sävert, J. M. Mikhailova, F. Krausz, M. C. Kaluza, and L. Veisz, Real-time observation of laser-driven electron acceleration, Nat. Phys. **7**, 543 (2011).

[4] O. Lundh, J. Lim, C. Rechatin, L. Ammoura, A. Ben-Ismaïl, X. Davoine, G. Gallot, J.-P. Goddet, E. Lefebvre, V. Malka, and J. Faure, Few femtosecond, few kiloampere electron bunch produced by a laser–plasma accelerator, Nat. Phys. **7**, 219 (2011).

[5] C. Rechatin, J. Faure, A. Ben-Ismaïl, J. Lim, R. Fitour, A. Specka, H. Videau, A. Tafzi, F. Burgy, and V. Malka, Controlling the Phase-Space Volume of Injected Electrons in a Laser-Plasma Accelerator, Phys. Rev. Lett. **102**, 164801 (2009).

[6] R. Weingartner, S. Raith, A. Popp, S. Chou, J. Wenz, K. Khrennikov, M. Heigoldt, A. R. Maier, N. Kajumba, M. Fuchs, B. Zeitler, F. Krausz, S. Karsch, and F. Grüner, Ultralow emittance electron beams from a laser-wakefield accelerator, Phys. Rev. Accel. Beams **15**, 111302 (2012).

[7] A. Pukhov and J. Meyer-ter-Vehn, Laser wake field acceleration: The highly non-linear broken-wave regime, Appl. Phys. B **74**, 355 (2002).

[8] D. H. Froula, C. E. Clayton, T. Döppner, K. A. Marsh, C. P. J. Barty, L. Divol, R. A. Fonseca, S. H. Glenzer, C. Joshi, W. Lu, S. F. Martins, P. Michel, W. B. Mori, J. P. Palastro, B. B. Pollock, A. Pak, J. E. Ralph, J. S. Ross, C. W. Siders, L. O. Silva, and T. Wang, Measurements of the Critical Power for Self-Injection of Electrons in a Laser Wakefield Accelerator, Phys. Rev. Lett. **103**, 215006 (2009).

[9] S. P. D. Mangles, G. Genoud, M. S. Bloom, M. Burza, Z. Najmudin, A. Persson, K. Svensson, A. G. R. Thomas, and C.-G. Wahlström, Self-injection threshold in self-guided laser wakefield accelerators, Phys. Rev. Accel. Beams **15**, 011302 (2012).

[10] Y. Glinec, J. Faure, A. Guemnie-Tafo, V. Malka, H. Monard, J. P. Larbre, V. De Waele, J. L. Marignier, and M. Mostafavi, Absolute calibration for a broad range single shot electron spectrometer, Rev. Sci. Instrum. **77**, 103301 (2006).

[11] A. Buck, K. Zeil, A. Popp, K. Schmid, A. Jochmann, S. D. Kraft, B. Hidding, T. Kudyakov, C. M. S. Sears, L. Veisz, S. Karsch, J. Pawelke, R. Sauerbrey, T. Cowan, F. Krausz, and U. Schramm, Absolute charge calibration of scintillating screens for relativistic electron detection, Rev. Sci. Instrum. **81**, 033301 (2010).

[12] T. Auguste, P. Monot, L.-A. Lompré, G. Mainfray, and C. Manus, Defocusing effects of a picosecond terawatt laser pulse in an underdense plasma, Opt. Commun. **89**, 145 (1992).

[13] P. Gibbon, *Short Pulse Laser Interactions with Matter, An Introduction* (Imperial College Press, London, 2005).

[14] P. Mora and J. Thomas M. Antonsen, Kinetic modeling of intense, short laser pulses propagating in tenuous plasmas, Phys. Plasmas **4**, 217 (1997).

[15] S. Semushin and V. Malka, High density gas jet nozzle design for laser target production, Rev. Sci. Instrum. **72**, 2961 (2001).

[16] C. Nordling and J. Österman, *Physics Handbook*, 7th ed. (Studentlitteratur, Lund, 2004).

[17] K. Schmid and L. Veisz, Supersonic gas jets for laser-plasma experiments, Rev. Sci. Instrum. **83**, 053304 (2012).

[18] G. R. Plateau, N. H. Matlis, C. G. R. Geddes, A. J. Gonsalves, S. Shiraishi, C. Lin, R. A. van Mourik, and W. P. Leemans, Wavefront-sensor-based electron density measurements for laser-plasma accelerators, Rev. Sci. Instrum. **81**, 033108 (2010).

[19] S. Corde, C. Thaury, A. Lifschitz, G. Lambert, K. Ta Phuoc, X. Davoine, R. Lehe, D. Douillet, A. Rousse, and V. Malka, Observation of longitudinal and transverse self-injections in laser-plasma accelerators, Nat. Commun. **4**, 1501 (2013).

Paper II

Self-Injection Threshold in Self-Guided Laser Wakefield Accelerators

S. P. D. Mangles, G. Genoud, M. S. Bloom, M. Burza, Z. Najmudin, A. Persson, K. Svensson, A. G. R. Thomas, & C.-G. Wahlström.

Phys. Rev. ST Accel. Beams **15**, 011302 (2012).

PHYSICAL REVIEW SPECIAL TOPICS - ACCELERATORS AND BEAMS **15**, 011302 (2012)

Self-injection threshold in self-guided laser wakefield accelerators

S. P. D. Mangles,[1] G. Genoud,[2] M. S. Bloom,[1] M. Burza,[2] Z. Najmudin,[1]
A. Persson,[2] K. Svensson,[2] A. G. R. Thomas,[3] and C.-G. Wahlström[2]
[1]*The Blackett Laboratory, Imperial College London, SW7 2AZ, United Kingdom*
[2]*Department of Physics, Lund University, P.O. Box 118, S-22100 Lund, Sweden*
[3]*Center for Ultrafast Optical Science, University of Michigan, Ann Arbor, Michigan 48109, USA*
(Received 7 January 2011; published 19 January 2012)

A laser pulse traveling through a plasma can excite large amplitude plasma waves that can be used to accelerate relativistic electron beams in a very short distance—a technique called laser wakefield acceleration. Many wakefield acceleration experiments rely on the process of wave breaking, or self-injection, to inject electrons into the wave, while other injection techniques rely on operation without self-injection. We present an experimental study into the parameters, including the pulse energy, focal spot quality, and pulse power, that determine whether or not a wakefield accelerator will self-inject. By taking into account the processes of self-focusing and pulse compression we are able to extend a previously described theoretical model, where the minimum bubble size $k_p r_b$ required for trapping is not constant but varies slowly with density and find excellent agreement with this model.

DOI: 10.1103/PhysRevSTAB.15.011302 PACS numbers: 52.38.Kd, 41.75.Jv, 52.35.Mw

Laser wakefield acceleration, where an intense laser pulse drives a plasma wave with a relativistic phase velocity, is a promising technique for the development of compact, or ''tabletop,'' particle accelerators and radiation sources. Plasma waves driven in moderate density plasmas can support electric fields over a thousand times stronger than those in conventional accelerators. Laser driven plasma waves have demonstrated electron acceleration to $\simeq$ 1 GeV in distances $\simeq$ 1 cm [1–3]. These compact particle accelerators have significant potential as bright x-ray sources [4–6] offering peak brightness comparable to 3rd generation synchrotron sources in x-ray flashes on the order of just 10 fs.

At the heart of the laser wakefield acceleration concept is the fact that electron plasma waves with relativistic phase velocities are driven to very large amplitudes, where they become highly nonlinear. If the plasma wave is driven beyond a threshold amplitude, the wave breaks. When the wave is driven far beyond the wave breaking threshold, the wave structure is destroyed and large amounts of charge can be accelerated to high energy but with a broad energy spread [7]. With appropriately shaped laser pulses this normally catastrophic process of wave breaking can be tamed to produce high quality beams of electrons. This is because close to the wave breaking threshold the nature of wave breaking changes—some electrons from the background plasma can become trapped in the wave without destroying the wave structure, a process called self-injection.

The highly nonlinear broken wave regime [8] is used in many experiments to produce quasimonoenergetic electron beams [9–11]. In such experiments a threshold plasma density is commonly observed, below which no electron beams are produced. Because of the inverse scaling of the electron beam energy with plasma density, the highest energy beams achievable with a given laser system are achieved just above the threshold, and it is well known that many of the beam parameters including the spectrum and stability are also optimized just above the threshold density [12,13]. It is also well known that to achieve self-injection at lower densities higher power lasers are required—although the exact scaling of the threshold with laser power is not well known. A number of techniques to improve the electron beam parameters including stability and total charge have recently been demonstrated by using alternative injection schemes [14–18]. Crucially these schemes all rely on operating the laser wakefield accelerator (LWFA) below the self-injection threshold. A number of recent purely theoretical papers have addressed the dynamics of wave breaking or self-injection [19–22]. Clearly a good understanding of the self-injection threshold is important for the development of laser wakefield accelerators. We report here on a series of experiments which identify the key laser and plasma parameters needed to predict the density threshold and we develop a model capable of predicting the self-injection threshold density for a given set of experimental parameters.

In LWFA experiments the laser pulse self-focuses due to the transverse nonlinear refractive index gradient of the plasma [23,24] and the spot size decreases towards a matched spot size. This matched spot size occurs when the ponderomotive force of the laser balances the space charge force of the plasma bubble formed. In situations

where there is no loss of energy during self-focusing, nor any change in the pulse duration, the final matched spot size, and hence the final intensity, is simply a function of $\alpha P/P_c$. P is the laser power; α is the fraction of laser energy within the full width at half maximum intensity of the focal spot—important because energy in the wings of the spot are not self-focused by the plasma wave and so do not contribute; P_c is the laser power where relativistic self-focusing dominates over diffraction, $P_c = (8\pi\epsilon_0 m_e^2 c^5/e^2)(n_c/n_e) \simeq 17 n_c/n_e$ GW (where n_e is the background plasma electron density and n_c is the critical density for propagation of the laser in the plasma). We might therefore expect that the self-injection threshold would occur at a fixed value of $\alpha P/P_c$ [25]. However, it is also known that the longitudinal nonlinear refractive index gradient also has a significant effect on the pulse properties [26,27] and we expect this to have an affect on the self-injection threshold.

The experiment was carried out using the multi-TW laser at the Lund Laser Centre. The laser delivered pulse energies of up to 0.7 J in pulses as short as 40 fs, corresponding to a peak power of 18 TW. An f/9 off-axis parabolic mirror was used to focus the pulse. A deformable mirror was used to optimize the focal spot, producing a spot size of 16 ± 1 μm FWHM. For a Gaussian focal spot the theoretical maximum fraction of energy within the FWHM is $\alpha = 1/2$, the best focus that we obtained had $\alpha = 0.48$. The focal plane was positioned onto the front edge of a supersonic helium gas jet with an approximately flat top profile of length 1.8 ± 0.1 mm.

To investigate the self-injection threshold, we studied the effect of the plasma density n_e, the total laser energy E, the focal spot quality α, and the pulse duration τ on the amount of charge in the electron beam. We chose to use the total charge in the electron beam as the diagnostic of self-injection as it provides a clear unambiguous signal of an electron beam.

The charge was measured using an electron beam profile monitor, consisting of a Lanex screen placed on the back surface of a wedge (which was used to collect the transmitted laser light). The wedge was 1 cm thick and made of glass and therefore prevented electrons below approximately 4 MeV reaching the Lanex. The Lanex screen was imaged onto a 12 bit CCD camera. To reduce the amount of background light from the interaction, a narrow band interference filter matched to the peak emission of the Lanex screen was placed in front of the camera. In addition, the camera was triggered several microseconds after the interaction but within the lifetime of the Lanex fluorescence. The Lanex screen was calibrated using the absolute efficiency data, absolute response of the CCD camera, and the details of the imaging system [28]. A beam profile monitor was used in preference to an electron spectrometer due to the fact that it has a higher sensitivity (i.e. the signal produced by a low charge beam dispersed inside a spectrometer will drop below the background level, whereas the same low charge beam will produce a bright image on the profile monitor). Also close to the threshold we do not expect the electrons to have particularly high energy (i.e. injection could be occurring but the electron beam energy could be outside the range of the electron spectrometer).

The gas jet could produce electron densities up to $n_e = 5 \times 10^{19}$ cm^{-3}. The laser pulse energy was varied by altering the energy pumping the final laser amplifier. We used the deformable mirror to reduce α by adding varying amounts of spherical aberration. Spherical aberration has the effect of decreasing α without introducing asymmetry to the focal spot and without significantly affecting its size. Degrading the focal spot symmetrically was desirable as asymmetric pulses can drive asymmetric wakes which can have a strong effect on the dynamics of self-injection [29]. The pulse duration was altered by changing the separation of the gratings in the compressor. Changing the grating separation introduced both a chirp to the pulse spectrum and a skew to the pulse envelope. To take this into account, we investigated both positive and negative chirps.

Figure 1 shows the effect of varying the laser pulse energy within the focal spot on the self-injection threshold. Keeping the total laser energy constant and degrading the focal spot (i.e. lowering α) moves the threshold to higher plasma densities. We also observe an increase in the threshold density when we keep α constant and reduce the laser pulse energy. In fact, we find that the two effects are equivalent, i.e., that the threshold shifts according to the product αE. This demonstrates that it is only the energy within the FWHM of the focal spot that contributes to driving the plasma wave. This emphasizes the importance

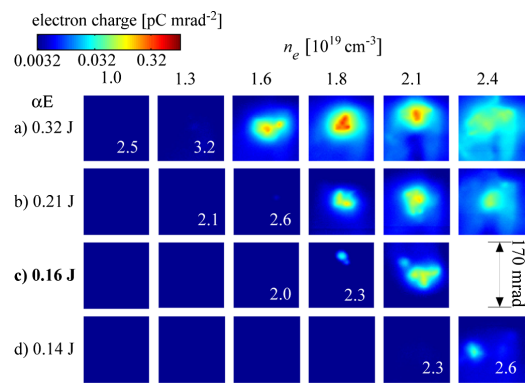

FIG. 1. Electron beam profiles for various plasma densities for different values of the amount of laser energy within the FWHM of the focal spot. (a), (b), and (d) kept the total laser energy constant but varied α whereas (c) reduced the laser energy. Each panel is an average of five shots and is displayed on a logarithmic color scale.

of laser focal spot quality in LWFA experiments [30], which are often performed with $\alpha \approx 0.3$ [2,25]. Improving the focal spot could therefore result in a significant increase in the electron beam energy achievable from a given laser system.

The observed variation of the threshold with αE is as expected for one based on $\alpha P/P_c$ but this can only be confirmed by the behavior of the threshold when we vary the laser pulse duration, keeping αE constant. When we do this we see markedly different behavior.

We kept the plasma density constant, at a value just above the threshold density for the optimally compressed pulse. At this density ($n_e = 1.6 \times 10^{19}$ cm^{-3}), with full laser energy ($\alpha E = 0.32$ J) and the fully compressed pulse ($\tau = 42$ fs) we observed a bright electron beam. When we reduced either the plasma density or the pulse energy by a small factor (20%–25%) this beam disappeared, i.e., we dropped below the threshold. Even after increasing the pulse duration by a factor of 2, electrons are clearly still injected, as shown in Fig. 2. This is true regardless of the chirp of the laser pulse, however we do see an enhancement of the total charge using positively chirped (red at the front) pulses as reported previously [31]. These pulses have a fast rising edge indicating that the precise shape of the pulse may play a role in the total charge injected. The direction of chirp of the pulse may also affect the rate at which pulse compression occurs [32]. For both directions of chirp the fact that the threshold behavior is so significantly different to that observed when varying αE suggests that pulse compression is indeed playing an important role in determining whether or not the accelerator reaches wave breaking.

In Fig. 3 we plot the total charge observed on the profile monitor screen for the various data sets. Figure 3(a) shows the total charge, plotted against the pulse power normalized to the critical power for self-focusing, for the data sets where we varied the plasma density and the energy within the focal spot (either by varying the spot quality α or total pulse energy E). The charge rises rapidly with increasing $\alpha P/P_c$ until eventually reaching a plateau at

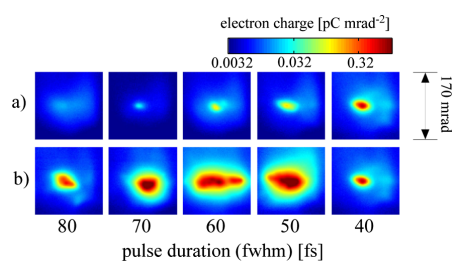

FIG. 2. Electron beam profiles for various pulse durations at fixed αE and at a plasma density just above the threshold density for injection for 40 fs pulses. The pulse duration was varied by changing the compressor grating separation which introduces a chirp to the pulse: (a) negative chirp; (b) positive chirp.

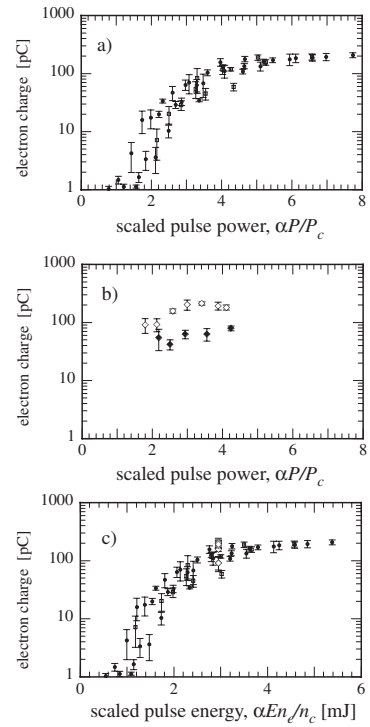

FIG. 3. (a) Electron charge (>4 MeV) versus $\alpha P/P_c$ keeping the pulse duration constant but varying focal spot quality and plasma density (closed circles) or total pulse energy and plasma density (open squares) but keeping pulse duration constant. (b) Electron charge versus $\alpha P/P_c$ varying pulse duration while keeping plasma density and energy in focal spot constant. (c) Data from (a) and (b) plotted versus $\alpha E n_e/n_c$. Each data point is an average of five shots and the error bars represent 1 standard deviation.

around $\alpha P/P_c \approx 4$. There is an increase in the total charge of a factor of 10 between $\alpha P/P_c = 2$ and $\alpha P/P_c = 4$ for both sets of data. The fact that both data sets lie on the same curve confirms the fact that it is the energy within the focal spot which determines the wakefield behavior. This supports the hypothesis that energy in the wings of the focal spot is not coupled into the accelerator: energy in the wings of the spot is effectively wasted.

Figure 3(b) shows the charge plotted against $\alpha P/P_c$ for a data set where we kept the plasma density and αE constant but varied the pulse duration (by introducing either positive or negative chirp). The markedly different behavior is once again apparent: rather than the rapid increase of charge between $\alpha P/P_c = 2$ and $\alpha P/P_c = 4$ the charge is approximately constant for each data set.

Figure 3(c) plots all of the data sets (varying α, E, and τ) against a scaled pulse energy $\alpha E n_e/n_c$ rather than the

scaled pulse power. The fact that the pulse duration data set now fits closely with the αE data sets confirms that pulse compression is playing an important role in determining whether or not the wakefield accelerator reaches self-injection.

A recent paper that examined the trajectory of electrons inside the plasma bubble [21] predicts that self-trapping will occur when the radius of the plasma bubble (r_b) is larger than a certain value given by

$$k_p r_b > 2\sqrt{\ln(2\gamma_p^2) - 1}, \tag{1}$$

where $\gamma_p \approx \sqrt{n_c/(3n_e)}$ [33] is the Lorentz factor associated with the phase velocity of the bubble. When this condition is met, an electron starting at rest a distance r_b from the laser axis and following an elliptical trajectory in the bubble fields (thus defining the edge of the bubble) will be accelerated by the bubble fields up to $\gamma_p m_e c^2$ by the time it reaches the back of the bubble. A key feature of this model is that the normalized bubble size required for self-injection $k_p r_b$ is not constant with density. As Eq. (1) depends only on the plasma density and bubble size, we can determine the minimum pulse properties required to reach the threshold by noting that the radius of the bubble is related to the pulse energy and duration through [34]

$$k_p r_b = 2\sqrt{2}\left(\frac{\alpha E}{\tau P_c}\right)^{1/6}. \tag{2}$$

Combining Eqs. (1) and (2) yields an expression for the minimum pulse energy required to reach self-injection:

$$\alpha E > \frac{\pi \epsilon_0 m_e^2 c^5}{e^2}\left[\ln\left(\frac{2n_c}{3n_e}\right) - 1\right]^3 \frac{n_c}{n_e}\tau(l), \tag{3}$$

where $\tau(l)$ is the pulse duration after a propagation length l. A simple model for the rate of pulse compression was put forward in Ref. [27] based on the fact that the front of the pulse travels at the group velocity of the laser in the plasma and the back of the pulse travels in vacuum, this produces $\tau(l) \approx \tau_0 - (n_e l)/(2cn_c)$. The interaction length will be limited by either the length of the plasma target or the pump depletion length $l_{\mathrm{pd}} \simeq c\tau_0 n_c/n_e$ [34]. For the depletion limited case Eq. (3) reduces to

$$\frac{\alpha P}{P_c} > \frac{1}{16}\left[\ln\left(\frac{2n_c}{3n_e}\right) - 1\right]^3. \tag{4}$$

The threshold density for self-injection for a given experiment can be calculated from (3) and (4). This model requires knowledge of the initial pulse energy, pulse duration, and the length of the plasma to predict the threshold. As Eqs. (3) and (4) are transcendental, the density threshold for a given laser system must be found numerically.

A previous study showed that, at low density, the threshold is approximately $\alpha P/P_c > 3$ [25], this can be rearranged into a similar form to Eq. (3):

$$\alpha E > 3\frac{\pi \epsilon_0 m_e^2 c^5}{e^2}\frac{n_c}{n_e}\tau_0. \tag{5}$$

We can then use Eq. (5) to predict the density threshold for specific experimental conditions. To use this model only the initial pulse power is required to calculate the threshold density. Combining $\alpha P/P_c > 3$ and Eq. (2) reveals that this threshold model is also equivalent to stating that the minimum bubble size for self-trapping is constant with density ($k_p r_b > 3.4$) in contrast to Eq. (1).

In Fig. 4 we plot the variation of the observed threshold density with laser energy (αE). We have defined the experimentally observed threshold density as lying in the region between the highest density where we observe no electron beam and the lowest density where we clearly observe a beam. We also show the theoretical threshold density based on Eqs. (3) and (4), and the predicted threshold based on Eq. (5). Its agreement with the experimental data indicates that our model accurately predicts the self-injection threshold, confirming that the threshold is reached because the laser pulse undergoes intensity amplification due to a combination of pulse compression and self-focusing.

Our measurements of the threshold density for self-injection have been made with only moderate laser pulse energies ~1 J. Many laser wakefield experiments are now being performed with pulse energies ~10 J and the validity of this model at these higher laser energies can be verified by applying it to previously published data. We restrict ourselves to data obtained from experiments with gas jets as guiding structures can affect the trapping threshold by changing the way pulse evolution occurs [30] or by introducing additional effects such as ionization injection [35]. To calculate the density threshold for a particular set of experimental parameters, the following information is required: the laser energy E, the focal spot quality α, the initial pulse duration τ, and the maximum plasma length l. Equations (3) and (4) or Eq. (5) can then be used to calculate the expected density threshold for the two models. Kneip *et al.* [2], using a 10 J, 45 fs, 800 nm laser pulse

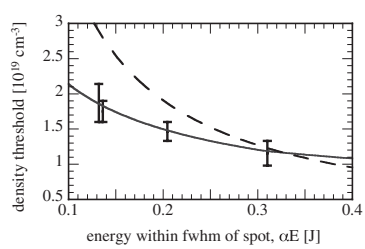

FIG. 4. Observed density threshold as a function of laser energy (αE) for our experiment. The solid curve represents our threshold model. The dashed curve represents a threshold based on $\alpha P/P_c > 3$.

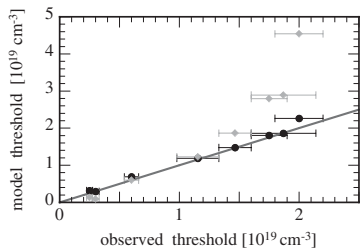

FIG. 5. Plot of reported density threshold, n_t, versus predicted density threshold, n_{model}, for this and other published experiments [2,11,25,36]. Circles show the predictions of our model, diamonds show the threshold based on $\alpha P/P_c > 3$. The line indicates $n_t = n_{\mathrm{model}}$.

with $\alpha = 0.3$, observed a threshold density of $n_e = 2$–3×10^{18} cm^{-3} in an 8.5 mm long plasma; our model predicts that the threshold density for self-injection should occur at $n_e \approx 3 \times 10^{18}$ cm^{-3}. Froula *et al.* [25], using a 60 fs, 800 nm laser with $\alpha E \approx 6$ J, observed a threshold density of $n_e \approx 3 \times 10^{18}$ cm^{-3} in an 8.0 mm plasma; our model also predicts $n_e \approx 3 \times 10^{18}$ cm^{-3}. Schmid *et al.* [36] using an 8 fs, 840 nm laser with $\alpha E \approx 15$ mJ, observed electron beams at a density of $n_e \approx 2 \times 10^{19}$ cm^{-3} in a plasma 300 μm long; our model predicts a threshold of $n_e \approx 2.2 \times 10^{19}$ cm^{-3}. Faure *et al.* [11], using a 33 fs, 820 mn laser, reported a dramatic decrease in the number of accelerated electrons at $n_e \approx 6 \times 10^{18}$ cm^{-3} in a 3 mm gas jet with $\alpha E \approx 0.5$ J. Our model predicts a threshold density of $n_e \approx 7 \times 10^{18}$ cm^{-3}.

These additional data points, together with those from this experiment, are presented in Fig. 5. Because of the fact that our model does not depend on a single experimental parameter, we plot the experimentally observed density threshold n_t for each experiment on the x axis and against the calculated threshold n_{model} obtained using either Eqs. (3) and (4) or Eq. (5). Figure 5 shows that our model is in good agreement with experiments over nearly 3 orders of magnitude in laser energy, whereas the threshold based on Eq. (5) matches the observed threshold over only a very limited range of pulse energies: it overestimates the threshold density for low energy laser systems and, on the other hand, would significantly underestimate the threshold for very high energy laser systems.

We note that simulations by Yi *et al.* [22] show that, at very low density and an initial laser spot size less than the matched spot size, diffraction of the laser pulse leads to a lengthening of the bubble which plays a role in determining self-injection. In that work they see self-injection with a 200 J, 150 fs laser pulse at a density of $n_e = 10^{17}$ cm^{-3}. Our model predicts that the threshold would be $n_e \approx 4 \times 10^{17}$ cm^{-3}—actually in reasonable agreement with [22], however our model relies on pulse compression occurring over ≈ 10 cm whereas Yi *et al.* show that in their simulations injection occurs after just 5 mm. This indicates that our model is only valid for initial laser spot sizes *greater than or equal to* the matched spot size (as is the case for the experiments shown in Fig. 5).

We now use our model to predict the self-injection threshold density for lasers currently under construction. For example, our model predicts that a 10 PW laser (300 J in 30 fs, $\lambda = 0.9$ μm, such as the Vulcan 10 PW laser at the Rutherford Appleton Lab, or the ELI Beamlines facility in the Czech Republic) could produce electron injection at as low as $n_e \approx 2 \times 10^{17}$ cm^{-3} (assuming $\alpha = 0.5$) in a 6 cm long plasma. For a 1 PW laser (40 J in 40 fs, $\lambda = 0.8$ μm, such as the Berkley Lab Laser Accelerator, BELLA), our model predicts that self-injection will occur at a density of $n_e \approx 9 \times 10^{17}$ cm^{-3} in 2.4 cm.

The lower the threshold density of a wakefield accelerator, the higher the maximum beam energy. However, for self-injecting accelerators there must be acceleration after injection, requiring operation at densities slightly above this threshold so that injection occurs earlier in the interaction.

In summary, we have measured the effect of various laser parameters on the self-injection threshold in laser wakefield accelerators. The simple model we use relies on the fact that pulse compression and self-focusing occur and that only the energy within the FWHM of the focal spot contributes towards driving the plasma wave. We find that in cases where the interaction is limited by pump depletion, the threshold can be expressed as a ratio of P/P_c, but this ratio is not the same for all laser systems: for higher power lasers the threshold occurs at a higher value of P/P_c than for lower power lasers. When the plasma length is shorter than the pump depletion length, we find that the length of the plasma is an important parameter in determining the injection threshold.

ACKNOWLEDGMENTS

This work was supported by the Royal Society, EPSRC (Grant No. EP/I014462/1); the Swedish Research Council (including the Linné grant to the LLC); the Knut and Alice Wallenberg Foundation; the EU Access to Research Infrastructures activity, FP7 Grant Agreement No 228334: Laserlab Europe, the Lund University X-ray Centre (LUXC); and the Marie Curie Early Stage Training Site MAXLAS (Contract No. MEST-CT-2005-020356).

[1] W. P. Leemans *et al.*, Nature Phys. **2**, 696 (2006).
[2] S. Kneip *et al.*, Phys. Rev. Lett. **103**, 035002 (2009).
[3] C. E. Clayton *et al.*, Phys. Rev. Lett. **105**, 105003 (2010).
[4] A. Rousse *et al.*, Phys. Rev. Lett. **93**, 135005 (2004).
[5] S. Kneip *et al.*, Nature Phys. **6**, 980 (2010).
[6] M. Fuchs *et al.*, Nature Phys. **5**, 826 (2009).
[7] A. Modena *et al.*, Nature (London) **377**, 606 (1995).

[8] A. Pukhov and J. Meyer-ter Vehn, Appl. Phys. B **74**, 355 (2002).
[9] S. P. D. Mangles *et al.*, Nature (London) **431**, 535 (2004).
[10] C. G. R. Geddes *et al.*, Nature (London) **431**, 538 (2004).
[11] J. Faure *et al.*, Nature (London) **431**, 541 (2004).
[12] V. Malka *et al.*, Phys. Plasmas **12**, 056702 (2005).
[13] S. P. D. Mangles *et al.*, Phys. Plasmas **14**, 056702 (2007).
[14] J. Faure *et al.*, Nature (London) **444**, 737 (2006).
[15] C. McGuffey *et al.*, Phys. Rev. Lett. **104**, 025004 (2010).
[16] A. Pak *et al.*, Phys. Rev. Lett. **104**, 025003 (2010).
[17] C. G. R. Geddes *et al.*, Phys. Rev. Lett. **100**, 215004 (2008).
[18] K. Schmid *et al.*, Phys. Rev. ST Accel. Beams **13**, 091301 (2010).
[19] S. Kalmykov *et al.*, Phys. Rev. Lett. **103**, 135004 (2009).
[20] I. Kostyukov *et al.*, Phys. Rev. Lett. **103**, 175003 (2009).
[21] A. G. R. Thomas, Phys. Plasmas **17**, 056708 (2010).
[22] S. A. Yi, V. Khudik, S. Kalmykov, and G. Shvets, Plasma Phys. Controlled Fusion **53**, 014012 (2011).
[23] A. G. R. Thomas *et al.*, Phys. Rev. Lett. **98**, 095004 (2007).
[24] J. E. Ralph *et al.*, Phys. Rev. Lett. **102**, 175003 (2009).
[25] D. H. Froula *et al.*, Phys. Rev. Lett. **103**, 215006 (2009).
[26] J. Faure *et al.*, Phys. Rev. Lett. **95**, 205003 (2005).
[27] J. Schreiber *et al.*, Phys. Rev. Lett. **105**, 235003 (2010).
[28] Y. Glinec *et al.*, Rev. Sci. Instrum. **77**, 103301 (2006).
[29] S. P. D. Mangles *et al.*, Appl. Phys. Lett. **95**, 181106 (2009).
[30] T. P. A. Ibbotson *et al.*, Phys. Rev. ST Accel. Beams **13**, 031301 (2010).
[31] W. P. Leemans *et al.*, Phys. Rev. Lett. **89**, 174802 (2002).
[32] E. S. Dodd and D. Umstadter, Phys. Plasmas **8**, 3531 (2001).
[33] C. D. Decker *et al.*, Phys. Plasmas **3**, 2047 (1996).
[34] W. Lu *et al.*, Phys. Rev. ST Accel. Beams **10**, 061301 (2007).
[35] T. P. Rowlands-Rees *et al.*, Phys. Rev. Lett. **100**, 105005 (2008).
[36] K. Schmid *et al.*, Phys. Rev. Lett. **102**, 124801 (2009).

Paper III

Increasing Energy Coupling into Plasma Waves by Tailoring the Laser Radial Focal Spot Distribution in a Laser Wakefield Accelerator

G. Genoud, M. S. Bloom, J. Vieira, M. Burza, Z. Najmudin, A. Persson, L. O. Silva, K. Svensson, C.-G. Wahlström, & S. P. D. Mangles.

Phys. Plasmas **20**, 064501 (2013).

PHYSICS OF PLASMAS **20**, 064501 (2013)

Increasing energy coupling into plasma waves by tailoring the laser radial focal spot distribution in a laser wakefield accelerator

G. Genoud,[1] M. S. Bloom,[2] J. Vieira,[3] M. Burza,[1] Z. Najmudin,[2] A. Persson,[1] L. O. Silva,[3] K. Svensson,[1] C.-G. Wahlström,[1] and S. P. D. Mangles[2,a)]
[1]*Department of Physics, Lund University, P.O. Box 118, S-22100 Lund, Sweden*
[2]*John Adams Institute for Accelerator Science, Imperial College London, London SW7 2AZ, United Kingdom*
[3]*GoLP/Instituto de Plasmas e Fusão Nuclear-Laboratório Associado, Instituto Superior Técnico, 1049-001 Lisboa, Portugal*

(Received 14 February 2013; accepted 3 May 2013; published online 10 June 2013)

By controlling the focal spot quality with a deformable mirror, we are able to show that increasing the fraction of pulse energy contained within the central part of the focal spot, while keeping the total energy and central spot size constant, significantly increases the amount of energy transferred to the wakefield: Our measurements show that the laser loses significantly more laser energy and undergoes greater redshifting and that more charge is produced in the accelerated beam. Three dimensional particle in cell simulations performed with accurate representations of the measured focal spot intensity distribution confirm that energy in the wings of the focal spot is effectively wasted. Even though self-focusing occurs, energy in the wings of the focal spot distribution is not coupled into the wakefield, emphasising the vital importance of high quality focal spot profiles in experiments. © *2013 AIP Publishing LLC*. [http://dx.doi.org/10.1063/1.4810795]

Laser wakefield accelerators have attracted increased attention in recent years as potential compact particle accelerators and radiation sources.[1–5] In a laser wakefield accelerator, the accelerating structure is an electron plasma wave oscillating in the wake of an intense laser pulse. These plasma waves can have very strong accelerating forces, as much as 1000 times greater than can be achieved in conventional radio-frequency accelerators.

In laser wakefield accelerators, higher energy electron beams can be produced by operating at lower plasma densities with higher power lasers:[6] Lower densities are needed to increase the time that relativistic electrons can stay in-phase with the plasma wave; higher power lasers are needed to drive high amplitude plasma waves at these lower densities. In the so-called "self-guided, self-injection" regime early experiments with 10–20 TW laser pulses produced electron beams at energies $\simeq 100\,\mathrm{MeV}$ at plasma densities of $n_e \simeq 10^{19}\,\mathrm{cm}^{-3}$ in acceleration lengths $\simeq 1\,\mathrm{mm}$.[1–3] Higher power $\simeq 200\,\mathrm{TW}$ lasers are now capable of producing $\simeq 1\,\mathrm{GeV}$ beams at plasma densities of $n_e \simeq 4 \times 10^{18}\,\mathrm{cm}^{-3}$ in $\simeq 10\,\mathrm{mm}$.[7,8]

Although laser power is a key factor in determining the minimum density at which a sufficiently large amplitude plasma wave can be driven,[6] this cannot be done by arbitrarily reducing the pulse duration due to the relationship between pulse duration and pump depletion.[9] As a result, increasing the electron beam energy produced by laser wakefield accelerators has relied on increasing the energy of the laser pulse. Unfortunately, this has often been achieved at the expense of focal spot quality.

The effects of realistic focal spots have been studied numerically,[10] and it has been observed that higher quality focal spots can lower the threshold for injection.[6,11] Asymmetries present in the laser's focal spot are also known to deteriorate the electron beam properties (but promote the production of x-rays).[12] This article examines the deleterious effects that a poor quality focal spot can have on laser wakefield accelerator performance in an experiment, where we deliberately control the focal spot quality. Our study demonstrates that energy contained in the wings of the focal spot is effectively wasted because it is not coupled into the plasma wave, i.e., the process of self-focusing does not help to "collect" this pulse energy.

The experiment was carried out using the multi-TW laser at the Lund Laser Centre. The laser delivered pulse energies of up to 0.7 J in pulses as short as 42 fs, corresponding to a peak power of 18 TW. An *f*/9 off-axis parabolic mirror was used to focus the pulse. A deformable mirror was used to optimise the focal spot, producing a spot size of $16 \pm 1\,\mu\mathrm{m}$ fwhm. For a gaussian focal spot, the theoretical maximum fraction of energy within the fwhm is $\alpha = 1/2$; we could achieve up to $\alpha = 0.47$. The focal plane was positioned onto the front edge of a supersonic helium gas jet with an approximately flat-top profile of length $1.8 \pm 0.1\,\mathrm{mm}$. We were able to control the quality of the laser focus using the deformable mirror. By deliberately adding spherical aberration to the wavefront, we could vary α while keeping the spot size and total energy constant, thereby mimicking the focal spot quality of high power laser systems. Two experimental radial profiles of such focal spots are shown in Fig. 6(a), for $\alpha = 0.47$ and $\alpha = 0.20$. One clearly sees the effect of decreasing α.

To diagnose the effect of α on the laser wakefield accelerator, we used a number of simultaneous diagnostics. We investigated the quality of self-guiding by imaging the laser beam as it leaves the plasma. We investigated the production of plasma waves by measuring the transmitted energy and spectrum of the laser pulse, and we investigated the trapping

a)Electronic mail: stuart.mangles@imperial.ac.uk

of charge in the wakefield using an electron beam profile monitor. The experimental set-up is shown in Fig. 1.

Fig. 2 shows how the exit mode of the laser varies with plasma density for two different values of α. As we increase the plasma density, the exit mode size decreases due to self-guiding.[13] The energy contained in the exit mode also decreases with increasing plasma density, as more energy is deposited into the plasma wake. Perhaps the most important feature of Fig. 2 is that as the plasma density is increased, there is clearly less energy in the exit mode for the high quality focal spot.

By comparing the initial energy within the fwhm of the laser focus (αE) to the final energy contained in the fwhm of the exit modes, we can quantify the energy transferred from the laser pulse to the wakefield. The results of this analysis are shown in Fig. 3. For pulses with the same total energy, the higher the quality of focal spot the greater the amount of energy that is coupled into the wakefield. The poorest quality focal spot ($\alpha = 0.20$, containing 140 mJ within the fwhm) transfers 100 mJ or 70%. The highest quality focal spot ($\alpha = 0.47$, containing 330 mJ within the fwhm) transfers 320 mJ or more than 90%. The increased efficiency of energy transfer for high α occurs because the plasma wave amplitude is higher for longer due to the increased rates of pulse evolution.

If the laser energy exiting the plasma is reduced because the laser pulse is driving a plasma wave, then this will be apparent in the transmitted laser spectrum.[14] The longitudinal refractive index gradient of a laser driven plasma wave is such that the front of the laser pulse becomes red-shifted[9,15] due to self-phase modulation and photon deceleration. In a linear plasma wave driven by a pulse of duration $c\tau \approx \lambda_p/2$, the back of the pulse sits in a symmetric blue-shifting refractive index gradient. However, in the blow-out regime, the back of the laser pulse travels inside the bubble, where there is a very low electron density, so the back of the pulse will not experience significant blue-shifting. A signature of bubble formation is therefore asymmetric broadening of the laser spectrum.[9]

Our measurements of the transmitted laser spectrum do indeed show that the most significant effect is a shift towards the red, and that this red-shifting is significantly enhanced

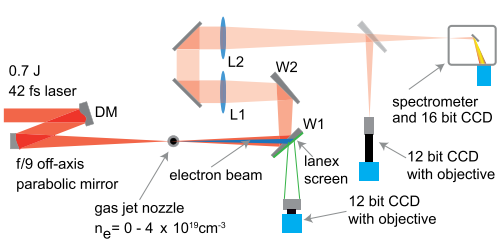

FIG. 1. Schematic of experimental layout. The 0.7 J, 42 fs laser pulse is reflected from the deformable mirror (DM) and focused into a 2 mm supersonic helium gas jet. Glass wedges (W1 and W2) are used to attenuate the transmitted laser beam, a factor of $\simeq$100 before lenses (L1 and L2) are used to image the exit mode onto the diagnostics. A Kodak Lanex regular screen placed on the rear side of W1 acts as an electron beam profile screen, which also serves to measure the total charge in the beam for energies >4 MeV.

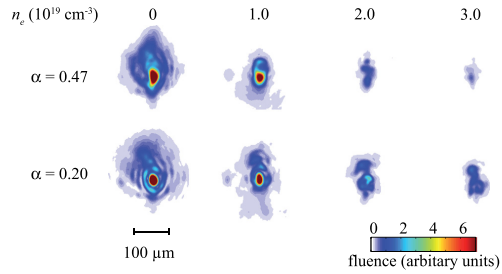

FIG. 2. Images of the laser mode at the exit of the plasma (2 mm from focus) as a function of plasma density for two different quality focal spots ($\alpha = 0.47$ and $\alpha = 0.20$). All the images are on the same colour table.

for higher α. To quantify the spectra, we define three quantities; the mean frequency and the red and blue limits of the spectrum. Frequencies below the red limit contain 15.2% of the total energy; frequencies above the blue limit contain only 15.2% of the total energy, thus delimiting the width of the spectrum. Fig. 4 shows how the spectrum varies as a function of plasma density for two values of α. Increasing the density increases the amount of spectral broadening, but the broadening is markedly asymmetric: the blue limit remains approximately constant, but the red limit becomes significantly larger, as expected for highly non-linear plasma waves. This asymmetry is significantly more pronounced for large α, e.g., at $n_e = 1.5 \times 10^{19}\,\mathrm{cm}^{-3}$ the red limit almost doubles from -6% for $\alpha = 0.20$ to -10% for $\alpha = 0.47$.

Larger amplitude wakes can trap and accelerate more charge, so further evidence that better quality focal spots drive higher amplitude plasma waves can be found by examining the total charge accelerated in the experiment, as measured using the beam profile monitor.

Fig. 5 shows the variation of total charge as a function of plasma density and α. At each density, the higher the value of α the more charge is accelerated. The charge increase for higher quality focal spots can be explained as being due to two effects. First, a pulse with a higher quality

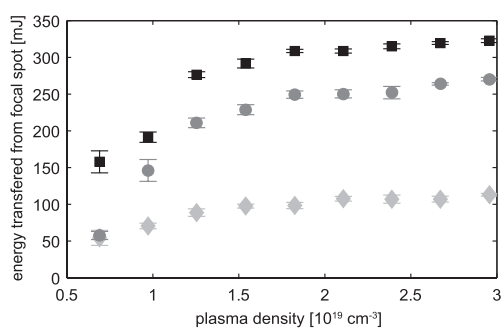

FIG. 3. Energy depleted from the central part of the focal spot (fwhm) of the laser pulse as a function of plasma density for different quality focal spots. Black squares: $\alpha = 0.47$ (330 mJ within the fwhm); Grey circles: $\alpha = 0.40$ (280 mJ within the fwhm); Light grey diamonds: $\alpha = 0.20$ (140 mJ within the fwhm). The total pulse energy was 700 mJ in all three cases. Each point is an average of five shots, error bars are the standard error.

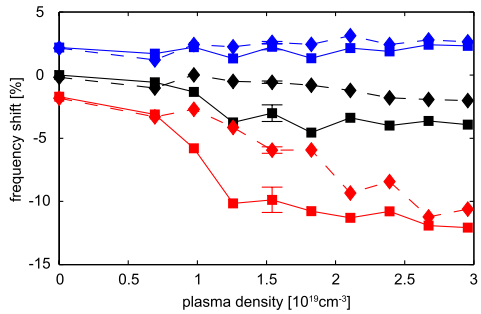

FIG. 4. Variation of the transmitted optical spectrum with focal spot quality as a function of plasma density. Diamonds: $\alpha = 0.20$; Squares: $\alpha = 0.47$ (black data points: central frequency; red data points: red limit of spectrum; blue data points: blue limit of the spectrum. Limits described in the text). Each point represents an average from at least five shots, the error bar shown represents a typical standard error. The frequency axis is expressed as the percentage difference from the vacuum laser central frequency, i.e., $100(\omega - \omega_0)/\omega_0$.

focal spot will reach the threshold for self-injection earlier in the interaction.[6] Earlier injection allows more charge to be trapped, if injection occurs continuously, while the wake amplitude is above the injection threshold. Second, larger α results in a larger maximum wake amplitude at a given density, which will be capable of trapping more charge. It is likely that both of these effects contribute to the observed behaviour in our experiment.

We have carried out a series of three dimensional particle-in-cell simulations with the Osiris 2.0 framework to further examine the effects of focal spot quality on the transmitted laser pulse and on the wakefield itself. To model the effect of focal spot quality, the radial profile of the laser pulse was initialised in the simulation using a sum of Laguerre-Gauss polynomials,[10] these are a natural choice to describe a cylindrically symmetric laser pulse (as is the case for the spherical aberration studied here). The radial pulse envelope was represented by the function $a(r) = \exp\left(-\frac{r^2}{w_0^2}\right)\sum_0^n a_n L_n\left(\frac{2r^2}{w_0^2}\right)$, where $a(r)$ is the

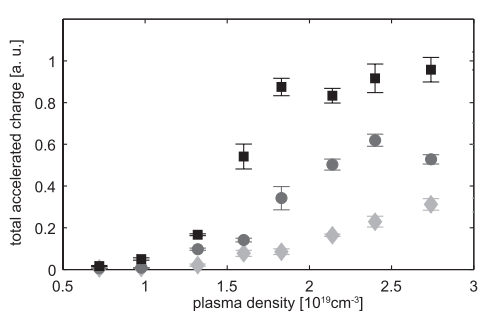

FIG. 5. Variation of the total accelerated charge with plasma density for different quality focal spots. Black squares: $\alpha = 0.47$ (330 mJ within the fwhm); Grey circles: $\alpha = 0.40$ (280 mJ within the fwhm); Light grey diamonds: $\alpha = 0.20$ (140 mJ within the fwhm). The total pulse energy was 700 mJ in all three cases. Each point is an average of at least five shots, error bars are the standard error.

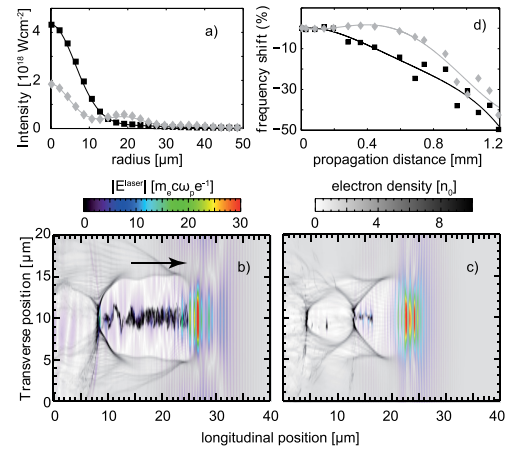

FIG. 6. (a) Radially averaged experimental focal spot intensity distributions (marks) and the Laguerre-Gauss polynomial representation used in the 3D simulations (solid lines). Black squares: $\alpha = 0.47$; Light grey diamonds: $\alpha = 0.20$. (b) Snapshots of the wakefield produced in 3D simulations at $n_e = 2 \times 10^{19}$ cm^{-3} after 1 mm propagation for $\alpha = 0.47$) and (c) $\alpha = 0.20$. The greyscale image shows the electron density on which is superimposed a colour image of the laser electric field amplitude. (d) Variation of laser spectrum as the laser propagates in the two simulations (solid lines are a polynomial fit of the data points).

normalised vector potential at radial coordinate r, a_n is the amplitude of each Laguerre-Gauss mode, w_0 is the beam waist, and L_n is the n^{th} Laguerre polynomial. To represent the radially averaged experiment focal spot profiles, it was only necessary to include the first four orders in the expansion. The measured focal spot intensity distribution and the representation used in the simulations are shown for $\alpha = 0.47$ and $\alpha = 0.20$ in Fig. 6(a).

In the simulations, the laser pulse field temporal envelope had a fhwm duration of 42 fs. The plasma density profile consisted of a 100 μm linear rise from vacuum up to a density of $n_e = 2 \times 10^{19}$ cm^{-3}, which remained constant for 1.85 mm before falling linearly to zero again over 100 μm, this closely represents the experimentally measured density profile. The simulation cell size was $0.105 \times 0.234 \times 0.234$ μm^3 with two particles per cell.

The simulations clearly show the dramatic effect, the quality of the focal spot has on a wakefield accelerator, as it can be observed in the snapshots shown in Figs. 6(b) and (c). The higher quality focal spot evolves more rapidly, achieving the conditions needed for self-injection after the laser has propagated approximately 240 μm, the poor quality spot run does not inject until the laser has propagated 840 μm. As a result of reaching the injection conditions earlier, significantly more charge is injected into the wake when the laser has a good quality focal spot, by more than a factor of three, the earlier injection also allows the electrons to reach higher energy.

Fig. 6(d) shows how the laser spectrum varies throughout the simulation. This is calculated from the k-spectrum of the laser pulse at various stages inside the plasma. We assume that, if the radiation were to exit the plasma at each measurement point, its mean frequency would correspond to

$\langle\omega\rangle = \langle k\rangle/c$. This analysis shows a very large amount of red shifting of the laser pulse. For example, a polynomial fit of the data points shows that the mean frequency shifts by approximately 20% for $\alpha = 0.47$ after 0.7 mm of propagation. For $\alpha = 0.20$, we see a shift of only $\approx$5% at the same point. The trend from the simulations is clearly similar to that observed in the experiment; however, the experiment never observes these very large red shifts. We believe that this is because the experimental measurement captures all of the laser light, including any of the pulse energy that does not contribute to wakefield excitation, whereas in the simulation radiation that is not guided has a significant diffraction angle and is able to leave the simulation box. This means that the experimental data are always dominated by a significant fraction of unshifted laser light. In addition, on some laser shots the red shift was so large that it was not captured by the CCD camera, which also contributes to the discrepancy between experiment and simulations. Nevertheless, the simulations and experiment are in good qualitative agreement—higher quality focal spots undergo more red-shifting than poorer quality ones, and this is due to the excitation of larger amplitude plasma waves.

In conclusion, by employing a suite of simultaneous diagnostics to measure various properties of the transmitted laser pulse as well as the total amount of trapped charge in the electron beam, we have been able to demonstrate that the quality of the focal spot is a crucial parameter in determining the performance of a laser wakefield accelerator. Lower quality laser focal spots have significant energy content in the wings of the focal distribution, and we show that this energy is effectively wasted, i.e., it is not captured by the process of self-focusing and is therefore not coupled in the plasma wave, only the energy contained inside the central spot is properly captured by the accelerator structure. For the same total pulse energy, lower quality focal spots therefore drive lower amplitude plasma waves. We therefore suggest that the quality of the laser focus should be considered as an equally important parameter to pulse duration and total pulse energy for laser wakefield accelerator systems.

Our demonstration that only the fraction of pulse energy contained within the central part of the focal spot is coupled into the plasma wave suggests that even greater coupling could possibly be achieved by tailoring the focal spot profile to have $\alpha \to 1$, by creating super-gaussian focal spot shapes. This could be achieved, for example, by using combination of deformable mirrors and phase plate masks, or operating in the near-field of a much tighter focus with an appropriate density ramp.

This work was supported by the Royal Society; EPSRC (Grant No. EP/I014462/1); the Swedish Research Council (including the Linné grant to the LLC); the Knut and Alice Wallenberg Foundation; the EU Access to Research Infrastructures activity, FP7 Grant Agreement No. 228334: Laserlab Europe, the Lund University X-ray Centre (LUXC); and the Marie Curie Early Stage Training Site MAXLAS (Contract No. MEST-CT-2005-020356).

[1]S. P. D. Mangles, C. D. Murphy, Z. Najmudin, A. G. R. Thomas, J. L. Collier, A. E. Dangor, E. J. Divall, P. S. Foster, J. G. Gallacher, C. J. Hooker, D. A. Jaroszynski, A. J. Langley, W. B. Mori, P. A. Norreys, F. S. Tsung, R. Viskup, B. R. Walton, and K. Krushelnick, Nature **431**, 535 (2004).
[2]C. G. R. Geddes, C. Toth, J. van Tilborg, E. Esarey, C. B. Schroeder, D. Bruhwiler, C. Nieter, J. Cary, and W. P. Leemans, Nature **431**, 538 (2004).
[3]J. Faure, Y. Glinec, A. Pukhov, S. Kiselev, S. Gordienko, E. Lefebvre, J.-P. Rousseau, F. Burgy, and V. Malka, Nature **431**, 541 (2004).
[4]A. Rousse, K. T. Phuoc, R. Shah, A. Pukhov, E. Lefebvre, V. Malka, S. Kiselev, F. Burgy, J.-P. Rousseau, D. Umstadter, and D. Hulin, Phys. Rev. Lett. **93**, 135005 (2004).
[5]S. Kneip, C. McGuffey, J. L. Martins, S. F. Martins, C. Bellei, V. Chvykov, F. Dollar, R. Fonseca, C. Huntington, G. Kalintchenko, A. Maksimchuk, S. P. D. Mangles, T. Matsuoka, S. R. Nagel, C. A. J. Palmer, J. Schreiber, K. T. Phuoc, A. G. R. Thomas, V. Yanovsky, L. O. Silva, K. Krushelnick, and Z. Najmudin, Nature Phys. **6**, 980 (2010).
[6]S. P. D. Mangles, G. Genoud, M. S. Bloom, M. Burza, Z. Najmudin, A. Persson, K. Svensson, A. G. R. Thomas, and C.-G. Wahlström, Phys. Rev. ST Accel. Beams **15**, 011302 (2012).
[7]S. Kneip, S. R. Nagel, S. F. Martins, S. P. D. Mangles, C. Bellei, O. Chekhlov, R. J. Clarke, N. Delerue, E. J. Divall, G. Doucas, K. Ertel, F. Fiuza, R. Fonseca, P. Foster, S. J. Hawkes, C. J. Hooker, K. Krusheknick, W. B. Mori, C. J. Palmer, K. T. Phuoc, P. P. Rajeev, J. Schreiber, M. J. V. Streeter, D. Urner, J. Vieira, L. O. Silva, and Z. Najmudin, Phys. Rev. Lett. **103**, 35002 (2009).
[8]D. H. Froula, C. E. Clayton, T. Döppner, K. A. Marsh, C. P. J. Barty, L. Divol, R. A. Fonseca, S. H. Glenzer, C. Joshi, W. Lu, S. F. Martins, P. Michel, W. B. Mori, J. P. Palastro, B. B. Pollock, A. Pak, J. E. Ralph, J. S. Ross, C. W. Siders, L. O. Silva, and T. Wang, Phys. Rev. Lett. **103**, 215006 (2009).
[9]W. Lu, M. Tzoufras, C. Joshi, F. S. Tsung, W. B. Mori, J. Vieira, R. A. Fonseca, and L. O. Silva, Phys. Rev. ST Accel. Beams **10**, 61301 (2007).
[10]J. Vieira, S. F. Martins, F. Fiza, C. K. Huang, W. B. Mori, S. P. D. Mangles, S. Kneip, S. Nagel, Z. Najmudin, and L. O. Silva, Plasma Phys. Controlled Fusion **54**, 055010 (2012).
[11]T. P. A. Ibbotson, N. Bourgeois, T. P. Rowlands-Rees, L. S. Caballero, S. I. Bajlekov, P. A. Walker, S. Kneip, S. P. D. Mangles, S. R. Nagel, C. A. J. Palmer, N. Delerue, G. Doucas, D. Urner, O. Chekhlov, R. J. Clarke, E. Divall, K. Ertel, P. Foster, S. J. Hawkes, C. J. Hooker, B. Parry, P. P. Rajeev, M. J. V. Streeter, and S. M. Hooker, New J. Phys. **12**, 045008 (2010).
[12]S. P. D. Mangles, G. Genoud, S. Kneip, M. Burza, K. Cassou, B. Cros, N. P. Dover, C. Kamperidis, Z. Najmudin, A. Persson, J. Schreiber, F. Wojda, and C.-G. Wahlström, Appl. Phys. Lett. **95**, 181106 (2009).
[13]A. G. R. Thomas, Z. Najmudin, S. P. D. Mangles, C. D. Murphy, A. E. Dangor, C. Kamperidis, K. L. Lancaster, W. B. Mori, P. A. Norreys, W. Rozmus, and K. Krushelnick, Phys. Rev. Lett. **98**, 95004 (2007).
[14]F. Wojda, K. Cassou, G. Genoud, M. Burza, Y. Glinec, O. Lundh, A. Persson, G. Vieux, E. Brunetti, R. Shanks, D. Jaroszynski, N. E. Andreev, C.-G. Wahlström, and B. Cros, Phys. Rev. E **80**, 066403 (2009).
[15]J. Schreiber, C. Bellei, S. P. D. Mangles, C. Kamperidis, S. Kneip, S. R. Nagel, C. A. J. Palmer, P. P. Rajeev, M. J. V. Streeter, and Z. Najmudin, Phys. Rev. Lett. **105**, 235003 (2010).

Paper IV

Laser Wakefield Acceleration using Wire Produced Double Density Ramps

M. Burza, A. Gonoskov, K. Svensson, F. Wojda, A. Persson, M. Hansson, G. Genoud, M. Marklund, C.-G. Wahlström, & O. Lundh.

Phys. Rev. St Accel. Beams **16**, 011301 (2013).

PHYSICAL REVIEW SPECIAL TOPICS - ACCELERATORS AND BEAMS **16**, 011301 (2013)

Laser wakefield acceleration using wire produced double density ramps

M. Burza,[1] A. Gonoskov,[2,3] K. Svensson,[1] F. Wojda,[1] A. Persson,[1] M. Hansson,[1] G. Genoud,[1] M. Marklund,[2] C.-G. Wahlström,[1] and O. Lundh[1]

[1]*Department of Physics, Lund University, P.O. Box 118, SE-221 00 Lund, Sweden*
[2]*Department of Physics, Umeå University, SE-901 87 Umeå, Sweden*
[3]*Institute of Applied Physics, Russian Academy of Sciences, 46 Ulyanov Street, Nizhny Novgorod 603950, Russia*

(Received 22 May 2012; published 8 January 2013)

A novel approach to implement and control electron injection into the accelerating phase of a laser wakefield accelerator is presented. It utilizes a wire, which is introduced into the flow of a supersonic gas jet creating shock waves and three regions of differing plasma electron density. If tailored appropriately, the laser plasma interaction takes place in three stages: Laser self-compression, electron injection, and acceleration in the second plasma wave period. Compared to self-injection by wave breaking of a nonlinear plasma wave in a constant density plasma, this scheme increases beam charge by up to 1 order of magnitude in the quasimonoenergetic regime. Electron acceleration in the second plasma wave period reduces electron beam divergence by $\approx 25\%$, and the localized injection at the density downramps results in spectra with less than a few percent relative spread.

DOI: 10.1103/PhysRevSTAB.16.011301 PACS numbers: 41.75.Jv, 52.35.Tc, 52.38.−r, 52.50.Jm

Plasma-based laser-driven electron accelerators can produce strong longitudinal fields, $\sim$100 GV/m, in the collective electron oscillations in the wake of an intense laser pulse [1]. This gives an advantage over conventional accelerators using rf cavities regarding the relatively compact high-power tabletop laser systems readily available [2].

In most experiments, injection of electrons into the accelerating structure relies on breaking of the plasma wave, which can thus self-inject electrons. This scheme is rather simple and quasimonoenergetic beams have been produced [3–5]. Electron beams of low spectral spread and divergence are necessary for these accelerators to be attractive for applications [6–8]. However, the wave breaking process is highly nonlinear, and in order to achieve higher quality beams, means to control the injection process are required. Both the amount of charge and the time of electron injection from the background plasma into the accelerating and focusing phase of the wakefield are crucial [9–11]. Here, self-injection [12–14] is inferior to most schemes with external injection control, such as colliding pulse techniques [15–18], ionization injection [19,20], or gradients in plasma electron density [21–24], which are used in this experiment. At the downwards gradient the plasma wavelength increases rapidly, the plasma wave breaks and electrons are trapped.

Shock waves resulting in very abrupt density transitions have been produced previously with a knife edge introduced into a supersonic gas flow [25]. By this, a well-defined shock wave and a density downwards gradient is provided on the laser axis. Alternatively, an auxiliary pulse produced an electron depleted region by formation of an ionization channel followed by hydrodynamic expansion [26,27]. Our experiment relates to these, as plasma densities are modulated on the laser axis to control injection externally.

We present a novel, staged, three step, laser wakefield accelerator that utilizes a thin wire crossing the supersonic flow of a gas jet. In this scheme, extremely sharp density transitions and shock waves facilitate gradient injection. These transitions may be of only some microns length [28]. In the first stage, comprised of a constant plasma density prior to reaching the first shock front, the pulse propagates and may thus match itself to the plasma conditions by relativistic self-focusing, self-modulation and temporal compression, with only a negligible amount of charge being trapped. After a variable length, adjustable by the wire position along the optical axis, the laser pulse reaches the second stage, where the first shock front, originating from the wire, in combination with the subsequent expansion fan produces gradients that enable injection. During the transition to the third stage, the plasma density increases from the density-diluted region right above the wire to the final constant density region. The plasma wavelength shrinks rapidly, which under certain circumstances enables a controlled charge transfer of the previously injected electrons from the first into the second plasma wave period. This mechanism, which is driven by inertia, may in addition have a filtering effect on the previously injected charges. The dominant process, however, is a new injection at the second shock front. The proceeding constant density plasma is finally utilized for electron acceleration driven by the already matched laser pulse.

The experiment was conducted at the Lund Laser Centre, Sweden, where a Ti:Sa CPA laser system provided pulses at 800 nm central wavelength with 42 fs duration and 1 J energy. The laser field is horizontally polarized. A deformable mirror and an $f = 75$ cm off-axis parabolic mirror facilitated a nearly diffraction limited focal spot, 0.7 mm above the orifice of a 3 mm diameter supersonic gas nozzle. The laser was focused at the boundary of the gas jet producing a spot with 15 μm diameter (intensity FWHM). A motorized holder positioned a wire above the nozzle but below the laser optical axis (z axis). This produced three distinct plasma density regions for the laser interaction as schematized by the white broken line function in Fig. 6. To tailor and model plasma electron densities for simulations, interferometric measurements were carried out using hydrogen at 9 bar backing pressure. It was found that the laser pulse initially encounters a region of approximately constant electron density (region I), which was determined to 6×10^{18} cm^{-3}. After ≈ 1 mm it encounters the first shock wave and a downwards gradient, followed by region II, where the plasma density is reduced to 3×10^{18} cm^{-3} over ≈ 300 μm. After a second shock wave transition, region III is reached. Here the density is approximately the same as in region I and it is here the main acceleration takes place. Plasma densities scale linearly with backing pressure. Adjustments of wire position, thickness, Mach number, and backing pressure tailor gradients, lengths, and density ratios between region I and region II to match the requirements for electron injection and laser guiding. Shock wave divergence angle and density ramps were found to be symmetric as long as the wire is $<$0.5 mm off the nozzle center. Without wire, the plasma density is almost constant and comparable to that at the plateau regions I and III.

As diagnostics served a top view camera and a permanent magnet electron spectrometer equipped with a Lanex screen (Kodak Lanex Regular), whose emission was recorded by a 16 bit CCD camera. Based on previous work [29,30], the electron spectrometer is calibrated in absolute charge. The setup is depicted in Fig. 1.

Stainless steel wires with 300, 200, 50, and 25 μm diameter were tested, but only the latter two were found to trigger injection, with the clearly best performance with the 25 μm wire. Thicker wires inevitably increase the length and depth of the density-diluted region II, promoting diffraction and making it difficult to maintain a sufficiently focused laser pulse for region III.

Hydrogen and helium were both tested as target gas together with the wire but while hydrogen could deliver electron beams in more than 90% of the shots; helium was much less reliable with an optimized injection probability of less than 20%. This is in line with parallel studies investigating the influence of the target gas on beam quality and reliability in a constant density gas jet [31]. Thus, in the following, results obtained with hydrogen are presented.

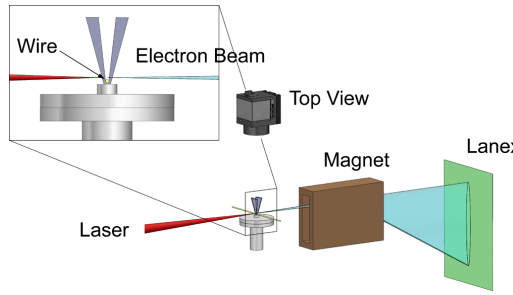

FIG. 1. Experimental setup: The laser pulse enters from the left and impinges on the gas jet 0.7 mm above the nozzle. The wire is positioned ≈ 0.2 mm above the orifice. Top view and a permanent magnet Lanex electron spectrometer serve as primary diagnostics. The position $z = 0$ along the laser axis is centered above the nozzle.

A wire height scan revealed that the probability for the production of electron beams increases with reduced distance to the optical axis. However, when closer than 0.65 mm the lifetime of the wire is reduced. As no improved performance on the production of electron beams could be observed in the range between 0.35 and 0.50 mm, the latter position was chosen. Here, the 25 μm wire survived about 60 to 100 shots.

A z scan conducted with the 25 μm wire, 0.50 mm below the laser optical axis, and with a backing pressure below but close to the threshold for self-injection, revealed the sensitivity of the wire position along the optical axis on the production of electron beams (threshold is defined here as the constant plasma density resulting in beams with $<$10% of the maximum charge observed during a pressure scan in the quasimonoenergetic regime). This window was found to be ≈ 200 μm wide only. Outside this, the beam charge is comparable to the self-injection case without density modulation.

Pressure scans were carried out at what was found to be the optimum spatial parameters, employing the 25 μm diameter wire at 0.50 mm distance to the optical axis and at a longitudinal z position 0.07 mm from the nozzle center towards the off-axis parabolic mirror. The wire injection scheme was found to be rather robust with regard to backing pressure. Below the self-modulated laser wakefield accelerator (LWFA) regime at 11 bar, the beam charge is increased by 1 order of magnitude, as illustrated in Fig. 2. With the wire, electron beam divergence is not affected by the overall plasma density but is on average only 75% compared to the self-injection case. On rare occasions, a beam divergence down to 2 mrad could be demonstrated, which is less than the minimum divergence achieved without wire.

Example spectra can be seen in Fig. 3, showing the spectral range from 43 MeV to infinity. A relative spectral spread $\frac{\Delta E}{E} \leq 4\%$ can be calculated. Note however, that

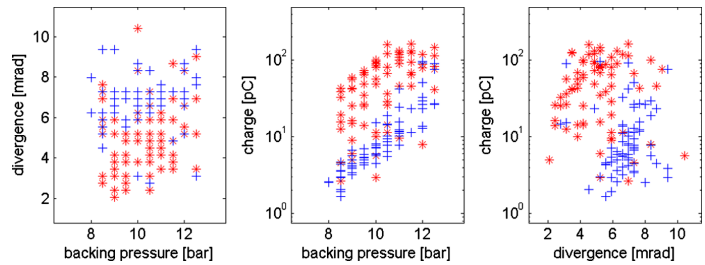

FIG. 2. Comparison of divergence and charge of electron beams using hydrogen as target gas. The red stars represent shots with the wire 0.5 mm below the laser axis, and blue crosses represent LWFA with nonlinear wave breaking and self-injection. Every data point corresponds to one shot. The failure rate with wire is below 5% and thus comparable to the wireless self-injection. Note the increased brightness indicated by the results in the figure to the right.

spectrometer dispersion and divergence have not been deconvoluted here. In fact, 4 mrad FWHM (see Fig. 3) produces an apparent $\frac{\Delta E}{E} \approx 4\%$ (FWHM) at 100 MeV, thus the real relative spectral spread is below what can be resolved with this particular spectrometer but less than a few percent. Electron beam mean energies are generally lower with the wire. The effect of the wire is threefold: It injects a charge $\sim$10 times higher than that available without wire while at the same time providing beams with clean quasimonoenergetic spectra and reduced divergence, thus brightness is increased dramatically. A weak self-injected background charge can be identified in most of the shots. Within limits, energy tuning becomes possible by altering the z position of the wire as illustrated in Fig. 3. From this a field of ≈ 250 GV/m and an acceleration length of ≈ 0.4 mm may be estimated, indicating that acceleration for the wire-injected beams effectively only takes place in stage III. The background charge, which is higher in energy, must therefore result from injection in an earlier stage, or resemble an injected dark current exposed to higher acceleration fields. If we assume this background not to be accelerated over a much longer distance than the wire-injected charge, this indicates that acceleration of the wire-injected charge takes place in a later plasma wave period as field strengths decrease with increasing number of plasma wave oscillation periods behind the laser driver. This is supported by beam profile measurements that show an ellipticity in the beam divergence for the self-injected beams only, as illustrated in Fig. 4, which can be understood as an effect due to the interaction of the injected electrons with the laser field inside the first plasma wave period [32].

Figure 5 shows spectra with and without wire at backing pressures that result in comparable beam charges for both cases. Wire injection at 9 bar is thus compared to self-injection at 12 bar. Note that low-energy artifacts, carrying a significant amount of charge, appear >20 pC in the spectra of self-injected beams, while spectra of wire-injected beams are cleaner. The tendency of decreasing peak energy with increasing charge due to beam loading [10] is clearly visible in the wire injection case and indicates that injection probably occurs at the same z position.

The 3D fully relativistic parallel PIC code ELMIS [33] was used to investigate the physical mechanisms in the modulated density during laser propagation. In the simulation 140 attoseconds corresponded to one time step and an $80 \times 80 \times 80$ μm^3 box was represented by

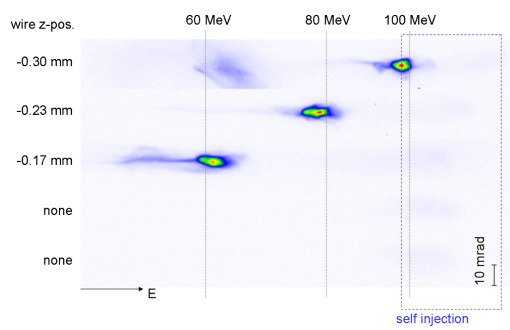

FIG. 3. Example spectra with comparable charge and variable wire position as recorded on the Lanex screen using 9.5 bar backing pressure. Besides the rather strong peak when the wire is present, a weak background self-injection can be seen in all spectra.

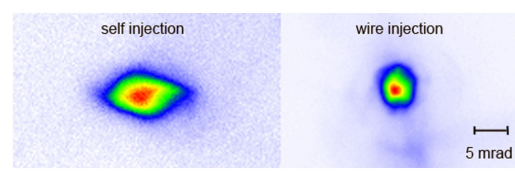

FIG. 4. Beam profile measurements acquired with helium illustrate different eccentricities for the two cases without wire on the left and with wire on the right, shown on an equal lateral and normalized color scale.

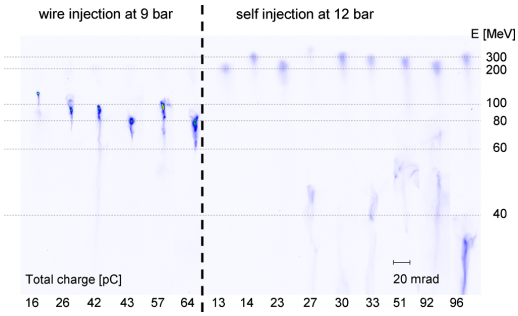

FIG. 5. Example spectra of beams with variable charge and fixed wire position; left: wire injection at 9 bar backing pressure; right: self-injection at 12 bar backing pressure to compensate for the charge increase in the wire injection case as indicated in Fig. 2. Each group has been sorted according to integrated charge and the spectra are displayed on an equal lateral and normalized color scale.

$1024 \times 256 \times 256$ cells. The ions (H^+) were mobile. During the simulation the average number of virtual particles was 1 billion. Laser parameters were taken from the experiment. As the resolution for the measured plasma densities was limited to ~ 100 μm, the exact distribution is unknown. Still, the interferometric data does provide useful information about densities and lengths of each section while steeper gradients such as shock fronts remain concealed. In combination with theoretical considerations and fluid simulations by Wang *et al.* [34], a profile resembled by the broken line function in Fig. 6 is very likely and thus used for the simulations. This density distribution is fully consistent with the acquired interferometric data. It should be noted though that estimated gas jet temperatures in the experiment are in the range 10–50 K only, and are thus 1 order of magnitude lower than those simulated by Wang *et al.* [34]. Moreover, in our case, the distance between wire and plasma channel was about 3 times larger than what was presented in that particular paper.

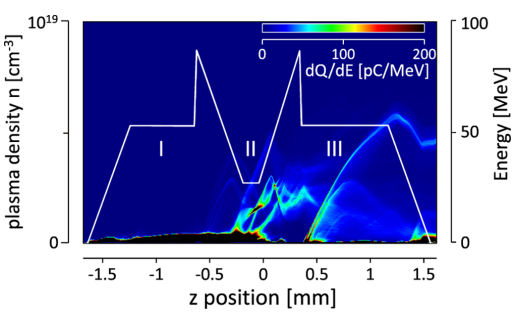

FIG. 6. Electron energy distribution as a function of the laser pulse z position and plasma density distribution (white curve).

Additionally, those simulations were carried out with helium while we used hydrogen, which at these low temperatures requires a different equation of state.

With the proposed density distribution, simulations show that when traversing region I, the laser pulse gets focused transversely and generates a highly nonlinear plasma wave, which does not reach breaking and thus facilitates neither longitudinal nor transverse self-injection of electrons. In line with previous studies [21,22,35] at the density downramp, which is the expansion fan originating from the wire, the cavities of the nonlinear plasma wave rapidly expand behind the laser pulse and thereby catch electrons accumulated between the buckets. In region II these electrons form an electron bunch. At the entry to region III, the cavity size shrinks again. With the assumed shallow inward gradients however, injected electrons are dephased after the transition and are not accelerated further. The following outward density shock wave enables a second injection of a new bunch into the second plasma wave period, which is accelerated throughout region III.

The initial dephasing and renewed injection of electrons upon entering stage III, followed by a rapid acceleration over no more than half a millimeter until the end of the gas jet, explains the rather short acceleration distances that can be derived from the field estimates related to Fig. 3. This also leads to the observed lower final energy of the electrons compared to the self-injection case. The localized injection results in highly monoenergetic beams both in simulation and experiment. When increasing the height above the wire, a decrease in gradient strengths together with an extension of region II explains the reduced probability for the production of electron beams when operating at too large a distance. That the electrons are accelerated in the second plasma wave period, isolated from the laser pulse, as suggested by simulations and indicated experimentally, may as well explain the reduced divergence.

In conclusion, a wire injection scheme has successfully been demonstrated as an alternative to some more complex setups facilitating controlled injection. Beam features include a reduction in divergence by 25% and an increase in bunch charge by up to 1 order of magnitude if compared to beams of electrons accelerated in the quasimonoenergetic, nonlinear, self-injection regime. Their spectra are tunable and show less than a few percent relative spread. Simulations confirm the experimental findings with respect to external injection control, acceleration in the second plasma wave period, and resulting spectral distribution.

ACKNOWLEDGMENTS

We acknowledge the support of the Swedish Research Council, the Knut and Alice Wallenberg Foundation, the Lund University X-Ray Centre, the European Research Council Contract No. 204059-QPQV, the Swedish Research Council Contract No. 2010-3727, and the Swedish National Infrastructure for Computing.

[1] T. Tajima and J. Dawson, Phys. Rev. Lett. **43**, 267 (1979).
[2] S. Backus, C. G. Durfee, M. M. Murnane, and H. C. Kapteyn, Rev. Sci. Instrum. **69**, 1207 (1998).
[3] C. G. R. Geddes, Cs. Toth, J. van Tilborg, E. Esarey, C. B. Schroeder, D. Bruhwiler, C. Nieter, J. Cary, and W. P. Leemans, Nature (London) **431**, 538 (2004).
[4] J. Faure, Y. Glinec, A. Pukhov, S. Kiselev, S. Gordienko, E. Lefebvre, J.-P. Rousseau, F. Burgy, and V. Malka, Nature (London) **431**, 541 (2004).
[5] S. P. D. Mangles *et al.*, Nature (London) **431**, 535 (2004).
[6] K. Nakajima *et al.*, Nat. Phys. **4**, 92 (2008).
[7] H.-P. Schlenvoigt *et al.*, Nat. Phys. **4**, 130 (2007).
[8] M. Fuchs *et al.*, Nat. Phys.**5**, 826 (2009).
[9] M. Tzoufras, W. Lu, F. Tsung, C. Huang, W. Mori, T. Katsouleas, J. Vieira, R. Fonseca, and L. Silva, Phys. Rev. Lett. **101**, 145002 (2008).
[10] C. Rechatin, X. Davoine, A. Lifschitz, A. Ben Ismail, J. Lim, E. Lefebvre, J. Faure, and V. Malka, Phys. Rev. Lett. **103**, 194804 (2009).
[11] C. Rechatin, J. Faure, A. Ben-Ismail, J. Lim, R. Fitour, A. Specka, H. Videau, A. Tafzi, F. Burgy, and V. Malka, Phys. Rev. Lett. **102**, 164801 (2009).
[12] I. Kostyukov and E. Nerush, Phys. Rev. Lett. **103**, 175003 (2009).
[13] S. V. Bulanov, F. Pegoraro, A. M. Pukhov, and A. S. Sakharov, Phys. Rev. Lett. **78**, 4205 (1997).
[14] A. Zhidkov, J. Koga, T. Hosokai, K. Kinoshita, and M. Uesaka, Phys. Plasmas **11**, 5379 (2004).
[15] E. Esarey, R. Hubbard, W. Leemans, A. Ting, and P. Sprangle, Phys. Rev. Lett. **79**, 2682 (1997).
[16] V. Malka, J. Faure, C. Rechatin, A. Ben-Ismail, J. K. Lim, X. Davoine, and E. Lefebvre, Phys. Plasmas **16**, 056703 (2009).
[17] A. Beck, X. Davoine, and E. Lefebvre, New J. Phys. **13**, 093016 (2011).
[18] J. Faure, C. Rechatin, A. Norlin, A. Lifschitz, Y. Glinec, and V. Malka, Nature (London) **444**, 737 (2006).
[19] A. Pak, K. A. Marsh, S. F. Martins, W. Lu, W. B. Mori, and C. Joshi, Phys. Rev. Lett. **104**, 025003 (2010).
[20] C. McGuffey *et al.*, Phys. Rev. Lett. **104**, 025004 (2010).
[21] S. Bulanov, N. Naumova, F. Pegoraro, and J. Sakai, Phys. Rev. E **58**, R5257 (1998).
[22] H. Suk, N. Barov, J. Rosenzweig, and E. Esarey, Phys. Rev. Lett. **86**, 1011 (2001).
[23] C. G. R. Geddes, K. Nakamura, G. Plateau, Cs. Toth, E. Cormier-Michel, E. Esarey, C. Schroeder, J. Cary, and W. Leemans, Phys. Rev. Lett. **100**, 215004 (2008).
[24] A. J. Gonsalves *et al.*, Nat. Phys. **7**, 862 (2011).
[25] K. Schmid, A. Buck, C. Sears, J. Mikhailova, R. Tautz, D. Herrmann, M. Geissler, F. Krausz, and L. Veisz, Phys. Rev. ST Accel. Beams **13**, 091301 (2010).
[26] J. Faure, C. Rechatin, O. Lundh, L. Ammoura, and V. Malka, Phys. Plasmas **17**, 083107 (2010).
[27] C.-T. Hsieh, C.-M. Huang, C.-L. Chang, Y.-C. Ho, Y.-S. Chen, J.-Y. Lin, J. Wang, and S.-Y. Chen, Phys. Rev. Lett. **96**, 095001 (2006).
[28] A. C. Kermode *et al.*, *Mechanics of Flight* (Pearson Education, Harlow, England, 2006).
[29] Y. Glinec, J. Faure, A. Guemnie-Tafo, V. Malka, H. Monard, J. P. Larbre, V. De Waele, J. L. Marignier, and M. Mostafavi, Rev. Sci. Instrum. **77**, 103301 (2006).
[30] A. Buck *et al.*, Rev. Sci. Instrum. **81**, 033301 (2010).
[31] K. Svensson (unpublished).
[32] S. P. D. Mangles *et al.*, Phys. Rev. Lett. **96**, 215001 (2006).
[33] URL http://www.ipfran.ru/english/structure/lab334/simlight.html.
[34] C. Wang, J. Li, J. Sun, and X. Luo, Phys. Rev. ST Accel. Beams **15**, 020401 (2012).
[35] R. G. Hemker, N. Hafz, and M. Uesaka, Phys. Rev. ST Accel. Beams **5**, 041301 (2002).

Paper V

Down-Ramp Injection and Independently Controlled Acceleration of Electrons in a Tailored Laser Wakefield Accelerator

M. Hansson, B. Aurand, X. Davoine, H. Ekerfelt, K. Svensson, A. Persson, C.-G. Wahlström, & O. Lundh.

Phys. Rev. ST Accel. Beams **18**, 071303 (2015).

PHYSICAL REVIEW SPECIAL TOPICS—ACCELERATORS AND BEAMS **18,** 071303 (2015)

Down-ramp injection and independently controlled acceleration of electrons in a tailored laser wakefield accelerator

M. Hansson,[1,*] B. Aurand,[1] X. Davoine,[2] H. Ekerfelt,[1] K. Svensson,[1]
A. Persson,[1] C.-G. Wahlström,[1] and O. Lundh[1,†]

[1]*Department of Physics, Lund University, P.O. Box 118, S-22100 Lund, Sweden*
[2]*CEA, DAM, DIF, Bruyères-le-Châtel, 91297 Arpajon, France*

(Received 23 March 2015; published 8 July 2015)

We report on a study on controlled injection of electrons into the accelerating phase of a plasma wakefield accelerator by tailoring the target density distribution using two independent sources of gas. The tailored density distribution is achieved experimentally by inserting a narrow nozzle, with an orifice diameter of only 400 μm, into a jet of gas supplied from a 2 mm diameter nozzle. The combination of these two nozzles is used to create two regions of different density connected by a density gradient. Using this setup we show independent control of the charge and energy distribution of the bunches of accelerated electron as well as decreased shot-to-shot fluctuations in these quantities compared to self-injection in a single gas jet. Although the energy spectra are broad after injection, simulations show that further acceleration acts to compress the energy distribution and to yield peaked energy spectra.

DOI: 10.1103/PhysRevSTAB.18.071303 PACS numbers: 41.75.Jv, 52.35.-g, 52.38.-r, 52.50.Jm

Benefiting from the high electric fields that can be sustained in a plasma wave, laser wakefield accelerators [1] appear promising as compact sources of highly relativistic electrons and X-rays. Quasi-monoenergetic bunches of highly relativistic electrons were first observed in 2004 [2–4], by self-injection through wave-breaking. Since then, much effort has been made on controlling the injection of electrons into the accelerating plasma structure. Different mechanisms for injection, such as injection by colliding laser pulses [5–7] and ionization [8–11] and injection in density down-ramps [12–16] etc., have been proposed and studied both theoretically and experimentally.

The mechanism of density down-ramp injection is typically divided into two regimes; short density ramps (of the order of the plasma wavelength, λ_p) and long density ramps ($> \lambda_p$). Short density ramps have been produced experimentally, for example by optical plasma formation and expansion [17] and by shock waves [15,18] in gas jets. Due to the well-localized injection point, electron bunches with peaked energy spectra can be generated. In longer density ramps [14,16], injections occur over a longer distance, and thus initially give broad energy spectra. However, after further acceleration of the electrons, the energy spectra can become peaked.

The mechanism of density down-ramp injection relies on breaking of the plasma density wave that follows a laser pulse. This occurs when the electrons that constitute the plasma wave approaches and exceeds the phase velocity of the wave. For laser wakefield accelerators based on self-injection this is achieved by driving the plasma density oscillations to such high amplitude that wave-breaking occurs. In contrast, density down-ramp injection exploits the gradually increasing plasma wavelength in the ramp. Behind the driving laser pulse, this results in a decreased phase velocity of the plasma density wave and can thus be used to reach the conditions for wave-breaking.

In this article, we present a study, experimentally and numerically, on controlled injection of electrons into the accelerating field of a laser wakefield accelerator, based on long density down-ramps, and the subsequent acceleration of the injected electrons in the following low density plasma. The aim is to improve our understanding of the physics behind both injection in density down-ramps and the subsequent acceleration.

Controlled injection is achieved in this experiment using two separate nozzles to supply the gas in the interaction region. In contrast to the work presented in Ref. [16], where ionization-induced injection is employed in combination with a density down-ramp, the electrons are injected in this experiment solely by density down-ramp injection. Furthermore, our experimental setup allows for continuous variation of the length of the plasma after the injection point, as compared to Refs. [14,16]. We show that this density distribution can be used to separately control the amount of charge and the electron kinetic energy in the bunches of accelerated electrons. The shot-to-shot fluctuations, in total charge and energy distribution, achieved using this setup are significantly smaller compared to the beams accelerated in the self-injection scheme in a single

*martin.hansson@fysik.lth.se
†olle.lundh@fysik.lth.se

gas jet. The conclusions presented in this article are based on experiments, performed using a multi-terawatt laser at the Lund Laser Centre, and supported by particle-in-cell (PIC) simulations using the code CALDER-CIRC [19].

The laser pulses, each containing 650 mJ of energy and with a duration (FWHM) of 40 fs, are focused to an almost circular spot with 19 μm diameter (FWHM), using an $f = 0.765$ m off-axis parabolic mirror. The peak intensity of the laser pulses, when focused in vacuum, is determined to 3.7×10^{18} W/cm^2, corresponding to a normalized vector potential of 1.3.

Two separate nozzles are used to provide the desired density distribution of hydrogen gas in the interaction region, as illustrated in Fig. 1(a), and is ionized by the leading edge of each laser pulse. The main part of the gas is supplied by a nozzle with an exit diameter of 2 mm, with its orifice located 1 mm from the optical axis. This nozzle provides an almost cylindrically symmetric jet of gas toward the optical axis, and is typically positioned such that the laser pulse is focused on the front edge of the density distribution. Additionally, a narrow metallic tube, with an orifice diameter of 400 μm, is inserted into the jet, perpendicular to both the optical axis and the direction of the main jet. Gas is supplied through this tube to provide an additional, localized, contribution to the density in the interaction region with the laser pulse.

The total neutral density distribution, along the optical axis, of the gas provided from these two nozzles is characterized off-line by measuring, using a wavefront sensor, the additional optical path length introduced by the gas in an optical probe beam [20]. The optical path length introduced by the gas provided from the 2 mm nozzle is first measured and the density distribution is calculated assuming circular symmetry. The narrow tube is inserted into the flow from the 2 mm nozzle and the wavefront is again measured, first without any gas supplied from the narrow tube. By comparing the wavefront with and without the narrow tube inserted in the flow we conclude that the gas distribution is essentially unaffected by inserting this tube. Finally, the difference in optical path length is measured with gas supplied simultaneously from the main nozzle and from the narrow tube, as shown in Fig. 1(b). This allows the contribution from the narrow tube to the total gas density to be determined assuming circular symmetry close to the orifice, and the final total density profile, shown in Fig. 1(c), to be calculated.

The total density distribution along the optical axis contains a peak and a plateau joined together by a gradient. As will be shown, under suitable chosen conditions, density down-ramp injection of electrons into the accelerating phase of a laser plasma wakefield occurs in this gradient and the electrons are subsequently accelerated in the remaining plasma.

The backing pressures supplied independently to each nozzle are used to control the density in the peak and the plateau. The density profile from the 2 mm gas nozzle is approximately flat over 0.7 mm which corresponds to the maximum plateau length. The density in the plateau is used to control the plasma wavelength in this region and is also used to tune the strength of the accelerating field. Furthermore, the two nozzles are separately mounted on 3-axis translation stages which allow full control of the position of the two density distributions both relative to each other and relative to the laser focus. By moving the 2 mm nozzle along the optical axis, while keeping the narrow nozzle fixed, the length of the density plateau is varied. This degree of freedom provides a mean to perform studies of the acceleration independently of the injection of electrons.

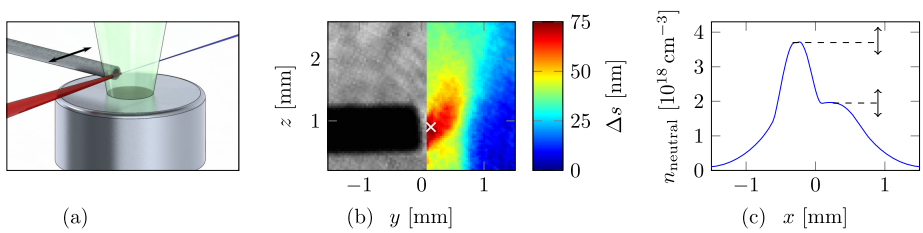

FIG. 1. A schematic illustration of the experimental setup is shown in (a). The laser pulses (red) are focused on the front edge of the gas jet provided from a 2 mm nozzle with its orifice located 1 mm from the optical axis. A narrow tube is inserted into the jet, with its orifice 0.2 mm from the optical axis, and provides locally an additional amount of gas. The electrons (blue) accelerated in the interaction propagate along the optical axis. Measurements, using a wavefront sensor, of the additional optical path length introduced by the gas in an optical probe beam allows the neutral gas density profile to be determined. In (b) the additional path length (Δs) introduced by the gas, supplied from both nozzles simultaneously, is shown in the color scale in the part not obstructed by the narrow tube. The 2 mm nozzle is located just below the edge of the image and supplies a flow of gas along the vertical (z) axis. The shadow of the narrow tube marks its position in the left part of the figure. The optical axis of the main laser beam is perpendicular to the plane of the figure and its position in the plane is marked as a white cross. The typical neutral gas density (n_{neutral}) distribution along the optical (x) axis used in this experiment is shown in (c). The tube can be moved along the optical axis to change the position of the density peak and thus also the density down-ramp. Furthermore, the density in the peak and plateau can be varied independently.

Measurements of the density distributions show that the gradient between the two regions is approximately 230 μm long and is unaffected by changing the backing pressure within the range used in this experiment. Thus, the density down-ramp becomes sharper as the backing pressure to the narrow tube is increased, which allowed for studies to be performed of the dependence of the number of injected electrons on the gradient.

The electrons accelerated in the plasma are observed by letting them impact on a scintillating screen (KODAK LANEX REGULAR), imaged onto a 16-bit CCD-camera (PRINCETON PHOTONMAX 1024). The amount of charge impacting on the scintillating screen is determined using published calibration factors for the screen [21] and by calibration of the response of the CCD-camera through the imaging optics. Furthermore, a 10 cm long dipole magnet with a peak field strength of 0.7 T can be inserted in the electron beam to disperse the electrons according to energy before impacting on the scintillating screen. This allows for the energy spectrum, above a cutoff energy of 40 MeV, of the electron beams to be determined. The electron energy dispersion on the scintillating screen was calibrated by numerically tracing electrons of different energies through the dipole magnetic field, according to the experimental geometry.

Electrons were first injected and accelerated in a target where gas was supplied only from the 2 mm gas nozzle. The threshold in electron number density in the plateau for required self-injection was found to be approximately 11×10^{18} cm^{-3}. The observed beams of electrons had the typical characteristics of self-injection in gas jets [22,23], with limited reproducibility and a bunch charge of the order of 30 pC with a standard deviation higher than 50%.

The electron number density provided from the 2 mm nozzle was lowered well below threshold for injection (to 3×10^{18} cm^{-3}). When adding gas also from the narrow tube, beams of accelerated electrons were observed [see Fig. 2(a)] for *every* laser pulse sent onto the target. The bunches of accelerated electrons injected using this composite gas target contain only of the order of 1 pC and their spectra typically contain a broad peak [see Fig. 2(b)]. Furthermore, the shot-to-shot stability in charge and energy of the electron beams, with standard deviations 13% and 5%, respectively, is far better than the stability of the beams injected through the self-injection mechanism in a single gas jet. This indicates that the local increase of gas in the interaction region facilitates the injection of electrons into the accelerating wakefield, and the reproducibility suggests that the mechanism is different from the self-injection observed when only supplying gas from one nozzle.

The kinetic energy of the accelerated electrons could be controlled by varying the remaining plasma length after the density down-ramp. This was done by moving the 2 mm gas nozzle, while keeping the position of the down-ramp

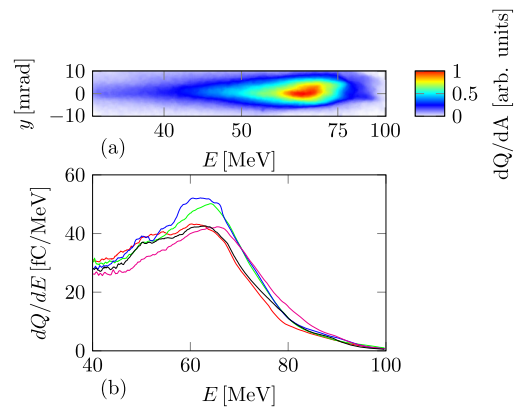

FIG. 2. Typical image of the dispersed electrons impacting on the scintillating screen (a) in a color map representing amount of charge per area. The total amount of charge is approximately 1.5 pC and the beams have a divergence of 10 mrad. Calculated energy spectra of electrons accelerated in five consecutive shots (b). The energy spectra of the electrons accelerated using this target typically contains a broad peak at an energy that is tunable from 50 to 80 MeV. The shot-to-shot fluctuations in charge and average energy achieved using this setup are significantly better compared to self-injection.

fixed with respect to the laser focus in vacuum. The resulting dependence of the peak electron energy on the length of the remaining plasma is shown in Fig. 3 for two different densities in the plateau. The result shows that a longer plasma, after the density down-ramp, provides higher energy of the electrons. This corresponds well with the estimated dephasing length [24] $L_d \approx 3$ mm, i.e., the maximum length an injected electron can stay in the accelerating phase of the wakefield, which is much longer than the plateau.

Assuming that the movement of the 2 mm gas nozzle has minor effects on the position of injection, the average accelerating electric field is estimated by fitting a line to each series of data. This gives a value of 37 MV/mm at a density of 2.6×10^{18} cm^{-3} in the plateau and 50 MV/mm at a density of 3.25×10^{18} cm^{-3}.

These accelerating electric fields are quite low compared to most other studies of laser wakefield acceleration using similar laser parameters [15]. This can be explained by two parts; first, the electron number density in the plateau is relatively low compared to studies in which the accelerator is operated close to the threshold for self-injection. This leads to a lower peak electric field in the accelerating region in our experiments. Second, as the electrons are injected when the plasma wake is growing longitudinally behind the laser pulse, in a long gradient, the electrons will be distributed longitudinally over a length approximately equal to $\Delta\lambda_p$, where $\Delta\lambda_p$ is the difference in plasma

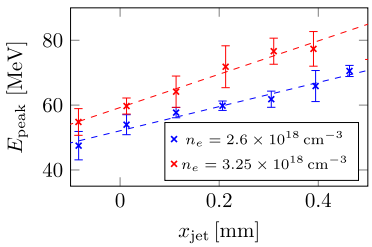

FIG. 3. Peak energy against relative jet position along the optical axis for two different plateau densities. The acceleration length in the plateau after the density down-ramp is controlled by the position of the gas jet. Zero on the x-axis corresponds to the position where the density down-ramp is approximately centered in the density distribution from the jet. Each data point corresponds to 10 consecutive shots and the error bars indicate one standard deviation in each direction. While the electron number density in the peak is kept constant at 11×10^{18} cm^{-3}, the peak energy increases linearly (dashed blue line) with the relative jet position.

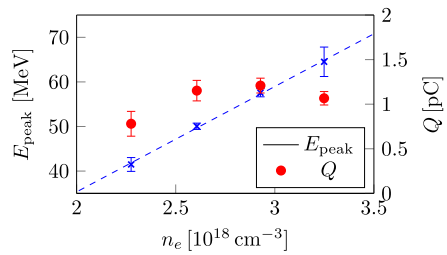

FIG. 4. Peak energy (blue) and total charge (red) against electron number density in the plateau. Each data point corresponds to 10 consecutive shots and the error bars indicate one standard deviation in each direction. The peak energy increases linearly (dashed blue line) with the electron number density, whereas the total charge shows no such trend. The electron number density in the peak is kept constant at 11×10^{18} cm^{-3}.

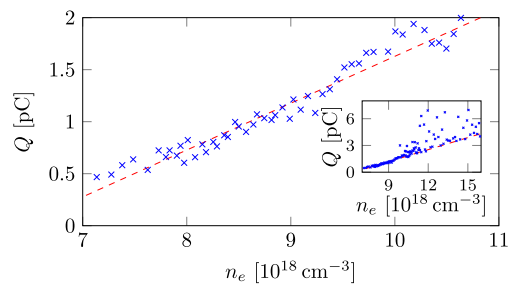

FIG. 5. Charge, above 40 MeV, as a function of electron number density in the peak. The positions of the two nozzles are kept fixed and the electron number density in the plateau is kept constant at 3.25×10^{18} cm^{-3}. At low peak densities, the amount of injected charge increases linearly with only small shot-to-shot fluctuations (standard deviation of 0.09 pC) around the fitted line (red dashed). At densities above 10×10^{18} cm^{-3} (shown in the inset), large fluctuations occur. However, the fluctuations only contribute to an increase in the total charge and indicate two different mechanisms of injection. The onset of the large fluctuations coincides with the electron number density threshold for self-injection.

wavelength in the peak and the plateau regions. As the plasma wavelength increases from 11 μm in the peak where the electron number density is 11×10^{18} cm^{-3} to 19 μm for the electron number density in the plateau of 3.25×10^{18} cm^{-3}, the injected electrons will be distributed along 8 μm in the first plasma period. Thus, the injected electrons are distributed over approximately 40% of the first plasma wave period, and the average electric field experienced by the injected electrons is lower than if they were all placed in the back of the first plasma wave period, which is the case for self-injection.

The influence of the electron number density in the plateau after the density down-ramp was studied while keeping the electron number density in the peak constant at 11×10^{18} cm^{-3}. The resulting kinetic energy of the accelerated electrons showed a strong dependence on this electron number density (see Fig. 4).

While varying the energy of the electrons, using either of the methods described above, the charge did not show significant variations compared to the standard deviation. We conclude that the energy of the electrons could be controlled independently of the amount of injected charge, by changing either the electron number density in the plateau or the length of the plateau. The amount of charge in the electron beams could be separately controlled, within a certain range, by varying the peak density while keeping the plateau density constant. No trend is observed in the electron energy spectra while varying the peak density, whereas the beam charge shows a clear dependence on the electron number density in the peak as shown in Fig. 5. Up to an electron number density of 10×10^{18} cm^{-3}, the charge increases linearly with electron number density in the peak. By increasing this density by only 40% (from 7.1×10^{18} cm^{-3} to 10×10^{18} cm^{-3}), the observed charge was increased by more than a factor of 3. Furthermore, the standard deviation of the shot-to-shot fluctuations in charge around the fitted linear dependence on peak electron number density is smaller than 0.1 pC (standard deviation). Thus, the relative charge fluctuations are significantly smaller using this setup than in our experiments for self-injection using a single gas jet.

An interesting feature is observed in the charge dependence as the electron number density in the peak is increased beyond 10×10^{18} cm^{-3}, shown in the inset in Fig. 5. At these densities the shot-to-shot fluctuations in charge are much larger than for lower densities. Remarkably, there

is not a single data point below the line that follows the charge dependence for densities below 10×10^{18} cm^{-3}. The images of the dispersed electrons on the scintillating screen show that the electron beams, for peak densities above 10×10^{18} cm^{-3} typically contain two components. One component with spectral shape and total charge similar to the ones observed at lower peak density is present on every shot. In addition, some beams contain a second component with higher charge and different spectral shape. The shot-to-shot fluctuations in this component is significantly larger than the fluctuations in the first component. We interpret this feature as injection of electrons through two different mechanisms; the stable, low charge component which is present on every shot is injected as the laser pulse propagate through the density down-ramp. The second component, which is only present above a certain threshold value for the electron number density in the peak, could be due to self-injection in the peak. This interpretation is supported by the observation that the value of the electron number density above which the second component starts to appear is the same as the electron number density threshold for self-injection observed in our experiments using a single gas jet.

To further support our interpretations of the experimental results, particle-in-cell simulations are performed using the code CALDER-CIRC [19]. In the simulations, the electron number density profile is approximated by a piecewise linear function, including two regions of constant density joined together by a linear gradient as shown in Fig. 6(a). The laser pulse parameters are chosen to correspond to those used in the experiments.

From the simulations, it is observed that the laser pulse undergoes self-focusing and self-compression in the increasing density and excite a highly nonlinear wakefield as the laser pulse reaches the density peak. However, no electrons are injected into the accelerating structure in this region [see Fig. 6(b)], as the wakefield is not yet strong enough for self-injection. As the laser pulse propagates through the linear density down-ramp, the wakefield structure increases in size and a certain portion of the background electrons become located within the electron void behind the laser pulse [see Fig. 6(c)]. The injection of electrons into the wakefield stops when the rear end of the first plasma period reaches the end of the density down-ramp, whereas the already injected electrons become further accelerated in the remaining plasma.

The observations from the simulations of injection in the density down-ramp and consecutive acceleration in the following plateau agree perfectly with the experimental observations presented above. For example, from Fig. 6(a) it is clear that the final energy of the electrons can be controlled by varying the length of the plasma after the density down-ramp.

It is further evident from the solid curves in Fig. 6(b–c) that the maximum accelerating field is much lower in the

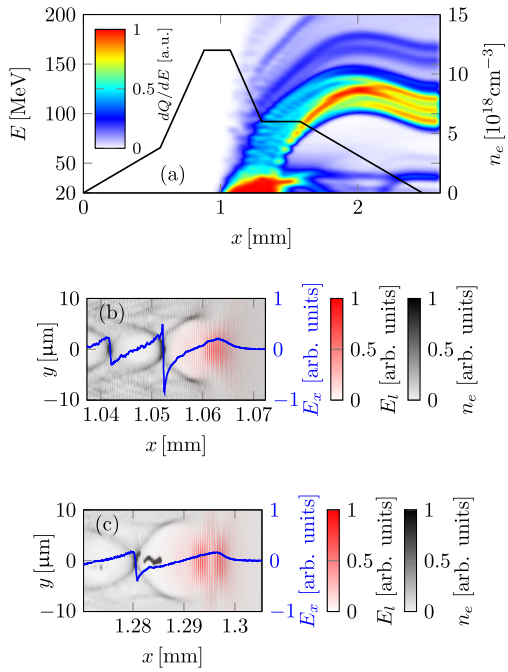

FIG. 6. Simulated evolution of the electron spectrum as the laser pulse propagates through the plasma (a) and local electron number density distribution before (b) and after (c) the density down-ramp along with the laser field (red) and accelerating electric field (blue). Injection of electrons into the wakefield structure occurs in the density down-ramp, located between ≈1.1 mm and ≈1.35 mm. The injected electrons are accelerated in the density plateau and the final electron energy spectrum contains a peak centered around 105 MeV and a FWHM of 20 MeV. In (c) electrons have been trapped after being injected as the plasma wavelength gradually increased in the density down-ramp. Thus, the electrons are distributed longitudinally over a distance approximately equal to $\Delta\lambda_p \approx 5$ μm.

low electron number density of the plateau than in the peak. Also, since the electrons are distributed longitudinally the average electric field experienced by the injected electrons is lower than if all electrons would be located at the back of the first plasma wave period.

Furthermore, it is observed in the simulations that the wakefield structure is close to breaking already before the density down-ramp and only minor changes in the parameters for the simulation result in self-injection there. This agrees well with the experimental findings, in which two populations of accelerated electrons are identified at high densities (see Fig. 5).

The results from the simulations can also be used to understand the shape of electron energy spectra of the beams of accelerated electrons. In Fig. 7, the longitudinal

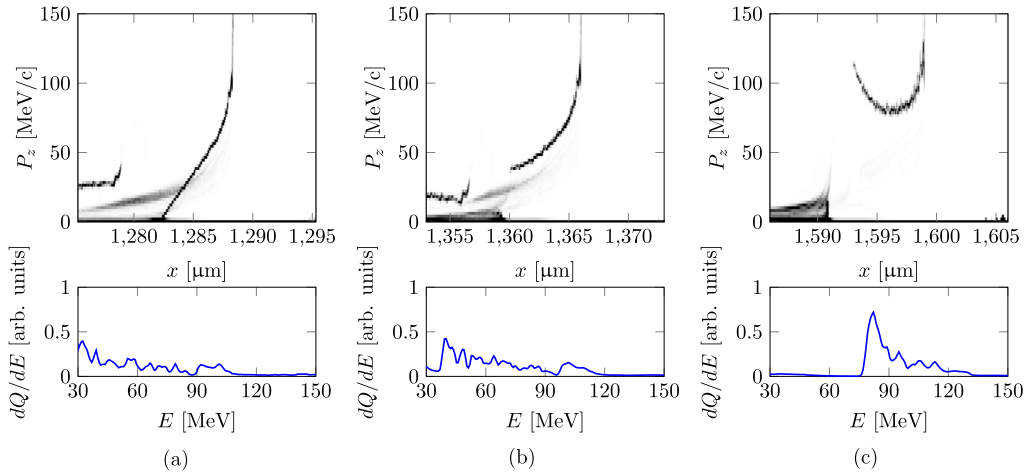

FIG. 7. Simulated compression of longitudinal phase-space distribution of injected electrons in the density plateau. In the first step (a) the laser pulse has just propagated through the density down-ramp, and the injected electrons are distributed along a line with a slope approximately equal to 12 MeV/c/μm, corresponding to a large energy spread in the total energy spectrum. After acceleration over 75 μm (b), the average energy of the injected electrons has increased, and the phase-space distribution starts to diverge from a line. After further acceleration over 240 μm (c), the phase-space distribution has deformed into a U-shape, corresponding to a peaked energy spectrum. The compression of the phase-space distribution to yield a peaked energy spectrum occurs because the injected electrons are distributed longitudinally, and thus experience different accelerating field. The slope of the front part of the injected electrons is too large, and this part of the electron distribution is not compressed.

phase-space distribution of the electrons is shown at three different locations along the optical axis following the laser pulse. Immediately after the density down-ramp [Fig. 7(a)], the injected electrons are distributed along a line in phase-space, corresponding to a spread both in energy and longitudinal position. After propagating a short distance, the average energy of the injected electrons is increased [Fig. 7(b)]. Furthermore, since the electrons have a longitudinal spread, they experience different electric field strength. Locally, this results in a rotation of the phase-space distribution of electrons, and globally the phase-space distribution appears to be bending. In the final step [Fig. 7(c)], the distribution of electrons has been deformed into a U-shape, corresponding to an increased distribution of electrons at an energy corresponding to the bottom of the U-shape. Thus, the rotation and bending of the original phase-space distribution of electrons thus acts to compress the energy spectrum.

In conclusion, we have demonstrated independent control of the number of injected electrons and their final energy distribution in a laser wakefield accelerator using a simple setup to tailor the density distribution. It has been shown that electrons are injected in the density down-ramp between two regions of different electron number density. The shot-to-shot fluctuations in both charge and energy are greatly improved in comparison to electron beams generated by self-injection. The same setup will be used in future experiments to study acceleration over longer distances and also to study localized ionization-induced injection.

ACKNOWLEDGMENTS

We acknowledge the support of the Swedish Research Council, the Knut and Alice Wallenberg Foundation, the Swedish Foundation for Strategic Research, Laserlab-Europe/CHARPAC (Grant Agreement No. 284464, EC's 7th Framework Programme) and EuCARD2/ANAC2 (Grant Agreement No. 312453, EC's 7th Framework Programme).

[1] T. Tajima and J. M. Dawson, Phys. Rev. Lett. **43**, 267 (1979).

[2] C. G. R. Geddes, C. Toth, J. van Tilborg, E. Esarey, C. B. Schroeder, D. Bruhwiler, C. Nieter, J. Cary, and W. P. Leemans, Nature (London) **431**, 538 (2004).

[3] J. Faure, Y. Glinec, A. Pukhov, S. Kiselev, S. Gordienko, E. Lefebvre, J.-P. Rousseau, F. Burgy, and V. Malka, Nature (London) **431**, 541 (2004).

[4] S. P. D. Mangles, C. D. Murphy, Z. Najmudin, A. G. R. Thomas, J. L. Collier, A. E. Dangor, E. J. Divall, P. S. Foster, J. G. Gallacher, C. J. Hooker, D. A. Jaroszynski, A. J. Langley, W. B. Mori, P. A. Norreys, F. S. Tsung,

R. Viskup, B. R. Walton, and K. Krushelnick, Nature (London) **431**, 535 (2004).

[5] D. Umstadter, J. K. Kim, and E. Dodd, Phys. Rev. Lett. **76**, 2073 (1996).

[6] E. Esarey, R. F. Hubbard, W. P. Leemans, A. Ting, and P. Sprangle, Phys. Rev. Lett. **79**, 2682 (1997).

[7] J. Faure, C. Rechatin, A. Norlin, A. Lifschitz, Y. Glinec, and V. Malka, Nature (London) **444**, 737 (2006).

[8] A. Pak, K. A. Marsh, S. F. Martins, W. Lu, W. B. Mori, and C. Joshi, Phys. Rev. Lett. **104**, 025003 (2010).

[9] C. McGuffey, A. G. R. Thomas, W. Schumaker, T. Matsuoka, V. Chvykov, F. J. Dollar, G. Kalintchenko, V. Yanovsky, A. Maksimchuk, K. Krushelnick, V. Y. Bychenkov, I. V. Glazyrin, and A. V. Karpeev, Phys. Rev. Lett. **104**, 025004 (2010).

[10] M. Chen, E. Esarey, C. B. Schroeder, C. G. R. Geddes, and W. P. Leemans, Phys. Plasmas **19**, 033101 (2012).

[11] F. G. Desforges, B. S. Paradkar, M. Hansson, J. Ju, L. Senje, T. L. Audet, A. Persson, S. Dobosz-Dufrénoy, O. Lundh, G. Maynard, P. Monot, J.-L. Vay, C.-G. Wahlström, and B. Cros, Phys. Plasmas **21**, 120703 (2014).

[12] S. Bulanov, N. Naumova, F. Pegoraro, and J. Sakai, Phys. Rev. E **58**, R5257 (1998).

[13] H. Suk, N. Barov, J. B. Rosenzweig, and E. Esarey, Phys. Rev. Lett. **86**, 1011 (2001).

[14] A. J. Gonsalves, K. Nakamura, C. Lin, D. Panasenko, S. Shiraishi, T. Sokollik, C. Benedetti, C. B. Schroeder, C. G. R. Geddes, J. van Tilborg, J. Osterhoff, E. Esarey, C. Toth, and W. P. Leemans, Nat. Phys. **7**, 862 (2011).

[15] M. Burza, A. Gonoskov, K. Svensson, F. Wojda, A. Persson, M. Hansson, G. Genoud, M. Marklund, C.-G. Wahlström, and O. Lundh, Phys. Rev. ST Accel. Beams **16**, 011301 (2013).

[16] G. Golovin, S. Chen, N. Powers, C. Liu, S. Banerjee, J. Zhang, M. Zeng, Z. Sheng, and D. Umstadter, Phys. Rev. ST Accel. Beams **18**, 011301 (2015).

[17] J. Faure, C. Rechatin, O. Lundh, L. Ammoura, and V. Malka, Phys. Plasmas **17**, 083107 (2010).

[18] K. Schmid, A. Buck, C. M. S. Sears, J. M. Mikhailova, R. Tautz, D. Herrmann, M. Geissler, F. Krausz, and L. Veisz, Phys. Rev. ST Accel. Beams **13**, 091301 (2010).

[19] A. Lifschitz, X. Davoine, E. Lefebvre, J. Faure, C. Rechatin, and V. Malka, J. Comput. Phys. **228**, 1803 (2009).

[20] G. R. Plateau, N. H. Matlis, C. G. R. Geddes, A. J. Gonsalves, S. Shiraishi, C. Lin, R. A. van Mourik, and W. P. Leemans, Rev. Sci. Instrum. **81**, 033108 (2010).

[21] A. Buck, K. Zeil, A. Popp, K. Schmid, A. Jochmann, S. D. Kraft, B. Hidding, T. Kudyakov, C. M. S. Sears, L. Veisz, S. Karsch, J. Pawelke, R. Sauerbrey, T. Cowan, F. Krausz, and U. Schramm, Rev. Sci. Instrum. **81**, 033301 (2010).

[22] S. P. D. Mangles, A. G. R. Thomas, O. Lundh, F. Lindau, M. C. Kaluza, A. Persson, C.-G. Wahlström, K. Krushelnick, and Z. Najmudin, Phys. Plasmas **14**, 056702 (2007).

[23] M. Hansson, L. Senje, A. Persson, O. Lundh, C.-G. Wahlström, F. G. Desforges, J. Ju, T. L. Audet, B. Cros, S. D. Dufrénoy, and P. Monot, Phys. Rev. ST Accel. Beams **17**, 031303 (2014).

[24] E. Esarey, C. B. Schroeder, and W. P. Leemans, Rev. Mod. Phys. **81**, 1229 (2009).

Paper VI

Study of Electron Acceleration and X-Ray Radiation as a Function of Plasma Density in Capillary-Guided Laser Wakefield Accelerators

J. Ju, K. Svensson, H. Ferrari, A. Döpp, G. Genoud, F. Wojda, M. Burza, A. Persson, O. Lundh, C.-G. Wahlström, & B. Cros.

Phys. Plasmas **20**, 083106 (2013).

PHYSICS OF PLASMAS **20**, 083106 (2013)

Study of electron acceleration and x-ray radiation as a function of plasma density in capillary-guided laser wakefield accelerators

J. Ju,[1] K. Svensson,[2] H. Ferrari,[3] A. Döpp,[1] G. Genoud,[2] F. Wojda,[2] M. Burza,[2] A. Persson,[2] O. Lundh,[2] C.-G. Wahlström,[2] and B. Cros[1,a)]
[1]*Laboratoire de Physique des Gaz et des Plasmas, CNRS-Université Paris-Sud, 91405 Orsay, France*
[2]*Department of Physics, Lund University, P.O. Box 118, S-22100 Lund, Sweden*
[3]*Consejo Nacional de Investigaciones Científicas y Técnicas (CONICET) and CNEA-CAB, Argentina*

(Received 3 May 2013; accepted 15 July 2013; published online 6 August 2013)

Laser wakefield electron acceleration in the blow-out regime and the associated betatron X-ray radiation were investigated experimentally as a function of the plasma density in a configuration where the laser is guided. Dielectric capillary tubes were employed to assist the laser keeping self-focused over a long distance by collecting the laser energy around its central focal spot. With a 40 fs, 16 TW pulsed laser, electron bunches with tens of pC charge were measured to be accelerated to an energy up to 300 MeV, accompanied by X-ray emission with a peak brightness of the order of 10^{21} ph/s/mm^2/mrad^2/0.1%BW. Electron trapping and acceleration were studied using the emitted X-ray beam distribution to map the acceleration process; the number of betatron oscillations performed by the electrons was inferred from the correlation between measured X-ray fluence and beam charge. A study of the stability of electron and X-ray generation suggests that the fluctuation of X-ray emission can be reduced by stabilizing the beam charge. The experimental results are in good agreement with 3D particle-in-cell (PIC) simulation. © *2013 AIP Publishing LLC*. [http://dx.doi.org/10.1063/1.4817747]

I. INTRODUCTION

Laser wakefield acceleration (LWFA) is a mechanism with a high potential for the development of compact electron and radiation sources and accelerating structures scalable to high electron energy. A few decades ago, relativistic plasma waves driven by intense laser pulses were proposed as means to accelerate electrons due to the ultra-high longitudinal electric field that can be sustained by a plasma.[1] Since then, laser wakefield acceleration mechanisms have been investigated theoretically, numerically, and experimentally, and remarkable progress has been made worldwide.[2] A first breakthrough was achieved in 2004 when the generation of peaked electron distributions with an energy of ~100 MeV was demonstrated.[3–5] Subsequently, electrons at the 1 GeV level were reported in an experiment where the acceleration length was extended with a plasma channel to a few centimeters.[6] In LWFA, plasma wave excitation relies on the ponderomotive force of a short, intense laser pulse expelling electrons out of the high laser intensity regions. For high enough laser intensity, typically above 10^{18} W/cm^2, plasma electrons can be completely expelled out of the intense laser volume and self-trapped in the accelerating potential of the plasma wave.[7] In addition to the accelerating fields associated with the plasma wave, the accelerated electrons experience transverse fields. Thus, these electrons can undergo strong transverse oscillations, known as betatron oscillations, giving rise to the emission of synchrotron-like radiation, which has been studied theoretically[8,9] and observed experimentally.[10–13] This X-ray source is very attractive for applications to time-resolved imaging due to its compactness and its intrinsic properties as it is spatially coherent, brilliant, with duration as short as a few femtoseconds, and perfectly synchronized to the pump laser.[11]

The plasma density and length are key parameters to control the laser plasma interaction regime and therefore the regime of operation of the accelerator. Laser wakefield excitation in long plasmas is of interest either in the blow-out regime, where simulations[7] show that using long plasmas at relatively low densities is a way to achieve electron acceleration to the multi-GeV range and beyond, or in the more linear acceleration regime[14] for multi-stage acceleration. To achieve low density plasmas, and guide the intense laser over a long enough distance, using capillary tubes[15] has several advantages:[16] the plasma density inside capillary tubes can be arbitrarily low, as the laser beam is guided by reflection from the tube walls and there is no density requirement for guiding, so that different plasma density ranges can be explored; the capillary tube provides a shock-free gas medium, beneficial for generating stable electrons[17] and X-rays; the capillary tube is able to collect part of the laser energy in the wings around the central focal spot to assist laser guiding over a longer distance than in a gas jet or gas cell.[18,19] Especially in the case of laser guiding by capillary tubes with radius larger than twice the waist of the focal spot, nearly all the laser energy can be collected by the interplay of self-focusing and reflection from the capillary wall, leading to a higher laser peak intensity and longer distance of self-focusing than in a medium without boundary. Electron self-injection near threshold and acceleration inside capillary tubes were observed previously with a moderately intense laser.[18–20] Operating around the threshold of self-injection, electrons were observed only in a narrow density regime,[19] and the photon energy (~1 keV) and X-ray fluence was lower than 1×10^5 ph/mrad^2.

In this paper, we present a study of electron self-injection in long plasmas produced inside capillary tubes for a value of

a)Electronic mail: brigitte.cros@u-psud.fr

the input laser intensity around 5.4×10^{18} W/cm^2. Highlights from the same experiment were published previously;[21] here a detailed analysis is presented, including simulation results. The influence of the plasma density and of the capillary tube parameters on electron energy, beam charge, electron self-trapping, and X-ray intensity are characterized using the measured electron and X-ray beams. The X-ray profile is geometrically related to the emission positions in the plasma by the rim of the capillary exit and provides a good probe of the acceleration process. We also address the stability of the accelerated electrons and the corresponding X-ray radiation. Those results are compared with numerical particle-in-cell (PIC) simulation results obtained with the code CALDER-CIRC.[22]

II. EXPERIMENT

A. Experimental setup

An experiment was carried out with the multi-terawatt laser at the Lund Laser Centre (LLC) in Sweden. The titanium-doped sapphire (Ti:Sa) laser operates in the chirped pulse amplification mode and was able to deliver a laser pulse with an energy of 650 mJ at 800 nm central wavelength on target, and a FWHM pulse duration of 40 fs. Figure 1 illustrates the experimental setup. The laser beam was focused 1 mm inside the capillary tubes by a $f = 76$ cm off-axis parabola. Using a motorized holder composed of three translation and two rotation stages, capillary tubes were aligned on the laser axis. The capillary tubes are made of glass: their inner surface is optically smooth at the laser wavelength, and their walls are thick, with an external diameter of 5.5 mm. Hydrogen gas was filled into the capillary tubes through two ~270 μm wide slits situated at 2.5 mm from each capillary end. The plasma density inside the capillary tubes was adjusted by a gas regulator controlling the upstream reservoir pressure.[23] A 10 cm long permanent magnet with a central field of 0.7 T over a 15 mm gap deflected electrons downwards onto a scintillating (Kodak Lanex Regular) screen which was imaged by a 12-bit charge-coupled device (CCD) camera. Electrons with energies below 42 MeV could not reach the Lanex screen and were thus not recorded. The Lanex screen was protected by an aluminum shield from direct exposure to the laser light, and a narrow-band interference filter (IF) was placed in front of the CCD camera to reduce background light. A tracking code was developed to retrieve electron spectra from the raw images of Lanex, and the beam charge was evaluated from the absolute calibration of Lanex.[24,25] The beam charge shown in Ref. 21 was underestimated by a factor of ~2.3 owing to an incorrect determination of the transmission of the IF filter. Corrected values are given in this paper. On the same laser shots, the far-field betatron radiation was also recorded using a 16-bit X-ray CCD camera placed about 110 cm away from the capillary exit. This camera has a 13×13 mm^2 chip, corresponding to a collecting angle of 12×12 mrad^2. A set of thin metallic filters (Zr: 3 μm, Sn: 3 μm, V: 3 μm, Fe: 3 μm, Ni: 5 μm) with different X-ray absorption edges was inserted in front of the X-ray camera to allow an estimation of the photon spectra. Two beryllium windows with a total thickness of 300 μm and a 5 mm air gap in the X-ray path in front of the X-ray camera prevented detection of photons with energy less than 2 keV.

The energy distribution in the transverse plane delivered by the laser system exhibits a nearly flat-top cylindrically symmetrical distribution before focusing. In the focal plane, the corresponding energy distribution is close to an Airy distribution, as shown in Fig. 2. The focal spot shown in Fig. 2(a) was obtained by tuning a deformable mirror placed after the compressor to compensate for aberrations in the laser wavefront. The average radius of the focal spot at the first minimum can be determined from the radial profile of energy distribution averaged over the angles to be 19.7 ± 0.8 μm, which yields an on-axis peak intensity of $(5.4 \pm 0.1) \times 10^{18}$ W/cm^2 and a normalized laser vector potential of $a_0 \simeq 1.6$. The energy fraction contained within the grey shaded area in Fig. 2(b) is estimated to be equal to about 43% of the laser energy in the focal plane, which is comparable with the theoretical prediction of ~47% energy within FWHM for an Airy distribution.

The capillary tubes employed in this experiment range from 152 μm to 254 μm in diameter and 10 mm to 30 mm in length. For the focal spot shown in Fig. 2, the focal spot diameter at the first minimum over capillary diameter ratio is in the range 0.26 to 0.16 and gives rise to multimode[15] excitation at the entrance of the capillary tubes.

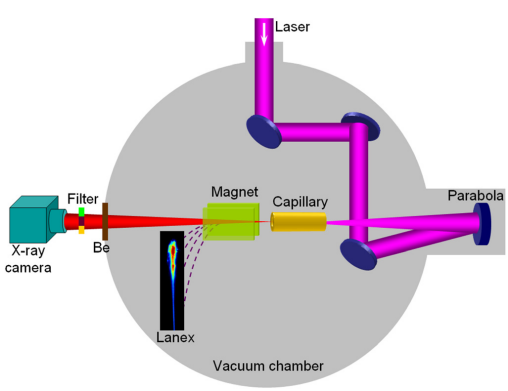

FIG. 1. Schematic diagram of the experimental arrangement. Elements inside the grey area are under vacuum. The Lanex screen shows a typical energy spectrum of the accelerated electrons obtained in experiment.

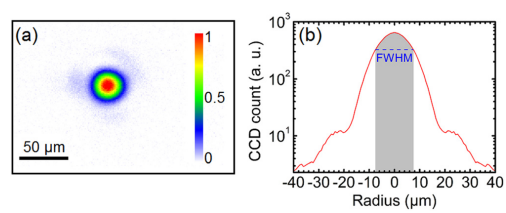

FIG. 2. (a) Energy distribution in the focal plane normalized to its maximum, (b) averaged radial profile of laser energy in logarithmic scale. The energy in the grey shaded area, of diameter equal to FWHM, represents about 43% of the laser energy in the focal spot.

B. Electron acceleration

Over the whole capillary parameter range explored, electron beams with charge in the range 1 to 150 pC were observed, and the electron spectra were found to sensitively depend on plasma density. As mentioned previously, the beam charge determined experimentally takes into account electrons with an energy above the detector lower limit of 42 MeV. Examples of energy spectra, obtained for a 10 mm long capillary with a diameter of 178 μm, are shown in Fig. 3 for two different values of the plasma electron density; raw Lanex images are shown in panels (a) and (c), while the corresponding spectra are plotted in (b) and (d) after summing in the transverse direction and rescaling to account for magnet dispersion. Accelerated electrons with a maximum energy of 300 MeV and a charge of ~2 pC were obtained for a plasma density $n_e = (5.4 \pm 0.3) \times 10^{18}$ cm^{-3} as shown in Figs. 3(a) and 3(b). The maximum energy is defined when the energy spectrum decreases to 10% of its peak value. The electron beam FWHM divergence in the case of Fig. 3(b) is about 5.2 mrad. It was found that at such a low plasma density, the electron beam properties exhibit large shot-to-shot fluctuations, due to the fact that LWFA operates just above the threshold of self-injection.[20] When a higher plasma density, $n_e = (8.1 \pm 0.5) \times 10^{18}$ cm^{-3}, was used electron beams with a higher charge were produced, about 40 pC for the example of Figs. 3(c) and 3(d). In this case, the maximum electron energy was limited to 120 MeV. Moreover, several structures are observed in the raw image of Fig. 3(c), which can be interpreted as resulting from multiple electrons trapping inside the bubble along the acceleration distance or electrons emergence from different plasma buckets.

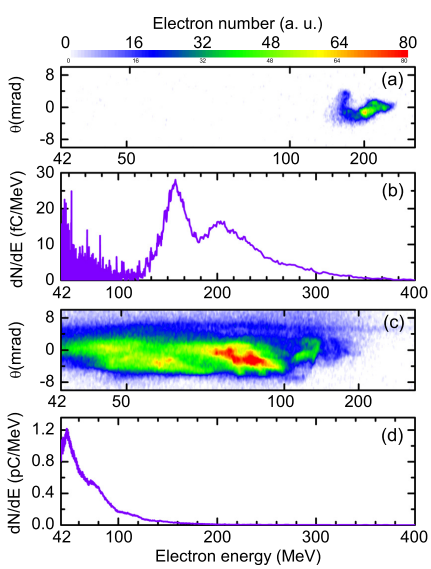

FIG. 3. Raw Lanex images and their corresponding energy spectra inside a 10 mm long, 178 μm diameter capillary tube at plasma electron densities: $(5.4 \pm 0.3) \times 10^{18}$ cm^{-3} for (a)–(b) and $(8.1 \pm 0.5) \times 10^{18}$ cm^{-3} for (c)–(d), respectively.[21]

In contrast to the narrow density range where self-electron trapping occurs at lower laser intensities, around 0.8×10^{18} W/cm^2 in our previous experiments,[19,20] for the value of intensity used for the results presented in this paper, electrons were detected in a broad range of plasma densities above the threshold for self-injection, as shown in Fig. 4. In this figure, the maximum electron beam energy (a), and the charge estimated for the corresponding shots (b), are plotted as functions of the plasma electron density, inside a 10 mm long, 178 μm diameter capillary tube. The black squares are experimental results, each point corresponding to one single laser shot and error bars to the precision of the measurements.

Figure 4(a) shows that the highest value of maximum beam energy is achieved for the lowest value of electron density where self-injection occurs, and that the beam maximum energy decreases as the plasma density is increased, in agreement with previous findings.[3,26] The measured dependence of beam maximum energy behaves as $1/n_e$ and can be compared to the phenomenological scaling law developed for the 3D non-linear regime,[7] when the electron maximum energy is limited by dephasing: $\mathcal{E}\,[\mathrm{MeV}] = \frac{1}{3} a_0 n_c / n_e$, where n_c is the critical density. Dephasing occurs when an accelerated electron slips forward in the plasma wave and enters a decelerating phase; its characteristic length is given in this non-linear regime by $L_{dph} = \frac{4}{3}\sqrt{a_0} n_c / (n_e k_p)$ where k_p is the plasma wave wavenumber. The experimental points are in a region of the graph limited by curves with values of a_0 in the range 1.1 to 2.6, which can be interpreted as effective values of a_0 over the whole plasma length. The point of highest electron energy in Fig. 4(a) corresponds to a curve with $a_0 = 2.6$. During the

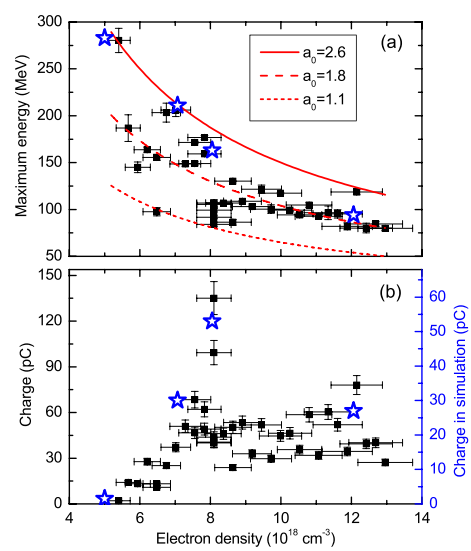

FIG. 4. (a) Maximum electron beam energy and (b) charge as a function of plasma electron density, at the output of a 10 mm long, 178 μm diameter capillary tube. The black squares are experimental results, each point corresponding to one single laser shot. Blue stars are the results of PIC simulations. The curves in (a) show the predictions of scaling laws obtained for the three values of a_0 indicated in the legend.

propagation in the plasma, the increase of laser intensity is linked to pulse compression and self-focusing as the incident power P is above $P_c[\mathrm{GW}] \simeq 17 n_c/n_e$, the critical power for self-focusing: $2.8P_c < P < 7.2P_c$. The maximum energy values measured agree with simulation results, plotted as blue stars, as will be presented in Sec. III.

The dephasing length L_{dph} is calculated to be about 1.6 mm for $n_e = 5.4 \times 10^{18}\,\mathrm{cm}^{-3}$. L_{dph} becomes shorter at higher plasma densities, and the capillary length, L_{cap}, was always longer than the dephasing length in this experiment. The electrons observed in this experiment were thus accelerated over the dephasing length and decelerated, so that their output energies are in general lower than the prediction of the scaling law. The electron maximum energy obtained by PIC simulation at the output of the capillary tube agrees well with experimental observations. At low density, the simulation data are consistent with the curve for $a_0 = 2.6$, while they start to deviate from it and approach the curve for $a_0 = 1.8$ as density increases, as the result of the shorter dephasing length and longer propagation distance inside the capillary beyond the dephasing length.

For plasma densities below $8 \times 10^{18}\,\mathrm{cm}^{-3}$, the measured electron energy exhibits larger shot-to-shot fluctuations than in the larger density range. This can be attributed to electron injection just above the threshold of self-trapping, observed previously[20] to be around $P/P_c \simeq 3.3$, corresponding here to a density of about $6 \times 10^{18}\,\mathrm{cm}^{-3}$.

Figure 4(b) shows that the beam charge reaches a maximum around the value of plasma density, $n_e = 8 \times 10^{18}\,\mathrm{cm}^{-3}$ in the experiment and the simulation. This observation can be understood as follows. Here, the characteristic depletion length of laser energy is given by $L_{dpl} = c\tau n_c/n_e$ and is larger than the dephasing length in the range of electron density studied. Electron injection and acceleration occur above the threshold and the amount of accelerated charge increases with the density, as the value of the ratio P/P_c is increased for a fixed incident laser power. The increase of accelerated charge above $n_e = 5 \times 10^{18}\,\mathrm{cm}^{-3}$ can be explained by more efficient electron self-trapping occurring for a higher ratio of P/P_c, as observed in Ref. 27 and by the decrease of the phase velocity of the plasma wave. For densities larger than $n_e = 8 \times 10^{18}\,\mathrm{cm}^{-3}$, the dephasing and pump depletion length being less than 1 mm and 2 mm, respectively, in this range of plasma density, some electrons are scattered during the propagating in the remaining part of the plasma,[28] roughly 5 mm long, and do not reach the detector. The main contribution to the difference of beam charge in simulation and experiment is due to electrons going out from the simulation box. The simulation box [as seen in Fig. 12(c)] moves forward with the group velocity of the laser in the plasma $v_g \simeq 0.998c$, while the accelerated electrons in the first plasma bucket move nearly with speed of light c, so more and more electrons overrun the front boundary of the simulation box and get lost with computation time increasing, leading to the observed lower beam charges in simulation.

C. Betatron radiation

In the regime of acceleration described in Sec. I, trapped electrons, if injected off-axis or with some transverse momentum, oscillate transversely during acceleration and generate intense X-ray emission, often referred to as betatron radiation.[10] A relativistic electron with a total energy of $\gamma m_e c^2$ wiggles at the betatron frequency $\omega_\beta = \omega_p/\sqrt{2\gamma}$, where ω_p is the plasma frequency. The radiated spectrum is determined by the strength parameter $K = \gamma r_\beta \omega_\beta/c$, where r_β is the amplitude of the electron oscillation. When $K \gg 1$ (regime for our experimental condition[21]), the on-axis X-ray radiation has a synchrotron-like spectrum,[8] characterized by $d^2I/dEd\Omega|_{\theta=0} \propto (E/E_c)^2 \mathcal{K}^2_{2/3}(E/E_c)$. The critical energy is defined as $E_c = 3\hbar K\gamma^2\omega_\beta$, and $\mathcal{K}_{2/3}$ is the modified Bessel function of the second kind. The properties of the X-ray emission therefore depend on the accelerated electrons beam charge, energy, and oscillation amplitude, and through these quantities, on the plasma density. For instance, Fig. 5 shows the X-ray images corresponding to the shots of Fig. 3 at two different plasma densities. Figure 5(a) shows that no X-ray was detected for the low density case: although the electron energy is relatively high for this shot, the associated beam charge was too low to generate a signal on the CCD. On the contrary, as seen in Fig. 5(b), a strong X-ray signal was measured for the shot at higher plasma density owing to a higher beam charge. The different filters can be clearly seen, together with the grid supporting them. The round structure near the edges of the image is due to the filters holder blocking the edges of the beam.

The photon energy was quantitatively determined using the transmissions of the X-ray beam through different metals, and a least squares method.[11] For each metallic filter i, the theoretical camera response is calculated as the product of the filter transmission, $T_i(E)$, the transmission of 5 mm of air and 300 μm of beryllium, $T(E)$, and the CCD quantum efficiency $Q(E)$, as $C_i^{the} = \int \frac{d^2I}{dEd\Omega} T_i(E)T(E)Q(E)\,dE$. Assuming a synchrotron like spectrum, and minimizing the difference between theoretical and experimental camera responses for different filters, $\sum_i (C_i^{the} - C_i^{exp})^2$, gives the best fit of critical energy E_c. For the case of Fig. 5(b) obtained in a 10 mm long, 178 μm diameter capillary tube, the critical energy was evaluated to be 5.4 keV at $n_e \simeq 8 \times 10^{18}\,\mathrm{cm}^{-3}$.

Figure 6 shows that betatron X-ray radiation can be tuned by varying the plasma density. In this case, the X-ray fluence peaks at $5.7 \times 10^5\,\mathrm{ph/mrad}^2$ for $n_e \simeq 8 \times 10^{18}\,\mathrm{cm}^{-3}$ and behaves similarly as the beam charge given in Fig. 4(b). At lower plasma densities, the electron number decreases rapidly, so the photon number diminishes accordingly. If the

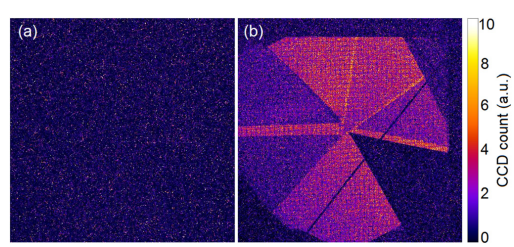

FIG. 5. X-ray beam images recorded on the X-ray CCD equipped with the set of metallic pieces described in the text; images (a) and (b) correspond to the shots of Figs. 3(a) and 3(c), respectively.[21]

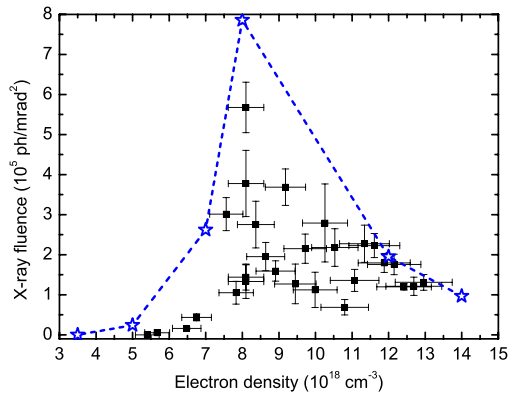

FIG. 6. X-ray fluence as a function of plasma electron density corresponding to the electron beams shown in Fig. 4. Each black square corresponds to one laser shot, blue stars represent the results obtained from 3D PIC simulation.

beam charge is too low, the X-ray signal finally vanishes, as seen in Fig. 5(a). Above the optimum density, the beam charge does not increase, while electron energy becomes lower as laser pump depletion length and the dephasing length shorten, which also leads to a drop of X-ray signal. This dependence of X-ray fluence on plasma density is well reproduced by simulation results, plotted as blue stars in Fig. 6.

Betatron X-ray radiation is also a powerful tool to investigate the acceleration process because of its strong dependence on the electron properties.[19,20,29] Figure 7 illustrates how the X-ray profile measured at the exit of capillary tubes can be used to determine the volume and locations inside the plasma where electrons are accelerated. X-rays are emitted as soon as electrons are trapped and wiggle in the plasma bubble. X-rays generated at different longitudinal positions inside the capillary tube will exit with an aperture cone determined by the capillary diameter, and the distance from the capillary exit. For an extended emission region inside the plasma, the X-ray image will exhibit a transition zone of varying intensity, which can be directly related to the length of the electron acceleration region inside the plasma.[19,20] In the following calculation, the X-ray source is assumed to be one dimensional, as its transverse size is of the order of a few microns and can be neglected compared to the typical longitudinal extension of the emission process (∼mm).

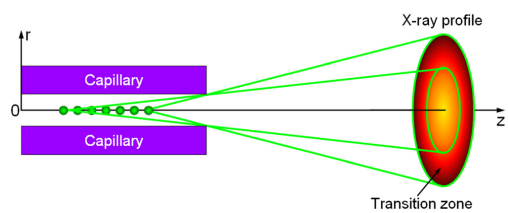

FIG. 7. Schematic illustration of the relation between the intensity distribution of the X-rays in the detector plane and the emission region inside a capillary tube.

Using the cylindrical coordinates illustrated in Fig. 7, the longitudinal profile of betatron emission $dI_X(z)/dz$ can be determined from the X-ray signal measured in the detector plane, $S(r,\theta)$, using[29]

$$\frac{dI_X(z)}{dz} = -\frac{1}{2\pi}\int_0^{2\pi} \frac{\partial S(r(z),\theta)}{\partial r}\frac{r^2(z)}{r_{cap}L_X}\,d\theta, \qquad (1)$$

with $r(z) = r_{cap}L_X/(L_{cap}-z)$. $L_X \simeq 110$ cm is the distance from the capillary exit to the detection plane; r_{cap}, L_{cap} stand for capillary radius and length, respectively.

The X-ray source is closer to the capillary exit when a short capillary tube is used, which geometrically produces a larger aperture shadow. For example, most of the shadow of the 10 mm long, 178 μm diameter capillary was beyond the X-ray detector size, as shown in Fig. 8(a). Only roughly a quarter of the beam going through the capillary could be recorded. As the shortest capillary tube studied, $L_{cap} = 10$ mm, is longer than the whole distance of laser evolution and electron acceleration (see Figs. 11 and 12), the X-ray emission due to electron trapping and acceleration is expected to be the same for a longer capillary tube. In order to determine the X-ray profile, a 30.5 mm long capillary tube was employed, for which all the X-ray beam confined by the capillary exit could be recorded, like in Fig. 8(b). The observed beam consists of a nearly homogeneous background together with a bright feature which suggests special electron trajectories in the plasma.[30] Excluding the section of the beam containing a bright feature inside the capillary shadow in Fig. 8(b), the radial profile of the X-ray signal averaged over the azimuthal angle was calculated and plotted in Fig. 8(c). Substituting this profile into Eq. (1), the longitudinal distribution of X-ray emission was obtained and plotted in Fig. 8(d) for five successive shots. $z = 0$ corresponds to the capillary entrance. It shows that electrons start to generate detectable X-rays with photon energy

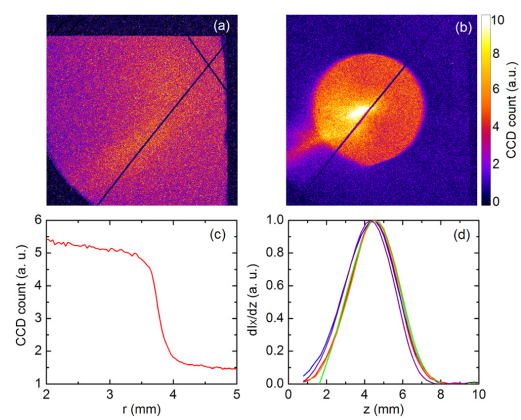

FIG. 8. X-ray beam distribution measured for $n_e = (8.1 \pm 0.5) \times 10^{18}$ cm^{-3} at the output of (a) a 10 mm long, 178 μm diameter capillary tube, (b) a 30.5 mm long, 178 μm diameter capillary tube; (c) averaged radial intensity of (b); (d) longitudinal profiles of X-ray emission, for five consecutive shots under the same conditions. The curves are normalized to their respective maxima.

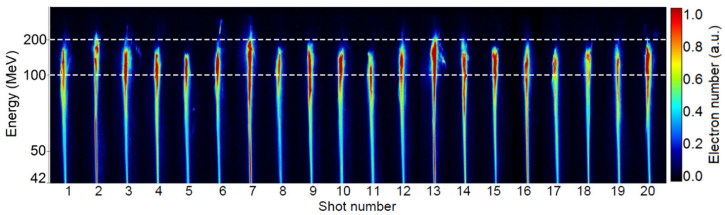

FIG. 9. Raw images of electron spectra for 20 consecutive shots measured at the output of a 10 mm long, 203 μm diameter capillary tube for $n_e = (7 \pm 0.4) \times 10^{18}$ cm^{-3}.

above 2 keV around $z \simeq 2$ mm. The photons become detectable (>2 keV) when the electron energy is higher than $\sim$50 MeV for the plasma density 8×10^{18} cm^{-3} and oscillation amplitude $r_\beta = 2\,\mu$m. After a distance corresponding to electron acceleration, the X-ray emission has a FWHM of about 3 mm, and peaks at $z \simeq 4.5$ mm, where the electrons reach their maximum energy, because the radiation power scales with γ^4. Afterwards, the X-ray emission decreases and stops at $z \simeq 7$ mm where the laser becomes too weak to sustain self-focusing (See Figs. 11 and 12). The precision of the above analysis is limited by the beam transverse source size. For the position of the emission peak at $z = 4.5$ mm, a beam size $r_\beta = 2\,\mu$m will result in the same intensity gradient on the detector as does a longitudinal emission extending $\sim$600 μm, which sets the resolution of the determination of the emission position.

D. Electrons and x-rays stability

Figure 6 shows that the X-ray fluence exhibits large shot-to-shot fluctuations. These fluctuations may be due to the process of electron injection, determining beam charge, or acceleration conditions, determining the electrons energy. Both effects contribute to the X-ray intensity, as shown in Sec. II C, where the X-ray distribution was used to characterize the acceleration process. In Fig. 8(d), the calculated longitudinal profiles of X-ray emission indicate a similar position and distance of X-ray emission for consecutive shots, which can be related to similar processes of electron acceleration. Thus, it can be assumed that the origin of the fluctuations lies more in the trapping conditions, and the amount of injected charge.

In order to get some insight on the origin of fluctuations, the stability of electrons and X-rays was examined. Figure 9 displays the electron spectra of 20 consecutive shots obtained with a 10 mm long, 203 μm diameter capillary tube. The plasma density was $n_e = (7 \pm 0.4) \times 10^{18}$ cm^{-3}, where strong signals could be obtained for both electrons and X-rays. For these parameters, electron injection occurred for every shot. On average, $\sim$45 pC electrons were accelerated to a maximum energy of $\sim$150 MeV.

For electrons, the measured maximum energy $\mathcal{E}_{max}$ (147 $\pm$ 12 MeV) and the mean energy $\bar{\mathcal{E}}_e$ (91 $\pm$ 7 MeV) both exhibit stability with standard deviation of 8%. The beam charge shows a shot-to-shot fluctuation of 17%. The percentages indicated in this section are the ratios of standard deviation over mean. The critical energy of X-ray shows a fluctuation of about 9%, and the X-ray fluence fluctuation was measured to be 12%. Note that these X-rays constitute the most intense on-axis part, measured by the detector with a small collecting angle, which may have smaller fluctuations than the total X-ray beam.

Figure 10 shows the measured X-ray fluence as a function of the measured beam charge, and a linear fit of the data. The slope of the linear fit is calculated to be 7.8×10^{-4} ph/mrad^2 per electron. The scaling developed for betatron radiation in ion channels[31] shows that the average number of photons emitted by an oscillating electron is given by $N_X \simeq 5.6 \times 10^{-3} N_\beta K$, where N_β is the number of betatron oscillations performed by the electron. The opening solid angle of the betatron radiation,[8] $\Omega = K/\gamma^2$, can be used to evaluate the strength parameter. The number of photons per solid angle can therefore be theoretically estimated to be $N_X/\Omega \simeq 5.6 \times 10^{-9} \gamma^2 N_\beta$ in unit of ph/mrad^2 per electron. By measuring electron energy, γ was evaluated as the average value plus/minus three times standard deviation to be $\gamma = 183 \pm 40$. Using the value of the slope of the linear fit in Figure 10, the number of electron oscillations is calculated to be $N_\beta \simeq 4 \pm 2$. From the experimental results in Fig. 10, we are thus able to estimate that the electron fulfills about four oscillations in the plasma. This finding is in reasonable agreement with the determined $N_\beta \simeq 5$ in PIC simulation for $n_e = 7 \times 10^{18}$ cm^{-3}.

The instability of beam charge is probably largely due to the process of electron self-injection. In the blow-out regime, the dynamics of electron self-injection is a complex process dependent on the laser non-linear evolution,[27] the bubble dynamics,[7] and beam loading.[32] As a result, a slight change to one of these processes, due, for example, to fluctuations of the laser energy distribution at the entrance of the plasma,

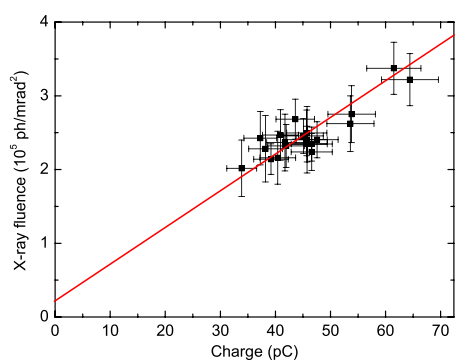

FIG. 10. X-ray fluence as a function of beam charge for the 20 shots shown in Fig. 9, where the red line is a linear fit.

will subsequently induce a large variation of beam charge, and consequently of the X-ray fluence. Stabilizing the electron beam charge would thus be a way to reduce shot-to-shot fluctuations and improve X-ray stability. The beam charge has been observed to be a considerably unstable parameter of the electron bunches produced in LWFA. Typically, the relative variation of beam charge (standard deviation/mean) is >50% for commonly used gas jets,[33] 16% for gas cell,[17] and down to 20% for advanced optical injection techniques.[34] Although there is no corresponding study on X-ray stability in the literature, it is still reasonable to stress that X-ray stability would be improved by controlling beam charge with some sophisticated approach, like the recent staged acceleration with separated nozzle injector[35] which showed that the charge stability can be reduced to 6% by small changes to the density profile.

III. SIMULATIONS

Simulations were performed with the 3D PIC code CALDER-CIRC.[22] Parameters were chosen close to experimental ones: a FWHM 40 fs laser pulse was taken as input condition with a normalized intensity of $a_0 = 1.6$, and the transverse profile measured experimentally as shown in Fig. 2(b). In the experiment, the laser focus in vacuum was set inside the capillary at 1 mm from the capillary entrance. A similar condition was studied in the simulation and compared to focusing position at 2.5 mm from the entrance. The gas density profile inside the capillary tubes is constant over the length situated between the two slits and decreases from the slits positions to the ends of the capillary tube. Numerical simulations using the commercial code FLUENT were performed to determine the gas distribution in the capillary tube and the density profile between the slits and the capillary exit.[23] For PIC simulations, the density profiles were simply assumed to be linearly increasing from 0 to a constant value of density, n_e, over a length of 3 mm, as shown in Figs. 11(a) and 12(a); the capillary entrance is located at $z = 0$ mm and the density plateau is assumed to start at $z = 2.5$ mm. The betatron radiation was calculated from Lineard-Wiechert potentials[8] by post-processing the trajectories of electrons with energies larger than 10 MeV. More details regarding the PIC simulation can be found in Ref. 20.

Simulations were carried out for different plasma electron densities and compared to experimental results. Whereas in the experiment the laser was focused 1 mm inside capillary tubes, it was found that simulations results are in better agreement with experiments for the simulation with focus at $z = 2.5$ mm, as can be seen in Figs. 4 and 6 where simulation results are plotted as blue stars. This sensitivity to focusing position is linked to laser propagation and evolution in the plasma. In the remaining part of this section, the behavior of the laser beam intensity, electron beam energy, and X-ray emission are examined along the capillary axis and the two cases of focus positions are compared for the case of $n_e = 8 \times 10^{18}$ cm^{-3}, at which both electrons and X-rays were systematically studied in experiment.

In the case of Fig. 11, after entering the plasma, the laser central bulk quickly self-focuses, and the normalized laser

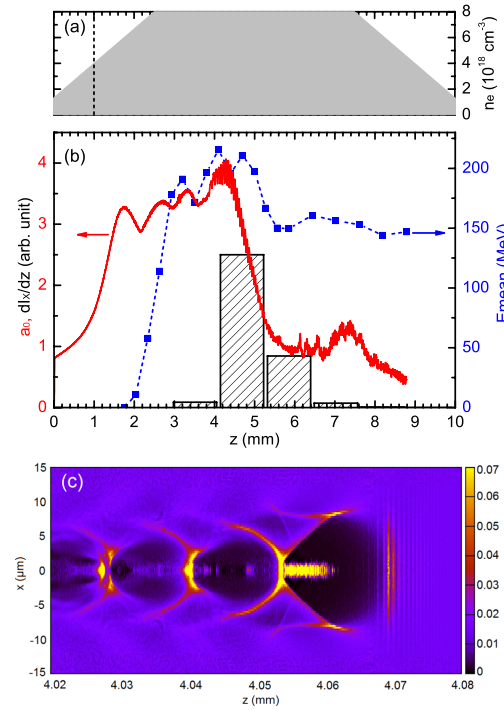

FIG. 11. Simulation results for $a_0 = 1.6$, and a background electron density $n_e = 8 \times 10^{18}$ cm^{-3}. (a) Density profile used in 3D PIC simulation with laser focus position in vacuum at $z = 1$ mm, indicated by a vertical dashed line. (b) Evolution of the normalized laser intensity (red solid line) and the mean energy (dashed blue line) of the electron bunch accelerated in the first plasma bucket. The histogram corresponds to the amplitude of X-ray emission in arbitrary unit. (c) Snapshot of plasma density around the position $z = 4.05$ mm, the laser propagates from left to right.

intensity increases up to $a_0 > 3$ at $z \simeq 1.7$ mm. With the help of capillary guiding and self-focusing, the laser propagates with a stable amplitude until $z \simeq 4.4$ mm. When most of the laser energy is transferred to the plasma wave, the laser becomes subsequently too weak to maintain self-focusing. This simulation result agrees well with the theoretical prediction[7] of laser pump depletion length $L_{dpl} \simeq 2.6$ mm. Closely following the laser pulse, a bubble with a radius of $\sim 7\ \mu$m is created, as illustrated in Fig. 11(c). An appreciable number of electrons starts to be trapped by the bubble after the first maximum of laser normalized intensity $z \simeq 2$ mm in Fig. 11(c), and the trapped electrons gain energy rapidly. The mean energy of the electron bunch produced in the first plasma bucket reaches a maximum of 215 MeV at $z \simeq 4.1$ mm and then decreases, because the electrons enter a decelerating phase. In addition, the laser intensity remains large enough ($a_0 > 3$) to trap electrons[33] over a few millimeters, so multiple electron trapping is seen in the simulation.

The betatron radiation produced by the electron beam is synchrotron-like but differs from the standard synchrotron spectrum given by $(E/E_c)^2 \mathcal{K}^2_{2/3}(E/E_c)$. That is because the accelerated electrons are widely-spread in energy and have

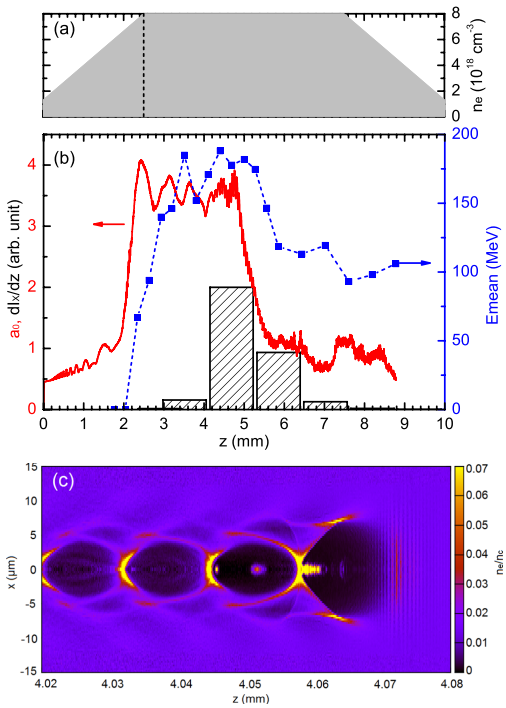

FIG. 12. Same as Fig. 11 with laser focus position in vacuum at z = 2.5 mm.

different oscillation amplitudes. Fitting the simulated spectrum with a standard synchrotron spectrum yields a critical energy of 7.7 keV, however, the simulated and the fitted spectra have a large difference in photon energy distribution. Therefore, it is more significant to define the critical energy E_c as the energy below or above which half power is radiated.[20] Accordingly E_c is 4.6 keV for this simulation case. The histogram in Fig. 11(b) represents the X-ray intensity, obtained by integrating photons from 1 to 10 keV, emitted at different longitudinal positions calculated over each 1 mm. It is seen that the X-ray generation extends from about $z = 3$ mm to around $z = 7.5$ mm and peaks at $z \simeq 4.6$ mm. This is in excellent agreement with the experimental observation presented in Fig. 8(d).

Simulations show that the X-ray pulse duration is ~35 fs at $n_e = 8 \times 10^{18}$ cm^{-3}, and the X-ray source radius was calculated to be[21] ~2 μm, which yields an X-ray peak brightness of the order of $\sim 1 \times 10^{21}$ ph/s/mm^2/mrad^2/0.1%BW. To our knowledge, this is the brightest X-ray source obtained with a 16 TW laser. Under the same laser conditions, the X-ray peak brightness is reduced by nearly two orders of magnitude when the capillary tube is replaced by a 2 mm gas jet,[21] because higher plasma densities are required to self-trap electrons over the length of the gas jet. Using a longer gas jet or a gas cell would also increase the X-ray brightness, but the use of a capillary tube enhances this effect by collecting the unfocused laser energy and reflecting it back to the axis.

The influence of the laser focus position can be evaluated by comparing Figs. 11 and 12. In Fig. 12, the laser focus position is located at the beginning of the density plateau and this leads to a faster self-focusing with a higher peak amplitude than in the case of Fig. 11. Then the laser amplitude oscillates with larger peak to peak amplitude. Electron injection occurs at about the same position $z \simeq 2$ mm, but the maximum value of the mean electron energy is higher in the case of Fig. 11 probably due to an increasing laser intensity from $z = 1.8$ to 4.5 mm. The X-ray emission shows a similar peak position around $z = 4.7$ mm. It can also be noticed in Fig. 12(c) that the number of electrons is lower in the first bucket after the laser pulse, which is essentially linked to different electron trapping processes dependant on laser evolution.

IV. CONCLUSION

In conclusion, electron acceleration by laser wakefield and the associated betatron radiation inside capillary tubes were experimentally studied with a 40 fs, 16 TW laser. Capillary tubes were used to collect the laser energy outside the focal spot central peak and assist laser self-focused over several millimeters. Operating in the blow-out regime, tens of pC electrons were accelerated up to ~300 MeV, and the X-ray peak brightness was estimated to be $\sim 1 \times 10^{21}$ ph/s/mm^2/mrad^2/0.1%BW, comparable to modern synchrotron light sources.

The X-ray emission was measured to be correlated to the accelerated electron beam charge. Therefore the production of a reliable beam charge would benefit future developments and applications of this table-top X-ray source. Moreover, the X-ray profile was used to investigate the acceleration process. This diagnostic provides a deeper insight of the physics of electron acceleration in long plasmas and can be compared to simulations. PIC simulations performed with parameters close to the experimental ones provide results in good agreement with experimental results. The agreement of the X-ray emission profile and location between simulation and experiment shows that the analysis of the X-ray emission is a powerful diagnostics, providing also information on the electron beam dynamics.

A comparison of two PIC simulations with different focus positions highlights the sensitivity of the laser propagation to the coupling conditions at the entrance of the plasma. Other parameters like the specific profile of density ramp, and the position and angle of the laser spot at the entrance of the capillary,[36] should also be taken into account in future simulations as well as in experiments, as they may be key parameters for improving the reliability of laser plasma accelerators.

ACKNOWLEDGMENTS

This experiment was funded by LASERLAB-EUROPE with Contract No. 228334, the Lund University X-ray Center (LUXC), the Swedish Research Council (including the Linné grant to LLC), and the Kunt and Alice Wallenberg Foundation. J. Ju acknowledges financial support from the Chinese Scholarship Council (CSC).

[1]T. Tajima and J. Dawson, Phys. Rev. Lett. **43**, 267 (1979).
[2]E. Esarey, C. B. Schroeder, and W. P. Leemans, Rev. Mod. Phys. **81**, 1229 (2009).
[3]S. P. D. Mangles, C. D. Murphy, Z. Najmudin, A. G. R. Thomas, J. L. Collier, A. E. Dangor, E. J. Divall, P. S. Foster, J. G. Gallacher, C. J. Hooker, D. A. Jaroszynski, A. J. Langley, W. B. Mori, P. A. Norreys, F. S. Tsung, R. Viskup, B. R. Walton, and K. Krushelnick, Nature **431**, 535 (2004).
[4]C. G. R. Geddes, Cs. Toth, J. van Tilborg, E. Esarey, C. B. Schroeder, D. Bruhwiler, C. Nieter, J. Cary, and W. P. Leemans, Nature **431**, 538 (2004).
[5]J. Faure, Y. Glinec, A. Pukhov, S. Kiselev, S. Gordienko, E. Lefebvre, J.-P. Rousseau, F. Burgy, and V. Malka, Nature **431**, 541 (2004).
[6]W. P. Leemans, B. Nagler, A. J. Gonsalves, Cs. Tóth, K. Nakamura, C. G. R. Geddes, E. Esarey, C. B. Schroeder, and S. M. Hooker, Nat. Phys. **2**, 696 (2006).
[7]W. Lu, M. Tzoufras, C. Joshi, F. S. Tsung, W. B. Mori, J. Viera, R. A. Fonseca, and L. O. Silva, Phys. Rev. ST Accel. Beams **10**, 061301 (2007).
[8]E. Esarey, B. A. Shadwick, P. Catravas, and W. P. Leemans, Phys. Rev. E **65**, 056505 (2002).
[9]A. G. R. Thomas, Phys. Plasmas **17**, 056708 (2010).
[10]A. Rousse, K. T. Phuoc, R. Shah, A. Pukhov, E. Lefebvre, V. Malka, S. Kiselev, F. Burgy, J.-P. Rousseau, D. Umstadter, and D. Hulin, Phys. Rev. Lett. **93**, 135005 (2004).
[11]S. Kneip, C. McGuffey, J. L. Martins, S. F. Martins, C. Bellei, V. Chvykov, F. Dollar, R. Fonseca, C. Huntington, G. Kalintchenko, A. Maksimchuk, S. P. D. Mangles, T. Matsuoka, S. R. Nagel, C. A. J. Palmer, J. Schreiber, K.-Ta. Phuoc, A. G. R. Thomas, V. Yanovsky, L. O. Silva, K. Krushelnick, and Z. Najmudin, Nat. Phys. **6**, 980 (2010).
[12]M. Schnell, A. Savert, B. Landgraf, M. Reuter, M. Nicolai, O. Jackel, C. Peth, T. Thiele, O. Jansen, A. Pukhov, O. Willi, M. C. Kaluza, and C. Spielmann, Phys. Rev. Lett. **108**, 075001 (2012).
[13]G. R. Plateau, C. G. R. Geddes, D. B. Thorn, M. Chen, C. Benedetti, E. Esarey, A. J. Gonsalves, N. H. Matlis, K. Nakamura, C. B. Schroeder, S. Shiraishi, T. Sokollik, J. van Tilborg, Cs. Toth, S. Trotsenko, T. S. Kim, M. Battaglia, Th. Stohlker, and W. P. Leemans, Phys. Rev. Lett. **109**, 064802 (2012).
[14]F. Wojda, K. Cassou, G. Genoud, M. Burza, Y. Glinec, O. Lundh, A. Persson, G. Vieux, E. Brunetti, R. P. Shanks, D. Jaroszynski, N. E. Andreev, C.-G. Wahlström, and B. Cros, Phys. Rev. E **80**, 066403 (2009).
[15]B. Cros, C. Courtois, G. Matthieussent, A. Di Bernardo, D. Batani, N. Andreev, and S. Kuznetsov, Phys. Rev. E **65**, 026405 (2002).
[16]D. P. Umstadter, Nature Photon. **5**, 576 (2011).
[17]J. Osterhoff, A. Popp, Zs. Major, B. Marx, T. P. Rowlands-Rees, M. Fuchs, M. Geissler, R. Horlein, B. Hidding, S. Becker, E. A. Peralta, U. Schramm, F. Gruner, D. Habs, F. Krausz, S. M. Hooker, and S. Karsch, Phys. Rev. Lett. **101**, 085002 (2008).
[18]H. E. Ferrari, A. Lifschitz, and B. Cros, Plasma Phys. Controlled Fusion. **53**, 014005 (2011).
[19]G. Genoud, K. Cassou, F. Wojda, H. E. Ferrari, C. Kamperidis, M. Burza, A. Persson, J. Uhlig, S. Kneip, S. P. D. Mangles, A. Lifschitz, B. Cros, and C.-G. Wahlstrom, Appl. Phys. B **105**, 309 (2011).
[20]H. E. Ferrari, A. F. Lifschitz, G. Maynard, and B. Cros, Phys. Plasmas **18**, 083108 (2011).
[21]J. Ju, K. Svensson, A. Dopp, H. E. Ferrari, K. Cassou, O. Neveu, G. Genoud, F. Wojda, M. Burza, A. Persson, O. Lundh, C.-G. Wahlstrom, and B. Cros, Appl. Phys. Lett. **100**, 191106 (2012).
[22]A. F. Lifschitz, X. Davoine, E. Lefebvre, J. Faure, C. Rechatin, and V. Malka, J. Comput. Phys. **228**, 1803 (2009).
[23]J. Ju and B. Cros, J. Appl. Phys. **112**, 113102 (2012).
[24]Y. Glinec, J. Faure, A. Guemnie-Tafo, V. Malka, H. Monard, J. P. Larbre, V. De Waele, J. L. Marignier, and M. Mostafavi, Rev. Sci. Instrum. **77**, 103301 (2006).
[25]A. Buck, K. Zeil, A. Popp, K. Schmid, A. Jochmann, S. D. Kraft, B. Hidding, T. Kudyakov, C. M. S. Sears, L. Veisz, S. Karsch, J. Pawelke, R. Sauerbrey, T. Cowan, F. Krausz, and U. Schramm, Rev. Sci. Instrum. **81**, 033301 (2010).
[26]S. Kneip, S. R. Nagel, S. F. Martins, S. P. D. Mangles, C. Bellei, O. Chekhlov, R. J. Clarke, N. Delerue, E. J. Divall, G. Doucas, K. Ertel, F. Fiuza, R. Fonseca, P. Foster, S. J. Hawkes, C. J. Hooker, K. Krushelnick, W. B. Mori, C. A. J. Palmer, K. Ta Phuoc, P. P. Rajeev, J. Schreiber, M. J. V. Streeter, D. Urner, J. Vieira, L. O. Silva, and Z. Najmudin, Phys. Rev. Lett. **103**, 035002 (2009).
[27]D. H. Froula, C. E. Clayton, T. Doppner, K. A. Marsh, C. P. J. Barty, L. Divol, R. A. Fonseca, S. H. Glenzer, C. Joshi, W. Lu, S. F. Martins, P. Michel, W. B. Mori, J. P. Palastro, B. B. Pollock, A. pak, J. E. Ralph, J. S. Ross, C. W. Siders, L. O. Silva, and T. Wang, Phys. Rev. Lett. **103**, 215006 (2009).
[28]C. M. Huntington, A. G. R. Thomas, C. McGuffey, T. Matsuoka, V. Chvykov, G. Kalintchenko, S. Kneip, Z. Najmudin, C. Palmer, V. Yanovsky, A. Maksimchuk, R. P. Drake, T. Katsouleas, and K. Krushelnick, Phys. Rev. Lett. **106**, 105001 (2011).
[29]S. Corde, C. Thaury, K.Ta Phuoc, A. Lifschitz, G. Lambert, J. Faure, O. Lundh, E. Benveniste, A. Ben-Ismail, L. Arantchuk, A. Marciniak, A. Stordeur, P. Brijesh, A. Rousse, A. Specka, and V. Malka, Phys. Rev. Lett. **107**, 215004 (2011).
[30]K. T. Phuoc, S. Corde, R. Shah, F. Albert, R. Fitour, J.-P. Rousseau, F. Burgy, B. Mercier, and A. Rousse, Phys. Rev. Lett. **97**, 225002 (2006).
[31]I. Kostyukov, S. Kiselev, and A. Pukhov, Phys. Plasmas **10**, 4818 (2003).
[32]C. Rechatin, J. Faure, X. Davoine, O. Lundh, J. Lim, A. Ben-Ismail, F. Burgy, A. Tafzi, A. Lifschitz, E. Lefebvre, and V. Malka, New J. Phys. **12**, 045023 (2010).
[33]S. P. D. Mangles, A. G. R. Thomas, O. Lundh, F. Lindau, M. C. Kaluza, A. Persson, C. G. Wahlstrom, K. Krushelnick, and Z. Najmudin, Phys. Plasmas **14**, 056702 (2007).
[34]J. Faure, C. Rechatin, A. Norlin, F. Burgy, A. Tafzi, J.-P. Rousseau, and V. Malka, Plasma Phys. Controlled Fusion **49**, B395 (2007).
[35]A. J. Gonsalves, K. Nakamura, C. Lin, D. Panasenko, S. Shiraishi, T. Sokollik, C. Benedetti, C. B. Schroeder, C. G. R. Geddes, J. van Tilborg, J. Osterhoff, E. Esarey, C. Toth, and W. P. Leemans, Nat. Phys. **7**, 862 (2011).
[36]M. Veysman, N. E. Andreev, K. Cassou, Y. Ayoul, G. Maynard, and B. Cros, J. Opt. Soc. Am. B **27**, 1400 (2010).

Paper VII

Analysis of X-Ray Emission and Electron Dynamics in a Capillary-Guided Laser Wakefield Accelerator

J. Ju, G. Genoud, H. E. Ferrari, O. Dadoun, B. Paradkar, K. Svensson, F. Wojda, M. Burza, A. Persson, O. Lundh, N. E. Andreev, C.-G. Wahlström, & B. Cros.

Phys. Rev. ST Accel. Beams **17**, 051302 (2014).

PHYSICAL REVIEW SPECIAL TOPICS - ACCELERATORS AND BEAMS **17,** 051302 (2014)

Analysis of x-ray emission and electron dynamics in a capillary-guided laser wakefield accelerator

J. Ju,[1] G. Genoud,[2] H. E. Ferrari,[3] O. Dadoun,[4] B. Paradkar,[1] K. Svensson,[2] F. Wojda,[2] M. Burza,[2] A. Persson,[2] O. Lundh,[2] N. E. Andreev,[5] C.-G. Wahlström,[2] and B. Cros[1,*]

[1]*Laboratoire de Physique des Gaz et des Plasmas, CNRS-Université Paris-Sud, 91405, Orsay, France*
[2]*Department of Physics, Lund University, P.O. Box 118, S-22100 Lund, Sweden*
[3]*Consejo Nacional de Investigaciones Científicas y Técnicas (CONICET), 8400 Bariloche, Argentina*
[4]*Laboratoire de l'Accélérateur Linéaire, CNRS-Université Paris-Sud, 91405, Orsay, France*
[5]*Joint Institute for High Temperatures, Russian Academy of Sciences, Moscow 125412, Russia*

(Received 30 January 2014; published 19 May 2014)

The dynamics of electron acceleration driven by laser wakefield inside a 30.5 mm long dielectric capillary tube is analyzed using radiation emitted in the x-ray range. 3D particle-in-cell simulations, performed with parameters close to the experimental ones, show that in long plasmas, the accelerated electrons catch up and finally overrun the driving laser owing to a higher velocity of the electrons in the plasma. The electrons are then transversely scattered by the laser pulse, and penetrate the capillary wall where they generate bremsstrahlung radiation, modeled using GEANT4 simulations. The signature of bremsstrahlung radiation is detected using an x-ray camera, together with the betatron radiation emitted during electron acceleration in the plasma bubble. The reflection of betatron radiation from the inner capillary surface also accounts for a fraction of the observed signal on the x-ray camera. The simulation results are in agreement with the experimental ones and provide a detailed description of the electron and radiation properties, useful for the design of laser wakefield accelerators or radiation sources using long plasma media.

DOI: 10.1103/PhysRevSTAB.17.051302 PACS numbers: 52.38.Kd, 52.38.Ph, 52.65.Rr

I. INTRODUCTION

Charged particle accelerators play an important role in the development of modern science and technology, as the produced high energy particle beams are essential for several domains of fundamental and applied research. The dissemination of radio-frequency (rf) accelerators is mainly limited by their cost, induced by the large size of the facility required to produce GeV electron beams, as the magnitude of accelerating electric field inside a rf cavity is limited by material breakdown to be less than ~100 MV/m. Alternatively, in the mechanism of laser wakefield acceleration (LWFA) [1,2] electrons can be accelerated by the ultra-high electric fields, typically a few hundreds of GV/m, associated with a plasma wave. It has been demonstrated that LWFA is capable of producing high energy electrons of the order of hundred MeV over a few millimeters [3–5].

In LWFA, plasma waves are excited by the ponderomotive force of a short, intense laser pulse, which expels electrons out of high laser intensity regions. In the nonlinear regime, plasma electrons can be completely expelled out of the intense laser volume and self-trapped in the accelerating potential of the plasma wave. Inside the bubblelike [6] accelerating cavity, electrons experience both longitudinal and transverse fields. Thus, these electrons can undergo strong transverse oscillations, known as betatron oscillations, giving rise to the emission of synchrotronlike radiation (called betatron radiation) [7–9], which has been observed and characterized in experiments [10–12].

Betatron radiation typically produces photons in the 1–10 keV range, and constitutes an attractive source for applications to time-resolved imaging due to its compactness and its intrinsic properties as it is brilliant, with duration as short as a few femtoseconds, and perfectly synchronized to the pump laser [11]. The x-ray properties depend on the accelerated electron energy, oscillation amplitude, betatron frequency, and through these quantities on the plasma density. Betatron radiation is thus an excellent diagnostic of the electron dynamics in LWFA. To increase the x-ray photon fluence and energy, electron energy and betatron amplitude can be maximized for a given plasma density. In order to achieve GeV-class electron beams [13] or betatron radiation with photon energy of ~100 keV or above [14], a few centimeter long plasma channels have been employed. The accelerated electron bunch has been observed to catch up with the laser

*brigitte.cros@u-psud.fr

tail in a millimeter-scale gas jet [15], or to propagate beyond the bubble center and interact with the laser pulse [14]. At high electron energy, when the laser frequency is a harmonic of the betatron frequency, a resonance occurs [16] and leads to a significant increase in the photon energy: for 700 MeV electron maximum energy, photons energies in the range 1–7 MeV have been measured [14].

Using femtosecond laser pulses of 16 TW peak power, we have shown that the x-ray peak brightness can be multiplied by a factor 30 when the laser beam is guided by a 10 mm long capillary tube instead of using a 2 mm long gas jet [17]. Electron bunches with tens of pC charge were measured to be accelerated to an energy up to 300 MeV, accompanied by x-ray emission with a peak brightness of the order of 10^{21} ph/s/mm^2/mrad^2/0.1%BW. The x-ray profile is geometrically related to the emission positions in the plasma by the rim of the capillary exit and provides a good probe of the acceleration process [12,18]. Using the emitted x-ray beam distribution to map the acceleration process, the number of betatron oscillations performed by accelerated electrons was inferred from the correlation between measured x-ray fluence and beam charge.

In this paper, we report on the analysis of the radiation emitted during the acceleration of an electron bunch by LWFA in a plasma long enough for the electron bunch to catch up with the laser pulse. The use of a capillary tube [19] to confine the gas and laser energy allows operation at arbitrary low plasma density and laser plasma interaction over long distances [12,20]. Electron acceleration in a 30.5 mm long capillary tube, where electrons are self-trapped and accelerated in the nonlinear bubble regime, and the associated radiation are analyzed. It is found that the trapped electrons are first accelerated and wiggled in the plasma bubble, producing betatron radiation, and furthermore the accelerated electrons catch up and overrun the driving laser pulse, a process during which electrons are scattered transversely by the laser ponderomotive force. Consequently, some of the accelerated electrons acquire a large transverse momentum and enter the downstream capillary wall, where they produce bremsstrahlung radiation. Numerical simulations of the electron acceleration process and radiation generation are performed to support the analysis of experimental observations.

II. EXPERIMENT

A. Setup

The experiment was conducted at the Lund Laser Centre (LLC) with the 10 Hz multi-terawatt Ti:Sapphire laser with a central wavelength of $\lambda_0 = 795$ nm, which delivered laser pulses of about 650 mJ on target within 40 fs duration (FWHM). The experimental arrangement is schematically illustrated in Fig. 1. The laser was focused inside capillary tubes, 1 mm after the entrance, using an off-axis parabolic mirror with focal length $f = 76$ cm. The laser focal

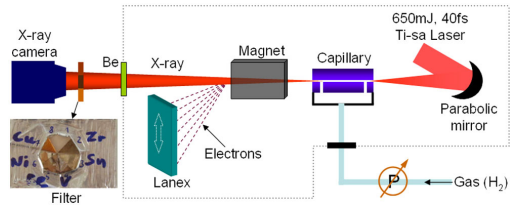

FIG. 1. Schematic illustration of the experimental setup. Elements within the dotted lines were in vacuum. The "pizza" filter consists of six different metals: Zr (3 μm), Sn (3 μm), V (3 μm), Fe (3 μm), Ni (5 μm), Cu (100 μm). All these metal pieces are attached onto a copper mesh together with a tin foil base.

spot was Airy-like with a radius at first minimum of 19.7 ± 0.8 μm, and a peak intensity of 5.4×10^{18} W/cm^2, corresponding to a normalized vector potential $a_0 \simeq 1.6$. A five-degree-of-freedom mounted motorized housing was used to align capillary tubes. Hydrogen gas was filled into the capillary tubes through two approximately 270 μm wide slits situated at 2.5 mm from the capillary ends [21]. To record electron spectra, a 10 cm long permanent magnet with central field of 0.7 T deflected the electrons onto a scintillating screen (Kodak Lanex Regular) imaged by a 12 bit charge coupled device (CCD) camera (not shown in Fig. 1). An aluminium plate was inserted in front of the Lanex screen to avoid its direct exposure to laser light. Electrons with energy less than 42 MeV could not reach the Lanex screen, and therefore not be recorded. A 16 bit cooled CCD camera was placed in air about 110 cm away from the capillary end to record x-ray radiation exiting the vacuum chamber through two 150 μm thick beryllium windows. The camera chip size was 13×13 mm^2, corresponding to a collecting solid angle of 12×12 mrad^2. A so-called "pizza" filter, composed of six sector-shaped pieces of different metal foils, was placed in the beam to determine the photon energy.

B. Results

Using capillary tubes with a diameter of 178 μm, and length in the range from 10 to 30.5 mm, electrons and x-rays were observed to depend strongly on the plasma density, and the x-ray fluence was maximized when the plasma density was $n_e = (8.1 \pm 0.5) \times 10^{18}$ cm^{-3}. For this value of density, electrons exhibit a Maxwellian-like spectral distribution with a cutoff energy as high as 200 MeV and a beam charge of approximately 135 pC [22]. Meanwhile, the accelerated electrons oscillate transversely at the betatron frequency $\omega_\beta \simeq \omega_p/\sqrt{2\gamma}$ due to the focusing force inside the plasma bubble, where ω_p and γ represent the plasma frequency and the relativistic factor, respectively. An electron with transverse oscillation amplitude r_0 generates electromagnetic radiation whose spectrum is determined by the wiggler strength parameter

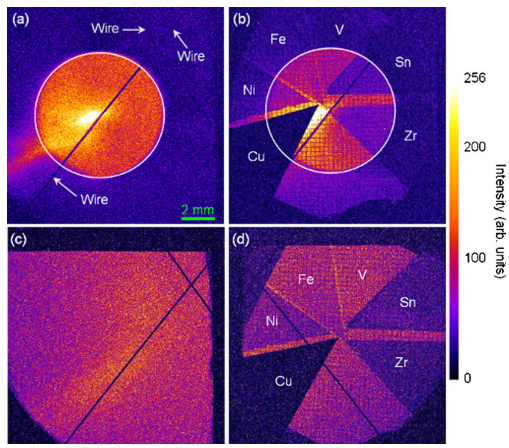

FIG. 2. Far-field x-ray images with or without the filter observed from capillary tubes with diameter of 178 μm and different lengths: (a)–(b) 30.5 mm, (c)–(d) 10 mm for a plasma density $(8.1 \pm 0.5) \times 10^{18}$ cm^{-3}. There was a stainless steel wire ($\phi = 50$ μm) cross placed in the radiation beam path 53 cm away from the capillary exit, which is clearly resolved by the secondary emission in (a). The white circles in (a)–(b) highlight the shadows of the capillary exit rim. Each subfigure has a size of 13×13 mm^2, and corresponds to one laser shot.

$K_\beta = \gamma r_0 \omega_\beta / c$, where c denotes the speed of light in vacuum. In our experimental condition $K_\beta \gg 1$, the emission spectrum is synchrotron-like [7].

Figure 2 shows far-field x-ray images recorded by the x-ray camera for a plasma density of $(8.1 \pm 0.5) \times 10^{18}$ cm^{-3} using a 30.5 mm long capillary tube [(a) and (b)] and a 10 mm long tube in (c) and (d). Each image corresponds to one laser shot. In Figs. 2(b) and (d), the filter set was used in front of the camera and different transmission regions can be clearly observed; in Fig. 2(d), the circular structure near the edges of the image is due to the filter holder blocking the edges of the beam. Clear shadows of the capillary exit rim, highlighted by white circles in Figs. 2(a) and (b) are observed owing to cropping of the betatron emission by the capillary walls. By analyzing the x-ray distribution at the edge of the beam displayed in Fig. 2, the process of betatron radiation and electron acceleration were determined [22] to start from $z \simeq 2$ mm and extend to $z \simeq 7$ mm, $z = 0$ corresponding to position of the capillary entrance on the longitudinal axis. In addition to betatron radiation inside the capillary rim, radiation can also be observed outside the white circle in Figs. 2(a) and (b). A cross made of stainless steel wires with a diameter of 50 μm was placed in the optical path approximately 53 cm after the capillary tube and about 57 cm from the x-ray camera. The shadows of the stainless steel wires, indicated by the arrows in Fig. 2(a), are clearly resolved even outside the rim of the capillary tube, providing evidence of another x-ray source illuminating the wires. Indeed, assuming x-ray sources located only in the range $z = 2$–7 mm inside the capillary tube, this region should be completely dark. This secondary emission can also be seen in the image with the filter [Fig. 2(b)], where there is still a detectable signal on the CCD camera behind the metal filters outside the shadow of the capillary exit rim. Without a secondary emission, the local signals through those metals would be as low as the noise level given by the copper part which blocks the secondary emission as well. This secondary emission was also detected with 20 mm long capillary tubes, but not as strong as with the 30.5 mm long capillary tube, and never with the 10 mm long tubes, which means the secondary emission depends on the capillary length. For the 10 mm long capillary tube shown in Figs. 2(c)–(d), roughly a quarter of the capillary shadow was recorded as the x-ray divergence is larger because the x-ray source is closer to the exit for these shorter capillary tubes. Before discussing in Sec. III the generation of secondary emission in long capillary tubes, we first examine the possibility for x-rays generated by betatron oscillations to be reflected from the inner capillary wall.

C. Discussion of x-ray reflection

The roughness of the inner wall of the capillary used in this experiment is known to be smaller than 100 nm as the driving laser has been measured to be guided in matched capillary tubes according to theoretical predictions [19]. As the roughness of similar capillary tubes has been measured by Li *et al.* [23] to be of the order of 1 nm, we evaluate in this section the fraction of the generated betatron radiation that would be reflected by a smooth capillary wall in our experimental conditions.

For clarity, the radiation detected inside the shadow of the capillary tube rim [i.e., inside the white circle in Figs. 2(a) and (b)] is called the main emission, as it exhibits a higher intensity. As radiation is detected for an angle larger than the cropping angle of the capillary exit, it could be envisaged that part of the radiation is reflected by the capillary inner surface and goes out of the capillary tube as a secondary emission, as illustrated in Fig. 3.

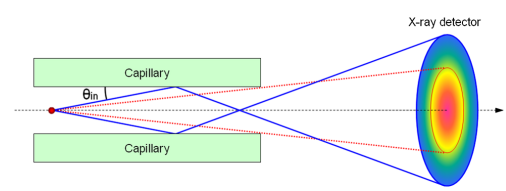

FIG. 3. Schematic illustration of x-rays cropped or reflected by the capillary tube. The cropped part confined within the two dotted lines is the main emission, and the solid lines indicate x-rays that would be reflected by the capillary inner surface to produce a secondary emission on the detector.

The x-ray intensity distribution in the detector plane, taking into account x-ray reflection, can be estimated as follows. The intensity of betatron radiation produced by a wiggling relativistic electron is given by [7]

$$\frac{d^2I}{dEd\Omega} \simeq \frac{3e^2}{2\pi^3\varepsilon_0 c}\gamma^2\xi^2(1+\gamma^2\theta^2) \times \left[\frac{\gamma^2\theta^2}{1+\gamma^2\theta^2}\mathcal{K}^2_{1/3}(\xi)+\mathcal{K}^2_{2/3}(\xi)\right], \quad (1)$$

where E denotes the photon energy, ε_0 is the permittivity of free space, and $\xi = (1+\gamma^2\theta^2)^{3/2}E/E_c$ with $E_c[\mathrm{keV}] = 1.1\times10^{-23}\gamma^2 n_e r_0$ representing the critical energy. θ is the emission angle with respect to the longitudinal axis, equal to the incident angle θ_{in} defined in Fig. 3. $\mathcal{K}_{1/3}$ and $\mathcal{K}_{2/3}$ are modified Bessel functions of order $1/3$ and $2/3$, respectively. At a given longitudinal position z inside the capillary tube, one can geometrically calculate the radial location on the detector, $r(z,\theta_{\mathrm{in}})$, where the radiation will be received, and evaluate the corresponding CCD counts at $r(z,\theta_{\mathrm{in}})$ by

$$C(r) = \int_{z_1}^{z_2}\int_{E_1}^{E_2}\frac{d^2I}{dEd\Omega}R_X T_{\mathrm{air}} T_{\mathrm{Be}} Q_{\mathrm{ccd}}\frac{E}{G_{\mathrm{ccd}}}dEdz, \quad (2)$$

where $z_1 = 2$ mm, $z_2 = 7$ mm represent the longitudinal positions limiting the source of betatron radiation inside the capillary tube [22], Q_{ccd}, G_{ccd} denote quantum efficiency and gain of the x-ray CCD camera, T_{air} and T_{Be} are x-ray transmissions through the 5 mm air gap and 300 μm thick beryllium windows in the optical path, respectively. R_X represents the x-ray reflectivity on the inner capillary wall, which depends on photon energy, incident angle, and roughness of inner capillary wall.

Considering the x-ray CCD quantum efficiency, E_1, E_2 were set to be 0.1 and 20 keV, respectively. The evolution of the gamma factor $\gamma(z)$ obtained from 3D PIC simulation [22] and the betatron oscillation amplitude $r_0 = 2$ μm found in experiment [17] were used to calculate Eq. (2). Figure 4(a) gives the x-ray reflectivity [24] for different surface roughness when the incident angle $\theta_{\mathrm{in}} = 4.5$ mrad, assuming the capillary tube is made of pure SiO_2. It shows that x-ray reflectivity drops for increasing surface roughness, and does not appreciably change for wall roughness smaller then 1 nm, whereas it becomes negligible for roughness larger than 50 nm. Figure 4(b) shows the x-ray reflectivity for a surface roughness of 1 nm as a function of incident angle θ_{in} and photon energy E, which was used to calculate $C(r)$ in Eq. (2). If the incident angle θ_{in} is so small that betatron radiation leaves the capillary tube without reflection, $R_X = 1$.

Figure 5(a) illustrates the x-ray pattern in the detector plane calculated numerically when the x-ray reflection at the inner wall of the capillary with roughness of 1 nm is taken into account as explained above. For comparison, Fig. 5(b) displays the numerical result when there is no x-ray reflection, namely photons hitting the capillary wall are lost; Figs. 5(c) and (d) are the lineout intensity profiles corresponding to $y = 0$ in Figs. 5(a) and (b), respectively. A sharp shadow of the capillary exit rim is produced and the x-ray beam is cropped in the absence of x-ray reflection [Figs. 5(b), (d)], whereas the rim shadow becomes blurred when x-ray reflection is taken into account. It suggests that x-ray reflection could contribute to the secondary emission shown in Figs. 2(a)–(b). However, the intensity patterns in Fig. 5 and in Fig. 2(a) are significantly different, as the results shown in Fig. 5 are obtained from a single-electron radiation model, whereas the experimental patterns are generated by a distribution of electrons with significant energy spread and spatial extension. In order to perform a quantitative comparison, we select a ring with radius $r = 5$ mm, located outside the rim shadow in Fig. 2(a), and where the x-ray reflection mainly modifies the profile in Fig. 5. According to Fig. 5(a), the normalized CCD count at $r = 5$ mm is about 0.07. The peak CCD count observed experimentally in Fig. 2(a) is around 3000, so the corresponding CCD count at $r = 5$ mm can be estimated to be

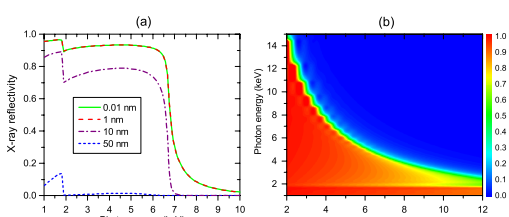

FIG. 4. (a) x-ray reflectivity as a function of photon energy for different surface roughness when $\theta_{\mathrm{in}} = 4.5$ mrad, and (b) x-ray reflectivity as a function of incident angle and photon energy for a surface roughness of 1 nm.

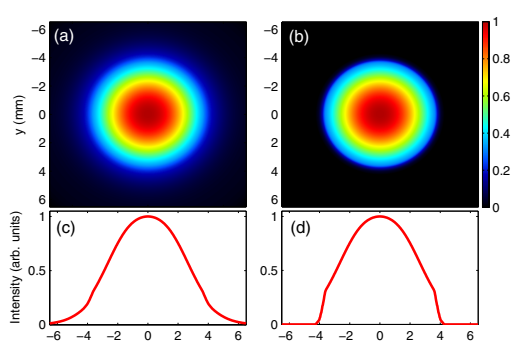

FIG. 5. Numerically calculated far-field x-ray patterns in the detector plane when (a) x-ray reflection was taken into account, (b) no x-ray reflection was considered. (c)–(d) are the corresponding intensity profiles through $y = 0$.

$3000 \times 0.07 = 210$. However for the case of Fig. 2(a), 410 ± 60 CCD counts were typically measured at $r = 5$ mm, which is about twice higher than this numerical prediction. It implies that besides x-ray reflection some other mechanism contributes to the formation of the secondary emission.

III. SIMULATION OF ELECTRON DYNAMICS

As 30.5 mm long plasmas are longer than the typical acceleration distance and laser depletion length for the parameters of our experiment, the electron dynamics during the acceleration process has to be investigated in detail. To do so, 3D particle-in-cell (PIC) simulations were performed with the code CALDER-CIRC [25] including the boundary condition of capillary tube described in Ref. [26]. The simulation parameters are set similar to the experimental ones. To shorten the time for parameter scan in 3D PIC simulations, a smaller capillary tube diameter of 152 μm was used. It was verified in simulation that the laser-plasma interaction is nearly the same for capillary tubes with 152 and 178 μm diameters owing to a relatively small laser focal spot. The laser pulse with $a_0 = 1.6$ and a FWHM pulse duration of 40 fs was focused 1 mm inside the capillary tube. A density plateau $n_e = 8 \times 10^{18}$ cm^{-3} is set between the two capillary slits; outside the plateau, the density fall is modeled as a 3 mm long linear density ramp decreasing from n_e to 0 [22]. Ten particles per cell, spatial mesh sizes $dz = \lambda_0/(8\pi)$, $dr = \lambda_0/\pi$ were used in the simulations.

Figure 6 shows one simulation case for a plasma density $n_e = 8 \times 10^{18}$ cm^{-3}. In Fig. 6(a), a plasma bubble is produced behind the laser and starts trapping electrons at $z \simeq 3.195$ mm. Afterwards, the accelerated electrons catch up with the laser tail and get scattered by the laser ponderomotive force. The increase in transverse size of the electron bunch can be seen in Fig. 6(c). The distance that it takes for a trapped electron (moving at nearly the speed of light c) to catch up with the driving laser can be approximated by $L = R_b c/(c - v_g)$. The bubble radius in Fig. 6(b) is $R_b \simeq 7$ μm, and the laser group velocity is given by $v_g = c\omega_0(\omega_0^2 + \omega_p^2)^{-1/2} \simeq 0.997c$, which yields $L \simeq 2.3$ mm. The laser pump depletion length can be evaluated [27] through $L_{pd} = c\tau_0\omega_0^2/\omega_p^2$ to be $L_{pd} \simeq$ 3 mm, where τ_0 denotes the laser pulse duration. Since L is comparable with L_{pd}, some electrons can catch up with the laser before the laser is depleted. During laser depletion, a fraction of the pulse propagates backward and interacts with the trailing electron bunch as can be seen in Fig. 6(c).

Figure 7 shows the distribution of the electron bunch in the transverse plane at different longitudinal positions, namely $z = 4.11$, 5.87, and 7.63 mm. The simulation parameters are the same as for Fig. 6. A tiny bright spot can be seen in Fig. 7(a), corresponding to the typical electron bunch distribution when it catches up with the driving laser. The bunch size is dramatically enlarged after interacting with the laser pulse [Fig. 7(b)], and afterwards the outmost electrons start reaching and entering into the capillary wall. Owing to a larger emittance of the electron bunch along the laser polarization direction [15], the bunch explosion is more pronounced in that direction as shown in Figs. 7(b)–(c). Figures 7(d)–(e) display typical trajectories of some electrons which are strongly scattered. Since the ponderomotive force does not depend on laser polarization, the electrons are expelled both along and perpendicular to the laser polarization direction.

In summary, PIC simulations show that in our experimental conditions, the accelerated electrons catch up with the laser pulse and are scattered when they overrun it. As a result, the electrons reach the capillary tube wall, where they produce bremsstrahlung radiation. It should be mentioned that the capillary radius used in the experiments (89 μm) is larger than that of the simulation case (76 μm), so the outmost scattered electrons should reach the real capillary wall at a longitudinal position downstream the case of Fig. 7(c) $z = 7.63$ mm. Therefore only a few electrons are likely to reach the capillary wall before $z = 10$ mm, which can explain why no detectable secondary emission was found in experiment with 10 mm long

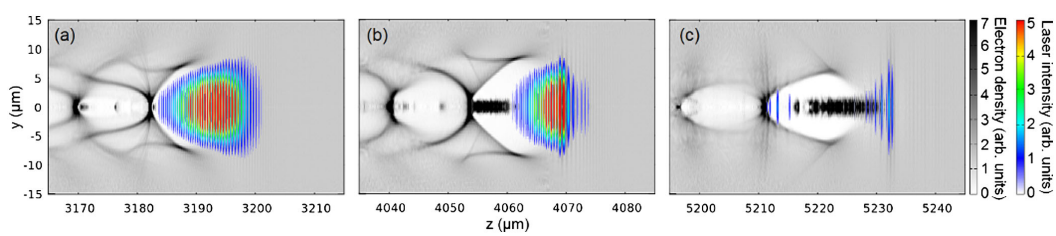

FIG. 6. Snapshots of plasma density (gray scale) and instantaneous laser intensity (color scale), in which the laser propagates from left to right at three different positions along the axis of capillary tube. Electron trapping starts at $z \simeq 3.195$ mm in (a), and at $z \simeq 4.065$ mm (b) a large amount of electrons are trapped and accelerated in the first plasma bubble, where the head of the electron bunch catches up with the laser. The electrons interact with the laser and get modulated at $z \simeq 5.225$ mm (c), where the transverse size of the electron bunch is appreciably increased.

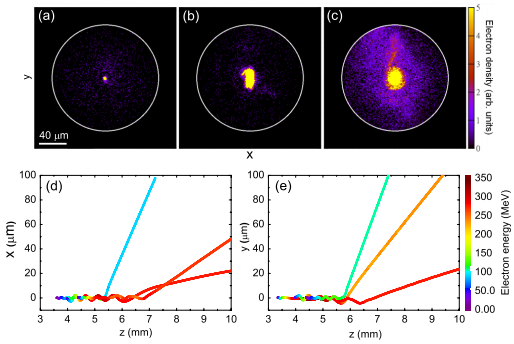

FIG. 7. Electron distribution in the transverse plane at different longitudinal positions (a) 4.11 mm, (b) 5.87 mm, and (c) 7.63 mm, where the circle indicates the capillary border of 152 μm diameter. The increase in electron beam size is clearly visible. The laser is polarized along the vertical (y) axis. Typical electron trajectories in the planes (d) perpendicular and (e) parallel with the laser polarization. The simulation parameters are the same as for Fig. 6.

capillary tubes. For longer capillary tubes, more electrons interact with the capillary wall, which explains why secondary emission was detected for 20 mm long capillary tubes, and became much stronger for the 30.5 mm long tube in our experiments. In order to evaluate the amplitude of this secondary emission, we have modeled the generation of bremsstrahlung radiation by the electron distribution obtained from PIC simulations.

IV. MODELING OF BREMSSTRAHLUNG RADIATION

In order to determine the amount of secondary emission shown in Figs. 2(a)–(b) that could be produced by bremsstrahlung radiation, we have calculated the spectrum and angular distribution of bremsstrahlung radiation, and evaluated the signal generated on the x-ray camera, sensitive to 1–20 keV photons and with a collecting solid angle of 12×12 mrad^2. The bremsstrahlung radiation produced by the electron bunch was calculated using the code GEANT4 [28], which simulates the passage of particles through matter using the Monte-Carlo method. Particle transport is described taking into account the processes of bremsstrahlung, multiple scattering, and ionization, while the produced electromagnetic radiation experiences the processes of photoelectric effect, Compton scattering, and conversion into electron-positron pair.

The bremsstrahlung modeling is initialized with the electron beam obtained from PIC simulation at $z = 7.63$ mm, where the electron bunch has already been modulated after overrunning the laser pulse, but not yet reached the capillary wall. After $z = 7.63$ mm, both experimental and PIC simulation results [22] show that

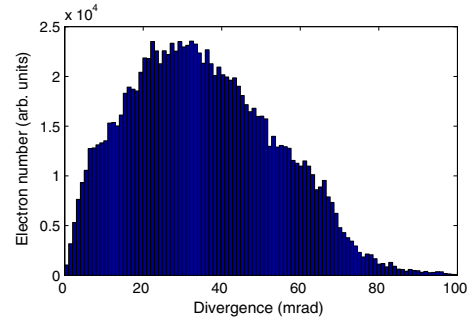

FIG. 8. Angular distribution of the electron bunch obtained from PIC simulation at $z = 7.63$ mm.

the laser becomes depleted so that it cannot considerably modulate the electron bunch. The electron beam transverse distribution used in the GEANT4 simulation is shown in Fig. 7(c), and the corresponding beam divergence is shown in Fig. 8, where the divergence angle is defined as $\theta_d = \arctan[(p_x^2 + p_y^2)^{1/2}/p_z]$ with p_j representing electron momentum along the j axis. In the GEANT4 calculation, 4×10^4 macroelectrons were used. The capillary tube, taken as pure SiO_2, is 30.5 mm long with inner and outer radii of 89 μm and 2.75 mm, respectively. The two Be windows with total thickness of 300 μm and the 5 mm air gap, as illustrated in Fig. 1, were included in the modeling as well.

Figure 9 shows the particle trajectories in the capillary wall, where the red, blue, and green lines represent the trajectories of electrons, positrons, and photons, respectively. It shows that numerous photons are produced by bremsstrahlung radiation when electrons pass through the capillary wall, and most of the photons move forward very directionally. The spectrum of the emitted photons and their angular distribution are given in Fig. 10. The overall spectrum [Fig. 10(a)] exponentially drops with only a few photons remaining beyond 200 MeV. Figure 10(c) shows the spectrum for photon energy below 500 keV, indicating the spectral intensity peaks around 20 keV, and diminishes when photon energy decreases toward zero.

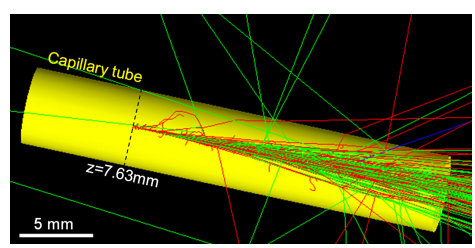

FIG. 9. Trajectories of 50 simulated particles in the capillary part (yellow) from the GEANT4 modeling: photons (green), electrons (red), and positrons (blue).

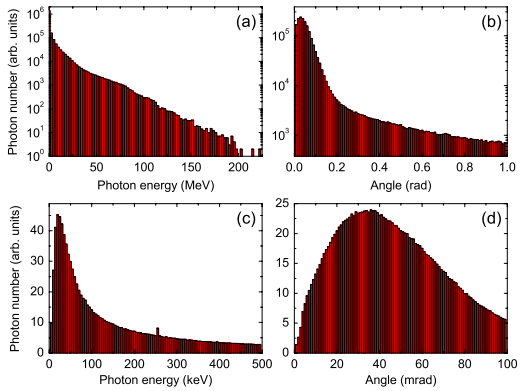

FIG. 10. (a) Spectrum and (b) angular distribution of the total bremsstrahlung radiation in logarithmic scale. (c) Spectrum for 0–500 keV photons and (d) angular distribution for 0–100 mrad.

Furthermore, most of the photons are collimated within a divergence cone of 100 mrad as shown in Fig. 10(b). Particularly, a peak at $\theta \simeq 35$ mrad is observed in Fig. 10(d). This peak perfectly coincides with the divergence peak of the electron beam given in Fig. 8, implying the photons are indeed generated by the scattered electrons.

It is important to check whether this bremsstrahlung radiation could be detected by the x-ray camera and furthermore induce the x-ray halos observed in Fig. 2. First, the photon number generated by bremsstrahlung radiation needs to be estimated. Here we particularly consider the photons with a divergence of $4 < \theta < 5$ mrad, corresponding to a ring of 4.5×10^4 pixels outside the capillary shadow (the white circle) in Fig. 2(a), where the signal could be induced by the bremsstrahlung photons. The charge of the electron bunch is ~80 pC in experiments [22], and the electron-to-photon ($4 < \theta < 6$ mrad) conversion efficiency is found to be 0.7% in the GEANT4 simulation, which yields 3.7×10^6 photons produced in the angle range of 4–5 mrad. The average fluence is therefore calculated to be approximately 80 photons per pixel. We shall furthermore estimate the resulting CCD counts. To do so, only the photons with energy less than 50 keV were taken into account, because the detector responsivity for higher energy photons is negligible. Using the radiation spectrum obtained in the simulation and the quantum efficiency of the x-ray camera, we estimate that this radiation could produce an average CCD count of around 270 for $4 < \theta < 5$ mrad. It should be noted that the relatively low CCD count is due to the poor detector responsivity for high energy photons, and not to a low fluence of bremsstrahlung photons.

In summary, the above numerical calculations show that x-ray reflection and bremsstrahlung radiation can together yield 480 (210 + 270) CCD counts outside the shadow of the capillary border, which is consistent with the experimental observation of about 410 ± 60 CCD counts. We therefore conclude that x-ray reflection and bremsstrahlung radiation both contribute to the secondary emission observed in experiments.

V. CONCLUSION

In conclusion, we analyzed the dynamics of electrons acceleration by laser wakefield inside a long plasma medium when the laser is guided by a dielectric capillary tube. It was found that the accelerated electrons are scattered when they catch up and overrun the driving laser pulse. This phenomenon is undesired for the generation of collimated beams of high energy electrons, and can be avoided by making the laser pump depletion length shorter than the dephasing length, so the laser becomes greatly damped before the electrons catch up with it. Betatron radiation is emitted over a distance of about 5 mm and generates a bright beam, with a peak brightness of the order of 10^{21} ph/s/mm^2/mrad^2/0.1%BW, detected on the x-ray CCD. In addition to betatron radiation detected inside the shadow of the capillary tube, the x-ray images exhibit the signature of secondary emission in the x-ray range.

The detailed analysis of this secondary emission shows that it may be produced by two mechanisms: x-ray reflection from the inner capillary surface and bremsstrahlung radiation produced when scattered electrons propagate inside the wall of the capillary tube. It was not possible to discriminate the contributions of the two mechanisms in the present experimental configuration; the selective detection of photons with energy larger than 20 keV should provide a clear signature of bremsstrahlung radiation in future work. According to simulations, 10^8–10^9 photons per shot with photon energy extending up to ~200 MeV can be generated by bremsstrahlung radiation for an electron beam obtained in our experiments with a charge of the order of 100 pC. Such gamma-ray beams are very directional and as intense as those generated by schemes like Compton scattering [29], which can be applied to imaging the interior structure of dense objects [30].

ACKNOWLEDGMENTS

This work was funded by LASERLAB-EUROPE (Grant Agreement No. 228334), the Triangle de la Physique Contract No. 2011-086TMULTIPLACCELE, the Lund University x-ray Center (LUXC), the Swedish Research Council (including the Linné grant to LLC), the Swedish Foundation for Strategic Research (SSF), and the Knut and Alice Wallenberg Foundation. J. Ju acknowledges financial support from Chinese Scholarship Council (CSC).

[1] T. Tajima, and J. Dawson, Phys. Rev. Lett. **43**, 267 (1979).
[2] E. Esarey, C. B. Schroeder, and W. P. Leemans, Rev. Mod. Phys. **81**, 1229 (2009).

[3] S. P. D. Mangles, C. D. Murphy, Z. Najmudin, A. G. R. Thomas, J. L. Collier, A. E. Dangor, E. J. Divall, P. S. Foster, J. G. Gallacher, C. J. Hooker, D. A. Jaroszynski, A. J. Langley, W. B. Mori, P. A. Norreys, F. S. Tsung, R. Viskup, B. R. Walton, and K. Krushelnick, Nature (London) **431**, 535 (2004).

[4] C. G. R. Geddes, Cs. Toth, J. van Tilborg, E. Esarey, C. B. Schroeder, D. Bruhwiler, C. Nieter, J. Cary, and W. P. Leemans, Nature (London) **431**, 538 (2004).

[5] J. Faure, Y. Glinec, A. Pukhov, S. Kiselev, S. Gordienko, E. Lefebvre, J. P. Rousseau, F. Burgy, and V. Malka, Nature (London) **431**, 541 (2004).

[6] A. Pukhov, and J. Meyer-ter-Vehn, Appl. Phys. B **74**, 355 (2002).

[7] E. Esarey, B. A. Shadwick, P. Catravas, and W. P. Leemans, Phys. Rev. E **65**, 056505 (2002).

[8] A. G. R. Thomas, Phys. Plasmas **17**, 056708 (2010).

[9] S. Corde, K. Ta Phuoc, G. Lambert, R. Fitour, V. Malka, A. Rousse, A. Beck, and E. Lefebvre, Rev. Mod. Phys. **85**, 1 (2013).

[10] A. Rousse, K. Ta Phuoc, R. Shah, A. Pukhov, E. Lefebvre, V. Malka, S. Kiselev, F. Burgy, J. P. Rousseau, D. Umstadter, and D. Hulin, Phys. Rev. Lett. **93**, 066403 (2004).

[11] S. Kneip, C. McGuffey, J. L. Martins, S. F. Martins, C. Bellei, V. Chvykov, F. Dollar, R. Fonseca, C. Huntington, G. Kalintchenko, A. Maksimchuk, S. P. D. Mangles, T. Matsuoka, S. R. Nagel, C. A. J. Palmer, J. Schreiber, K. Ta Phuoc, A. G. R. Thomas, V. Yanovsky, L. O. Silva, K. Krushelnick, and Z. Najmudin, Nat. Phys. **6**, 980 (2010).

[12] G. Genoud, K. Cassou, F. Wojda, H. E. Ferrari, C. Kamperidis, M. Burza, A. Persson, J. Uhlig, S. Kneip, S. P. D. Mangles, A. Lifschitz, B. Cros, and C.-G. Wahlstrom, Appl. Phys. B **105**, 309 (2011).

[13] W. P. Leemans, B. Nagler, A. J. Gonsalves, Cs. Tóth, K. Nakamura, C. G. R. Geddes, E. Esarey, C. B. Schroeder, and S. M. Hooker, Nat. Phys. **2**, 696 (2006).

[14] S. Cipiccia, M. R. Islam, B. Ersfeld, R. P. Shanks, E. Brunetti, G. Vieux, X. Yang, R. C. Issac, S. M. Wiggins, G. H. Welsh, M.-P. Anania, D. Maneuski, R. Montgomery, G. Smith, M. Hoek, D. J. Hamilton, N. R. C. Lemos, D. Symes, P. P. Rajeev, V. O. Shea, J. M. Dias, and D. A. Jaroszynski, Nat. Phys. **7**, 867 (2011).

[15] S. P. D. Mangles, A. G. R. Thomas, M. C. Kaluza, O. Lundh, F. Lindau, A. Persson, F. S. Tsung, Z. Najmudin, W. B. Mori, C.-G. Wahlstrom, and K. Krushelnick, Phys. Rev. Lett. **96**, 215001 (2006).

[16] I. Nam, M. S. Hur, H. S. Uhm, N. A. M. Hafz, and H. Suk, Phys. Plasmas **18**, 043107 (2011).

[17] J. Ju, K. Svensson, A. Dopp, H. E. Ferrari, K. Cassou, O. Neveu, G. Genoud, F. Wojda, M. Burza, A. Persson, O. Lundh, C.-G. Wahlstrom, and B. Cros, Appl. Phys. Lett. **100**, 191106 (2012).

[18] S. Corde, C. Thaury, K. Ta Phuoc, A. Lifschitz, G. Lambert, J. Faure, O. Lundh, E. Benveniste, A. Ben-Ismail, L. Arantchuk, A. Marciniak, A. Stordeur, P. Brijesh, A. Rousse, A. Specka, and V. Malka, Phys. Rev. Lett. **107**, 215004 (2011).

[19] B. Cros, C. Courtois, G. Matthieussent, A. Di Bernardo, D. Batani, N. Andreev, and S. Kuznetsov, Phys. Rev. E **65**, 026405 (2002).

[20] H. E. Ferrari, A. F. Lifschitz, G. Maynard, and B. Cros, Phys. Plasmas **18**, 083108 (2011).

[21] J. Ju, and B. Cros, J. Appl. Phys. **112**, 113102 (2012).

[22] J. Ju, K. Svensson, H. Ferrari, A. Dopp, G. Genoud, F. Wojda, M. Burza, A. Persson, O. Lundh, C.-G. Wahlstrom, and B. Cros, Phys. Plasmas **20**, 083106 (2013).

[23] Y.-D. Li, X.-Y. Lin, Z.-Y. Tan, T.-X. Sun, and Z.-G. Liu, Chin. Phys. B **20**, 040702 (2011).

[24] The center for X-Ray optics, http://www.cxro.lbl.gov/.

[25] A. F. Lifschitz, X. Davoine, E. Lefebvre, J. Faure, C. Rechatin, and V. Malka, J. Comput. Phys. **228**, 1803 (2009).

[26] H. E. Ferrari, A. Lifschitz, and B. Cros, Plasma Phys. Controlled Fusion **53**, 014005 (2011).

[27] W. Lu, M. Tzoufras, C. Joshi, F. S. Tsung, W. B. Mori, J. Viera, R. A. Fonseca, and L. O. Silva, Phys. Rev. ST Accel. Beams **10**, 061301 (2007).

[28] S. Agostinelli *et al.*, Nucl. Instrum. Methods Phys. Res., Sect. A **506**, 250 (2003).

[29] S. Chen, N. D. Powers, I. Ghebregziabher, C. M. Maharjan, C. Liu, G. Golovin, S. Banerjee, J. Zhang, N. Cunningham, A. Moorti, S. Clarke, S. Pozzi, and D. P. Umstadter, Phys. Rev. Lett. **110**, 155003 (2013).

[30] A. Ben-Ismail, O. Lundh, C. Rechatin, J. K. Lim, J. Faure, S. Corde, and V. Malka, Appl. Phys. Lett. **98**, 264101 (2011).

Paper VIII

Enhancement of X-Rays Generated by a Guided Laser Wakefield Accelerator inside Capillary Tubes

J. Ju, K. Svensson, A. Döpp, H. E. Ferrari, K. Cassou, O. Neveu, G. Genoud, F. Wojda, M. Burza, A. Persson, O. Lundh, C.-G. Wahlström, & B. Cros.

Appl. Phys. Lett. **100**, 191106 (2012).

APPLIED PHYSICS LETTERS **100**, 191106 (2012)

Enhancement of x-rays generated by a guided laser wakefield accelerator inside capillary tubes

J. Ju,[1] K. Svensson,[2] A. Döpp,[1] H. E. Ferrari,[3] K. Cassou,[1] O. Neveu,[1] G. Genoud,[2] F. Wojda,[2] M. Burza,[2] A. Persson,[2] O. Lundh,[2] C.-G. Wahlström,[2] and B. Cros[1,a)]
[1]*Laboratoire de Physique des Gaz et des Plasmas, CNRS-Université Paris-Sud 11, 91405 Orsay, France*
[2]*Department of Physics, Lund University, P.O. Box 118, S-22100 Lund, Sweden*
[3]*Consejo Nacional de Investigaciones Científicas y Técnicas (CONICET), 8400 Bariloche, Argentina*

(Received 17 January 2012; accepted 24 April 2012; published online 9 May 2012)

Electrons accelerated in the nonlinear regime in a laser wakefield accelerator experience transverse oscillations inside the plasma cavity, giving rise to ultra-short pulsed x-rays, also called the betatron radiation. We show that the fluence of x-ray can be enhanced by more than one order of magnitude when the laser is guided by a 10 mm long capillary tube instead of interacting with a 2 mm gas jet. X-rays with a synchrotron-like spectrum and associated critical energy ~5 keV, with a peak brightness of $\sim 1 \times 10^{21}$ ph/s/mm^2/mrad^2/0.1%BW, were achieved by employing 16 TW laser pulses. © *2012 American Institute of Physics*. [http://dx.doi.org/10.1063/1.4712594]

Since their discovery, x-rays have contributed to many fields of science and the development of new x-ray sources is an active field of research. Ultra-short x-ray pulses[1,2] can be generated in a laser wakefield accelerator (LWFA). In the so-called blow-out regime of LWFAs, the ponderomotive force of an intense laser pulse focused in a plasma blows the electrons out of a volume of radius similar to the laser focal spot radius. The charge separation between electrons and ions is associated to electric fields with an amplitude of the order of ~100 GV/m. These fields can trap and accelerate longitudinally plasma electrons to high energy, typically 100 MeV, over only a few millimetres, and at the same time wiggle the electrons transversely. The x-ray pulses produced by this mechanism have spectra similar to synchrotron radiation and are often called the betatron radiation. The betatron radiation has intrinsically striking features for ultra-fast imaging: a pulse duration on the femtosecond scale[3] and a perfect synchronization to the pump laser.

The use of such x-rays sources for imaging applications has already been demonstrated[4,5] with photon energies in the range of 1–10 keV and peak brightness of 10^{22} ph/s/mm^2/mrad^2/0.1%BW. As they are produced by relatively compact laser systems, they have a large potential for dissemination among various user communities. Their development has thus attracted a lot of attention in the past few years, mostly to characterize their properties[3,6,7] or to control them.[8,9] Scalings developed for betatron radiation predict that the x-ray photon energy and brightness can be enhanced by increasing the laser intensity or/and decreasing the plasma density.[10] For example, x-rays extending to 50 keV were observed[11] by using a peak focused intensity larger than 10^{20} W/cm^2. The use of laser guiding in capillary tubes has been shown to enable electron acceleration and x-ray emission at low plasma density and low laser intensity.[12,13]

In this letter, we report on the ability to increase the number of photons produced in the 2–10 keV range by using a lower density, longer plasma inside capillary tubes, compared to the plasma density and length usually achieved with gas jets. Using 16 TW laser pulses, the generated x-ray peak brightness is multiplied by 30 when the laser beam is guided by a 10 mm long capillary tube instead of using a 2 mm long gas jet.

Experiments were performed at the Lund Laser Centre, Sweden, where a Ti:Sa, 800 nm central wavelength, laser system delivers an energy of up to 1 J in 40 fs full width at half maximum (FWHM) pulses. A deformable mirror is used after compression to compensate for wavefront distortions in the focal plane. The laser beam was focused, using a $f/15$ off-axis parabola, to an Airy-like spot with 19.7 ± 0.8 μm radius at first minimum. With an energy of 650 mJ in the focal plane, the peak intensity was estimated to be $(5.4 \pm 0.1) \times 10^{18}$ W/cm^2, giving a normalized laser strength parameter $a_0 = 1.6$. Capillary tubes filled with hydrogen gas were used to confine the gas and to partially guide the laser beam. The spectra of electrons accelerated in either a gas jet or capillary tubes were measured by a spectrometer, composed of a 10 cm long permanent magnet, with a central magnetic field of 0.7 T, deflecting the electrons subsequently intercepted by a phosphor screen (Kodak Lanex Regular) imaged onto a CCD camera. Electrons below 42 MeV did not reach the phosphor screen and were not detected. The beam charge was obtained by the absolute calibration of the Lanex screen.[14] X-rays generated by betatron oscillations in the LWFAs were recorded by a x-ray CCD camera placed 110 cm away from the capillary exit on the laser axis, providing a collection angle of 12×12 mrad^2. The x-ray camera was located outside the vacuum chamber, behind a 300 μm thick beryllium window and a 5 mm air gap. A set of metallic filters (V, Fe, Ni, Sn, and Zr), held together by a 30 μm wire grid, were used in front of the camera to determine the critical energy associated to the x-ray spectrum in the range of 2–10 keV.

Fig. 1 shows the main characteristics of the electrons and x-rays produced inside a 10 mm long, 178 μm diameter capillary tube for two values of the plasma electron density, n_e. The electron energy spectra in (b) and (e) were extracted from the raw Lanex images seen in (a) and (d), respectively, by summing in the vertical direction and rescaling in the horizontal direction to account for magnet dispersion.

a)Electronic mail: brigitte.cros@u-psud.fr.

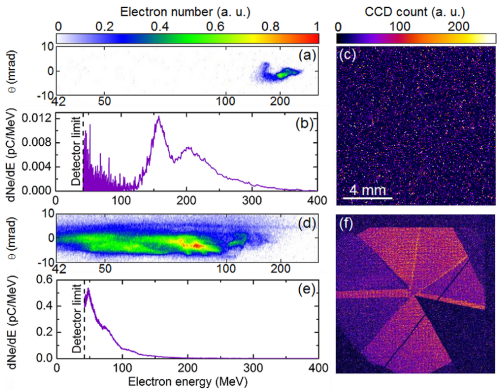

FIG. 1. Single shot raw Lanex images, energy spectra, and x-ray beam images obtained after a 10 mm long, 178 μm diameter capillary tube for two values of the plasma electron density: (a)–(c) $n_e = (5.4 \pm 0.3) \times 10^{18}$ cm^{-3}; (d)–(f) $n_e = (8.1 \pm 0.5) \times 10^{18}$ cm^{-3}.

The electron spectra typically exhibit rather large energy spread, and the total charge and maximum energy are strongly dependent on the plasma electron density. The lower density case is close to the density injection threshold[13] and leads to a maximum energy of the order of 300 MeV (measured at 10% of the maximum of the spectrum), with a low beam charge of 0.9 pC and a divergence FWHM of 5.2 mrad. No x-rays were detected for this shot as seen in Fig. 1(c). At $n_e = (8.1 \pm 0.5) \times 10^{18}$ cm^{-3}, a 18 pC electron bunch was measured with a maximum energy of ~120 MeV, as shown in Fig. 1(e). The corresponding beam divergence is about 5.8 mrad. Fig. 1(f) shows the associated x-ray beam transmitted through the different filters.

The x-ray spectrum can be characterized by a synchrotron-like[2] spectrum of the form $d^2I/(dEd\Omega)_{\theta=0} \propto (E/E_c)^2 \mathcal{K}^2_{2/3}(E/E_c)$, where $\mathcal{K}_{2/3}$ is the modified Bessel function of order 2/3. The critical energy is given by $E_c = 3\hbar K\gamma^2\omega_\beta$, where $K = \gamma r_\beta \omega_\beta / c$ is the wiggler strength parameter with $\gamma, r_\beta, \omega_\beta$ denoting the relativistic factor, the amplitude, and frequency of betatron oscillation, respectively. The critical energy was evaluated from the transmission of x-rays through the different metal filters with a least squares method.[11] In the case of Fig. 1(f), it was found to be 5.4 keV, which is higher than in previous observations[1,12] with similar laser power.

The maximum x-ray fluence measured is $(5.7 \pm 0.6) \times 10^5$ ph/mrad^2 [Fig. 1(f)]. To estimate the peak brightness of this x-ray source, the source size and duration are needed. The source size can be estimated from the expression of critical energy[15] as $r_\beta = E_c c/3\hbar\gamma^3\omega_\beta^2$. The relativistic factor is determined using the mean energy of the electron spectra $\bar{E}_e$, where $\bar{E}_e$ is the average of electron energies weighted by their respective spectral intensities. For the shot plotted in Fig. 1(e), $\bar{E}_e$ is calculated to be 88 ± 4 MeV, and the source size estimated to be $r_\beta = 2 \pm 0.3$ μm. This estimation is validated by 3D simulations performed with the particle-in-cell code CALDER-CIRC,[16] for input parameters close to the experimental ones. They show that the laser pulse non linear evolution in the 178 μm diameter capillary tube leads to a maximum normalized vector potential in the range of $4 < a_0 < 5.5$ and produces accelerated electrons with a mean energy of about 130 MeV. The transverse and longitudinal sizes of the electron bunch in the simulation are 1.3 μm and 10 μm (~35 fs), respectively, in reasonable agreement with the estimation from the measurements. The peak brightness achieved in our experiment is estimated, using $r_\beta = 2$ μm, to be $\sim 1 \times 10^{21}$ ph/s/mm^2/mrad^2/0.1%BW, and the wiggler strength parameter, $K \simeq 10$. Taking into account the divergence of the x-ray beam, $\theta = K/\gamma$, the estimated total photon number over the whole spectrum is of the order of 10^9 per shot.

The x-ray fluence can be changed by varying the plasma density, as presented in Fig. 2 for two different capillaries. In both cases, the x-ray fluence is maximum for a density of the order of 8×10^{18} cm^{-3}. The influence of the plasma electron density on the x-ray fluence can be understood as a result of the influence of the density on the laser propagation and related electron injection and acceleration. For the parameters of this experiment, at lower densities, electron trapping is not efficient, resulting in a lower beam charge, as seen in Fig. 1. As the plasma density is increased, trapping becomes more efficient and more charge can be accelerated, but the acceleration length and thus the electron energy become smaller due to the shortening of the electron dephasing and laser depletion lengths. For the given laser intensity, the maximum x-ray fluence is achieved in the 10 mm long capillary tube. Simulations in the 178 μm capillary tube for the optimum electron density show that the overall process of laser non-linear evolution, electron injection and acceleration, and x-ray emission occur over the first 10 mm of

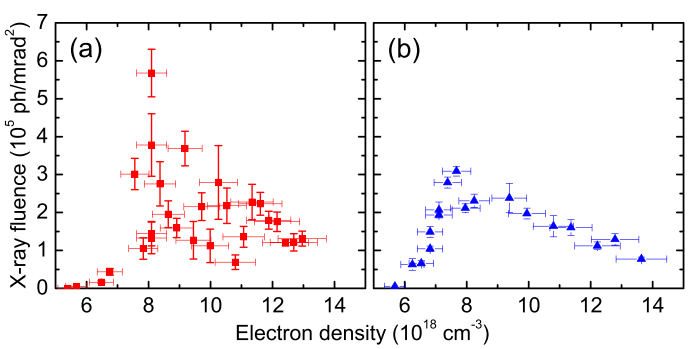

FIG. 2. X-ray fluence as a function of the plasma electron density for (a) a 10 mm long, 178 μm diameter capillary and (b) a 20 mm long, 152 μm diameter capillary; the other parameters are the same as for Fig. 1.

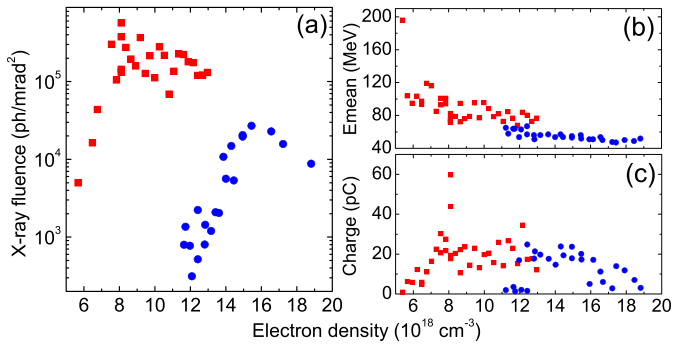

FIG. 3. (a) X-ray fluence, (b) mean energy, and (c) charge of electrons as a function of plasma density for the 10 mm long capillary (red squares) and the 2 mm gas jet (blue dots).

propagation. Fluctuations of the x-ray fluence are smaller at the output of the 152 μm diameter, 20 mm long capillary: this can be attributed to the fact that the capillary diameter is smaller favoring a more stable laser guiding. In this case, more x-rays are produced at low densities: it can be due to higher intensities achieved locally inside the capillary, or an evolution of the laser pulse leading to electron injection and acceleration over a distance larger than 10 mm.

The enhancement of the x-ray fluence due to the length and density of the plasma is demonstrated in Fig. 3 by the comparison of the x-ray fluence measured for two targets, 10 mm long capillary tube and 2 mm gas jet, for the same experimental conditions.

It shows that for the intensity used in this experiment, the use of a capillary tube allows electron self-injection to happen at lower density than in the gas jet. The capillary provides a long distance for laser evolution to the threshold required for self-trapping[12,13] and helps collecting and refocusing the energy initially in the wings of the laser spot;[16] the excitation of multiple modes and their beating can also give rise locally to higher intensity than in vacuum, thus favoring an increase of a_0. For the gas jet, electron trapping starts around $n_e = 11 \times 10^{18}$ cm^{-3}, which results in lower energy electrons, as electron energy inversely depends on plasma density. In the intermediate density range of $(11-13) \times 10^{18}$ cm^{-3}, a higher mean electron energy is achieved when the capillary is employed. The maximum x-ray fluence in the capillary corresponds to the density where the maximum electron charge is measured. The maximum x-ray fluence obtained with the gas jet is 2.7×10^4 ph/mrad^2 for $n_e = 15 \times 10^{18}$ cm^{-3}. Using the values obtained from experimental data, $E_c = 4.6$ keV, $\bar{E}_e = 56$ MeV, the source size is estimated to be 2.4 μm, and the corresponding peak brightness is $\sim 3 \times 10^{19}$ ph/s/mm^2/mrad^2/0.1%BW, similar to the result of Ref. 1.

In conclusion, we demonstrate that betatron radiation is significantly enhanced by guiding the laser in a capillary tube allowing electron acceleration in a low density, long plasma. In particular, $\sim 1 \times 10^{21}$ ph/s/mm^2/mrad^2/0.1%BW is the brightest x-ray beam achieved with a <20 TW laser. The dependence of the x-ray beam parameters on the capillary tube diameter and length provides additional control of the interaction, and its systematic study will be the subject of future work.

This work was supported by LASERLAB-EUROPE (Grant Agreement No. 228334), the Triangle de la Physique (Grant Agreement NEXT-2009-064 T), the Lund University X-ray Center (LUXC), the Swedish Research Council (including the Linné grant to LLC), and the Knut and Alice Wallenberg Foundation. J. Ju acknowledges financial support from the Chinese Scholarship Council.

[1]A. Rousse, K. Ta Phuoc, R. Shah, A. Pukhov, E. Lefebvre, V. Malka, S. Kiselev, F. Burgy, J.-P. Rousseau, D. Umstadter, and D. Hulin, Phys. Rev. Lett. **93**, 135005 (2004).
[2]E. Esarey, B. A. Shadwick, P. Catravas, and W. P. Leemans, Phys. Rev. E **65**, 056505 (2002).
[3]K. Ta phuoc, R. Fitour, A. Tafzi, T. Garl, N. Artemiev, R. Shah, F. Albert, D. Boschetto, A. Rousse, D.-E. Kim, A. Pukhov, V. Seredov, and I. Kostyukov, Phys. Plasmas **14**, 080701 (2007).
[4]S. Kneip, C. McGuffey, F. Dollar, M. S. Bloom, V. Chvykov, G. Kalintchenlko, K. Krushelnick, A. Maksimchuk, S. P. D. Mangles, T. Matsuoka, Z. Najmudin, C. A. J. Palmer, J. Schreiber, W. Schumaker, A. G. R. Thomas, and V. Yanovsky, Appl. Phys. Lett. **99**, 093701 (2011).
[5]S. Fourmaux, S. Corde, K. Ta Phuoc, P. Lassonde, G. Lebrun, S. Payeur, F. Martin, S. Sebban, V. Malka, A. Rousse, and J. C. Kieffer, Opt. Lett. **36**, 2426 (2011).
[6]R. C. Shah, F. Albert, K. Ta Phuoc, O. Shevchenko, D. Boschetto, A. Pukhov, S. kiselev, F. Burgy, J.-P. Rousseau, and A. Rousse, Phys. Rev. E **74**, 045401(R) (2006).
[7]S. Fourmaux, S. Corde, K. Ta Phuoc, P. M. Leguay, S. Payeur, P. Lassonde, S. Gnedyuk, G. Lebrun, C. Fourment, V. Malka, S. Sebban, A. Rousse, and J. C. Kieffer, New J. Phys. **13**, 033017 (2011).
[8]S. P. D. Mangles, G. Genoud, S. Kneip, M. Burza, K. Cassou, B. Cros, N. P. Dover, C. Kamperidis, Z. Najmudin, A. Persson, J. Schreiber, F. Wojda, and C.-G. Wahlström, Appl. Phys. Lett. **95**, 181106 (2009).
[9]K. Ta Phuoc, E. Esarey, V. Leurent, E. Cormier-Michel, C. G. R. Geddes, C. B. Schroeder, A. Rousse, and W. P. Leemans, Phys. Plasmas **15**, 063102 (2008).
[10]A. G. R. Thomas, Phys. Plasmas **17**, 056708 (2010).
[11]S. Kneip, S. R. Nagel, C. Bellei, N. Bourgeois, A. E. Dangor, A. Gopal, R. Heathcote, S. P. D. Mangles, J. R. Marquès, A. Maksimchuk, P. M. Nilson, K. Ta Phuoc, S. Reed, M. Tzoufras, F. S. Tsung, L. Willingale, W. B. Mori, A. Rousse, K. Krushelnick, and Z. Najmudin, Phys. Rev. Lett. **100**, 105006 (2008).
[12]G. Genoud, K. Cassou, F. Wojda, H. E. Ferrari, C. Kamperidis, M. Burza, A. Persson, J. Uhlig, S. Kneip, S. P. D. Mangles, A. Lifschitz, B. Cros, and C.-G. Wahlström, Appl. Phys. B **105**, 309 (2011).
[13]H. E. Ferrari, A. F. Lifschitz, G. Maynard, and B. Cros, Phys. Plasmas **18**, 083108 (2011).
[14]Y. Glinec, J. Faure, A. Guemnie-Tafo, V. Malka, H. Monard, J. P. Larbre, V. De Waele, J. L. Marignier, and M. Mostafavi, Rev. Sci. Instrum. **77**, 103301 (2006).
[15]F. Albert, R. Shah, K. Ta Phuoc, R. Fitour, F. Burgy, J.-P. Rousseau, A. Tafzi, D. Douillet, T. Lefrou, and A. Rousse, Phys. Rev. E **77**, 056402 (2008).
[16]H. E. Ferrari, A. Lifschitz, and B. Cros, Plasma Phys. Controlled Fusion **53**, 014005 (2011).

Paper IX

A Setup for Studies of Laser-Driven Proton Acceleration at the Lund Laser Centre

B. Aurand, M. Hansson, L. Senje, K. Svensson, A. Persson, D. Neely, O. Lundh, & C.-G. Wahlström.

Laser Part. Beams **33**, p. 59 (2015).

Laser and Particle Beams (2015), *33*, 59–64.

doi:10.1017/S0263034614000779

A setup for studies of laser-driven proton acceleration at the Lund Laser Centre

B. AURAND,[1] M. HANSSON,[1] L. SENJE,[1] K. SVENSSON,[1] A. PERSSON,[1] D. NEELY,[2] O. LUNDH,[1] AND C.-G. WAHLSTRÖM[1]

[1]Department of Physics, Lund University, Lund, Sweden
[2]Central Laser Facility, STFC Rutherford Appleton Laboratory, Didcot, United Kingdom

(RECEIVED 8 September 2014; ACCEPTED 26 October 2014)

Abstract

We report on a setup for the investigation of proton acceleration in the regime of target normal sheath acceleration. The main interest here is to focus on stable laser beam parameters as well as a reliable target setup and diagnostics in order to do extensive and systematic studies on the acceleration mechanism. A motorized target alignment system in combination with large target mounts allows for up to 340 shots with high repetition rate without breaking the vacuum. This performance is used to conduct experiments with a split mirror setup exploring the effect of spatial and temporal separation between the pulses on the acceleration mechanism and on the resulting proton beam.

Keywords: Laser-ion acceleration; Mirror design; Radiation detectors

INTRODUCTION

Within the last decade, tremendous progress has been made in the field of laser ion acceleration. First demonstrated *Wilks et al.*, 2001 by the mechanism of target normal sheath acceleration (TNSA) nowadays provides a source for ultra-short proton bunches with energies up to several tens of MeV (Daido *et al.*, 2012; Passoni *et al.*, 2010). An ultra-intense laser pulse ($I > 10^{16}$ W/cm^2) which interacts with the front-side of a μm-thick target foil drives a massive electron current toward the rear-side of the target. The electrons exiting the target on the scale of the Debye-length create a charge separation field between them and the positively charged remaining bulk. This generates an electric field in the order of a few TV/m. In this field, which can be considered static on the timescale of a several 100's of fs up to a few ps (Schreiber *et al.*, 2006), protons and heavier ions like carbon or oxygen — mainly from the hydrocarbon contamination layer on the target — are accelerated.

Numerous studies on the mechanism of TNSA have been made so far, e.g., the investigation of the dependence on laser parameters like the focal spot size (Brenner *et al.*, 2011), energy (Coury *et al.*, 2012), or pulse duration (Robson *et al.*, 2007), studies on the electron current driven in the target (Tresca *et al.*, 2011; Coury *et al.*, 2013), or different target geometry (Schwoerer *et al.*, 2006; Ramakrishna *et al.*, 2010; Hegelich *et al.*, 2006; Burza *et al.*, 2011). In our current study on TNSA acceleration, we focus on the influence of two independent laser pulses with different temporal and spatial separation, interacting with the target and driving the acceleration. In this paper we describe the technical part of the setup, which includes laser and particle diagnostics as well as the target and optical probing system.

Address correspondence and reprint request to Bastian Aurand, Department of Physics, Lund University, 22100 Lund, Sweden.
E-mail: bastian.aurand@uni-duesseldorf.de

LASER SYSTEM

The Lund terawatt laser is a Ti:Sapphire based CPA (Strickland & Mourou, 1985) laser system with four amplification stages situated in the basement of the Physics Department at Lund university. A dedicated diagnostic table setup next to the compressor allows the verification of the laser beam parameters on a daily basis. The pulse duration is measured with a second order single-shot autocorrelator. A third order scanning autocorrelator (Amplitude, Sequoia®) is used to measure the laser contrast. Besides that, the spectrum (RGB, Qwave®) and the spectral phase (Avesta, SPIDER SP-120) are recorded. A mirror in the beam line with a designed leakage of 1.5% allows for on-shot recording of autocorrelation and laser spectrum. Typical pulse parameters are an energy $E_L = 0.9$ J at a pulse duration of $\tau_L = 35$ fs. The laser contrast is $0.5–1 \times 10^{-9}$ up to 50 ps before the main

pulse. A beam position system controls piezo mirrors in the amplifier chain and compensates for long term drifts which helps to keep laser parameters stable during operation.

A deformable mirror (DM) with a clear aperture of 65 mm, segmented in 32 piezo controlled areas (NightN Ltd., DM2-65-32) in the beam line enables corrections of the wavefront downstream. The 45 mm diameter beam is guided in vacuum and can be delivered into two different target areas by flipping one of the beam line mirrors. One of the target areas is mainly dedicated to laser wakefield acceleration (LWFA) (Desforges *et al*., 2014; Hansson *et al*., 2014) experiments, whereas the other target area mainly for proton experiments. The radiation shielding allows simultaneous experiments on electrons in one room and preparation of ion acceleration experiments in the other room. Both cylindrical experimental chambers with an inner diameter of 108 cm and a height of 37 cm are accessible by removing the lid or flanges on the side of the vacuum vessel. In the following, we will focus on the proton setup only (Fig. 1).

TARGET SYSTEM

Below the proton chamber is a housing containing an electrically insulated and Faraday-shielded xyz-linear stage system (Newport, GTS70). Using optical encoded position sensors and double-shielded cables, malfunction events due to electro-magnetic pulses do not occur. All stages have a travel range of 70 mm at a velocity of up to 50 mm/s with an on-axis accuracy of $\pm 1\,\mu$m and a bi-directional position reproducibility of 100 nm. The upper part of the target mount holds a three-point load, multi-purpose holder on which different kinds of self-centering targets can be mounted. Additional tip/tilt screws enable target adjustments perpendicular to the motion axis which is checked for every target with a micrometer caliper. Primarily used is an matrix target mount with 340 (17×20) independent target positions of 1 mm diameter and 2.5 mm separation (Fig. 2a). The mount consists of two comb shaped plates where a target foil can be clamped in between (Fig. 2b). Using an additional spacer, double layered target configurations or grids for proton imaging purposes can be realized.

The position of the target chamber center (TCC) which is the dedicated focus position is defined by the overlap of two external lasers beams, each referenced to the center of two opposed flanges on the chamber wall. This position is transferred to an alignment needle on the target mount and verified during major rebuilds. The target is aligned in the TCC using the laser focus diagnostic, observing the

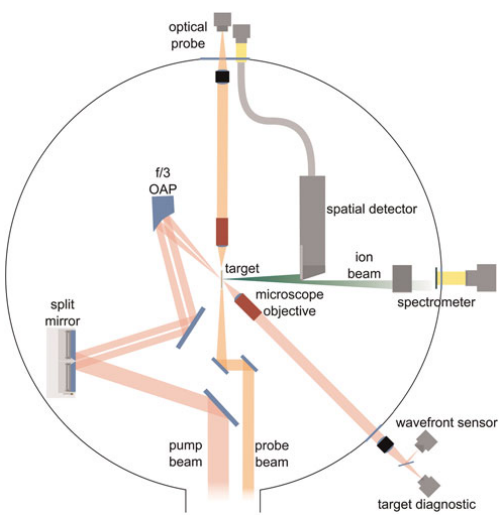

Fig. 1. Experimental setup for proton acceleration in the TNSA regime. The incident laser pulse is divided by a split-mirror into two beams which can be spatially and temporally shifted with respect to each other. Both beams are focused by the same OAP onto the target. The accelerated protons can be sent to a spectrometer for an energy measurement or a spatial detector in order to determine the beam profile. An independent optical probe can be used to do shadowgraphy or interferometry of the target rear surface.

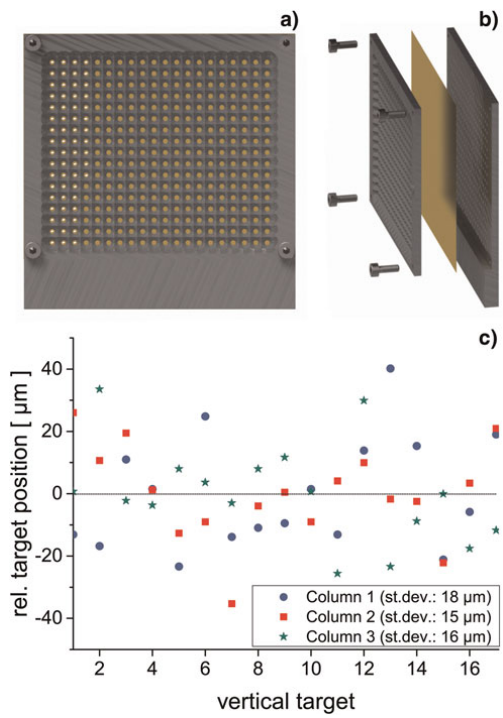

Fig. 2. (**a**) Matrix target mount with 340 (17×20) independent target positions. (**b**) The mount consists of two comb shaped plates in where the target foil is clamped in between (**c**) Scan of the relative focal position for a column wise vertical movement of a 3 µm Al foil. The standard deviation in each column is less than 18 µm.

reflection of a monochromatic light source from the target rear surface at an angle of 45°. This diagnostic is based on an infinity corrected 10× objective (Mitutoyo, Plan Apo NIR) with a working distance of 31 mm, imaging the laser focal plane onto a camera outside the vacuum vessel. Alternatively, for the laser alignment, the beam can be sent to a modified Hartmann sensor (Hartmann, 1900; Primot *et al*., 1995) (Phasics, SID4) to measure the wavefront. Note that within this setup using a DM, wavefront corrections for all optical elements up to the final focusing parabola can be included. The small depth of the focus diagnostic (4.1 μm) and the additional observation angle allow for a position accuracy of 2–3 μm with respect to the objective.

The typical procedure in order to take a series of shots is a columnwise pre-inspection of the target, regarding foil condition and possible wrinkles. This allows for a burst-mode of up to 17 shots within 1 min by moving the target vertically to the next position without any further inspection. Measurements of the focus position (Fig. 2c) for a pre-aligned target show a deviation of less than 18 μm, which is significantly smaller than the Rayleigh-length. This deviation is mainly given by imperfections during manufacturing of the target mount. The complete remote control of the target alignment enables a scan with a complete target in less than 1.5 h. Simultaneous monitoring and controlling of the laser parameters guarantee stable laser conditions. Further automated control of the target system, e.g., by target positioning via chromatic-confocal sensing (Ruprecht, A.K. *et al.* 2005) could increase the repetition rate and precision of the alignment.

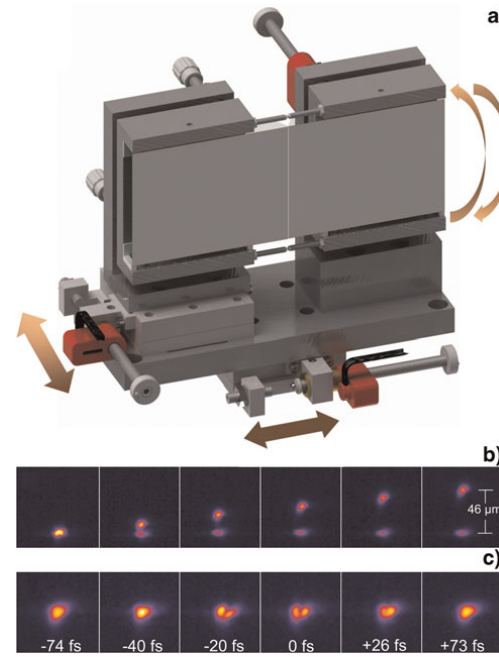

Fig. 3. (**a**) Split mirror setup generating two independent beams, which can be spatially and temporally shifted against each other. In addition the amount of energy in both parts can be changed. (**b**) Vertical focus separation by movement of one beam. (**c**) Interference structures are visible when the beams overlap within $\Delta t = \pm 20$ fs relative timing.

SPLIT MIRROR SETUP

Focusing of the laser is done by an off-axis parabolic mirror with 152 mm focal length (SORL, OAP 06-02-03/MMOA-3) giving a focal spot of 5 μm (FWHM) corresponding to a maximum intensity of 2×10^{19} W/cm^2 on the target and a measured Rayleigh-length of ($z_R \approx 50$ μm). One of the mirrors inside the experimental chamber consists of a specially designed split-mirror to generate two independent beams which can be spatially and temporally shifted with respect to each other (Fig. 3a). The setup is based on two protected silver mirrors sized 70×90 mm which have a thin edge to place them side by side, leaving a vertical gap of only a few tenths of a millimetre. Both mirrors are mounted separately and can be tilted horizontally and vertically using piezo-linear actuators (Newport, Picomotor). In addition, one of the mirrors is mounted on a linear stage allowing for a translation perpendicular to its surface. The introduced path difference of up to 20 mm in either direction at an incidence angle of ≈12° correspondes to a temporal delay of max. ±68 ps with respect to the fixed pulse. Finally, both mirrors can be moved sideways simultaneously to change the fraction of the incident beam on each mirror and therefore the energy ratio between the two pulses.

We deduce the minimal vertical movement of the beam in the focal plane to 150 nm/steps of the piezomotor tilting the mirror. In the given geometry, a vertical separation does not significantly change the length of each beam path, so it is not changing the relative timing between the two pulses. The bi-directional repeatability due to hysteresis effects in the mount is in the order of 5–6 μm. To avoid this effect, scans are always performed in one direction of movement (Fig. 3b).

The temporal overlap of the pulses is verified by the observation of an interference structure while both beams are spatially overlapped. The interference pattern is visible within a spatial range of 20 μm corresponding to ≈60 fs temporal range, showing a symmetric maximum (Fig. 3c). This method allows for a relative timing with a sub-pulse duration accuracy which is higher compared to methods like transverse probing of the generated plasma (Aurand *et al*., 2014).

Advantageous for all kinds of measurement series done with this setup are the common beam line and the focusing system downstream of the split-mirror, making the measurements insensitive to beam pointing fluctuations. Even if the absolute focus position of the system undergoes a small spatial jitter, the relative spatial and temporal separation of the beams remained fixed.

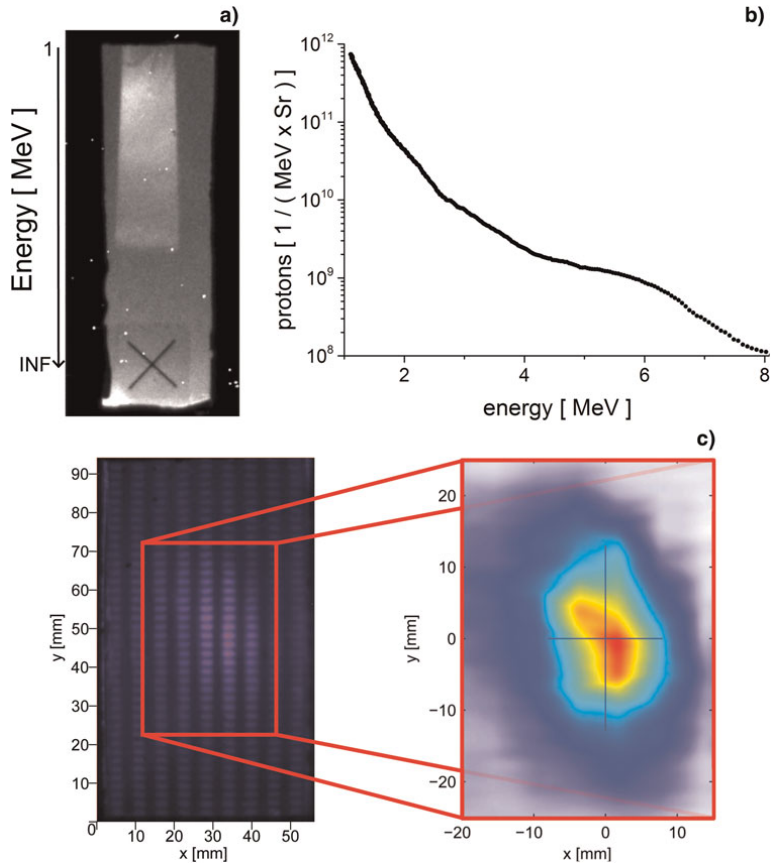

Fig. 4. Proton energy measurement from a 3 μm Al foil. (**a**) The raw data image obtained by the fluorescence of energy dispersed protons in a BC-408 scintillator in target normal direction. (**b**) Evaluated proton spectra using the calculated deflection curve and a cross calibration with CR-39 to get the absolute particle number. (**c**) Using the spatial detector, a beam profile of the accelerated particles can be taken. An Al filter grid in front of the detector allows for the subtraction of the electron background and a reconstruction of the proton beam profile.

ION DIAGNOSTIC

Ions are accelerated from the target rear surface. In order to be able to match the high repetition rate and the high number of shots per target, all diagnostics used in this setup have digital readouts.

The proton energy is determined by deflection of the proton beam in a magnetic field with an effective strength of $B_{Eff} = 0.69$ T and a length of 6 cm, which is situated in the target normal direction (47 ± 0.5) cm behind the target. A 1 mm horizontal entrance slit covers a solid angle of (8×10^{-5}) sr. Heavier ions are blocked by a 6 μm Al filter in front of the scintillator (St. Gobain, BC-408). The fluorescence signal is imaged by a 16-bit camera (Princeton, "PhotonMAX 1024")(Fig. 4a). To obtain the absolute particle number, a cross-calibration using a CR-39 trace detector was done (Cartwright *et al*., 1978) (Fig. 4b). The lowest detectable energy, determined by the setup geometry, is 1.2 MeV. The highest resolvable energy is ≈10 MeV.

The proton beam profile is measured by moving a scintillator (St. Gobain, BC-408) with a thickness of 500 μm into to the beam at a position of (65 ± 2) mm behind the target. The scintillator is placed in a light-shielded aluminum box with a 12 μm thick Al entrance window and an acceptance angle of 28°. The scintillator is imaged by an objective inside the box onto an optical fiber bundle, which transfers the signal out of the vacuum chamber onto a camera (Fig. 4c). Using a grid of Al bars with different thicknesses in front of the scintillator allows for an analytical subtraction of the electron background, superimposed with the signal, by taking the different stopping power for electrons and protons into account. In

contrast to a stack of radiochromic film (RCF), the energy selectivity of the scintillator is not very high. The signal is a superposition of all protons which are passing the filter and thus being transmitted or being stopped in the scintillator (d_{Scint} = 0.5 mm; 0.9 MeV ≤ E_{Stop} ≤ 7 MeV). In the future, a stack of scintillators with various thickness which are fluorescing at different wavelengths could be used to obtain an energy resolved signal (Green *et al*., 2011). Note that the response from a scintillator depends both on particle number and particle energy, which needs to be taken into account calculating absolute particle numbers (Green *et al*., 2011).

OPTICAL PROBE SETUP

A small amount (≈10 mJ) of the stretched pulse can be coupled from the last amplification stage of the laser system and sent to a separate pulse compressor. This part is compressed to roughly 60 fs and can optionally be frequency doubled ($\lambda_{2\omega}$= 400 nm). A specially designed curved target mount allows for probing along the target rear surface without being affected by the bright plasma on the front surface (Fig. 5a). A motorized linear stage with 150 mm travel enables controlled delay scans in a time window of up to 1 ns. The probe imaging system consists of a 20× infinity corrected objective (Mitutoyo, Plan Apo NIR) with a working distance of 20 mm. The image is collected by a camera outside the vacuum vessel. In this configuration, shadowgraphy can be obtained, with a resolution of 1 µm (Fig. 5b). By adding a Wollaston prism (Small *et al*., 1973) and two polarizers outside the chamber, Nomarski-interferometry can be done to determine the electron density (Fig. 5c).

OUTLOOK

The double pulse setup described above was developed and implemented within the last year and has been used for experiments. More than 4000 shots on targets have been conducted so far, investigating changes in particle-energy distribution and proton beam profile. Tentative results show a clear dependence of particle energy and proton beam divergence on the spatial separation of the two foci. A detailed analysis and comparison to numerical simulations is currently under investigation and will be reported accordingly.

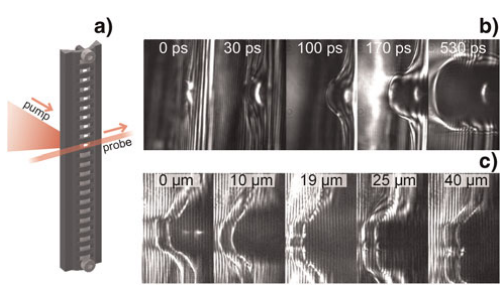

Fig. 5. (**a**) Curved target mount for transverse optical probing of the target rear surface. (**b**) High resolution shadowgraphy of an evolving plasma-plume, probed at different times compared to the pump-pulse. (**c**) Raw image by the Nomarski interferometric setup of two plasma-plumes for a fixed time but different separations, done by the split-mirror setup.

ACKNOWLEDGMENTS

We gratefully thank the Knut and Alice Wallenberg Foundation, the Swedish Research Council and the Swedish Foundation for Strategic Research for financial support. D. Neely acknowledges financial support by the UK Grant program: EP/K022415/1 (Advanced laser-ion acceleration strategies towards next generation healthcare).

REFERENCES

Aurand, B., Kuschel, S., Jäckel, O., Rödel, C., Zhao, H.Y., Herzer, S., Paz, A.E., Bierback, J., Polz, J., Elkin, B., Kamakar, A., Gibbon, P., Kaluza, M.C. & Kuehl, T. (2014). Enhanced radiation pressure-assisted acceleration by temporally tuned counter-propagating pulses. *Nucl. Inst. Meth. A* **740**, 033031.

Brenner, C.M., Green, J.S., Robinson, A.P.L., Carroll, D.C., Dromey, B., Foster, P.S., Kar, S., Li, Y.T., Markey, K., Spindloe, C., Streeter, M.J.V., Tolley, M., Wahlström, C.-G., Xu, M.H., Zepf, M., McKenna, P. & Neely, D. (2011). Dependence of laser accelerated protons on laser energy following the interaction of defocused, intense laser pulses with ultra-thin targets. *Lasers Part. Beams* **29**, 345–351.

Burza, M., Gonoskov, A., Genoud, G., Persson, A., Svensson, K., Quinn, M., McKenna, P., Marklund, M. & Wahlström, C.-G. (2011). Hollow microspheres as targets for staged laser-driven proton acceleration. *New J. Phys.* **13**, 013030.

Cartwright, B.G. & Shirk, E.K. (1978). A nuclear-track-recording polymer of unique sensitivity and resolution. *Nucl. Inst. Meth. A* **153**, 457–460.

Coury, M., Carroll, D.C., Robinson, A.P.L., Yuan, X.H., Brenner, C.M., Burza, M., Gray, R.J., Quinn, M.N., Lancaster, K.L., Li, Y.T., Lin, X.X., Tresca, O., Wahlström, C.-G., Neely, D. & McKenna, P. (2012). Influence of laser irradiated spot size on energetic electron injection and proton acceleration in foil targets. *Appl. Phys. Lett.* **100**, 074105.

Coury, M., Carroll, D.C., Robinson, A.P.L., Yuan, X.H., Brenner, C.M., Burza, M., Gray, R.J., Quinn, M.N., Lancaster, K.L., Li, Y.T., Lin, X.X., Tresca, O., Wahlström, C.-G., Neely, D. & McKenna, P. (2013). Injection and transport properties of fast electrons in ultra-intense laser-solid interactions. *Phys. Plasmas* **20**, 043104.

Daido, H., Nishiuchi, M. & S. Pirozhkov, S. (2012). Review of laser-driven ion sources and their applications. *Rep. Prog. Phys.* **75**, 056401.

Desforges, F.G., Hansson, M., Ju, J. Senje, L., Auder, T.L., Dobosz-Dufrenoy, S., Persson, A., Lundh, Wahlström, C.-G. & Cros, B. (2014). Reproducibility of electron beams from laser wakefield acceleration in capillary tubes. *Nucl. Instrum. Meth. A* **740**, 54–59.

Green, J., Borghesi, M., Brenner, C.M., Carroll, D.C., Dover, N.P., Foster, P.S., Gallegos, Pl., Green, S., Kirby, D., Kirkby, K.J., McKenna, P., Merchant, M.J., Najmudin, Z., Palmer, C.A.J., Parker, D., Prasad, R., Quinn, K.E., Rajeev,

P.P., Read, M.P., Romagnani, L., Schreiber, J., Streetse, M.J.V., Tresca, O., Wahlström, C.-G., Zeft, M. & Neely, D. (2011). Scintillator-based ion beam profiler for diagnosing laser-accelerated ion beams. *SPIE Proc.* **8079**, 807991.

Hansson, M., Senje, L., Persso, A., Lundh, O., Wahlström, C.-G., Desforges, F.G., Ju, J., Audet, T.L., Cros, B., Dobosz, S. & Monot, P. (2014). Enhanced stability of laser wakefield acceleration using dielectric capillary tubes. *Phys. Rev. ST AB* **17**, 031303.

Hartmann, J. (1900). Bemerkungenüber den Bau und die Justirung von Spektrographen. *Z. Instrumentenkunde* **20**, 17–27, 47–58.

Hegelich, B.M., Albright, B.J., Cobble, J., Flippo, K., Letzring, S., Paffett, M., Ruhl, H., Schreiber, J., Schulze, R.K. & Fernández, J.C. (2006). Laser acceleration of quasi-monoenergetic MeV ion beams. *Nat.* **439**, 441–444.

Passoni, M., Bertagna, L. & Zani, A. (2010). Target normal sheath acceleration: Theory, comparison with experiments and future perspectives. *New J. Phys.* **12**, 045012.

Primot, J. & Sogno, L. (1995). Achromatic three-wave (or more) lateral shearing interferometer. *Z. JOSA A* **12**, 2679–2685.

Ramakrishna, B., Murakami, M., Borghesi, M., Ehrentraut, L., Nickles, P.V., Schürer, M., Steinke, S., Psikal, J., Tikhonchuk, V. & Ter-Avetisyan, S. (2010). Laser-driven quasimonoenergetic proton burst from water spray target. *Phys. Plasmas* **17**, 083113.

Robson, L., Simpson, P.T., Clarke, R.J., Ledingham, K.W.D., Lindau, F., Lundh, O., McCanny, T., Mora, P., Neely, D., Wahlström, C.-G.,, Zepf, M. & McKenna, P. (2007). Scaling of proton acceleration driven by petawatt-laser plasma interactions. *Nat. Phys.* **3**, 58–62.

Ruprecht, A.K., Pruss, C., Tiziani, H.J., Wolfgan, O., Peter, L., Arndt, L., Mohr, J. & Lehmann, P. (2005). Confocal micro-optical distance sensor: Principle and design. *Z. SPIE Proc.* **5856**, 128–135.

Schreiber, J., Bell, F. Grüner, F., Schramm, U., Geissler, M., Schnüger, Ter-Avetisyan, S., Hegelich, B.M., Cobble, J., Brambrink, E., Fuchs, J., Auderbert, P. & Habs, D. (2006). Analytical model for ion acceleration by high-intensity laser pulses. *Phys. Rev. ST AB* **97**, 045005.

Schwoerer, H., Pfotenhauer, S. Jäckel, O., Amthor, K.-U., Liesfeld, B., Ziegler, W., Sauerbrey, R., Ledingham, K.W.D. & Esirkepov, T. (2006). Laser-plasma acceleration of quasi-monoenergetic protons from microstructured targets. *Nat.* **439**, 445–448.

Small, R.D., Sernas, V.A. & Page, R.H. (1972). Single beam Schlieren interferometer using a Wollaston prism. *Appl. Opt.* **11**, 858–862.

Strickland, D. & Mourou, G. (1985). Compression of amplified chirped optical pulses. *Opt. Commun.* **56**, 219–221.

Tresca, O., Carroll, D.C., Yuan, X.H., Aurand, B., Bagnoud, V., Brenner, C.M., Coury, M., Fils, J., Gray, R.J., Kühl, T., Li, C., Li, Y.T., Lin, X.X., Quinn, M.N., Evans, R.G., Zielbauer, B., Roth, M., Neely, D. & McKenna, P. (2011). Controlling the properties of ultra-intense laser proton sources using transverse refluxing of hot electrons in shaped mass-limited targets. *Plasma Phys. Contr. Fusion* **53**, 105008 .

Wilks, S.C., Langon, A.B., Cowan, T.E., Roth, M., Singh, M., Hatchett, S., Key, M.H., Pennington, D., MacKinnon, A. & Snaverly, R.A. (2001). Energetic proton generation in ultra-intense laser solid interactions. *Phys. Plasmas* **8**, 542–549.

Paper X

Manipulation of the Spatial Distribution of Laser-Accelerated Proton Beams by Varying the Laser Intensity Distribution

B. Aurand, L. Senje, K. Svensson, M. Hansson, A. Higginson, A. Gonoskov, M. Marklund, A. Persson, O. Lundh, D. Neely, P. McKenna, & C.-G. Wahlström.

Phys. Plasmas **23**, 023113 (2016).

PHYSICS OF PLASMAS 23, 023113 (2016)

Manipulation of the spatial distribution of laser-accelerated proton beams by varying the laser intensity distribution

B. Aurand,[1,2,a)] L. Senje,[1] K. Svensson,[1] M. Hansson,[1] A. Higginson,[3] A. Gonoskov,[4] M. Marklund,[4] A. Persson,[1] O. Lundh,[1] D. Neely,[5] P. McKenna,[3] and C.-G. Wahlström[1]
[1]*Department of Physics, Lund University, P.O. Box 118, 22100 Lund, Sweden*
[2]*Institut für Laser- und Plasmaphysik, Heinrich-Heine Universität, 40225 Düsseldorf, Germany*
[3]*SUPA Department of Physics, University of Strathclyde, Glasgow G4 0NG, United Kingdom*
[4]*Department of Applied Physics, Chalmers University of Technology, 41296 Gothenburg, Sweden*
[5]*Central Laser Facility, STFC, Rutherford Appleton Laboratory, OX11 0QX Didcot, United Kingdom*

(Received 25 October 2015; accepted 20 January 2016; published online 18 February 2016)

We report on a study of the spatial profile of proton beams produced through target normal sheath acceleration using flat target foils and changing the laser intensity distribution on the target front surface. This is done by either defocusing a single laser pulse or by using a split-pulse setup and irradiating the target with two identical laser pulses with variable spatial separation. The resulting proton beam profile and the energy spectrum are recorded as functions of the focal spot size of the single laser pulse and of the separation between the two pulses. A shaping of the resulting proton beam profile, related to both an increase in flux of low-energy protons in the target normal direction and a decrease in their divergence, in one or two dimensions, is observed. The results are explained by simple modelling of rear surface sheath field expansion, ionization, and projection of the resulting proton beam.
[http://dx.doi.org/10.1063/1.4942032]

I. INTRODUCTION

More than a decade ago, first experimental results[1,2] showed the possibility to accelerate protons to tens of MeV kinetic energy over a sub-mm length by using ultra-intense laser pulses irradiating the front side of μm-thick metal foils. The laser pulse forms a megaampere electron current inside the target penetrating through the rear surface and expanding into vacuum, leading to a charge separation on the scale of the Debye length. In the resulting electric field—which is of the order of up to a few TV/m—protons, mainly from the hydrocarbon contamination layer on the target rear surface, are quickly accelerated to high energies.[3,4]

This process, the target-normal-sheath-acceleration (TNSA) mechanism,[5] creates a continuous, Boltzmann-like, energy distribution up to a cut-off energy, which has attracted considerable interest, partly from a fundamental plasma physics point of view and partly because of its great potential for novel applications. It represents a very compact source of energetic ions. The pulse duration, at the source, is short, and the transverse emittance is very low.[6–8] Potential applications in medicine, material science, accelerator physics, and industry, for example, have been widely discussed.[3,9] However, in order to become a useful source for applications, a number of parameters must be greatly improved. For example, the shot-to-shot stability, the maximum proton energies, and the laser-to-proton energy conversion efficiencies must be increased. At the same time, the beam divergence should be reduced. In addition, for many applications, the proton energy distributions must be reduced, and ideally, a narrow energy spread achieved. All these improvements require further experimental and theoretical studies and enhanced understanding of the fundamental processes involved.

In typical TNSA experiments, using a flat metallic target foil irradiated on the front surface by a tightly focused laser pulse, the beam of protons leaves the target's rear surface centred along the target's normal (TN) direction. The maximum proton energy, E_{Prot}, within the beam depends on the peak laser intensity I_{L} and, thus, for a given laser pulse duration, both on the pulse energy and the irradiated spot size on the target. Brenner *et al.*[10] show that increasing I_{L} by increasing the pulse energy has a significantly larger influence on the total flux of protons than the same increase in intensity obtained by reducing the laser spot size. Xu *et al.*[11] and Green *et al.*[12] show that, with constant laser pulse energy and pulse duration, the total flux of protons can be increased by defocusing the laser at the target, even though the peak laser intensity is decreased. The proton beam divergence depends on the laser parameters and on the proton energies; the most energetic protons exhibit the smallest divergence.[13] Schollmeier *et al.*[14] used micro-structured target foils as a tool to demonstrate the effect of defocusing the laser beam on the generated proton beam. Several more studies have been reported in the literature regarding the proton beam divergence and laminarity[15] and how they can be manipulated, e.g., via the use of curved targets.[16,17] In this paper, we report on experimental studies of how the angular/spatial distribution of the proton beams can be manipulated without changing the target shape or composition, and instead by varying spatially the laser intensity distribution on the target's front surface. We keep the target and laser parameters fixed and vary the intensity distribution while monitoring the

[a)]Electronic mail: Bastian.Aurand@uni-duesseldorf.de

spatial proton beam profile. In recent studies, it was shown that by using a fixed, hollow, doughnut-like laser beam profile, the beam divergence, and energy profile could be manipulated.[18] Here, we vary the intensity distribution either by defocusing the laser on the target or by dividing the focused laser pulse into two spatially separated pulses, with a separation that can be continuously varied. In the first case, we find that the proton beam divergence can be significantly reduced by optimally defocusing the laser pulse, and in the second case that, with optimized separation between the two foci, the proton beam divergence is reduced in the direction of the separation of the foci, resulting in an elliptically shaped proton beam. These collimation effects, in one or two dimensions, are found to be mainly affecting the relatively large number of low energy protons. The number of low energy protons in the target's normal direction increases while their divergence decreases, resulting in intense beams of low-energy protons, collimated in one or two dimensions.

II. EXPERIMENTAL SETUP AND METHODS

The experiments were carried out using the Lund 10 Hz multi-terawatt laser system; a chirped-pulse amplification (CPA) based Ti:sapphire laser with a pulse duration of 35 fs and a temporal contrast better than 1×10^{-9} 50 ps before the main pulse. In the experiments presented here, the energy per pulse, on target, was kept fixed at 0.6 J. The experimental setup[19] is shown in Fig. 1(a). After compression, the 45 mm diameter beam was guided into the interaction chamber and sent onto a split-mirror setup (Figure 1(b)) before reaching an off-axis parabolic (OAP) focusing mirror. For the first part of the investigation, the split-mirror setup was positioned in a way that the full laser beam was reflected on one of the mirrors, and thus, only one focal spot was produced. Instead, the target foil was moved to different positions along the optical axis around the beam waist. For the second part of the investigation, the split-mirror setup was positioned such that each laser pulse was divided into two halves, resulting in two identical focused laser pulses hitting the target foil. The foil was then positioned in the focal plane of the focusing mirror while the separation between the two foci was varied between shots.

The split-mirror setup consists of two planes, protected silver mirrors of standard optical quality ($\lambda/10$ flatness). They have a vertically oriented wedged shaped edge in order to enable the mirrors to be mounted very close to each other, with a gap of only a few tenths of a millimetre, but with the possibility to move freely relative to each other. Due to a separate mounting, the mirrors can be tilted independently in vertical and horizontal directions. In addition, one of the mirrors is mounted on a linear translation stage, which moves the mirror perpendicular to its surface, enabling the relative optical path length and therefore the relative timing of the pulses to be accurately controlled. The complete split-mirror setup is further mounted on another linear translation stage moving it transversely with respect to the laser beam. This enables the split ratio of the pulses to be varied. Both beams are sent onto the same off-axis parabolic mirror, with 152 mm focal length and focused to a circular spot with radius $r_L = 2.5\ \mu$m (HWHM) reaching a peak intensity of $I_L = 2 \times 10^{19}$ W/cm^2.

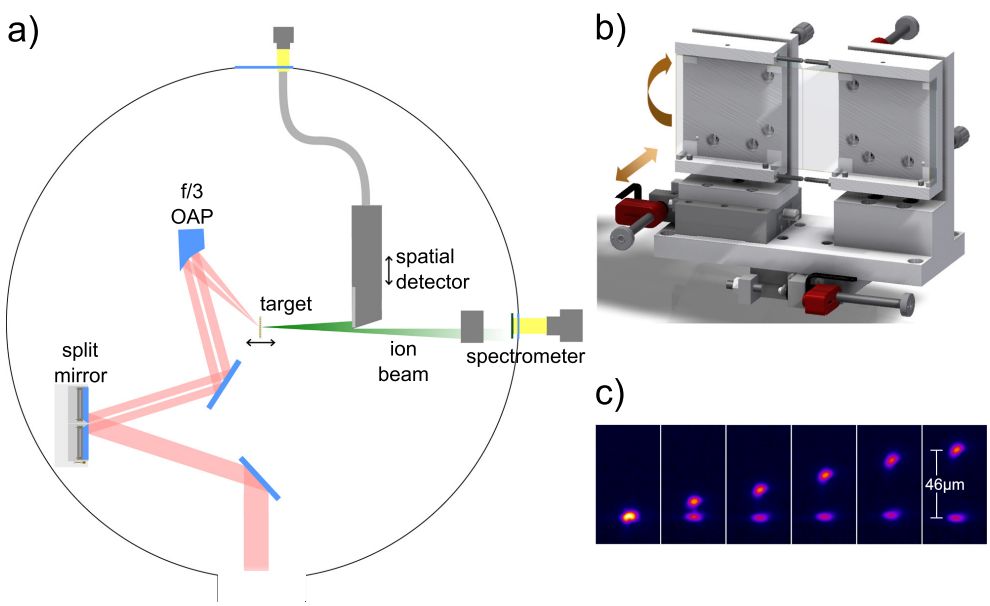

FIG. 1. (a) Experimental setup: The laser beam is guided onto the split-mirror and separated into two parts which are focused by an f/3 parabolic mirror onto the target. For diagnostics, either a spectrometer, consisting of a dipole magnetic field, a scintillator, and a camera, or a spatial detector to image the beam profile is used. (b) The split-mirror consists of two independently adjustable rectangular mirrors with a gap of a few tenths of a millimetre in between. (c) By tilting one of the mirrors, the spatial separation of the beams and the resulting foci can be varied.

Applying angular tilts in one direction to one of the mirrors, the two foci can be separated in that direction of the focal plane (Figure 1(c)). Note that this tilt is induced more than 1 m upstream of the interaction point and is in the order of some μ-rad. Neither a significant pulse front tilt nor a significant relative temporal difference between the beams is induced. By use of a deformable mirror in the beam line, the phase was corrected to ensure a good quality of the focus in the overlapped case. The slight horizontal elongation of the beam, which can be seen in Figure 1(c), is independent of the tilt direction. Fine adjustment of the temporal overlap can be done by adjustments of the relative path length while monitoring the interference patterns occurring in the focal plane when the foci have a spatial overlap. In the studies reported here, the splitting ratio was fixed at either 100:0 or 50:50, and the relative time delay $\Delta t = 0$.

As a target, we used 3 μm-thick Al foils mounted in a matrix target holder realizing 340 independent targets and where each new target can be aligned within a few seconds, with an accuracy of better than 18 μm (standard deviation) with respect to the laser focus position. The target is mounted at 45°, horizontally tilted, with respect to the laser axis.

In order to take advantage of the high repetition rate of the laser and the fast target alignment procedure, only online proton diagnostics were used. A magnetic-field based proton spectrometer disperses the protons, after passing through a 1 mm entrance pinhole, depending on their energy onto a scintillator (St. Gobain: BC-408; 500 μm thick), wrapped in a 12 μm thick aluminum foil to block heavy ions, which is monitored by a 16-bit camera (Princeton: PhotonMAX1024). The proton signal is collected in the target's normal direction covering a solid angle of 8×10^{-5} sr, and the energy uncertainty due to the pinhole size is $\Delta E/E \approx 10\%$. In addition, a spatial detector is used to monitor the spatial-intensity distribution of the proton beam.[20] A scintillator (St. Gobain: BC-408; 500 μm thick) is positioned (65 ± 2) mm behind the target in a light shielded box with a 12 μm thick and light tight Al entrance window. The scintillator emission is imaged onto an optical fibre bundle, which allows for the image to be transferred onto a 12-bit CCD camera placed outside the vacuum chamber. This enables a reconstruction of the two-dimensional proton beam spatial profile. With this detector setup, the signal is not energy selective, but represents a superposition of all protons, which are stopped in the scintillator ($0.9\,\text{MeV} < E_{\text{Stop}} < 7\,\text{MeV}$). We typically investigate protons with maximum kinetic energies of $E \leq 6$ MeV, so most protons are stopped in the scintillator. The signal from the detector is thus not representing the number of protons, but rather the deposited energy. By adding additional bars of aluminum with different thicknesses in front of the detector allowed us to distinguish between electrons and protons in the detector, which was used to calibrate the device.

III. EXPERIMENTAL RESULTS

A. Defocus scan with a single laser focus

When we use only one laser focus and move the target foil along the laser propagation axis, i.e., through the focus, we find, as expected, that the highest proton energy is obtained with the target at best focus ($r_{0\mu m} \approx 2.5\,\mu$m), where the peak intensity is the highest. The proton beam is then centered along the TN direction, and the profile, integrating over all protons with $E > 0.9$ MeV, is spatially round and smooth. However, the divergence dramatically decreases when the target foil is positioned at $\pm 375\,\mu$m ($r_{375\mu m} \approx 8.5\,\mu$m) or at $\pm 450\,\mu$m ($r_{450\mu m} \approx 10.5\,\mu$m) from best focus (see Figure 2(a)). This corresponds to approximately three to four Rayleigh lengths, and the peak laser intensity is reduced by roughly one order of magnitude. The laser beam profile was carefully investigated in order to ensure a homogeneous distribution of energy over the enlarged irradiated spot. The small difference in the intensity of the proton beam distribution. which can be seen in Figure 2(a) for target positions before and behind the focus, is not systematically different for the full measurement campaign, but they differ systematically within one measurement run with the same laser alignment. This might result mainly from the fact that a laser beam profile for a real laser is not only perfectly Gaussian but also to a smaller extent that a real focussing element is not perfectly parabolic. In this case, it can be shown by ray-tracing that there are small differences in local divergence and intensities on small scales within the beam profile.

The observed decrease in the proton beam divergence is not due to the decrease in the laser intensity, which is easily verified by reducing the laser energy with the target at a best

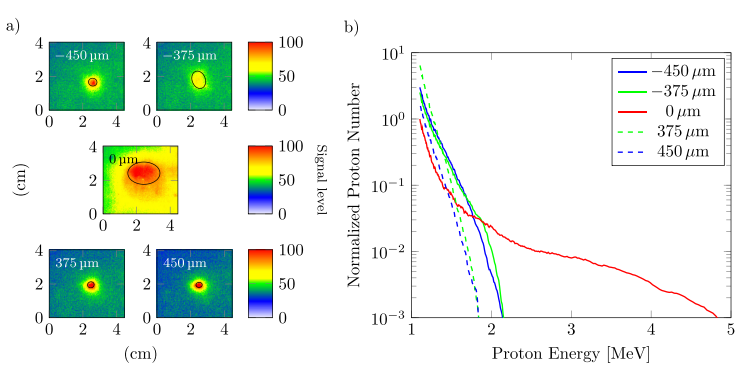

FIG. 2. (a) The proton beam profile for five representative shots measured with the spatial detector for the target foil positioned at best focus (middle) ($r_{0\mu m} \approx 2.5\,\mu$m), 375 μm ($r_{375\mu m} \approx 8.5\,\mu$m), and 450 μm ($r_{450\mu m} \approx 10.5\,\mu$m) before and after the focus (upper/lower). In the defocused case, the proton beam is collimated compared to best focus. The corresponding proton energy distribution in the TN direction is shown in (b).

focus. Instead, it represents a significant relative increase in the number of low energy protons propagating close to the TN direction. The overall lower proton energy results from the de-focusing and therefore the reduced sheath field strength.

Figure 2(b) shows the proton energy distribution observed in the TN direction with the target both at the best focus and defocused by 375 μm. This shows the significant relative increase in the number of low energy protons and a corresponding decrease in protons with the highest energies. This resembles the finding in Ref. 11, but here, it is evident that the increase in low-energy protons in the TN direction is partly due to a reduction in divergence of these protons. Defocusing the laser pulse thus leads to reduced divergence and a significantly increased relative flux of low energy protons in the centre of the beam, even though the maximum proton energy is reduced. Using different aluminum filters in front of the spatial detector reveals as well the finding that in the defocused case, the energy of the protons in the center of the beam decreases, while their particle number increases.

B. Two foci of equal intensity and variable separation with the target foil at the best focus

Using similar measurement methods compared to the previous paragraph, we find as expected that the highest proton energy is obtained with zero separation, i.e., when the two foci overlap and give rise to the highest peak intensity on target. The spatial beam profile is then round in the TN direction, and with the highest energy protons having the smallest divergence, consistent with several previous reports.[2,21,22] When separating the two foci in one direction, we find that the proton beam shape changes from circular to elliptical, with the minor axis in the direction of separation. When the separation is increased further, the proton beam profile becomes round again (see Figure 3(a)). Since this effect occurs both for horizontal and vertical tilt, it is concluded that it is not due to the incidence angle between the laser and target, e.g., caused by an elongated beam profile due to the projection on the target surface. The degree of ellipticity, defined as the ratio between the major and the minor axis of an ellipse fitted to 80% level in each proton dose distribution, is shown in Figure 3(a) for different separation of the foci. When placing a filter in front of the spatial detector, stopping protons with energy below 1.7 MeV, we find that the elliptical shape disappears and we are left with a significantly weaker but circular proton beam, for all values of foci separation.

This observation is similar to the case of defocusing as discussed above, where we observed a collimation in two dimensions of low energy protons when defocusing the laser on the target foil. Here, we also find a collimation of low energy protons, but now only in one direction. This is further verified by measuring the proton energy distribution in the TN direction, as a function of separation between the two foci. Figure 3(b) shows two plots of the proton energy distribution in the TN direction with the two foci separated at 9 μm and 30 μm divided by the distribution obtained with the two overlapping foci. The inset shows the original signal. These plots show the significant increase in the number of low energy protons obtained with the optimum separation, accompanied by a relative decrease in protons with the highest energies. With large separation (30 μm) between the two foci, two independent proton sources are obtained, with the

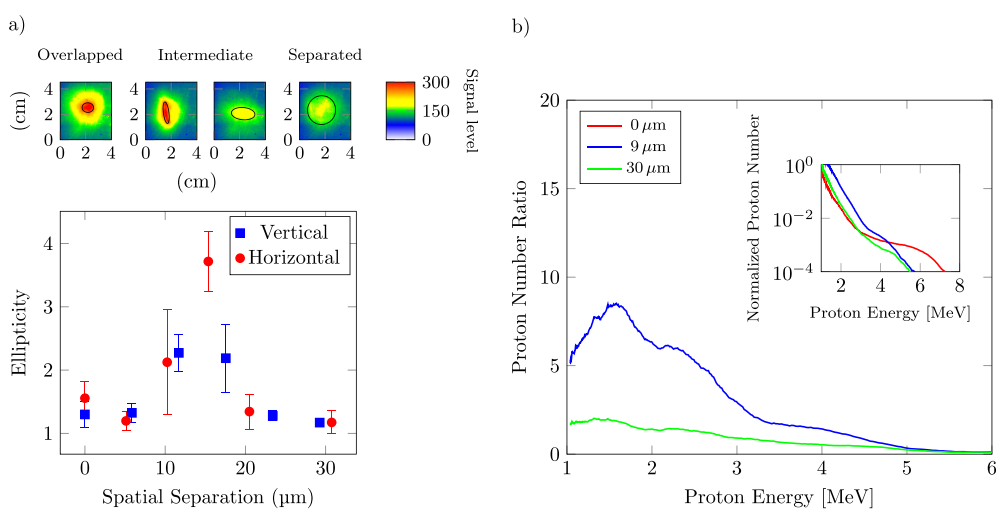

FIG. 3. (a) The upper figures show the measured proton beam profile for the case of two foci being overlapped or separated (horizontally or vertically). For an intermediate separation of ~3 focus diameters, the resulting beam profile becomes elliptical. Overlapping or separating the foci further results in a circular shaped profile. Calculating the ellipticity from the beam profile for different spatial separations in horizontal and vertical direction illustrates the change in the beam profile. (b) The inset shows the proton energy distribution in the forward direction for three different separations between the two focal spots. The large plot gives the energy distribution measured for the different separations divided by the corresponding distribution obtained in the case that both foci overlap (red curve 0 μm separation). For a separation of 9 μm, the number of low energy protons is increased.

same reduction in the maximum energy as for the optimum separation, but without the enhancement in proton flux at low energies. These graphs show that the elliptical shape observed with the spatial detector actually represents a collimation effect, with an increase in proton number in TN direction, and that this collimation mainly affects the low energy protons.

IV. MODELLING

A numerical model was developed to investigate how the size of the laser focus and the separation of the laser foci in the case of two beams may be expected to influence the resulting proton beam distribution. The model (an earlier version of which is described in Ref. 23) calculates how the evolving fast electron density distribution on a grid corresponding to the target rear surface maps into the beam of protons accelerated by TNSA. Fast electrons produced at the target front side in a given laser focus are assumed to be ballistically transported through the target in a beam with a fixed divergence angle. Transport phenomena such as collisions and self-generated fields are not accounted for, but are expected to have a limited effect in relatively thin targets.[24] Recirculation or refluxing of fast electrons within the foil is also neglected. It was validated in simulations that refluxing for a 35 fs-duration laser pulse will occur essentially only for target thicknesses of more than 3 μm. The rear-surface fast electron sheath dynamics, field-ionization of hydrogen, and the direction of projection of the resulting protons are calculated. Unlike more computationally intensive 3D Particle-in-Cell (PIC) modelling, this simpler approach enables a range of parametric scans to be performed relatively quickly, to explore the expected changes to the proton beam profile.

The initial diameter of the fast electron distribution at the target rear side, arising from a laser focal spot of radius r_L at the front side, is given by $d_e = 2(r_L + D\tan\theta_{1/2})$, where $\theta_{1/2}$ is the divergence half-angle of the electron beam as it propagates within the target of thickness D. The sheath profile due to the single laser focus is assumed to be parabolic.[24] In the case of two laser foci, two fast electron distributions are generated at the target rear, with the degree of overlap depending on the separation of the laser foci and the magnitude of $\theta_{1/2}$. In the calculations below, $D = 3\,\mu$m and $\theta_{1/2}$ is set to 30°. The target rear surface is defined as a spatial grid of 80×80 cells of 0.025 μm size, centred at $X = Y = 0$. Electrons arrive over the duration of the laser pulse, which is set equal to 35 fs. The magnitude of the sheath field increases with the increase in the fast electron number density over the first half (rising edge) of the laser pulse and thereafter decreases with time due to lateral expansion of the electron population. The maximum field strength is calculated (assuming a sharp boundary) as $E_{max} = E_0\sqrt{2/e_N}$, where e_N is Euler's number (2.7183), $E_0 = \sqrt{n_{e0}k_BT_e/\epsilon_0}$, ϵ_0 is the vacuum permittivity, and T_e and n_{e0} are the fast electron temperature and maximum density, respectively (as derived in Ref. 25). The fast electron temperature is determined from ponderomotive scaling.[26] The number of fast electrons generated, and thus the fast electron density, is calculated assuming a laser pulse energy of 0.6 J and a laser-to-fast electron energy conversion efficiency of 20%. The conversion efficiency is fixed at this value in the intensity range explored in this study, based on measurements reported in Ref. 27. The initial transverse sheath expansion velocity is set equal to 0.7c (as determined from a previous experiment[8] and simulations[28]), and it decreases exponentially with a 1/e time constant of 60 fs. The rate of reduction in the transverse expansion velocity is based on time- and space-resolved interferometry measurements of a probe beam reported in Ref. 8, scaled to the shorter laser pulse used in the present work. The sheath evolution is calculated in 0.8 fs steps.

Free protons are released by field ionization of a uniform layer of hydrogen, as calculated using the Ammosov-Delon-Krainov (ADK) rate[29] at each time step. Changes in the proton front due to the evolving electric field are calculated, and the local gradient to this front is used to determine the projection of the resulting beam of protons. The detector plane is defined by a 3 cm × 3 cm spatial grid with a resolution equal to 100 μm and is set 6.5 cm from target, to match the experimental conditions. The 2D proton beam spatial-intensity distributions calculated after 200 fs are compared with the measurements.

A. Defocusing

The simulations show that as the laser pulse is defocused, the maximum kinetic energy in the proton beam is reduced, but the number of low-energy protons increases. In addition, more gradual gradients in the sheath field lead to a reduction in the beam divergence. The result is therefore, at the optimum amount of defocusing, a narrow and intense beam of low energy protons. This is illustrated in Figure 4. Further defocusing reduces the laser intensity too much, and the proton beam quickly reduces in brightness. In the simulation, the proton distribution can be analyzed separately for different proton energies. When this is done, it is found that the observed intense and narrow beam is due to protons with kinetic energy less than 70% of the maximum energy obtained at best focus. This is in agreement with the experimental finding.

B. Two spatially separated foci

For the purposes of modelling the case of the two spatially separated foci, it is assumed that the fast electron population produced by each laser spot passes through the thin foil without interaction with the other and emerges at the rear side. The electron density at the rear surface is summed in regions of overlap, which enhances the sheath field. The results of these simulations show that as the spot separation is increased, the proton beam becomes elliptical, with the minor axis in the direction parallel to the separation direction (Figure 5). The maximum degree of ellipticity is obtained when the separation is ~3 focal spot diameters. As the separation is further increased, the two spots each give rise to independent circular proton beams. The spatial separation of these is not noticeable in the far-field detection plane, where a single round proton distribution is therefore observed. These simulation results are in excellent agreement with the experimental finding. In the simulation, the proton distribution can be analyzed separately for different proton energies. When this is done, it is found that the observed ellipticity is

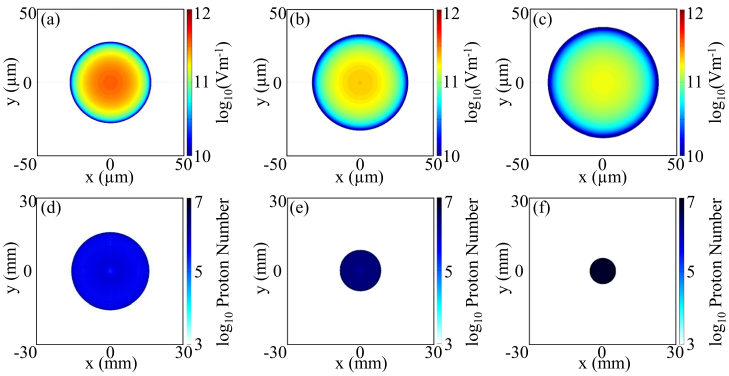

FIG. 4. Simulation results showing the electrostatic sheath field distribution after 200 fs for: (a) $r_L = 5\,\mu$m, (b) $r_L = 10\,\mu$m, and (c) $r_L = 15\,\mu$m. The corresponding proton beam profiles, integrated over the full proton energy range, are shown in (d)–(f), respectively. In the defocused case, the sheath field is larger and weaker, resulting in a proton beam with smaller divergence.

due to protons with kinetic energy less than 70% of the maximum energy. Analyzing only the high energy range of the proton energy distribution, circular beam profiles are found independently of spot separation. This is also in agreement with the experimental findings.

V. CONCLUSION

This article addresses the influence of defocusing and focus shaping of the laser pulse on the generated proton beam profile and the proton energy distribution. Defocusing a single laser beam by a few Rayleigh lengths on the target front surface results in a spatially larger electron distribution directed towards the target rear surface, which has a lower average energy due to the lower initial laser intensity. As a result, the created sheath field on the rear surface covers a larger area, resulting in a larger proton source size, but is weaker than in the case of a focused laser beam. The secondary accelerated beam of protons is more collimated, due to the larger electron distribution at the target rear side leading to a lesser electrostatic sheath field gradient, and therefore more directed electric field distribution. At the same time, the proton flux is increased due to the larger source size of protons being accelerated. This however results in a reduction of the electric field strength, leading to an overall lower proton energy.

By using two laser beams, to create two foci separated by a few laser spot diameters, we could transfer this effect of beam-shaping to a tool in order to generate a customized proton beam of high flux in one direction. In that case, the superposition of the shape of the two foci as well as the resulting electron distribution driven through the target forms an expanded sheath field in one direction at the target rear surface. The beam of accelerated protons is produced with a lower divergence in only one direction. We demonstrated that for our experimental parameters, this effect occurs for a focal spot separation between the two foci of approximately three focal spot diameters. A larger beam separation results in two independent proton sources,[30] each

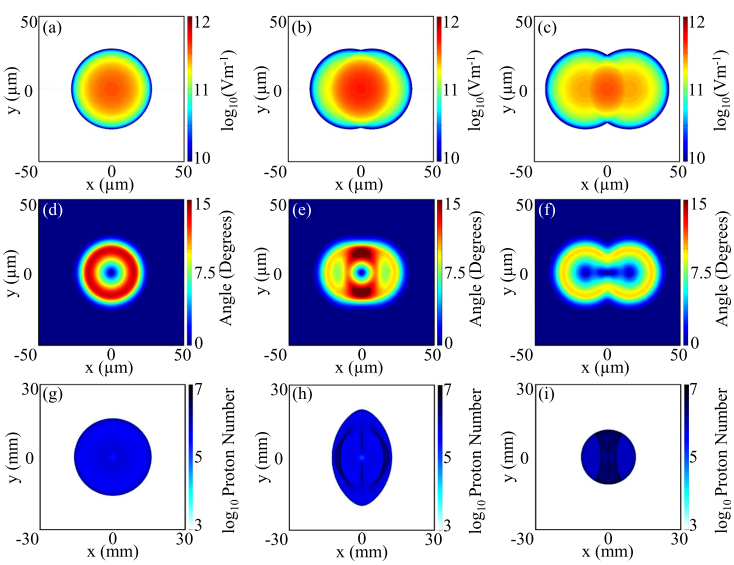

FIG. 5. Simulation results showing the electrostatic sheath field distribution after 200 fs for focal spot separation equal to: (a) 0 μm, (b) 15 μm, and (c) 30 μm. The corresponding angular proton distributions at the target surface are shown in (d)–(f), respectively, and the resulting proton beam distributions in the detector plane are shown in (g)–(i), respectively. At an optimum foci separation, corresponding to case (b), the divergence in the x-direction is significantly reduced.

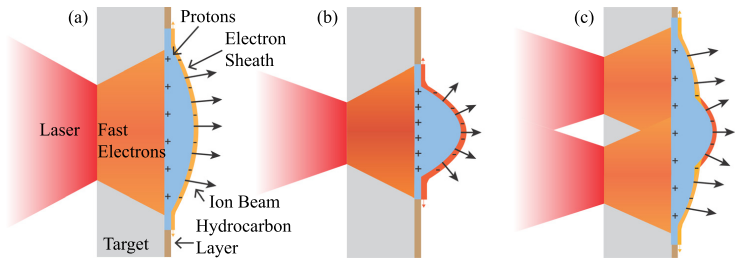

FIG. 6. Schematic illustration of the sheath fields formed by (a) a single defocused laser pulse; (b) two overlapped laser foci; and (c) two laser foci at a separation close to optimum to modify the sheath profile.

with high divergence but relative low energy. A smaller separation results in one proton source with high divergence and high energy, due to the addition of both laser beams. Figure 6 illustrates schematically the sheath expansion in three of the cases investigated experimentally. These results obtained by laser beam splitting presents an indirect measurement of the sheath field size, which was estimated to be in the order of 20 μm. This is in agreement with the results obtained in Ref. 31 using a laser system with a similar pulse duration as in our study, i.e., a few tens of femtoseconds. For longer laser pulse durations, where the electrons can be accelerated and recirculated within the target during the pulse duration, the sheath field becomes larger, as, e.g., obtained in Refs. 32 and 33.

In summary, the proton beam can be shaped by this effect, increasing the proton flux for the low energy proton part. The cost of this effect is a reduction in the maximum proton energy. For distinct applications which do not need high proton energies but a high proton flux with a shaped beam profile (e.g., proton beam writing[34] or radioisotope production[35]), this method might be sufficient to at least preform the beam profile before using collimators to create the desired shape. This enhances the process efficiency and reduces the number of protons which need to be dumped away creating unnecessary activation or radiation at the collimator. Using this technique on high energy lasers could be a scheme to accelerate protons as a fast ignition driver. Here, as well primarily a high proton flux is needed.

In the case studied above, both laser beams interact with the target at the same time. In further studies, one can introduce a temporal delay between the two pulses, which may result not only in a collimation but also in a change of direction of the proton beam due to a possible tilt of the sheath field front at the target rear surface. This may allow for a new method of combined beam collimation and shaping. Exploring the influence of varying the relative intensities of the two pulses is additional options for further studies.

ACKNOWLEDGMENTS

We gratefully thank the Knut and Alice Wallenberg Foundation, including their funding of the PLIONA project, the Swedish Research Council, and the Swedish Foundation for Strategic Research for financial support. We also acknowledge support from EPSRC (Grant No. EP/J003832/1) and Laserlab-Europe/CHARPAC (Grant Agreement No. 284464).

[1]E. L. Clark, K. Krushelnick, J. R. Davies, M. Zepf, M. Tatarakis, F. N. Beg, A. Machacek, P. A. Norreys, M. I. K. Santala, I. Watts, and A. E. Dangor, Phys. Rev. Lett. **84**, 670 (2000).
[2]R. A. Snavely, M. H. Key, S. P. Hatchett, T. E. Cowan, M. Roth, T. W. Phillips, M. A. Stoyer, E. A. Henry, T. C. Sangster, M. S. Singh, S. C. Wilks, A. MacKinnon, A. Offenberger, D. M. Pennington, K. Yasuike, A. B. Langdon, B. F. Lasinski, J. Johnson, M. D. Perry, and E. M. Campbell, Phys. Rev. Lett. **85**, 2945 (2000).
[3]H. Daido, M. Nishiuchi, and A. S. Prizhkov, Rep. Prog. Phys. **75**, 056401 (2012).
[4]M. Passoni, L. Bertagna, and A. Zani, New J. Phys. **12**, 045012 (2010).
[5]S. C. Wilks, A. B. Langdon, T. E. Cowan, M. Roth, M. Singh, S. Hatchett, M. H. Key, D. Pennington, A. MacKinnon, and R. A. Snavely, Phys. Plasmas **8**, 542 (2001).
[6]J. Fuchs, P. Antici, E. d'Humilres, E. Lefebvre, M. Borghesi, E. Brambrink, C. A. Cecchetti, M. Kaluza, V. Malka, M. Manclossi, S. Meyroneinc, P. Mora, J. Schreiber, T. Toncian, H. Pepinm, and P. Audebert, Nat. Phys. **2**, 48 (2006).
[7]J. Fuchs, C. A. Cecchetti, M. Borghesi, T. Grismayer, E. d'Humilres, P. Antici, S. Atzeni, P. Mora, A. Pipahl, L. Romagnani, A. Schiavi, Y. Sentoku, T. Toncian, P. Audebert, and O. Willi, Phys. Rev. Lett. **99**, 015002 (2007).
[8]S. Buffechoux, J. Psikal, M. Nakatsutsumi, L. Romagnani, A. Andreev, K. Zeil, M. Amin, P. Antici, T. Burris-Mog, A. Compant-La-Fontaine, E. d'Humieres, S. Fourmaux, S. Gaillard, F. Gobet, F. Hannachi, S. Kraft, A. Mancic, C. Plaisir, G. Sarri, M. Tarisien, T. Toncian, U. Schramm, M. Tampo, P. Audebert, O. Willi, T. E. Cowan, H. Pépin, V. Tikhonchuk, M. Borghesi, and J. Fuchs, Phys. Rev. Lett. **105**, 015005 (2010).
[9]K. W. D. Ledingham, P. R. Bolton, N. Shikazono, and C. M. C. Ma, Appl. Sci. **4**, 402 (2014).
[10]C. M. Brenner, J. S. Green, A. P. L. Robinson, D. C. Carroll, B. Dromey, P. S. Foster, S. Kar, Y. T. Li, K. Markey, C. Spindloe, M. J. V. Streeter, M. Tolley, C.-G. Wahlström, M. H. Xu, M. Zepf, P. McKenna, and D. Neely, Laser Part. Beams **29**, 345 (2011).
[11]M. H. Xu, Y. T. Li, D. C. Carroll, P. S. Foster, S. Hawkes, S. Kar, F. Liu, K. Markey, P. McKenna, M. J. V. Streeter, C. Spindloe, Z. M. Sheng, C.-G. Wahlström, M. Zepf, J. Zheng, J. Zhang, and D. Neely, Appl. Phys. Lett. **100**, 084101 (2012).
[12]J. S. Green, D. C. Carroll, C. Brenner, B. Dromey, P. S. Foster, S. Kar, Y. T. Li, K. Markey, P. McKenna, D. Neely, A. P. L. Robinson, M. J. V. Streeter, M. Tolley, C.-G. Wahlström, M. H. Xu, and M. Zepf, New J. Phys. **12**, 085012 (2010).
[13]J. Fuchs, T. E. Cowan, P. Audebert, H. Ruhl, L. Gremillet, A. Kemp, M. Allen, A. Blazevic, J.-C. Gauthier, M. Geissel, M. Hegelich, S. Karsch, P. Parks, M. Roth, Y. Sentoku, R. Stephens, and E. M. Campbell, Phys. Rev. Lett. **91**, 255002 (2003).
[14]M. Schollmeier, K. Harres, F. Nürnberg, A. Blazevic, P. Audebert, E. Brambrink, J. C. Fernández, K. A. Flippo, D. C. Gautier, M. Geißel, B. M. Hegelich, J. Schreiber, and M. Roth, Phys. Plasmas **15**, 053101 (2008).
[15]T. E. Cowan, J. Fuchs, H. Ruhl, A. Kemp, P. Audebert, M. Roth, R. Stephens, I. Barton, A. Blazevic, E. Brambrink, J. Cobble, J. Fernández, J.-C. Gauthier, M. Geissel, B. M. Hegelich, J. Kaae, S. Karsch, G. P. Le Sage, S. Letzring, M. Manclossi, S. Meyroneinc, A. Newkirk, H. Pépin, and N. Renard-LeGalloudec, Phys. Rev. Lett. **92**, 204801 (2004).
[16]P. K. Patel, A. J. Mackinnon, M. H. Key, T. E. Cowan, M. E. Foord, M. Allen, D. F. Price, H. Ruhl, P. T. Springer, and R. Stephens, Phys. Rev. Lett. **91**, 125004 (2003).
[17]M. Roth, A. Blazevic, M. Geissel, T. Schlegel, T. E. Cowan, M. Allen, J.-C. Gauthier, P. Audebert, J. Fuchs, J. Meyer-ter-Vehn, B. M. Hegelich,

S. Karsch, and A. Pukhov, Phys. Rev. Spec. Top. - Accel. Beams **5**, 061301 (2002).
[18]C. Brabetz, S. Busold, T. Cowan, O. Deppert, D. Jahn, O. Kester, M. Roth, D. Schumacher, and V. Bagnoud, Phys. Plasmas **22**, 013105 (2015).
[19]B. Aurand, M. Hansson, L. Senje, K. Svensson, A. Persson, D. Neely, O. Lundh, and C.-G. Wahlström, Laser Part. Beams **33**, 59 (2015).
[20]J. S. Green, M. Borghesi, C. M. Brenner, D. C. Carroll, N. P. Dover, P. S. Foster, P. Gallegos, S. Green, D. Kirby, K. J. Kirkby, P. McKenna, M. J. Merchant, Z. Najmudin, C. A. J. Palmer, D. Parker, R. Prasad, K. E. Quinn, P. P. Rajeev, M. P. Read, L. Romagnani, J. Schreiber, M. J. V. Streeter, O. Tresca, C.-G. Wahlström, M. Zepf, and D. Neely, Proc. SPIE **8079**, 807991 (2011).
[21]F. Nürnberg, M. Schollmeier, E. Brambrink, A. Blazevic, D. C. Carroll, K. Flippo, D. C. Gautier, M. Geißel, K. Harres, B. M. Hegelich, O. Lundh, K. Markey, P. McKenna, D. Neely, J. Schreiber, and M. Roth, Rev. Sci. Instrum. **80**, 033301 (2009).
[22]J. Schreiber, S. Ter-Avetisyan, E. Risse, M. P. Kalachnikov, P. V. Nickles, W. Sandner, U. Schramm, D. Habs, J. Witte, and M. Schnürer, Phys. Plasmas **13**, 033111 (2006).
[23]M. N. Quinn, D. C. Carroll, X. H. Yuan, M. Borghesi, R. J. Clarke, R. G. Evans, J. Fuchs, P. Gallegos, L. Lancia, and K. Quinn, Plasma Phys. Controlled Fusion **53**, 124012 (2011).
[24]X. H. Yuan, A. P. L. Robinson, M. N. Quinn, D. C. Carroll, M. Borghesi, R. J. Clarke, R. G. Evans, J. Fuchs, P. Gallegos, L. Lancia, D. Neely, K. Quinn, L. Romagnani, G. Sarri, P. A. Wilson, and P. McKenna, New J. Phys. **12**, 063018 (2010).
[25]T. Grismayer and P. Mora, Phys. Plasmas **13**, 032103 (2006).
[26]S. C. Wilks, W. L. Kruer, M. Tabak, and A. B. Langdon, Phys. Rev. Lett. **69**, 1383 (1992).
[27]P. M. Nilson, W. Theobald, J. Myatt, C. Stoeckl, M. Storm, O. V. Gotchev, J. D. Zuegel, R. Betti, D. D. Meyerhofer, and T. C. Sangster, Phys. Plasmas **15**, 056308 (2008).
[28]P. McKenna, D. C. Carroll, R. J. Clarke, R. G. Evans, K. W. D. Ledingham, F. Lindau, O. Lundh, T. McCanny, D. Neely, A. P. L. Robinson, L. Robson, P. T. Simpson, C.-G. Wahlström, and M. Zepf, Phys. Rev. Lett. **98**, 145001 (2007).
[29]M. V. Ammosov, N. B. Delone, and V. P. Krainov, Sov. Phys. - JETP **64**, 1191 (1986).
[30]O. Lundh, Y. Glinec, C. Homann, F. Lindau, A. Persson, C.-G. Wahlström, D. C. Carroll, and P. McKenna, Appl. Phys. Lett. **92**, 011504 (2008).
[31]O. Jäckel, J. Polz, S. M. Pfotenhauer, H.-P. Schlenvoigt, H. Schwoerer, and M. C. Kaluza, New J. Phys. **12**, 103027 (2010).
[32]J. Schreiber, M. Kaluza, F. Grüner, U. Schramm, B. M. Hegelich, J. Cobble, M. Geissler, E. Brambrink, J. Fuchs, P. Audebert, D. Habs, and K. Witte, Appl. Phys. B **79**, 1041 (2004).
[33]M. Borghesi, A. J. Mackinnon, D. H. Campbell, D. G. Hicks, S. Kar, P. K. Patel, D. Price, L. Romagnani, A. Schiavi, and O. Willi, Phys. Rev. Lett. **92**, 055003 (2004).
[34]F. Watt, M. B. H. Breese, A. A. Bettiol, and J. A. van Kan, Mater. Today **10**(6), 20 (2007).
[35]R. Clarke, S. Dorkings, D. Neely, and I. Musgrave, Proc. SPIE **8779**, 87791C (2013).

Paper XI

Transverse Expansion of the Electron Sheath during Laser Acceleration of Protons

K. Svensson, L. Senje, F. Mackenroth, A. Gonoskov, C. Harvey, B. Aurand, M. Hansson, A. Higginson, M. Dalui, O. Lundh, P. McKenna, A. Persson, & C.-G. Wahlström.

Manuscript.

Transverse Expansion of the Electron Sheath during Laser Acceleration of Protons

K. Svensson,[1,*] L. Senje,[1] F. Mackenroth,[2] A. Gonoskov,[2] C. Harvey,[2] B. Aurand,[1,3] M. Hansson,[1] A. Higginson,[4] M. Dalui,[1] O. Lundh,[1] P. McKenna,[4] A. Persson,[1] and C.-G. Wahlström[1,†]

[1] *Department of Physics, Lund University, 221 00 Lund, Sweden*
[2] *Chalmers University of Technology, 412 58 Gothenburg, Sweden*
[3] *Institut für Laser- and Plasmaphysik, Heinrich-Heine Universität, 40225 Düsseldorf, Germany*
[4] *SUPA Department of Physics, University of Strathclyde, Glasgow, G4 0NG, United Kingdom*

(Dated: August 23, 2016)

Transverse expansion of the electrostatic sheath during target normal sheath acceleration (TNSA) of protons is investigated experimentally using a setup with two synchronized laser pulses. The laser pulses are focused onto 3 µm thick aluminum foils at oblique angle of incidence in the horizontal plane. With the pulses spatially separated by less than three laser spot sizes the resulting proton beam profiles become elliptical. By introducing a small energy difference between the two pulses the ellipses are rotated, by a certain angle, but only if the spatial separation of the two pulses is in the vertical direction. The rotation angle is shown to depend on the relative energy content of the two pulses. These observed effects are found to be very sensitive to the temporal contrast of the laser pulses being good. A simple model describing the resulting transverse size of the electron sheath on the rear of the target as a function of the relative energy content between the foci is presented. The model assumes that the transverse expansion of the sheath, produced by each focus, has a preferred direction, which is in the forward direction in case for $J \times B$ heating.

The study of compact sources of laser-driven energetic proton beams is an active area of research, with many potential applications, such as medical treatment of cancer [1], production of short-lived isotopes [2], and ion implantation [3]. One acceleration process, called target normal sheath acceleration (TNSA), has been explored in several experiments and numerical studies [4, 5]. The process incorporates a short laser pulse, typically shorter than 1 ps, which carries an energy on the order of 1 J or more. The laser is usually focused onto the front surface of a thin foil, which instantly ionizes and becomes a plasma. The resulting plasma electron density, n_e, is higher than the critical density, $n_c = \epsilon_0 m_e \omega^2 / e^2$, for the laser radiation where ϵ_0 is the permittivity of free space, m_e is the electron mass, ω is the laser angular frequency, and e is the elementary charge. This has the effect that the laser pulse cannot propagate through the plasma and is partly reflected, while some of its energy is absorbed and heats electrons, which can traverse the target. There are different heating mechanisms contributing to the hot electron population, such as resonant absorption [6], vacuum heating [7], and $J \times B$ heating [8]. For high intensities and short plasma scale lengths, $J \times B$ heating is expected to dominate, which accelerates hot electrons along the laser propagation axis. As the electrons exit the rear of the target, they set up strong electrostatic sheath fields in which positively charged particles, present on the rear of the target, can be accelerated in the target normal direction.

In a recent study [9], we showed that, by varying the laser intensity distribution on the front of the target, the divergence of the resulting proton beam can be reduced. Irradiating the target simultaneously with two focused laser pulses, spatially separated by less than three spot sizes, the resulting proton beam had an elliptical profile, with its major axis perpendicular to the foci separation axis. However, separating the foci by more than three spot sizes resulted in two independent proton sources on the rear of the target, and the detected proton beam profiles became circular, just as if only one focus was used.

In this paper we present results obtained by altering the intensity ratio, ρ, between the two foci. The experimental study was performed using the multi-terawatt laser system at the Lund Laser Centre, which for this study delivered p-polarized laser pulses with duration of 40 fs (FWHM) and temporal contrast higher than 10^9. The total energy on target was 0.7 J. The experimental setup is illustrated in Fig. 1 [10], in which a split mirror divides the incoming laser pulse in two parts, both being focused by the same f/3 off-axis parabolic mirror (OAP) onto the front of a 3 µm aluminum foil at 45° incidence angle, resulting in two spots, each with a size of 5 µm intensity FWHM. By introducing a small tilt in one part of the split mirror, it is possible to introduce small horizontal and vertical separations between the two resulting foci, and their relative energy content can also be varied by moving the split mirror along its surface. The accelerated protons were detected the spatial detector situated 6.5 cm from the rear of the target. The spatial detector consisted of a scintillating screen (Saint-Gobain BC-408), which is imaged onto one end of a fiber bundle. The other end was imaged by a 12 bit camera, situated outside the experimental vacuum chamber. The scintillator was covered by a 13 µm aluminum foil to protect it from residual laser light and target debris. This foil also stopped protons with energy lower than 1 MeV.

Introducing a small energy difference between two ver-

* kristoffer.svensson@fysik.lth.se
† claes-goran.wahlstrom@fysik.lth.se

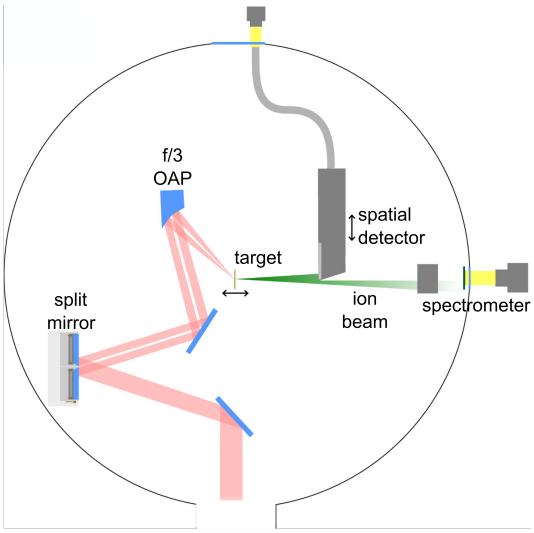

FIG. 1. The p-polarized laser pulse is guided onto the split mirror, where it is divided in two parts. Both of them are then sent towards an f/3 off-axis parabolic mirror, which focused the laser pulses onto the front of a 3 µm thick aluminum target foil. The accelerated protons were detected by either a spatial detector, situated 6.5 cm from the rear of the target, or a magnetic spectrometer. The illustration is taken from a publication [9] describing the experimental setup in more detail.

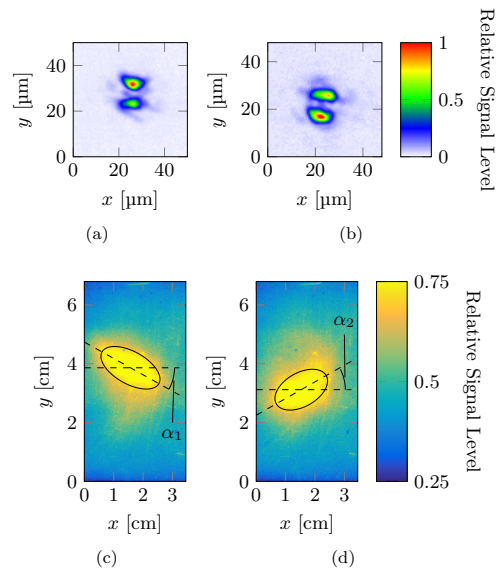

FIG. 2. Laser foci vertically separated 12 µm with (a) more energy on top ($\rho = 1.2$), and (b) more energy at the bottom ($\rho = 0.82$), with corresponding proton beam profiles depicted in (c) and (d), respectively. The proton beam profile rotation angle in (c) is $\alpha_1 = -29°$, and in (d) $\alpha_2 = +30°$. The ellipses are fitted to the 75 % signal level. All color scales are normalized to the maximum signal in each image, and both proton beam profiles are detected 6.5 cm from the target foil.

tically separated foci, elliptical proton beam profiles are obtained, as in Ref. [9]. In addition there is another interesting feature; the elliptical profile, shown in Fig. 2c, became tilted by an angle α_1. If the rotation angle of the ellipse depends on differences in intensity, I, between the two foci, inverting their positions should mirror the proton beam profile about the horizontal axis. This behavior is verified in Fig. 2d, where the target foil is irradiated by the intensity distribution shown in Fig. 2b.

To verify that the tilt is not caused by misaligned foci, we place the separated laser foci at an angle φ. By keeping the distance fixed at $d = 12$ µm and varying φ from 0° to 90°, the resulting α has a one-to-one relation. Thus, the observed effect, shown in Fig. 2, is larger than can be accounted for by any misalignments, estimated to ±5°, of the laser foci separation seen in Fig. 2a and (b).

For a horizontal separation of the laser foci, the elliptical proton beam profile is oriented vertically. However, introducing an energy difference for this configuration only results in very small deviations from the vertical orientation, well within the precision of the laser foci alignment.

These observations can be explained if the leading edge of the expanded electrostatic sheath field is tilted by an angle θ, as illustrated in Fig. 3. Since the incident angle of the laser is 45° in the horizontal plane, the sheath expansion is expected to have a preferred direction along the x-axis if $J \times B$ heating is dominating. Thus, separating the foci vertically (along the y-axis), and introducing a difference in expansion velocity through an intensity difference, the front edge of the resulting electron sheath is expected to become tilted. Separating the foci horizontally (along the x-axis), on the other hand, does not result in any tilt of the front of the electrostatic sheath field, which can be seen by setting $d = 0$ in Fig. 3.

To describe the observed effect, we construct a simple model describing the transverse expansion. In Fig. 3 the two foci are separated vertically by d and they create sheaths of resulting sizes x_1 and x_2. Here, it is assumed that $x_1 > x_2$, thus $\tan\theta = (x_1 - x_2)/d$.

Neglecting any changes in laser spot sizes due to the splitting of the laser pulse, and assuming that the pulse durations are unaffected, we introduce a relative scaling law for the resulting sheath field size as function of laser pulse energy, E, as

$$x(E) = \frac{E}{E_0} D + \mathcal{C}, \tag{1}$$

where E_0 is the threshold energy for proton emission, and $\mathcal{C}$ a constant. A series of PIC simulations showed

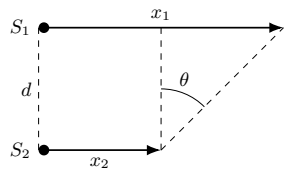

FIG. 3. Simple model where the two laser spots, S_1 and S_2, are separated by a distance d. Each laser spot creates a sheath which extends in the forward direction by x_1 and x_2, respectively.

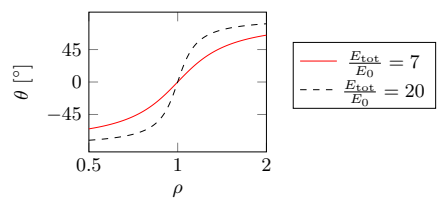

FIG. 4. Rotation angle of the electron sheath, θ, as predicted by Eq. 2 as function of foci energy ratio, ρ, for a few different $E_{\rm tot}/E_0$. It is apparent that for higher $E_{\rm tot}/E_0$ small changes in ρ results in large rotation angles (θ).

how the sheath size depends on the intensity of a single laser pulse, yielding $D = 11\,\mu$m for parameters similar to the experimental conditions. The rotation angle θ can then be determined from Fig. 3 as

$$\tan\theta = \frac{D}{d}\frac{E_{\rm tot}}{E_0}\frac{\rho-1}{\rho+1}, \qquad (2)$$

where $E_{\rm tot} = E_1 + E_2$ is the total laser pulse energy incident on the target, and $\rho = E_1/E_2$ is the ratio between the energy contained in respective foci, S_1 and S_2. Since the major axis of the elliptical proton beam profile is perpendicular to the foci separation axis, simple geometry gives that $\alpha = -\theta$.

The angles in Fig. 2, together with $d = 12\,\mu$m, the corresponding $E_{\rm tot}/E_0$ given by Eq. 2 is 7 for both $\rho = 1.2$ (Fig. 2c) and $\rho = 0.82$ (Fig. 2d). In Fig. 4, θ is plotted as function of ρ for $E_{\rm tot}/E_0 = 7$, and $E_{\rm tot}/E_0 = 20$. It is worth noting that θ is very sensitive to changes in the energy ratio close to $\rho = 1$ for high $E_{\rm tot}/E_0$, i.e. for high laser intensity. The lowest laser energy for proton emission is thus determined to 0.1 J, which is lower than what is seen experimentally. However, this experimental setup does not detect protons with energy lower than 1 MeV due to the aluminum foil covering the scintillator.

The effect of the elliptical beam profiles and their rotation is found to be very sensitive to the temporal contrast of the laser pulses. This is believed to be related to the plasma expansion on the front of the target. If the plasma has expanded, creating a plasma scale length long enough, prior to the arrival of the main pulses, the foci separation is effectively washed out. The model, describing the rotation of the elliptical proton beam profiles, also assumes that $J \times B$ heating is dominating, which is not the case if there is a considerable plasma expansion on the front of the target.

A more detailed study of how θ varies with ρ and $E_{\rm tot}$ could be used to benchmark more elaborate models of the transverse sheath expansion. Using the technique introduced in this paper, it could also be interesting to measure how the transverse expansion velocity and timescales depend on the incidence angle of the laser pulse, and laser intensity.

We acknowledge the support of the Swedish Research Council, the Knut and Alice Wallenberg Foundation, including their funding of the PLIONA project, and the Swedish Foundation for Strategic Research.

[1] S. V. Bulanov and V. S. Khoroshkov, Plasma Phys. Rep. **28**, 453 (2002).
[2] S. Fritzler, V. Malka, G. Grillon, J.-P. Rousseau, F. Burgy, E. Lefebvre, E. d'Humières, P. McKenna, and K. W. D. Ledingham, Appl. Phys. Lett. **83**, 3039 (2003).
[3] L. Torrisi, S. Gammino, A. M. Mezzasalma, J. Badziak, P. Parys, J. Wolowski, E. Woryna, J. Krása, L. Láska, M. Pfeifer, K. Rohlena, and F. P. Boody, Applied Surface Science **217**, 319 (2003).
[4] H. Daido, M. Nishiuchi, and A. S. Pirozhkov, Rep. Prog. Phys. **75**, 056401 (2012).
[5] A. Macchi, M. Borghesi, and M. Passoni, Rev. Mod. Phys. **85**, 751 (2013).
[6] J. P. Freidberg, R. W. Mitchell, R. L. Morse, and L. I. Rudsinski, Phys. Rev. Lett. **28**, 795 (1972).
[7] F. Brunel, Phys. Rev. Lett. **59**, 52 (1987).
[8] W. L. Kruer and K. Estabrook, Phys. Fluids **28**, 430 (1985).
[9] B. Aurand, L. Senje, K. Svensson, M. Hansson, A. Higginson, A. Gonoskov, M. Marklund, A. Persson, O. Lundh, D. Neely, P. McKenna, and C.-G. Wahlström, Phys. Plasmas **23**, 023113 (2016).
[10] B. Aurand, M. Hansson, L. Senje, K. Svensson, A. Persson, D. Neely, O. Lundh, and C.-G. Wahlström, Laser Part. Beams , 1 (2014).

Paper XII

Hollow Microspheres as Targets for Staged Laser-Driven Proton Acceleration

M. Burza, A. Gonoskov, G. Genoud, A. Persson, K. Svensson, M. Quinn, P. McKenna, M. Marklund, & C.-G. Wahlström.

New J. Phys. **13**, 013030 (2011).

New Journal of Physics
The open-access journal for physics

Hollow microspheres as targets for staged laser-driven proton acceleration

M Burza[1,5], A Gonoskov[2,3], G Genoud[1], A Persson[1], K Svensson[1], M Quinn[4], P McKenna[4], M Marklund[2] and C-G Wahlström[1]

[1] Department of Physics, Lund University, PO Box 118, SE-221 00 Lund, Sweden
[2] Department of Physics, Umeå University, SE-901 87 Umeå, Sweden
[3] Institute of Applied Physics, Russian Academy of Sciences, 46 Ulyanov Street, Nizhny Novgorod 603950, Russia
[4] SUPA Department of Physics, University of Strathclyde, Glasgow, G4 0NG, UK
E-mail: matthias.burza@fysik.lth.se

New Journal of Physics **13** (2011) 013030 (14pp)
Received 21 July 2010
Published 21 January 2011
Online at http://www.njp.org/
doi:10.1088/1367-2630/13/1/013030

Abstract. A coated hollow core microsphere is introduced as a novel target in ultra-intense laser–matter interaction experiments. In particular, it facilitates staged laser-driven proton acceleration by combining conventional target normal sheath acceleration (TNSA), power recycling of hot laterally spreading electrons and staging in a very simple and cheap target geometry. During TNSA of protons from one area of the sphere surface, laterally spreading hot electrons form a charge wave. Due to the spherical geometry, this wave refocuses on the opposite side of the sphere, where an opening has been laser micromachined. This leads to a strong transient charge separation field being set up there, which can post-accelerate those TNSA protons passing through the hole at the right time. Experimentally, the feasibility of using such targets is demonstrated. A redistribution is encountered in the experimental proton energy spectra, as predicted by particle-in-cell simulations and attributed to transient fields set up by oscillating currents on the sphere surface.

[5] Author to whom any correspondence should be addressed.

Contents

1. Introduction

Laser-driven ion acceleration is an area of research that currently attracts significant scientific interest. The ion beams produced in these experiments have several attractive characteristics, such as very low transverse emittance and small virtual source size [1] together with a short pulse duration (at the source). Proposed applications of this possibly compact ion beam source include ion radiotherapy for cancer treatment [2, 3], isotope production for medical imaging techniques [4], proton radiography of inertial fusion plasmas [5] and implementation as injectors for future ion accelerators.

In a typical experiment, a high-power laser pulse of short duration, $\leqslant$ps, is focused on the surface of a thin foil to an intensity exceeding $10^{19}\,\mathrm{W\,cm^{-2}}$. The laser interacts with target electrons and a population of hot electrons with a Maxwellian temperature of typically a few MeV is generated. A large fraction of these electrons traverse the target and build up exceptionally high electrostatic fields, $\sim$TV m^{-1}, at the rear surface of the foil, in a direction normal to the target surface. Atoms on the target surface are rapidly field ionized and accelerated. This is referred to as target normal sheath acceleration (TNSA) [6]. Because of the presence of hydrocarbon and water vapour on the surfaces of the foils (in typical vacuum conditions $\sim 10^{-5}$ mbar), protons are the dominating ion species. Due to their high charge-to-mass ratio, protons are more efficiently accelerated than heavier ions.

The acceleration of protons behind the target foil is very rapid, due to the high field strength. However, this field is present during a short time only, limiting the maximum energy reached by the protons. The energy spectra of these proton beams exhibit a longitudinal emittance comparable to that of conventional accelerators, with a quasi-exponential shape and a distinct cut-off energy [6]. The divergence of the proton beam is typically $\sim 30^{\circ}$ half-angle. Significant theoretical and experimental efforts have been devoted to the exploration of a means of boosting the maximum proton energy without the use of increasingly larger laser systems [7, 8].

Practical limitations in laser size and costs, laser materials and repetition rate are necessitating alternative or modified laser acceleration schemes and targets in order to further increase the peak proton energy. It has been found that the maximum proton energy and laser-to-ion energy conversion is enhanced by the use of ultra-thin targets in combination with laser pulses of high temporal contrast [9]. Staging, i.e. combining two or more accelerator stages in series,

may be one way to post-accelerate a selected portion of the protons accelerated in a preceding TNSA stage and thus raise the maximum proton energy and reduce the energy spread [10]. In parallel, extensive studies on controlling beam parameters such as collimation and means to produce quasi-monoenergetic energy distributions have been carried out [11, 12]. In particular, mass-limited targets can be used to reduce the energy spread of the protons [13]–[15]. Curved target foils [16], electrostatic charging of specially shaped targets [17] and separate focusing cylinders [18] enable spatial shaping of the proton beam.

In addition, experiments and numerical modelling have shown that while part of the hot electron distribution is passing through the target foil, a significant part is also spreading laterally along the target. McKenna *et al* [19] found that, when these electrons reach the target edges, after a time determined by the geometrical size of the target and the lateral electron transport velocity, they establish quasi-static electric fields, similar to the one produced behind the target during TNSA, resulting in ion acceleration from the edges. Normally, this mechanism just represents a loss of absorbed laser energy, which is converted to hot electrons but not contributing to the quasi-static sheath built up at the target rear side. In a recent study [15], however, using very small diameter targets, the refluxing of transversely spreading electrons was found to enhance and smooth the sheath field for TNSA from the rear surface.

In this paper, we discuss the use of hollow microspheres, as novel targets for laser acceleration of protons. With this target, several of the above features are combined, which may facilitate improved laser-to-proton efficiency, eventually leading to increased proton energy and reduced divergence. Lateral electron transport is here utilized to set up a post-acceleration field for staged acceleration.

The basic idea behind our approach is to use hollow microspheres with diameters of about 10–50 μm and sub-micrometer wall thickness. In each sphere a small circular opening is made. We refer to the position of this opening as the 'north pole' (see figure 1). A short pulse laser irradiates the sphere at the 'south pole', where TNSA takes place. The primary proton direction will be along the z-axis, defined as the axis from the south pole passing through the north pole of the sphere. The spherical surface, with TNSA taking place from the concave side, results in a collimated or even converging proton beam. Therefore, all the protons can be made to pass through the opening at the north pole. In addition—and this is the key point—electrons leaving the laser focus laterally in any direction along the sphere surface will be guided on different longitudes over the sphere and eventually reach the edge of the opening at the north pole simultaneously after some given time. A very strong quasi-static electric field is then formed in the opening, along the z-axis. This quasi-static field will post-accelerate protons passing through the opening at the correct time.

In our approach to test this idea, theoretical and experimental studies go hand in hand:

To test the experimental feasibility, we perform experiments, at the Lund High Power Laser Facility, with commercially available hollow microspheres of 50 μm diameter.[6] The walls of these spheres are made of glass with a thickness of 0.5–1 μm and coated with a $\sim$50 nm silver layer (see the inset of figure 1), which facilitates the optical alignment and guiding of electrons along the sphere surface. Openings of different sizes are laser micromachined. We present these experiments in section 2, including target preparation, fixation and alignment in the experimental setup together with first results.

[6] Such spheres are very low weight and low cost objects. They weigh only some tens of ng each and cost $\sim$1 USD for 10^5 Ag-coated spheres. The manufacturing of the hole at the north pole, however, is part of the local target preparation and not included in the price.

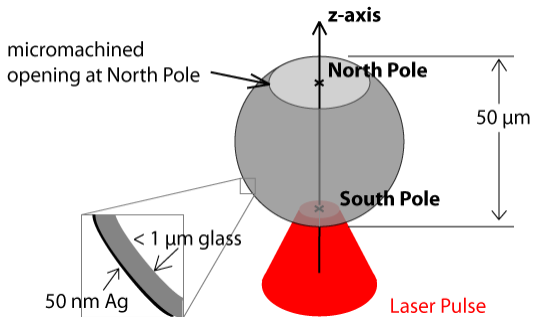

Figure 1. A glass hollow microsphere, with an ∼50 nm silver coating on its $\leqslant 1\ \mu$m thick wall, is struck by a laser pulse at the 'south pole'. TNSA protons are emitted through a circular opening at the 'north pole' and post-accelerated.

In parallel, we perform particle-in-cell (PIC) simulations of hollow conducting spheres with openings, irradiated by short laser pulses. These simulations, presented in section 3, qualitatively describe the dynamics involved.

We discuss the outlook and prospects for further experiments in section 4 and present the conclusions in section 5.

2. Experiment

2.1. Target preparation

Isolated spheres are suspended into a nylon mesh grid, where both the front and back sides of each sphere are accessible for further processing. Openings in the spheres are made with a confocal microscope-based laser micromachining setup. In a two-step process the silver coating is ablated in a well-defined region on the sphere surface, followed by ablation of the glass substrate. This is done with a lateral resolution of about 2 μm utilizing a femtosecond laser system running at 10 Hz repetition rate. Real-time target observation and a high numerical aperture in the setup facilitate both high drilling accuracy and control in the transverse direction, while at the same time preventing the TNSA surface inside the sphere from being damaged in the process.

Afterwards, the target, which is still fixed in the nylon mesh, is mounted in a holder. This also accommodates a gold mesh, placed close to the sphere's north pole, to extract information about proton trajectories, as will be discussed later.

2.2. Experimental setup

The Lund multi-terrawatt laser, which is a Ti : sapphire system based on chirped pulse amplification (CPA), is used for this experiment. In this experiment, it is tuned to 850 mJ pulse energy at 805 nm centre wavelength with a typical pulse duration of 42 fs FWHM. Due to the sub-micron thickness of the sphere walls and the thin silver coating on them, an amplified spontaneous emission (ASE) contrast better than 10^8 some tens of picoseconds prior to the pulse peak is desirable.

IOP Institute of Physics DEUTSCHE PHYSIKALISCHE GESELLSCHAFT

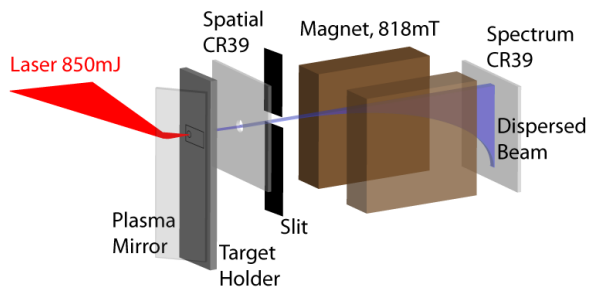

Figure 2. The laser pulse (red) is impinging on the PM at Brewster's angle, which reflects the pulse onto the target at normal incidence. After some centimetres of free passage the resulting particle beam (blue) reaches a CR-39 detector plate, which has the function of providing a lateral image of the beam profile and at the same time enabling a fraction of the beam to enter the slit of a subsequent permanent magnet spectrometer. After traversing the field, a vertically dispersed spectrum is recorded on a second CR-39 plate.

To optimize contrast on a very fast timescale, the convergent, horizontally polarized laser pulse hits a dielectric plasma mirror (PM) at Brewster's angle (3.0 ± 0.2 mm) prior to the primary focus. At this location, the PM is operating at $(8.5 \pm 1.1) \times 10^{15}$ W cm^{-2} spatially averaged peak intensity over the beam diameter (I_{centre}/e^2). When activated, it deflects the laser beam onto the target, at normal incidence (see figure 2).

Plasma mirror characteristics have been investigated by many groups (see e.g. [20]–[22]). A PM assembly, similar to the one applied in the present experiment, was utilized by Neely *et al* [9], using the Lund laser system. In that experiment, proton beams from Al foil targets as thin as 20 nm were observed. Our experiment relates to that one as the very thin silver coating on our target surface is of comparable thickness. Ray tracing, taking a 22 nm FWHM broad Gaussian spectrum and a p-polarized converging beam into account, predicts a contrast increase by a factor of 100 in our experiment (assuming a maximum reflectivity $\sim$50% from the PM [22]).

Together with a third-order autocorrelation contrast measurement, 2 ps prior to the main pulse, a contrast better than 10^6 on the target can be guaranteed for an intact rear TNSA surface during the first phase of acceleration. This contrast is due to non-perfect compression in the CPA chain and should not be mistaken for the ASE contrast, encountered on a longer picosecond timescale prior to the main pulse, which is of the order 10^{11} on the target.

The infrared (IR) pulse is focused by an $f/3$ off-axis parabolic mirror (OAP) down to a 4.4 μm spot diameter (intensity FWHM), containing 39% of the total energy and reaching a peak intensity of $\sim 3 \times 10^{19}$ W cm^{-2}. Target positioning is accomplished by a confocal imaging system: an expanded HeNe laser beam is superimposed with the IR and a confocal reflection from the silver-coated target surface is imaged, utilizing the OAP as an objective.

The detector system for protons, designed to simultaneously provide a spatial beam profile and a spectrum, is depicted in figure 2. It consists of a primary CR-39 plate at some centimetres distance from the target, which is utilized to characterize the transverse spatial beam profile. This plate is covered by a 6 μm Al foil, which stops protons below 0.5 MeV [23]. At its centre,

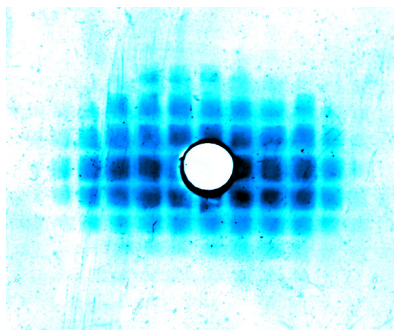

Figure 3. Proton beam profile on a CR-39 plate showing a magnified Au mesh image, recorded (24 ± 0.5) mm distance from the target.

a $\sim$4 mm diameter hole enables protons close to the target normal axis to continue to the momentum dispersive part of the detector and access an 88 μm wide entrance slit of a permanent magnet spectrometer, where they traverse a 51 mm long and 818 mT strong effective field. The vertically dispersed proton spectrum is then recorded by a second CR-39 plate with an accuracy of ± 0.2 MeV at 4 MeV proton energy. By this arrangement, spectra can be correlated to the lateral position within the particle beam.

2.3. Experimental measurements and results

After optimization of the PM working distance with the help of proton beams originating from flat 400 nm thick Al foil targets, shots were taken on machined and unmachined microspheres as well as on 0.9 μm thick Mylar foil targets.

Several shots were taken on machined microspheres with holes of typically 18 μm diameter. An example of a proton beam imprint originating from such a sphere on the spatial CR-39 plate, covered by 6 μm Al and located at (24.0 ± 0.5) mm distance from the target, can be seen in figure 3.

One can see a slightly oval beam profile. This slight asymmetry can be attributed either to a non-uniform Ag coating on the sphere's south pole or to grazing incidence of the laser energy around the z-axis due to the curved sphere surface: at a given latitude, the linear polarization of the laser pulse will be incident as p- or s-polarization on the spherical surface, depending on the azimuthal angle. Polarization effects will also facilitate different strengths of the surface currents, depending on the longitude where electrons propagate around the sphere [24].

One can further see the imprint of the earlier mentioned Au mesh on the spatial proton beam image, which is introduced into the proton beam path close to the target. This rectangularly shaped 4 μm thick mesh features squared holes with a nominal aperture of 11×11 μm^2 and a lateral wire width of 5 μm. It is fixed at (165 ± 2) μm distance from the rim of the opening of the microsphere. The motivation to introduce this mesh is twofold: firstly, it verifies that protons contributing to the signal on the spatial CR-39 plate are not due to edge emission at the north pole, which would have resulted in a distinctively different shadow image. Secondly, thanks to this mesh the protons can be shown to come from a virtual source located (54 ± 12) μm from the inner sphere TNSA surface, i.e. very close to the opening. This estimate is valid for the majority

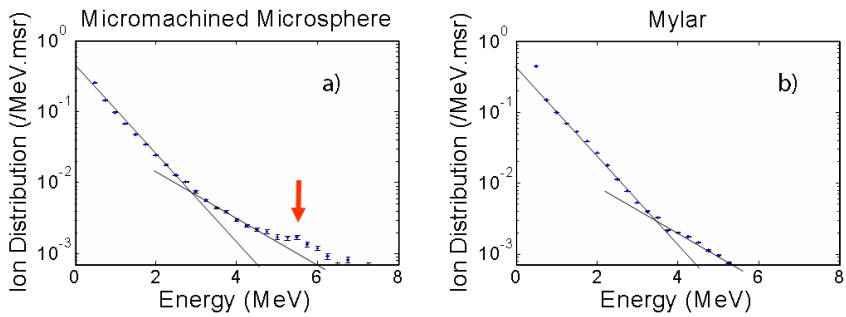

Figure 4. Normalized proton spectra from a microsphere target (a) and a Mylar plane foil (b). The red arrow in (a) indicates a region of constant yield in contrast to the strictly decreasing number density from plane foil TNSA experiments, such as the one depicted in (b); black lines are a dual-temperature guide to the eye.

of particles traversing the opening at late times, where we expect the surface oscillations to have vanished. In order to visualize the effects of a transient field emanating from the rim of the microsphere opening, one would have to filter this image to the appropriate energy. However, as will be discussed later, with our present experimental parameters, we expect only the fastest particles to be affected by these fields, so a filtered signal would become very weak.

By neglecting Coulomb repulsion between protons in the beam, and tracing proton trajectories further back, one can make a rough estimate about the proton emission surface. We find that proton emission seems to occur from a solid angle covering $\approx 140\pi$ msr of the inner shell, measured from the centre of the sphere. This compares to a focal spot, covering $\approx 8\pi$ msr (intensity FWHM), and is consistent with previous observations of the TNSA surface source area being considerably larger than the laser focus [25, 26]. The virtual proton source in a flat foil TNSA experiment [27] was pinpointed to several hundreds of microns distance before the target front side, i.e. the laser-irradiated side. A spherical target, such as the one used for isochoric heating [28, 29], combines ballistic proton propagation with target curvature and an altered electron distribution. A particle focus near the north pole is consistent with these findings.

To further verify that the protons are indeed emitted from the sphere interior, we irradiate closed hollow microspheres that have not gone through the laser micromachining stage. Lacking hydrogenic contaminations, such as water vapour, on the interior surface of the sphere, TNSA of protons is not expected to occur there. Indeed no protons with energies sufficient to be recorded by our diagnostics ($E_{\mathrm{proton}} > 0.8$ MeV) are observed. In addition, lacking the opening and retaining the silver coating, return currents will prevent the formation of a strong edge field at the north pole. This will be further discussed in section 3.1.

Spectra from sphere targets with openings between 18 and 20 μm were taken and a typical spectrum can be seen in figure 4(a). A clear high-energy 'cut off' is not visible in the data, and values above 8 MeV are ignored to ensure that the data presented here are at least one order of magnitude above the noise level. Reference shots are taken on flat 0.9 μm thick Mylar foil targets. A typical proton spectrum can be seen in figure 4(b). Even though the laser absorption

and particle yield are expected to be different as compared to the silver-coated glass surface of the microspheres (∼30 times higher particle number), those shots provide reference spectra, enabling the identification of special features in the microsphere spectra.

All microsphere spectra from the experimental study look very similar, but with an integrated particle yield varying by a factor of 4, which is twice as much as for the Mylar targets. There are indeed features present that could possibly be attributed to a secondary field interaction and a post-acceleration by a secondary field at the sphere opening, which is still prevailing during arrival of the fastest protons. In all microsphere spectra, there is a slight modification of particle yield between 5.5 and 6.5 MeV, where the counts per energy bin remain nearly constant (figure 4(a), red arrow) as compared to the strictly decreasing dual exponential decay observed from the flat foil targets, shot under the same experimental conditions (figure 4(b)). (Likewise, previous experiments carried out with various planar targets using the Lund laser system [30] have resulted in spectra very similar to the ones presented here for Mylar foils.) The plateau in the microsphere spectra can be understood in terms of a spectral redistribution of the order of 1 MeV of proton energies as a result of a secondary field interaction near the opening. Looking at the experiment the other way around, we can regard the protons as a probe for intracavity fields as well. A two-temperature curve fit provides comparable temperatures for low energies for both the targets ((0.6 ± 0.1) MeV and (0.5 ± 0.3) MeV for spheres and Mylar, respectively) but larger values for the high-energy component from the microsphere spectra ((2.0 ± 0.1) MeV) as compared to the foil spectra ((1.6 ± 0.3) MeV).

In the following section, we will discuss the modelling of the present experiment, giving insights into the dynamic processes of hot electron transport on the sphere surface and motivate the observed spectral features. Beyond that, we will consider a means to enhance the post-acceleration mechanism.

3. Simulations

To improve our understanding of the underlying dynamic processes, we have carried out a number of numerical experiments with the parallel PIC code Extreme Laser–Matter Interaction Simulator (ELMIS), developed by the SimLight group [31]. ELMIS is a relativistic code, which uses a parallel fast Fourier transform (FFT) technique to solve Maxwell's equations.

The processes involved in the setup are essentially of two-dimensional (2D) nature. Thus, we perform 2D simulations in order to retain the appropriate space and time scales while still not compromising the physical outcome. However, the 2D nature restricts the interpretation of these results to a qualitative level as scaling laws behave differently in 2D as compared to 3D space.

In the simulations a linearly polarized TEM00 laser pulse (where electric field lies in the plane of simulation) with $\tau_l = 50$ fs duration (Gaussian profile, FWHM) and a total energy of 1 J is focused to a 10 μm spot on the target surface. The laser field reaches a maximum field strength equal to $\sim 3.5\, a_{\mathrm{rel}}$, where $a_{\mathrm{rel}} = 2\pi mc^2/(e\lambda) \approx 3.2 \times 10^{12}\ \mathrm{V\,m^{-1}}$, e and m are the electron charge and mass, respectively, c is the speed of light and $\lambda = 1$ μm is the laser wavelength. This corresponds to a maximum intensity of $2 \times 10^{19}\ \mathrm{W\,cm^{-2}}$. The target consists of a hollow metal sphere with $D_{\mathrm{S}} = 32$ μm diameter and a 10 μm opening. It has a 0.5 μm thick wall, which in our 2D PIC simulation was considered as a (cylindrical) overdense plasma with the electron density of $50\, n_{\mathrm{crit}}$ and an Au^{6+} ion density of $50\, n_{\mathrm{crit}}/6$, where $n_{\mathrm{crit}} = \pi mc^2/(\lambda^2 e^2) \approx 1.1 \times 10^{21}\ \mathrm{cm^{-3}}$ is the critical density for $\lambda = 1$ μm.

To simulate TNSA, we consider a 100 nm contaminant layer of protons and electrons with a density $10\,n_{\mathrm{crit}}$, covering the internal surface of the target. The simulation is done for a box size of $64\,\mu$m $\times$ $64\,\mu$m (4096×4096 cells) with absorbing boundaries for the fields and accumulating boundaries for the particles. The initial plasma temperature is set to 16 keV, and the cell size is 15.625 nm, which is approximately 4 times the Debye length for the considered plasma. In the simulation, 100 virtual particles per cell are used for the electrons and Au^{6+} ions and 20 particles per cell are used for the protons; the total number of virtual particles is 4×10^7. The time steps are set to $(2\pi/\omega_{\mathrm{p}})/16 \approx 3 \times 10^{-17}$ s, where $\omega_{\mathrm{p}} = (4\pi e^2 50 n_{\mathrm{crit}}/m)^{1/2}$ is the plasma frequency. The duration limit of the simulation is set to when the leading protons in the accelerating bunch reach the simulation box boundary.

3.1. Simulation results

As the laser pulse reaches the target at the south pole it is reflected from the outer overdense plasma surface, initiating electron heating. This time is set to $t = 0$ in the simulation. Subsequently, protons undergo TNSA from the internal surface and move towards the north pole. A part of the heated electrons leave the plasma, thereby producing an electric field retaining part of the electrons to the target surface. Those trapped hot electrons move along the plasma layer, recirculating near the wall and conserving their momentum in the direction along the surface. Eventually they will arrive at the edge of the sphere opening, where they will leave and return to the plasma layer, thus setting up a charge separation field. This process, albeit for a flat target, was discussed and experimentally observed by McKenna *et al* [19]. Due to the relativistic intensity of the laser pulse, the electrons move with a speed close to c, thus forming a bunch size comparable to the longitudinal extension of the laser pulse ($c\tau_l = 15\,\mu$m). This bunch does not effectively carry any charges due to cold return currents within the plasma. However, due to the absence of a return current at the edges, the bunch produces a charge separation field. The simulation shows that this wave is then reflected from the opening at the north pole and heads back to the south pole, where it refocuses, passes through (collisionlessly) and continues moving towards the opening at the north pole again.

The dynamics are illustrated in figure 5(a), where the radial electric field at $3\,\mu$m distance from the sphere surface is plotted over time and latitude angle (180° corresponds to the south pole, while 0° represents the north pole). Figure 5(b) depicts the electric field component E_z along the z-axis, using red and blue colours. The evolution of the proton density along the z-axis is visualized by the grey distributions, in equidistant frames. In both pictures, one can identify large charge separation fields, set up at the rim due to the absence of a return current.

One can identify certain frames where the field becomes large, alternatingly at the north and the south pole. The periodicity can be estimated as $T_{\mathrm{d}} \approx \pi D_{\mathrm{S}}/v_{\mathrm{e}}$, where v_e is the velocity of the surface dipole wave. From our simulations we obtain $T_{\mathrm{d}} \approx 380$ fs, corresponding to a frequency of 2.64 THz and an electron wave velocity of $v_{\mathrm{e}} \approx 0.9\,c$.

When the surface dipole wave reaches the opening it produces electric field maxima at the north pole at times t_1, t_2, t_3 (see labels in figure 5(b)), which can be utilized for proton post-acceleration, i.e. staging. Those maxima exist only during relatively short periods. Thus, the timing of the proton bunch and the electron dipole wave is important. In order to have an effective post-acceleration, one would like protons to be pre-accelerated by the TNSA mechanism in such a way that they traverse the vicinity of the north pole when a maximum in accelerating field is present, resulting in a redistribution of the proton energy spectrum.

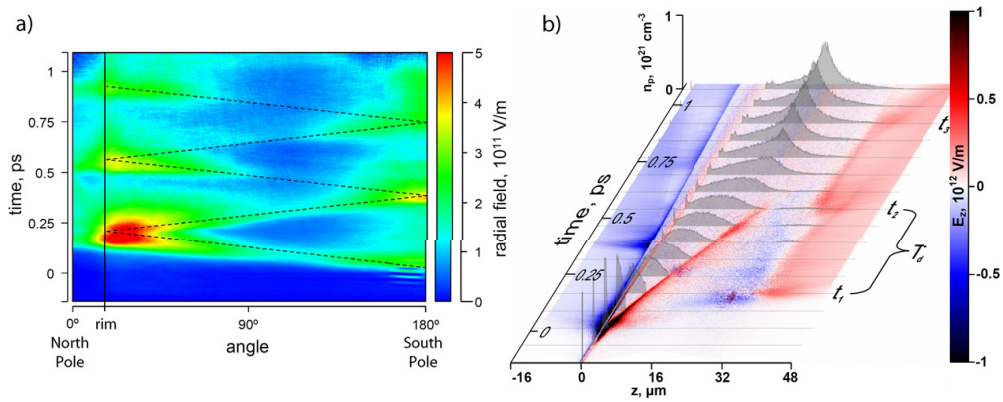

Figure 5. (a) Radial electric field strength, encountered at 3 μm distance from the surface as a function of time. (b) Electric field component E_z along the z-axis; grey plots depict the proton density evolution along the z-axis in equidistant frames.

It should be noted that the surface dipole wave oscillation amplitude decays, which implies that fewer oscillations prior to the proton passage provide a stronger post-acceleration. Additionally to the maxima, a weaker quasi-constant accelerating background field occurs at the opening from t_1 onwards, showing no significant decay on this timescale. Post-acceleration by this background field, which occurs due to a charge up of the sphere during laser irradiation, does not require an accurate timing for the proton passage. However, it provides smaller field strengths as compared to the surface dipole wave oscillations. The effect from both contributions can be seen in figure 6 in the upper marked region, labelled the 'post-acceleration stage', where the evolution of the proton energy distribution is displayed as a function of time. (Note that, due to the limited number of particles, modulations in these spatially integrated spectral distributions manifest themselves as lines that could easily be misinterpreted as trajectories.)

The final state of this simulation is summarized in figure 7 together with the emission angle–energy distribution in the inset, taking all protons into account. From this figure it can be seen that the considered geometry provides additional energy of several MeV for a part of the protons that form a bunch with a small divergence of about 8° half-angle.

4. Discussion and outlook

In the present simulation, a fraction of the protons, with kinetic energies around 9 MeV, reach the opening at time t_3 and pass through a spike in the accelerating field of the post-acceleration stage. However, the acceleration exerted on the protons by this field is relatively small. In 2D simulations, the charge increase due to refocusing of electron trajectories at the north pole is not fully reproduced. Even though qualitatively correct, the simulations are therefore expected to underestimate the field effects.

However, a larger fraction of the particles could be post-accelerated if the relative timing between the surface dipole wave and the proton arrival could be controlled. This could be done

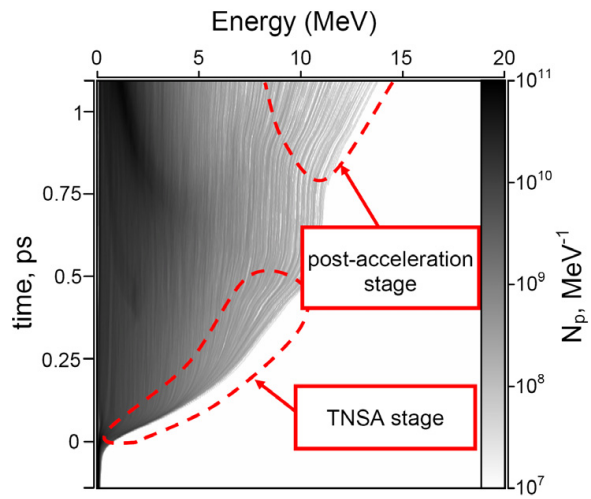

Figure 6. Spatially integrated proton energy distribution along the z-axis with colour-coded number density and its evolution in time.

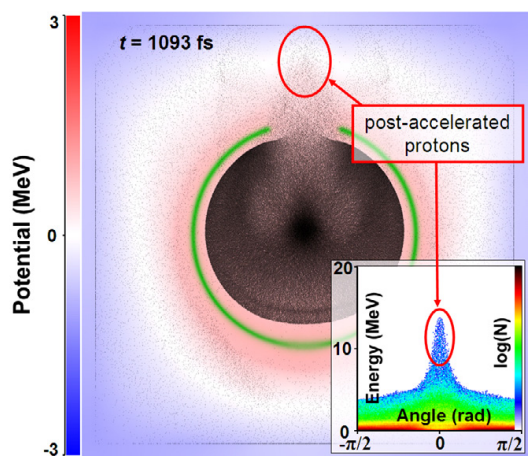

Figure 7. The final instant of the simulation and the corresponding angle–energy distribution of the protons.

either by making use of smaller spheres or oblate spheroidal targets to compensate for their different propagation velocities or by simply increasing the proton temperature in the TNSA stage as they are still moving non-relativistically. In the latter case, an energy of 9 MeV is sufficient for protons to reach the north pole at time t_3, while 37 MeV would be required for a passage at t_2 and GeV energies for t_1. TNSA acceleration to the GeV regime is not feasible, but 37 MeV should be within reach of short-pulse laser systems at intensities below $I_{\text{laser}} = 10^{21}$ W cm^{-2} [32, 33]. In addition, one might be able to reduce the velocity of the surface electron wave by surrounding the sphere with an appropriate dielectric.

With spheroids the advantages of spheres are conserved, but the relative distance for protons and electrons to propagate can be varied. Simulations with oblate spheroidal surfaces, performed as for the spherical targets above, show both stronger acceleration and a narrower collimation of the protons. Experimentally, however, such targets are not as easily available as spheres.

In the experiment, we irradiated the target at normal incidence to obtain maximum symmetry and facilitate direct comparison with our simulations. However, it is well known that by irradiating the target with p-polarized light at an angle, the efficiency of coupling laser energy to the plasma increases. This should, in our case, enhance both TNSA at the south pole and drive a significantly stronger transverse electron current along the target surface [24]. An extension of both simulation and experimental geometry to allow for non-normal incidence irradiation will be a topic for further study.

Finally, we would like to point out that our target has additional interesting features. One of them is an intermediate particle focus slightly outside the spatial boundaries of the target. This could be used for experiments in fundamental physics that require high proton flux, inherently synchronized with a high-power laser beam line. Additionally, as the microsphere acts as a cavity for electron surface dipole waves, it could provide an efficient means to produce THz radiation with high-intensity lasers. In such an experiment almost all the incident laser energy can be absorbed by irradiating the sphere through the opening at the north pole, launching an electron surface wave from the inside.

5. Conclusions

We have introduced a new scheme for staged laser-driven proton acceleration, using hollow microspheres as targets. On the one side of a microsphere, protons are accelerated by TNSA from the concave inner surface of the sphere. Laser-heated electrons that are spreading transversely in the target, as a charge wave, are refocused on the opposite side of the sphere, where they produce a strong but transient charge separation field in an opening located there. Protons passing through the opening at the correct time can thus be post-accelerated. We have done 2D PIC simulations that confirm that this process indeed occurs and that the electrons spread over the sphere as a charge wave. This wave was found to oscillate back and forth over the sphere while decaying in amplitude, forming charge separation fields in the opening at regular intervals. These simulations also show that protons arriving at the correct time, i.e. those protons that have the right kinetic energy, are post-accelerated. Experimentally we have demonstrated the technical feasibility of preparing and irradiating this type of target. In addition, the preliminary results show some signatures of post-acceleration, although the timing between the electron charge wave and the TNSA protons was far from optimal in this first experiment. Further work with improved relative timing is needed for fully exploring the potential of this new scheme and target geometry.

Acknowledgments

We acknowledge support from the Swedish Research Council (including contract no. 2007-4422 and the Linnaeus grant to the Lund Laser Centre), the Marie Curie Early Stage Training Site MAXLAS (MEST-CT-2005-020356) within the 6th European Framework Programme, the Knut and Alice Wallenberg Foundation, the Swedish National Infrastructure for Computing (SNIC)

and the EPSRC (grant no. EP/E048668/1). This research was further partially supported by the European Research Council under contract no. 204059-QPQV. We also thank D C Carroll for processing the CR-39 plates.

References

[1] Cowan T E *et al* 2004 Ultralow emittance, multi-MeV proton beams from a laser virtual-cathode plasma accelerator *Phys. Rev. Lett.* **92** 204801
[2] Malka V *et al* 2004 Practicability of protontherapy using compact laser systems *Med. Phys.* **31** 1587
[3] Linz U *et al* 2007 What will it take for laser driven proton accelerators to be applied to tumor therapy? *Phys. Rev. ST Accel. Beams* **10** 094801
[4] Spencer I *et al* 2001 Laser generation of proton beams for the production of short-lived positron emitting radioisotopes *Nucl. Inst. Methods Phys. Res.* B **183** 449
[5] Mackinnon A J *et al* 2006 Proton radiography of a laser-driven implosions *Phys. Rev. Lett.* **97** 045001
[6] Wilks S C *et al* 2001 Energetic proton generation in ultra-intense laser–solid interactions *Phys. Plasmas* **8** 542
[7] Glinec Y *et al* 2008 Evolution of energy spectrum from laser-accelerated protons with a 100 fs intense prepulse *Appl. Phys.* B **93** 317
[8] McKenna P *et al* 2008 Effects of front surface plasma expansion on proton acceleration in ultraintense laser irradiation of foil targets *Laser Part. Beams* **26** 591
[9] Neely D *et al* 2006 Enhanced proton beams from ultra thin targets driven by high contrast pulses *Appl. Phys. Lett.* **89** 021502
[10] Jaeckel O *et al* 2009 Staged laser ion acceleration *Proc. Conf. on Lasers and Electro-Optics 2009 and 2009 Conf. on Quantum Electronics and Laser Science (CLEO/QELS 2009) (Baltimore, MD, 2–4 June 2009)* pp 1–2
[11] Allen M *et al* 2003 Proton spectra from ultraintense laser–plasma interaction with thin foils: experiments, theory and simulation *Phys. Plasmas* **10** 3283
[12] Brantov A V *et al* 2006 Quasi-mono-energetic ion acceleration from a homogeneous composite target by an intense laser pulse *Phys. Plasmas* **13** 122705
[13] Schwoerer H *et al* 2006 Laser–plasma acceleration of quasi-monoenergetic protons from microstructured targets *Nature* **439** 445
[14] Sokollik T *et al* 2009 Directional laser-driven ion acceleration from microspheres *Phys. Rev. Lett.* **103** 135003
[15] Buffechoux S *et al* 2010 Hot electrons transverse refluxing in ultraintense laser–solid interactions *Phys. Rev. Lett.* **105** 015005
[16] Roth M *et al* 2002 Energetic ions generated by laser pulses: a detailed study on target properties *Phys. Rev. ST Accel. Beams* **5** 061301
[17] Kar S *et al* 2008 Dynamic control of laser-produced proton beams *Phys. Rev. Lett.* **100** 105004
[18] Toncian T *et al* 2006 Ultrafast laser-driven microlens to focus and energy-select mega-electron volt protons *Science* **312** 410
[19] McKenna P *et al* 2007 Lateral electron transport in high-intensity laser-irradiated foils diagnosed by ion emission *Phys. Rev. Lett.* **98** 145001
[20] Dromey B *et al* 2004 The plasma mirror—a subpicosecond optical switch for ultra high power lasers *Rev. Sci. Instrum.* **75** 3
[21] Doumy G *et al* 2004 Complete characterization of a plasma mirror for the production of high-contrast ultraintense laser pulses *Phys. Rev.* E **69** 026402
[22] Ziener Ch *et al* 2003 Specular reflectivity of plasma mirrors as a function of intensity, pulse duration and angle of incidence *J. Appl. Phys.* **93** 768

[23] National Institute of Science and Technology *PSTAR Database* http://www.physics.nist.gov/PhysRefData/Star/Text/PSTAR.html
[24] Psikal J *et al* 2010 Lateral hot electron transport and ion acceleration in femtosecond laser pulse interaction with thin foils *Phys. Plasmas* **17** 013102
[25] Roth M *et al* 2002 The generation of high-quality, intense ion beams by ultra-intense lasers *Plasma Phys. Control. Fusion* **44** 99
[26] Schreiber J *et al* 2004 Source-size measurements and charge distributions of ions accelerated from thin foils irradiated by high-intensity laser pulses *Appl. Phys.* B **79** 1041
[27] Borghesi M *et al* 2004 Multi-MeV proton source investigations in ultraintense laser–foil interactions *Phys. Rev. Lett.* **92** 055003
[28] Roth M *et al* 2005 Laser accelerated ions in ICF research prospects and experiments *Plasma Phys. Control. Fusion* **47** B841
[29] Patel P K *et al* 2003 Isochoric heating of solid-density matter with an ultrafast proton beam *Phys. Rev. Lett.* **91** 125004-1
[30] McKenna P *et al* 2006 High-intensity laser-driven proton acceleration: influence of pulse contrast *Phil. Trans. R. Soc.* A **364** 711
[31] http://www.ipfran.ru/english/structure/lab334/simlight.html
[32] Fuchs J *et al* 2006 Laser-driven proton scaling laws and new paths towards energy increase *Nat. Phys.* **2** 48
[33] Zeil K *et al* 2010 The scaling of proton energies in ultrashort pulse laser plasma acceleration *New J. Phys.* **12** 045015